The coupled dual boundary element-scaled boundary finite element method for efficient fracture mechanics

PhD Thesis

Gareth Bird
School of Engineering and Computing Sciences
Durham University

May 2012

Summary

A novel numerical method is presented for applications to general fracture mechanics problems in engineering. The coupled dual boundary element-scaled boundary finite element method (DBE-SBFEM) incorporates the numerical accuracy of the SBFEM and the geometric versatility of the DBEM. Background theory, detailed derivations and literature reviews accompany the extensions made to the methods constituents necessary for their coupling as part of the present work. The coupled DBE-SBFEM, its constituent components and their application to linear elastic fracture mechanics are critically assessed and presented with numerical examples to demonstrate both method convergence and improvements over previous work. Further, a proof of concept demonstrates an alternative formation of the DBEM that both negates the need for hyper-singular integration and lends itself to a wider variety of imposed boundary conditions. Conclusions to this work are drawn and further recommendations for research in this area are made.

Statement of copyright

Acknowledgements

The author gratefully acknowledges the School of Engineering and Computing Sciences, Durham University for both funding and support for the duration of his studies. In addition to his supervisors, Prof. Jon Trevelyan and Dr. Charles Augarde, the author thanks Prof. Andrew Deeks, Dr. Steve Chidgzey and Dr. Robert Simpson for discussions and input into my work.

For dragging his attitude towards code development out of the twentieth century, a number of people must also be thanked. Thanks goes to Brian Bird for insight into test-driven development frameworks, code structuring, subversion control and advice on debugging when all hope seemed lost. David Koh and colleagues at Tenuki *bv* (www.tenuki.nl) must be also acknowledged for furthering the development of the author's more modern approach to professional computer science and the influence this had on this code.

All those who suffered my ramblings and rants in the name of my work including Paul, Cathy, Steve, Derek, Dimos, Amy, Sarah, Chris, Chris, Richard, Zak, Will, Claire and Xiao Ying are thanked as well as the Technische Universiteit Eindhoven for office space while I wrote up my thesis. Thanks also to Erika for encouragement, inspiration and motivation.

Finally I must thank Gwen for helping and housing me (albeit abroad) and sharing the misery that is writing a thesis alongside employment in a different environment. Nowhere is there such a expert on scaled boundary finite elements whose reluctant knowledge was gained through the unselfish want to help rather than learn. I cannot thank her enough.

Nor Nestlé, for all those delicious Yorkies that kept me going.

Contents

Figures and tables

Nomenclature

Abbreviations

BEM	Boundary element method
BIE	Boundary integral equation
DBEM	Dual boundary element method
DBIE	Displacement boundary integral equation
DOF	Degree of freedom
FEM	Finite element method
SBFEM	Scaled boundary finite element method
SIF	Stress intensity factor
TBIE	Traction boundary integral equation
XFEM	eXtended finite element method

Mathematical notation

$\mathbf{A}$	Matrix of coefficients of unknowns
A_L	SBFEM left-hand side face
A_R	SBFEM right-hand side face
A_k	Constant used in description of general quadratic shape function
B_k	Constant used in description of general quadratic shape function
$\mathbf{B}_i$	SBFEM construction matrix
C	BEM constant used in the DBIE and TBIE
C_i	Constant material properties, $i = 1, 2$
C_k	Constant used in description of general quadratic shape function
D^*_{kij}	TBIE kernel $i, j, k = x, y$
$\mathbf{D}$	Elasticity matrix
E	Young's modulus
$\mathbf{E}_i$	SBFEM construction matrix, $i = 0, 1, 2$
$\mathbf{F}$	SBFEM modal scaling matrix

$\mathbf{G}$	BEM matrix of traction coefficients
$\mathbf{H}$	BEM matrix of displacement coefficients
$\mathbf{I}_n$	Identity matrix of size $n \times n$
$\mathbf{J}$	Jacobian matrix
K_i	Stress intensity factor for mode $i = \mathrm{I}, \mathrm{II}, \mathrm{III}$
ΔK_I	Range of K_I over a load cycle
$\mathbf{K}_\mathrm{S}$	SBFEM stiffness matrix
L	BEM number of elements
M_min	Minimum number of modes needed for error-free modal superposition
N_c	Number of load cycles
N_i	Shape function i
$\mathbf{N}$	Vector of N_i
P_f	BEM field point
P_s	BEM source point
$\mathbf{Q}$	Matrix of $\mathbf{q}_j$
$\mathbf{Q}_K$	Subset of $\mathbf{Q}$ corresponding to bounded domains
$\mathbf{Q}_\infty$	Subset of $\mathbf{Q}$ corresponding to unbounded domains
S^*_{kij}	TBIE kernel $i, j, k = x, y$
T^*_{ij}	DBIE kernel $i, j = x, y$
U^*_{ij}	DBIE kernel $i, j = x, y$
Y	Constant (order 10^0) describing geometric dependency of ΔK_I
$\mathbf{Z}$	SBFEM construction matrix
$\mathbf{a}$	BEM row vector of coefficients of unknown boundary displacements and tractions
a	Crack length
Δa	Change (increment) in crack length
$\tilde{\mathbf{a}}$	BEM row vector of coefficients of known boundary displacements

	and tractions
$\mathbf{b}$	Vector of known constants in linear system of equations
$\mathbf{c}$	SBFEM vector of c_j
$\tilde{\mathbf{c}}$	SBFEM vector of $\tilde{c}_j$
c_j	Constant corresponding to term j of solution to Euler-Cauchy second order partial differential equation
$\tilde{c}_j$	SBFEM contribution factor of mode j
e	BEM element number
f	BEM field point number
$\mathbf{g}_i$	BEM row vector of traction coefficients rows corresponding to row i in $\mathbf{G}$
$\mathbf{g}^e_{i+}$	BEM submatrix of traction coefficients rows corresponding to i and $i+1$ and columns corresponding to e in $\mathbf{G}$
g^e_{kij}	BEM j-direction traction coefficient of node k on element e for source point degree of freedom $i = x,y$, $j = x,y$, $k = 1..3$
$\mathbf{h}_i$	BEM row vector of displacement coefficients rows corresponding to row i in $\mathbf{H}$
$\mathbf{h}^e_{i+}$	BEM submatrix of displacement coefficients rows corresponding to i and $i+1$ and columns corresponding to e in $\mathbf{H}$
h^e_{kij}	BEM j-direction displacement coefficient of node k on element e for source point degree of freedom $i = x,y$, $j = x,y$, $k = 1..3$
$\square_i$	Indexing number of a parameter (e.g. $\mathbf{X}$) as a subscript, i.e. $\mathbf{X}_i$
$\square_j$	Indexing number of a parameter (e.g. $\mathbf{X}$) as a subscript, i.e. $\mathbf{X}_j$
j	Mode number
j_{K_I}	Mode I crack opening mode
j_{K_II}	Mode II crack opening mode
j_x	x-translation mode
j_y	y-translation mode
$\square_k$	Indexing number of a parameter (e.g. $\mathbf{X}$) as a subscript, i.e. $\mathbf{X}_k$

k	Cartesian direction of degree of freedom, $k = x, y$
l_e	Length of element e
m	SBFEM number of modes used in modal superposition
n	Number of degrees of freedom
$n(\Gamma)$	Outward normal with respect to boundary Γ
n_f	Outward normal at field point f
n_{f_i}	Outward normal component at field point f, $i = x, y$
n_s	Outward normal at source point s
p_i	Force of degree of freedom i
$\mathbf{p}$	Vector of p_i
$\tilde{\mathbf{p}}_\mathbf{j}$	SBFEM force mode j
$\tilde{\mathbf{p}}_{ij}$	SBFEM i^{th} component of force mode j
$\mathbf{q}_j$	SBFEM unscaled force mode j
q_{ij}	SBFEM i^{th} component of unscaled force mode j
$r(\Gamma)$	BEM separation from source point as a function of Γ
r_f	BEM discrete separation of source and field points
s	SBFEM circumferential coordinate
t_i	Traction of degree of freedom i
u_i	Displacement of degree of freedom i
$\mathbf{u}$	Vector of u_i
$\tilde{\mathbf{u}}_\mathbf{j}$	SBFEM displacement mode j
$\tilde{u}_{ij}$	SBFEM i^{th} component of displacement mode j
w_{ij}	Williams expansion coefficient, $i = 1..n, j = x, y$
x	Cartesian coordinate
$\mathbf{x}$	Vector of unknowns in linear system of equations
x_0	SBFEM scaling centre x-coordinate
y	Cartesian coordinate

y_0	SBFEM scaling centre y-coordinate
$\mathbf{\Gamma}$	Boundary
$\mathbf{\Xi}$	SBFEM matrix of eigenvectors
$\mathbf{\Lambda}$	SBFEM diagonal matrix of eigenvalues
$\mathbf{\Phi}$	Matrix of φ_j
$\mathbf{\Phi}_K$	Subset of $\mathbf{\Phi}$ corresponding to bounded domains
$\mathbf{\Phi}_\infty$	Subset of $\mathbf{\Phi}$ corresponding to unbounded domains
$\mathbf{\Psi}$	SBFEM construction matrix
Ω	Domain
α	BEM angle of smoothness between adjacent boundary facets
$\gamma_{\max}$	Maximum number of Gauss points used adaptive integration
$\gamma_{\min}$	Minimum number of Gauss points used adaptive integration
$\gamma_\imath$	Number of Gauss points used in iteration $\imath$ of adaptive integration
$\Delta\gamma$	Adaptive integration Gauss point increment rate
ε_i	Stress of degree of freedom i
η	Local coordinate axis
$\boldsymbol{\eta}$	Vector of η_i
η_i	Local coordinate of node i
θ	Polar coordinate angle
θ_f	BEM angular separation of source and field points
θ_p	Crack propagation angle
$\imath$	BEM adaptive integration iteration number
κ	Kosolov constant
$\kappa(\mathbf{X})$	Condition number of matrix $\mathbf{X}$
λ_j	SBFEM eigenvalue associated with mode
$\boldsymbol{\lambda}$	Vector of λ_j
μ	Shear modulus

ν	Poisson ratio
ξ	SBFEM radial coordinate
ξ_Γ	SBFEM constant evaluated at the boundary: $\xi_\Gamma = 1$
$\rho(\theta)$	Factor for scaling values on by Polar coordinate θ
σ_i	Stress of degree of freedom i
τ_g	BEM threshold of numerical accuracy required in adaptive integration of fundamental solution
τ_h	BEM threshold of numerical accuracy required in adaptive integration of fundamental solution
φ_j	SBFEM unscaled displacement mode j
φ_{ij}	SBFEM i^{th} component of unscaled displacement mode j
χ	Local coordinate axis, a subdivision of η

Publications

Author publications and acknowledgements resulting from the present work:

Journal articles

Bird, G.E., Trevelyan, J. and Augarde, C.E., 2010. A coupled BEM/Scaled boundary FEM formulation for accurate computations in linear elastic stress analysis. *Engineering Analysis with Boundary Elements*, 34(6), p599-610

Conference proceedings

Bird, G.E., Trevelyan, J., Augarde, C.E., Deeks, A.J. and Chidgzey, S.R., 2007. Coupling of the BEM with the SBFEM for fracture mechanics problems. In *Proceedings of the 6th UK conference on Boundary Integral Methods*. Durham, Durham University.

Bird, G.E., Trevelyan, J. and Augarde, C.E., 2008a. Efficient calculation of stress intensity factors using a coupled BEM-SBFEM algorithm. In *Programme of the joint 8th World Congress on Computational Mechanics & 5th European Congress on Computational Methods in Applied Sciences and Engineering*. Venice.

Bird, G.E., Trevelyan, J. and Augarde, C.E., 2008b. Coupling of the BEM and SBFEM for fracture mechanics. In *Proceedings of the 16th UK national conference on computational mechanics in engineering*. Newcastle, University of Newcastle.

Bird, G.E., Trevelyan, J. and Augarde, C.E., 2009a. A coupled boundary integral method for accurate computation of stress intensity factors. In *Proceedings of the 17th UK national conference on computational mechanics in engineering*. Nottingham, University of Nottingham.

Bird, G.E., Trevelyan, J. and Augarde, C.E., 2009b. A semi-discontinuous scaled boundary finite element for the coupled BEM-SBFEM. In *Proceedings of the 7th UK conference on Boundary Integral Methods*. Nottingham, University of Nottingham.

Acknowledgement

Chidgzey, S.R., Trevelyan, J. and Deeks, A.J., 2008. Coupling of the boundary element method and the scaled boundary finite element method for computations in fracture mechanics. *Computers and Structures*, 86(11-12), p1198-203.

1 Introduction

1.1 Introduction

The knowledge of cracks and their behaviour under stress can be invaluable in increasing the longevity of fractured mechanical systems. Accurate stress analysis that reliably estimates the severity of cracks and their need for attention can assist in maintenance programs and reduce financial overheads by the prediction and prevention of otherwise potentially catastrophic failures. This is of particular importance in industries that operate under low factors of safety or with tight profit margins. A recent and extreme example of such failure through fracture fatigue is the 2009 crash of the Aerospatiale (Eurocopter) AS332 L2 Super Puma near Peterhead, Scotland (Air Accidents Investigation Branch, 2011).

Academic problems can typically be solved to determine accurately and quickly some estimation of this need for intervention. Fundamental engineering principles may yield a solution analytical in nature without the need for any approximation. However, the range of problems that can be solved in this way is limited and if assumptions are made, such as simplifying the domain geometry, boundary conditions and material properties etc, such

that the problem can be solved analytically, this may lead to unacceptable inaccuracies. A typical engineering problem will require some degree of approximation in its definition, solution or both. So while computational modelling may provide a more accurate representation of the problem, the trade-off is in the numerical approximation of its solution.

Through improved computer aided design, a numerical representation of the problem can be defined with ease. Cross-application support has led inevitably to its increased standardisation. Thus, focus is geared more towards improving the solution to the existing geometric definition than using existing solutions that require simplification of the geometric definition. Typically both the geometry and its boundary conditions are approximated by some form of domain or boundary discretisation process, where the relative behaviour of discrete portions is approximated and solved globally by some numerical method. The most prominent is the versatile *finite element method* (FEM). There are many alternatives, however, including meshless and boundary integral methods, as well as more advanced methods based on the FEM.

The aim of the work presented here is the development and assessment of a new algorithm for the accurate solution of general fracture mechanics problems that retains the geometric flexibility expected by engineers. This is achieved by the coupling of the *boundary element method* (BEM) and the *scaled boundary finite element method* (SBFEM). The SBFEM is known to be suitable for applications to academic fracture mechanics problems, but is limited by geometric constraints that make it less suited to real engineering problems. The BEM is more geometrically-versatile, but, like the FEM, is known to be hindered by inaccuracies in the modelling of displacements around a loaded crack tip when a polynomial-based solution is assumed. The

approach taken in the present work is to couple the BEM and SBFEM in order to exploit their respective benefits.

1.2 Linear elastic fracture mechanics model

There are many models describing how materials deform and, under each model, many techniques, each with their own assumptions, advantages, disadvantages, accuracies, efficiencies and general suitability for particular applications. Under macro-scale stress analysis, forces acting over the infinitesimal area of a crack tip result in stress singularities which have traditionally been both academically interesting and computationally challenging. Attempts to describe a physical interpretation of the infinite stress found at the crack tip under a *linear elastic fracture mechanics* (LEFM) model may not be entirely practical.

It is fair to state that the LEFM model breaks down long before local stresses could be considered 'infinite'. Moreover, modelling improvements can be made by the consideration of basic plasticity right through to statistical (quantum) analysis of the material's atomic structure, combined with multi-scale analysis combining each model's respective advantages. However, it is also fair to state that real engineering problems exhibit rapidly-varying stresses and the LEFM model offers practical approximations in the vicinity of the crack with lower computational effort than more complete frameworks. Once the factors of safety found in engineering design and analysis are considered, a simplistic LEFM model may suffice.

1.3 Stress intensity factors

The stress singularities associated with a LEFM model found around the tip of

a loaded crack can be defined in terms of their independent modes of deformation described in Figure 1.

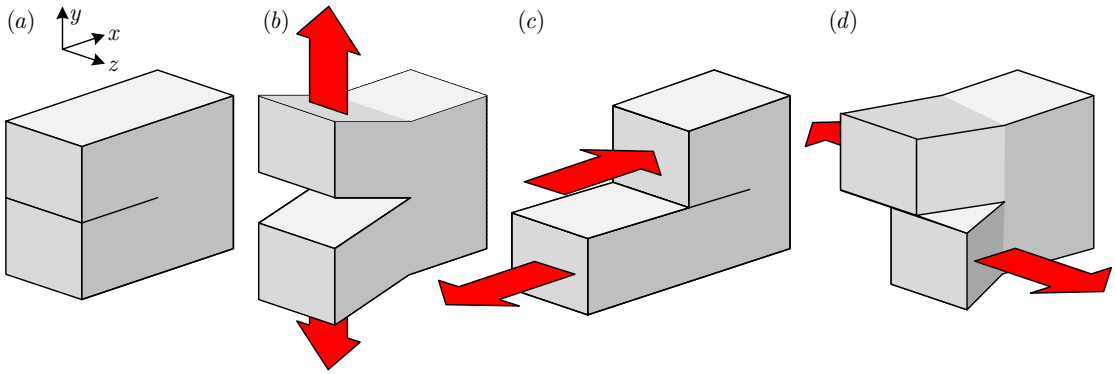

Figure 1. Three modes of deformation of (a) domain with a crack: (b) Mode I, (c) Mode II and (d) Mode III

The principles of LEFM (Griffith, 1920) were extended to define independent s*tress intensity factors* (Irwin, 1957), relating to each of these modes and describing the nature of a crack. Thus, for a given material, it is possible to quantify the severity of the crack and its need for attention. With reference to Figure 1, a local Cartesian system is defined with the x- and y-directions parallel and perpendicular to the crack face respectively; the z-direction is out-of-plane and parallel to the crack front. Throughout the present work, analyses are limited for simplicity to 2D, such that the third mode can be neglected.

The first two stress intensity factors are defined

$$K_{\mathrm{I}} = \lim_{r\to 0} \sigma_{yy}\sqrt{2\pi r}\Big|_{\theta=0} \tag{1.1}$$

$$K_{\mathrm{II}} = \lim_{r\to 0} \sigma_{xy}\sqrt{2\pi r}\Big|_{\theta=0} \tag{1.2}$$

where σ_{yy} and σ_{xy} are the local stress components at some polar coordinate (r,θ) from the crack tip. The effect of other stress fields at (r,θ) may distort

the estimation of K_{I} and K_{II}. Thus, it is common that stresses are evaluated in the immediate vicinity of the crack tip such that other stress fields, such as those due to the Poisson effect, offer little significant interference.

The stress intensity factors are considered local indicators: if, for a given material type, independent cracks are analysed, loaded such that the stresses local to the tip are identical, there will be no distinction[i] between the stress intensity factors for each of the different analyses, irrespective of the geometries and boundary conditions of an analysis (e.g. the support structure of a loaded aircraft wing or a simplified plate under laboratory conditions). This dependence only on material properties (and not geometry and boundary conditions) makes stress intensity factors attractive indicators of fracture and are used widely in industry where material properties are known and modelling is limited to regions around a crack tip.

1.4 Propagation

The maximum principal stress criterion predicts that crack propagation occurs in the direction perpendicular to the maximum principal stress (Portela *et al.*, 1993). This occurs at

$$K_{\mathrm{I}} \sin\theta_p + K_{\mathrm{II}}(3\cos\theta_p - 1) = 0 \tag{1.3}$$

where θ_p is the angle subtended from the x-axis in local Cartesian coordinate

[i] in 2D where a plane stress or plane strain assumption is made; in 3D, the differences in the local geometry describing the direction and shape of the crack front may influence the stress intensity factors.

system defined in Figure 1.

Though indicating the severity of the crack for a given static load, they can be used in conjunction with other parameters related to the geometry and boundary conditions as part of a dynamically-loaded system. For example, the *Paris Law* predicts the crack growth rate in a system, loaded cyclically between $\sigma_{\min}$ and $\sigma_{\max}$, is given by

$$\frac{\mathrm{d}a}{\mathrm{d}N_c} = C_1 \Delta K_{\mathrm{I}}^{C_2} \tag{1.4}$$

where a is the crack length, N_c is the number of load cycles and

$$\Delta K_{\mathrm{I}} = Y(\sigma_{\max} - \sigma_{\min})\sqrt{\pi a} \tag{1.5}$$

where selected approximate and typical values of material constants C_1 and C_2 are illustrated in Table 2, and constant Y is geometry-dependent.

Material	$\frac{C_1}{\mathrm{Nmm}^{-1/2}}$	C_2
Steel	10^{-11}	3
Aluminium	10^{-12}	3
Nickel	4×10^{-12}	3.3
Titanium	10^{-11}	5

Table 2. Paris Law constants, adapted from Roylance (Roylance, 1996)

For general geometries found in general engineering problems, Y is unknown and boundary conditions typically cannot be described so readily by a single applied load varying cyclically. Thus, equation (1.5) cannot be relied upon for estimating the crack growth rate in equation (1.4). Instead, ΔK_{I} is given by estimation of the range of stress intensity factors over a load cycle

$$\Delta K_{\mathrm{I}} = \left| K_{\mathrm{I}_{\max}} - K_{\mathrm{I}_{\min}} \right| \tag{1.6}$$

where $\{K_{\mathrm{I}_{\max}}, K_{\mathrm{I}_{\max}}\}$ are the stress intensity factors corresponding to load cases $\{\sigma_{\min}, \sigma_{\max}\}$. For the types of material in Table 2, the accurate estimation of stress intensity factors is of particular importance as errors raised to such a power magnify the errors in crack growth prediction.

For stress intensity factors to be of any engineering practicality, the underlying need for accurate computation of displacements and local stresses from which they derive is paramount. For additional concise reference, the author recommends Fleck *et al.* (Fleck *et al.*, 1994).

1.5 T-Stress

The T-stress is a non-singular stress term acting parallel to the crack plane (Tvergaard and Hutchinson, 1994) that acts in addition to the singular stresses described above. The value of T-stress for a given load is geometry dependent. So unlike the stress concentration factor, the T-stress can be used to give an indication of the effects of the geometry and its constraints in the near vicinity of a crack tip. Analysis of two domains with the same stress intensity factors (and thus the same local stresses) may have decidedly differing T-stress. The magnitude of the T-stresses relative to those of the stress intensity factors may indicate the significance of the higher order terms on the overall stress analysis of the domain and the validity using a LEFM model for the analysis.

While the propagation of cracks whose associated T-stress is negative have been shown to be dominated by the stress intensity factors, it has been observed that for those with a positive T-stress, propagation may deviate from

the expected crack path with some level of instability. (Cotterell and Rice, 1980). This had led some works to question the assumption that stress intensity factors alone govern crack propagation, and that T-stresses may have a significant impact. Contrary to traditional theory that suggests T-stresses should vanish under pure mode II problems, some such problems have been demonstrated by analytical solution to exhibit non-zero T-stresses (Fett, 2001). Further, there have been efforts to redefine the mode I and mode II (Ayatollahi *et al.*, 2005), such that a zero-value T-stress is no longer expected for such pure mode II problems. Inclusion of such specific examples involving fractured discs are beyond the scope of the present work, but are referenced for completeness with acknowledgement of this ongoing research of academic interest.

1.6 Williams expansion

The Williams expansion in displacement describes the displacements $\mathbf{u}_W$ local to a crack tip in an infinite plate subject to a uniaxial stress perpendicular to the crack in terms of stress intensity factors (Williams, 1957). With reference to Figure 3

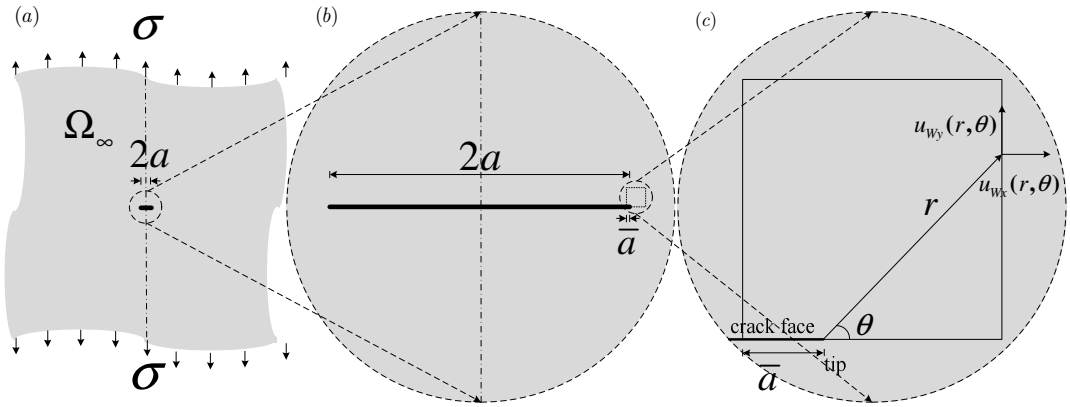

Figure 3. Stress analysis of (*a*) a through crack in an infinite plate (*b*) the region around the crack tip and (*c*) the Cartesian displacements at polar coordinates from the tip

$$\mathbf{u}_W = \begin{Bmatrix} u_{Wx} \\ u_{Wy} \end{Bmatrix} \tag{1.7}$$

the *x*- and *y*-direction displacements are given by

$$u_{Wx}(r,\theta) = \sum_{i=1}^{\infty} \frac{r^{i/2}}{2\mu} \left(C_{i1} W_{x1}(i) - C_{i2} W_{x2}(i) \right) \tag{1.8}$$

$$u_{Wy}(r,\theta) = \sum_{i=1}^{\infty} \frac{r^{i/2}}{2\mu} \left(C_{i2} W_{y2}(i) - C_{i2} W_{y2}(i) \right) \tag{1.9}$$

where

$$W_{x1}(i) = \left(\kappa + \frac{i}{2} + (-1)^i \right) \cos\frac{i}{2}\theta - \frac{i}{2}\cos\left(\frac{i}{2} - 2 \right)\theta \tag{1.10}$$

$$W_{x2}(i) = \left(\kappa + \frac{i}{2} - (-1)^i \right) \sin\frac{i}{2}\theta - \frac{i}{2}\sin\left(\frac{i}{2} - 2 \right)\theta \tag{1.11}$$

$$W_{y1}(i) = \left(\kappa - \frac{i}{2} - (-1)^i \right) \sin\frac{i}{2}\theta + \frac{i}{2}\sin\left(\frac{i}{2} - 2 \right)\theta \tag{1.12}$$

$$W_{y2}(i) = \left(\kappa - \frac{i}{2} + (-1)^i \right) \cos\frac{i}{2}\theta + \frac{i}{2}\cos\left(\frac{i}{2} - 2 \right)\theta \tag{1.13}$$

and κ is the Kosolov constant related the material's Poisson ratio ν by

$$\kappa = \begin{cases} \dfrac{3-\nu}{1+\nu} & \text{for plane stress} \\ 3+4\nu & \text{for plane strain} \end{cases} \tag{1.14}$$

and C_{i1} and C_{i2} are coefficients that corresponding to specific, identifiable terms in the series. The first coefficients in the series are related to the stress intensity factors by

$$C_{11} = \frac{K_{\mathrm{I}}}{\sqrt{2\pi}} \tag{1.15}$$

$$C_{12} = -\frac{K_{\mathrm{II}}}{\sqrt{2\pi}} \tag{1.16}$$

The T-stress T_{II} is related to the second coefficient in the series

$$C_{22} = \frac{T_{\mathrm{II}}}{4} \tag{1.17}$$

By neglecting the higher order terms, equations (1.8) and (1.9) reduce to

$$u_{Wx}(r,\theta) = \frac{K_{\mathrm{I}}}{\mu}\sqrt{\frac{r}{2\pi}}\left(\frac{(\kappa-1)}{2}\cos\frac{\theta}{2} + \sin^2\frac{\theta}{2}\right) \tag{1.18}$$

$$u_{Wy}(r,\theta) = \frac{K_{\mathrm{I}}}{\mu}\sqrt{\frac{r}{2\pi}}\left(\frac{(\kappa+1)}{2}\sin\frac{\theta}{2} - \cos^2\frac{\theta}{2}\right) \tag{1.19}$$

1.7 Numerical modelling of fracture mechanics problems

The BEM, its extension, the *Dual BEM* (DBEM), and the SBFEM are numerical methods that may be used to estimate the deformation of a loaded domain. New derivations of both the BEM and SBFEM are presented with particular efforts made to increase the understanding of SBFEM. New observations relating to the implementations of these methods are presented alongside extensions that facilitate their coupling. Further extensions and reformulations of these methods that improve their individual applicability are presented. These methods are assessed independently and then in coupled

forms using fracture mechanics problems to illustrate their relative strengths and weaknesses. The idealised examples (based on §1.6) with known solutions provide benchmarks that are indicative of their performance when applied to non-trivial examples whose solutions are not known. It should be noted that all analyses are undertaken on isotropic bodies. The methods in their presented forms are inappropriate for analysis of anisotropic bodies.

The work presented in this thesis represents an extension to initial work on this project (Chidgzey, 2007). Consequentially, the code used to obtain results in the author's early references owes some recognition to Chidgzey *et al.* for assistence in the SBFEM side of the project and Trevelyan *et al.* for assistance on the BEM side. However, all the code has since been rewritten under a more modern, computer science framework. A bottom-up approach to testing was taken to offer confidence that the presented results are the more characteristic of the methods than their respective implementation. The new code was written in MATLAB and makes use of some freely-available library functions, but otherwise has been developed by the author.

The presented coupled method and its efficient use of *reanalysis* (a method of identifying and reusing computed data) is specifically tailored towards linear elastic fracture mechanics problems in 2D isotropic bodies. Thus it is for this class of problem that the method best suited, and offers advantages over codes that are based on generic numerical methods (typically the more established FEM, and to a lesser extent, the BEM). For example, the code BEASY is based on the BEM, which, for a given number of degrees of freedom will be less accurate than the presented method owing to the BEM's poor piecewise isoparametric element-based polynomial approximations to non-polynomial functions. However, owing to the techniques to implement these generic

methods professionally, commercial software is expected to run faster despite its underlying methods rather than because of them.

1.8 Content outline

In §2 and §3, reviews of these numerical methods are presented. The BEM is well known, and as such, is not subject to as much rigorous detail as the less-well known SBFEM. However, with the focus of the present work directed towards their coupling, both methods are developed accordingly. To allow the reader to become familiar with the technical terms associated with each method beforehand, the literature surrounding both methods is reviewed at the close of each chapter.

The original concept of a coupled *boundary element-scaled boundary finite element method* (BE-SBFEM) is reviewed in §4. Its limitations are reviewed and addressed as part of the present work, serving to illustrate the development of the algorithm to include the *dual boundary element method* (DBEM).

As an extension to the BEM, the introduction of the DBEM in its existing form increases the geometric flexibility further. This coupled DBE-SBFEM is presented in §5 and includes the use of *reanalysis* to deliver an efficient algorithm applicable to general crack propagation schemes, but with a particular suitability to those of a predictor/corrector basis. The DBEM is reformulated in §6 in order to simplify its implementation and increase the range of applications to which it is suited.

The results and observations of the methods and their implementation are summarised and analysed critically in §7. Recommendations for further

research are made and concluding remarks drawn in §8. Supplementary information can be found in the appendices. The illustrations that accompany this thesis are original to the author unless otherwise stated.

1.9 Conclusion

The motivation behind the present work is the need for the estimation of stress intensity factors of loaded fractured systems. A new numerical algorithm coupling the BEM and SBFEM is proposed in order to calculate accurately the domain displacements on which the stress intensity factors are based. By combining the geometric flexibility of the BEM and the accuracy of the SBFEM, the method, built under a linear elastic framework, is expected to model real engineering domains with efficiency.

The implementation of this method has been undertaken using a modern computer science development and testing framework to improve code integrity and provide confidence in the results. A discussion of this implementation and the numerical results it yields will be presented, and overall conclusions and recommendations for further research are drawn.

2 Boundary element method

2.1 Introduction

In this chapter, the *boundary element method* (BEM) is introduced. After a brief overview, a detailed numerical formulation, with examples, is included to demonstrate the method's suitability for applications to fracture mechanics. Its other strengths and limitations are assessed. The *dual BEM* (DBEM), an extension to the BEM, is also discussed. The methods are presented alongside a critical assessment of their application to fracture mechanics, specifically in its suitability to extract accurately displacements near a crack tip. The data in numerical examples in this chapter are obtained by the development of the author's own code.

Some aspects of implementing the BEM and DBEM are introduced. An adaptive algorithm is assessed for use in non-singular integration of both the BEM and DBEM kernels. Analytical expressions for singular integration have been simplified and more generalised easing the BEM's implementation. This generalisation also facilitated a preliminary investigation into the optimisation of the local distribution of nodes defining their boundary elements. Other historical developments of the BEM and DBEM are discussed in a brief

literature review.

2.2 Numerical formulation

2.2.1 Method introduction

As the interest in the BEM in this thesis lies in the computation, application and extension of its underlying boundary integral equations, its complete derivation from its fundamental governing Laplace equation is not provided here. It is sufficient to state that the particular efforts have been made to address the practical implementation of the method in computer code, rather than the more general overviews offered elsewhere, beginning from the computation of the *boundary integral equation* (BIE) to form boundary integral equations as a basis for the method. This chapter summarises much of what is described in other more exhaustive derivations such as Ali and Rajakumar (2004), Beer (2001) and Becker (1992), to which the reader is directed for further details.

The BEM is a versatile method that can be applied to a number of areas. By modelling the boundary only, the BEM can be used to model both finite and infinite domains. When applied to linear elastic fracture mechanics, the BEM aims to model a domain's boundary displacement caused by its boundary tractions and other boundary constraints[ii]. The basis of the BEM is the *displacement boundary integral equation*, often abbreviated to BIE, but to distinguish between this and the *traction boundary integral equation* that

[ii] the effect of body loads is neglected in the present work without loss of generality

forms the basis of the DBEM, they will be abbreviated to DBIE and TBIE respectively.

Throughout this chapter, a 2D linear elastic domain is assumed, and the subscript 'B' is used to denote the boundary element method to allow distinction from, and comparison with, terms relating to other numerical methods in later chapters. The nomenclature of substructuring of the system matrices is inspired by the local substructuring of the author's BEM code and may not appear in this manner in the literature or other BEM codes. It should be noted that the BEM kernels described in the following sections use explicit indexing and are not tensors.

2.2.2 Displacement boundary integral equation

For a stress field represented by

$$\sigma_x = \frac{\partial^2 \phi}{\partial x^2}, \sigma_y = \frac{\partial^2 \phi}{\partial y^2}, \tau_{xy} = -\frac{\partial^2 \phi}{\partial x \partial y} \tag{2.1}$$

by substitution into the compatibility equations, with reference to Rajakumar (2004), Beer (2001) and Becker (1992), it can be seen that force equilibrium is satisfied by the governing biharmonic equation

$$\frac{\partial^4 \phi}{\partial x^4} + \frac{\partial^4 \phi}{\partial y^4} + 2\frac{\partial^4 \phi}{\partial x^2 \partial y^2} = 0 \tag{2.2}$$

where ϕ is the Airy stress function. The BEM is based on the solution to equation (2.2), and is be written in terms of fundamental solutions that can be solved for a given set of boundary conditions.

Thus for a domain Ω_B with n degrees of freedom, the x- and y-direction

boundary displacements can be described as functions of s, a circumferential coordinate system coincident with the boundary Γ_B. The DBIE defines these displacements $u_x(s)$ and $u_y(s)$, at some point $s = P_s$ (called the *source point*), in terms of the integrals of all boundary displacements and tractions multiplied by their respective kernels (called the BEM *fundamental solutions*), and a constant $C(P_s)$

$$C(P_s)\begin{Bmatrix} u_x(P_s) \\ u_y(P_s) \end{Bmatrix} + \int_{\Gamma_B} \begin{bmatrix} T^*_{xx}(P_s,P_f) & T^*_{xy}(P_s,P_f) \\ T^*_{yx}(P_s,P_f) & T^*_{yy}(P_s,P_f) \end{bmatrix} \begin{Bmatrix} u_x(P_f) \\ u_y(P_f) \end{Bmatrix} d\Gamma_B - \ldots$$
$$\int_{\Gamma_B} \begin{bmatrix} U^*_{xx}(P_s,P_f) & U^*_{xy}(P_s,P_f) \\ U^*_{yx}(P_s,P_f) & U^*_{yy}(P_s,P_f) \end{bmatrix} \begin{Bmatrix} t_x(P_f) \\ t_y(P_f) \end{Bmatrix} d\Gamma_B = \begin{Bmatrix} 0 \\ 0 \end{Bmatrix} \tag{2.3}$$

where $u_x(P_f)$, $u_y(P_f)$, $t_x(P_f)$ and $t_y(P_f)$ are the boundary displacements and tractions at $s = P_f$ (called the *field point*). The constant $C(P_s)$ is a parameter defined by the nature of the geometry at P_s, given by

$$C(P_s) = \frac{\alpha}{2\pi} \tag{2.4}$$

where the angle of smoothness α is defined by the interior angle subtended by the material between boundary facets to either side of P_s, as illustrated in Figure 4. This term is known as the 'jump term'. The fundamental solutions vary in s and are functions of the separation of the field and source points r and the outward unit normal $\mathbf{n}(s)$ evaluated at $s = P_f$, and material constants, where

$$r = \left| P_f - P_s \right| \tag{2.5}$$

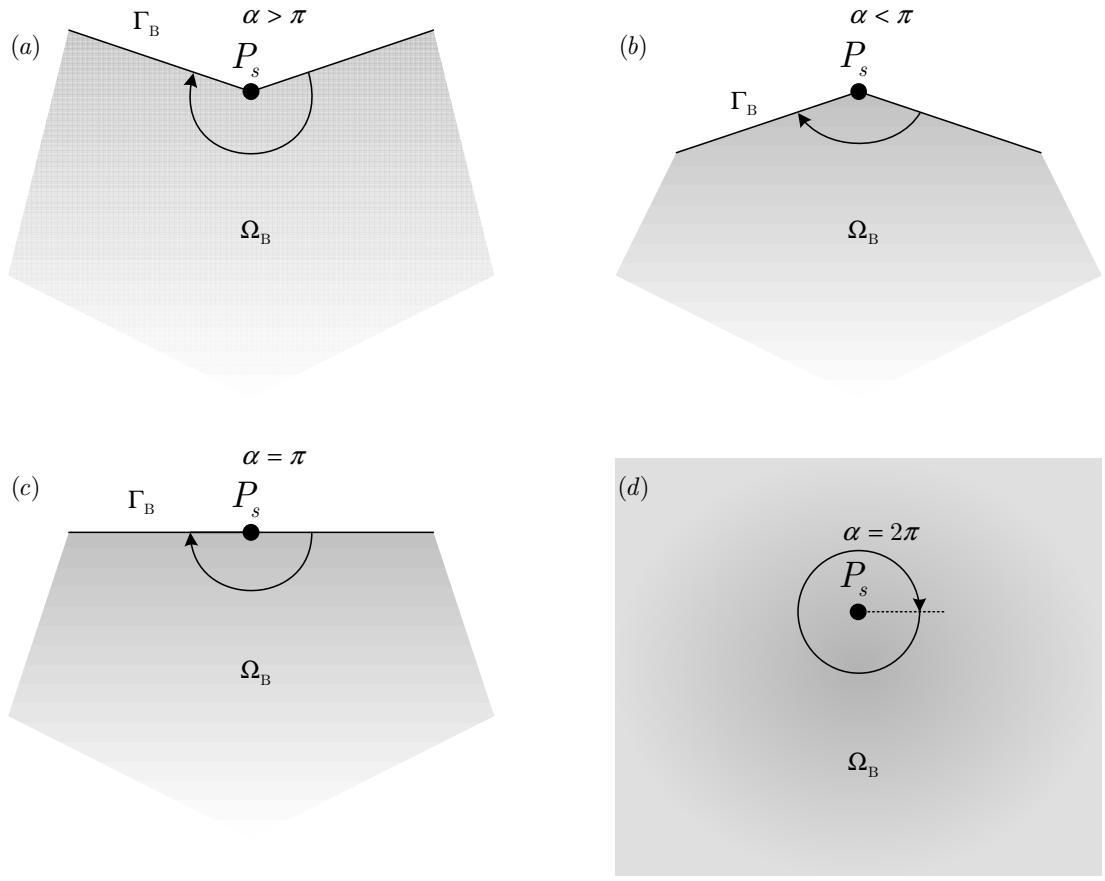

Figure 4. The angle of smoothness at P_s on the boundary where $(a)\,\alpha < \pi$ forming an interior angle, $(b)\,\alpha > \pi$ forming an exterior angle, $(c)\,\alpha = \pi$ forming a smooth boundary and (d) an interior point where $\alpha = 2\pi$

The DBIE fundamental solutions are given by

$$T^*_{xx}(P_s,P_f) = \frac{-1}{4\pi(1-\nu)r}\frac{\partial r}{\partial n(P_f)}\left((1-2\nu)+2\left(\frac{\partial r}{\partial x}\right)^2\right) \tag{2.6}$$

$$T^*_{xy}(P_s,P_f) = \frac{-1}{4\pi(1-\nu)r}\left(2\frac{\partial r}{\partial x}\frac{\partial r}{\partial y}\frac{\partial r}{\partial n(P_f)}-(1-2\nu)\left(\frac{\partial r}{\partial x}n_y(P_f)-\frac{\partial r}{\partial y}n_x(P_f)\right)\right) \tag{2.7}$$

$$T^*_{yx}(P_s,P_f) = \frac{-1}{4\pi(1-\nu)r}\left(2\frac{\partial r}{\partial x}\frac{\partial r}{\partial y}\frac{\partial r}{\partial n(P_f)}-(1-2\nu)\left(\frac{\partial r}{\partial y}n_x(P_f)-\frac{\partial r}{\partial x}n_y(P_f)\right)\right) \tag{2.8}$$

$$T^*_{yy}(P_s,P_f) = \frac{-1}{4\pi(1-\nu)r}\frac{\partial r}{\partial n(P_f)}\left((1-2\nu)+2\left(\frac{\partial r}{\partial y}\right)^2\right) \tag{2.9}$$

$$U^*_{xx}(P_s,P_f) = \frac{1}{8\pi\mu(1-\nu)}\left((3-4\nu)\ln\left(\frac{1}{r}\right)+\left(\frac{\partial r}{\partial x}\right)^2\right) \tag{2.10}$$

$$U^*_{xy}(P_s,P_f) = \frac{1}{8\pi\mu(1-\nu)}\frac{\partial r}{\partial x}\frac{\partial r}{\partial y} \tag{2.11}$$

$$U^*_{yx}(P_s,P_f) = \frac{1}{8\pi\mu(1-\nu)}\frac{\partial r}{\partial y}\frac{\partial r}{\partial x} \tag{2.12}$$

$$U^*_{yy}(P_s,P_f) = \frac{1}{8\pi\mu(1-\nu)}\left((3-4\nu)\ln\left(\frac{1}{r}\right)+\left(\frac{\partial r}{\partial y}\right)^2\right) \tag{2.13}$$

where μ is the shear modulus of the material given by

$$\mu = \frac{E}{2(1+\nu)} \tag{2.14}$$

where E and ν are the Young's modulus and Poisson's ratio of the material, and $n_x(s)$ and $n_y(s)$ are the x- and y-direction components of $\mathbf{n}(s)$

$$\mathbf{n}(s) = \begin{Bmatrix} n_x(s) \\ n_y(s) \end{Bmatrix} \tag{2.15}$$

For a unit-circular boundary, illustrated in Figure 5, these kernels are smooth and continuous, as illustrated in Figure 6 and Figure 7 where arbitrary engineering materials are used. For the portions of boundary in which P_f is sufficiently far from P_s, these kernels are well-behaved and the integrals of such present few computational difficulties. Further, as shown in the figures, as P_f approaches P_s, there may exist a singularity that requires more careful consideration.

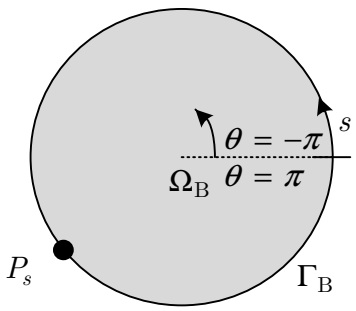

Figure 5. Sample source point on a circular boundary in which s can be described as a function of θ

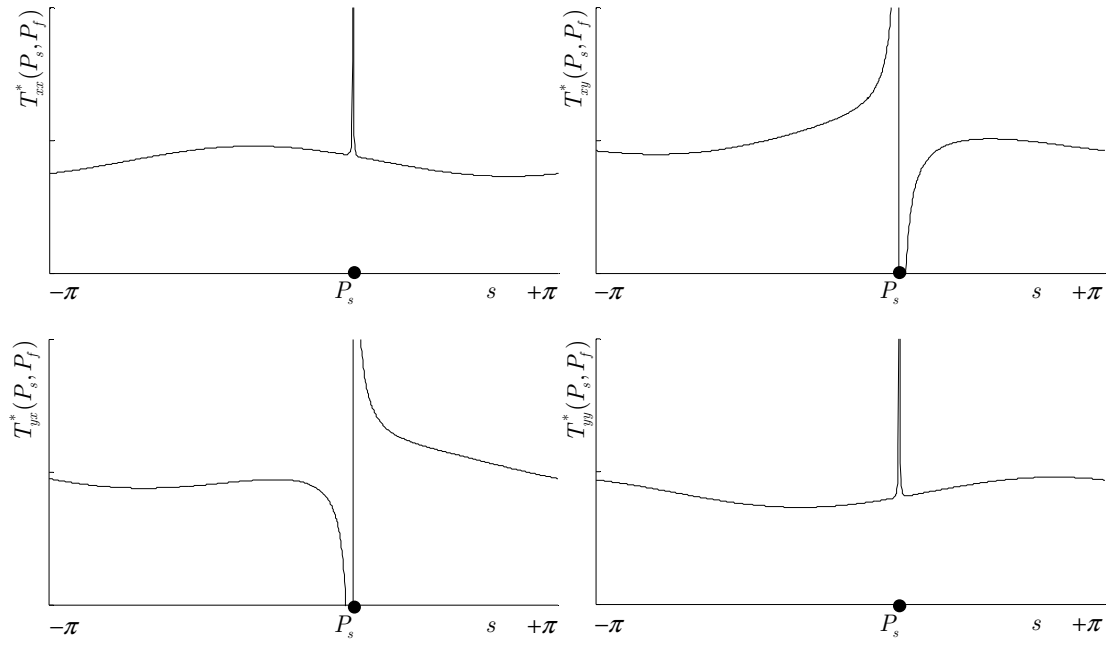

Figure 6. Illustration of $T^*_{ij}(P_s,P_f)$ kernels for a circular domain, $i,j = x,y$

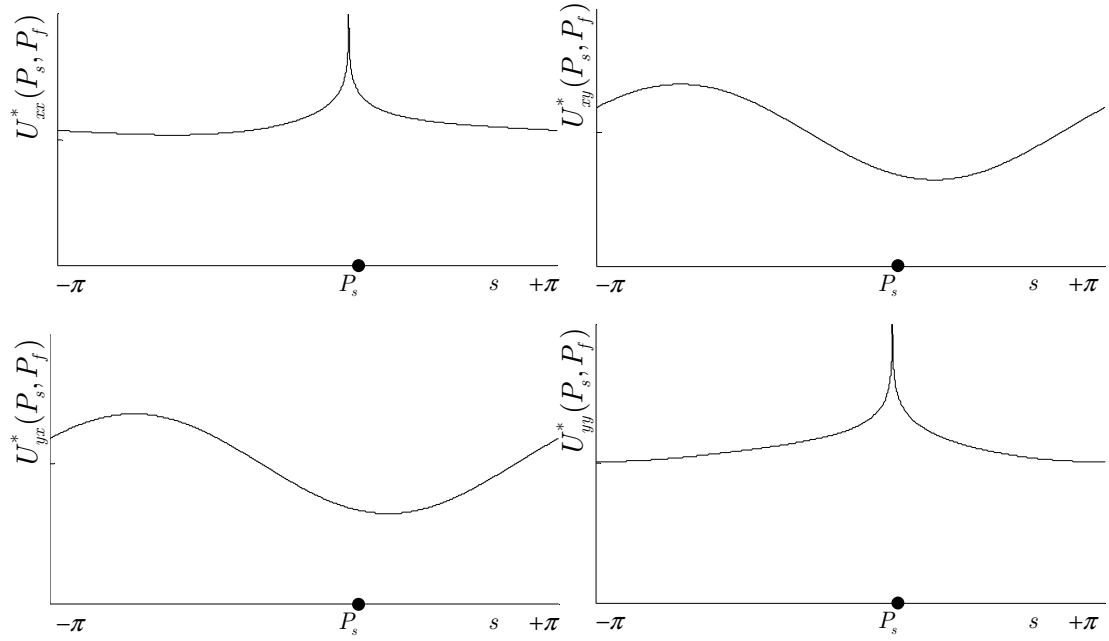

Figure 7. Illustration of $U^*_{ij}(P_s,P_f)$ kernels for a circular domain, $i,j = x,y$

For practical, non-circular domains, these kernels exhibit discontinuities, particularly at 90° corners owing to step changes in unit normals. To compute the integrals in equation (2.3), Γ_{B} is discretised into L discrete boundary

portions[iii]

$$C(P_s)\begin{Bmatrix} u_x(P_s) \\ u_y(P_s) \end{Bmatrix} + \sum_{e=1}^{L} \begin{Bmatrix} \hat{\mathbf{h}}_x^e(P_s) \\ \hat{\mathbf{h}}_y^e(P_s) \end{Bmatrix} \mathbf{u}^e - \sum_{e=1}^{L} \begin{Bmatrix} \mathbf{g}_x^e(P_s) \\ \mathbf{g}_y^e(P_s) \end{Bmatrix} \mathbf{t}^e = \begin{Bmatrix} 0 \\ 0 \end{Bmatrix} \tag{2.16}$$

or

$$C(P_s)\mathbf{u}(P_s) + \sum_{e=1}^{L} \hat{\mathbf{H}}^e(P_s)\mathbf{u}^e - \sum_{e=1}^{L} \mathbf{G}^e(P_s)\mathbf{t}^e = \mathbf{0} \tag{2.17}$$

where

$$\mathbf{u}(s) = \begin{Bmatrix} u_x(s) \\ u_y(s) \end{Bmatrix} \tag{2.18}$$

and $\hat{\mathbf{H}}^e(P_s)$ and $\mathbf{G}^e(P_s)$ are the coefficients of the displacements $\mathbf{u}^e$ and tractions $\mathbf{t}^e$, the degrees of freedom of boundary portion e. The computation of equation (2.17) yields

$$C(P_s)\mathbf{u}(P_s) + \hat{\mathbf{H}}(P_s)\mathbf{u} - \mathbf{G}(P_s)\mathbf{t} = \mathbf{0} \tag{2.19}$$

where $\mathbf{u}$ and $\mathbf{t}$ are the column vectors of length n describing the displacements and tractions of the whole boundary, and $\hat{\mathbf{H}}(P_s)$ and $\mathbf{G}(P_s)$ are their respective coefficients.

As both P_s and P_f are on the boundary, if the discretisation process is such that the source point coincides with a field point, where $P_s = P_f$, the constant

[iii] The term 'boundary portion' is used without loss of generality. The usual (non-general) discretisation process, and that which is adopted here, results in a piecewise polynomial approximation to the boundary displacements and tractions over e through the calculation of nodal values and elemental interpolation. This process is described later.

$C(P_s)$ can be assimilated into the coefficient of $\mathbf{u}(P_f)$

$$h_{ij}^{ek}(P_s) = \begin{cases} \hat{h}_{ij}^{ek}(P_s) + C(P_s) & P_s = P_f \\ \hat{h}_{ij}^{ek}(P_s) & \text{otherwise} \end{cases} \tag{2.20}$$

where, with reference to Appendix A, $i, j = x, y$ and $k = 1...n^e$, the number of degrees of freedom of boundary portion e.

Equation (2.19) is thus reduced to

$$\mathbf{H}(P_s)\mathbf{u} - \mathbf{G}(P_s)\mathbf{t} = \mathbf{0} \tag{2.21}$$

2.2.3 Traction boundary integral equation

The TBIE forms an alternative for cases when uniqueness of the equations in (2.31) cannot be guaranteed, such as when sections of the boundary overlap and source points are coincident. The TBIE is given by

$$C(P_s)\begin{Bmatrix} t_x(P_s) \\ t_y(P_s) \end{Bmatrix} + \begin{bmatrix} n_x(P_s) & 0 & n_y(P_s) & 0 \\ 0 & n_x(P_s) & 0 & n_y(P_s) \end{bmatrix} \int_{\Gamma_B} \begin{bmatrix} S^*_{xxx} & S^*_{xxy} \\ S^*_{xyx} & S^*_{xyy} \\ S^*_{yxx} & S^*_{xyy} \\ S^*_{yyx} & S^*_{yyy} \end{bmatrix} \begin{Bmatrix} u_x(P_f) \\ u_y(P_f) \end{Bmatrix} \mathrm{d}\Gamma_B - ...$$
$$\begin{bmatrix} n_x(P_s) & 0 & n_y(P_s) & 0 \\ 0 & n_x(P_s) & 0 & n_y(P_s) \end{bmatrix} \int_{\Gamma_B} \begin{bmatrix} D^*_{xxx} & D^*_{xxy} \\ D^*_{xyx} & D^*_{xyy} \\ D^*_{yxx} & D^*_{xyy} \\ D^*_{yyx} & D^*_{yyy} \end{bmatrix} \begin{Bmatrix} t_x(P_f) \\ t_y(P_f) \end{Bmatrix} \mathrm{d}\Gamma_B = \begin{Bmatrix} 0 \\ 0 \end{Bmatrix} \tag{2.22}$$

where it can be seen the 'jump term' is associated with the tractions $t_x(s)$ and $t_y(s)$ at the source point. The TBIE fundamental solutions are given by the tensors

$$S^*_{kij}(P_s,P_f)=\frac{\mu}{4\pi(1-\nu)r^2}\Bigg\{\ \ ...$$
$$n_i(P_s)\Bigg[(1-2\nu)\delta_{jk}-2\nu\frac{\partial r}{\partial x_j}\frac{\partial r}{\partial x_k}\Bigg]+...$$
$$n_j(P_s)\Bigg[(1-2\nu)\delta_{ik}-2\nu\frac{\partial r}{\partial x_i}\frac{\partial r}{\partial x_k}\Bigg]+...$$
$$n_k(P_s)\Bigg[(1-2\nu)\delta_{ij}-2\nu\frac{\partial r}{\partial x_i}\frac{\partial r}{\partial x_j}\Bigg]+...$$
$$2\frac{\partial r}{\partial n(P_s)}\Bigg[\delta_{ik}\frac{\partial r}{\partial x_j}+\delta_{jk}\frac{\partial r}{\partial x_i}-\frac{\partial r}{\partial x_k}\Bigg((1-2\nu)\delta_{ij}-4\frac{\partial r}{\partial x_i}\frac{\partial r}{\partial x_j}\frac{\partial r}{\partial x_k}\Bigg)\Bigg]\Bigg\} \tag{2.23}$$

$$D^*_{kij}(P_s,P_f)=\frac{1}{4\pi(1-\nu)r}\Bigg[(1-2\nu)\Bigg(\delta_{jk}\frac{\partial r}{\partial x_i}+\delta_{ik}\frac{\partial r}{\partial x_j}+\delta_{ij}\frac{\partial r}{\partial x_k}\Bigg)+2\frac{\partial r}{\partial x_i}\frac{\partial r}{\partial x_j}\frac{\partial r}{\partial x_k}\Bigg] \tag{2.24}$$

where $k,i,j=x,y$ and δ_{ij} is the Kronecker delta.

Following a manner similar to that of the DBIE, the TBIE is discretised in into L boundary portions

$$C(P_s)\begin{Bmatrix}t_x(P_s)\\t_y(P_s)\end{Bmatrix}+\sum_{e=1}^{L}\begin{Bmatrix}\mathbf{h}'^e_x(P_s)\\\mathbf{h}'^e_y(P_s)\end{Bmatrix}\mathbf{u}^e-\sum_{e=1}^{L}\begin{Bmatrix}\hat{\mathbf{g}}'^e_x(P_s)\\\hat{\mathbf{g}}'^e_y(P_s)\end{Bmatrix}\mathbf{t}^e=\begin{Bmatrix}0\\0\end{Bmatrix} \tag{2.25}$$

or

$$C(P_s)\mathbf{t}(P_s)+\sum_{e=1}^{L}\mathbf{H}'^e(P_s)\mathbf{u}^e-\sum_{e=1}^{L}\hat{\mathbf{G}}'^e(P_s)\mathbf{t}^e=\mathbf{0} \tag{2.26}$$

where

$$\mathbf{t}(s)=\begin{Bmatrix}t_x(s)\\t_y(s)\end{Bmatrix} \tag{2.27}$$

By the assimilation of the constant $C(P_s)$ into the coefficient of $\mathbf{t}(P_f)$ at $P_s=P_f$

$$g'^{ek}_{ij}(P_s) = \begin{cases} \hat{g}'^{ek}_{ij}(P_s) + C(P_s) & P_s = P_f \\ \hat{g}'^{ek}_{ij}(P_s) & \text{otherwise} \end{cases} \tag{2.28}$$

equation (2.26) is reduced to

$$\mathbf{H}'(P_s)\mathbf{u} - \mathbf{G}'(P_s)\mathbf{t} = \mathbf{0} \tag{2.29}$$

where, with reference to Appendix A, $i, j = x, y$ and $k = 1...n^e$, the number of degrees of freedom of boundary portion e.

The TBIE is used in the formation of the DBEM, which is described in §2.6.

2.2.4 Method solution

By the repeated movement of the source point to new locations on s and computing $\mathbf{H}(P_s)$ and $\mathbf{G}(P_s)$ using the DBIE, or $\mathbf{H}'(P_s)$ and $\mathbf{G}'(P_s)$ using the TBIE, n equations (i.e. $n/2$ sets of the two equations defined in either (2.16), (2.25) or combinations of the two equations) can be assembled describing the displacements at each source point

$$\mathbf{Hu} - \mathbf{Gt} = 0 \tag{2.30}$$

where $\mathbf{H}$ and $\mathbf{G}$ are known as the displacement and traction *influence matrices*.

For each degree of freedom, and in each direction, it is assumed that either a Dirichlet (displacement) or Neumann (traction) boundary condition is known. By their application to equation (2.30)

$$\mathbf{Ax} = \tilde{\mathbf{A}}\tilde{\mathbf{x}} \tag{2.31}$$

or, since the entire right hand side is now known

$$\mathbf{Ax} = \mathbf{b} \tag{2.32}$$

where $\mathbf{x}$ and $\tilde{\mathbf{x}}$ are vectors of the unknown and known displacements and tractions, and $\mathbf{A}$ and $\tilde{\mathbf{A}}$ are their respective coefficients. This linear system can be solved for all unknown boundary displacements and tractions. Unlike the comparable *finite element method* (FEM), this BEM system matrix will be non-symmetric and fully populated and methods geared towards solving FEM systems may be unsuitable for solving BEM systems. However, for a given problem, the size of the BEM system will typically be much smaller than that of a comparable FEM system. There are many solvers tailored specifically to the characteristics of the BEM system, with the *generalised minimal residual* (GMRES) solver (Saad and Schultz, 1986) a popular such example.

2.3 Discretisation

The geometric boundary Γ_{B} is discretised in the usual manner by means of a piecewise polynomial isoparametric boundary element approximation, such that each source point corresponds with an element node defining the geometry. Unlike the FEM, the system matrices in the BEM do not define a local (elemental) stiffness, merely a set of coefficients relating the displacements and tractions on a global (boundary) level. The distribution of nodes on an element is, in principle, arbitrary for the BEM. However, certain nodal distributions may require specific computational considerations and are often selected specifically for reasons of convenience, i.e. even though the governing BEM equation may still hold, certain configurations of nodal distribution may result in incomputable integrals of hyper-singular equations. Continuous, discontinuous and semi-discontinuous elements can be selected as necessary for use in the BEM without the need for additional constraint equations. The motivation for, and definition and application of, such elements is now presented.

The two-dimensional geometric characteristics of a discrete boundary element e may be mapped, via a suitable transformation, into a one-dimensional axis bounded by $-1 \le \eta \le 1$. A quadratic boundary element e is defined by the local distribution of its three nodes $\boldsymbol{\eta}^e$

$$\boldsymbol{\eta}^e = \{\eta_1 \quad \eta_2 \quad \eta_3\} \tag{2.33}$$

Such quadratic elements are assumed throughout this thesis. Generally

$$-1 \le \eta_1 < \eta_2 < \eta_3 \le 1 \tag{2.34}$$

and typically

$$\eta_2 = 0 \tag{2.35}$$
$$\eta_1 = -\eta_3 \tag{2.36}$$

Exceptions to equations (2.34) to (2.36) are highlighted below.

2.3.1 Continuous elements

Continuous boundary elements exhibit nodal connectivity between neighbouring elements, thus

$$-1 = \eta_1 < \eta_2 < \eta_3 = 1 \tag{2.37}$$

and have the appearance of one dimensional elements used in the FEM, as illustrated in Figure 8.

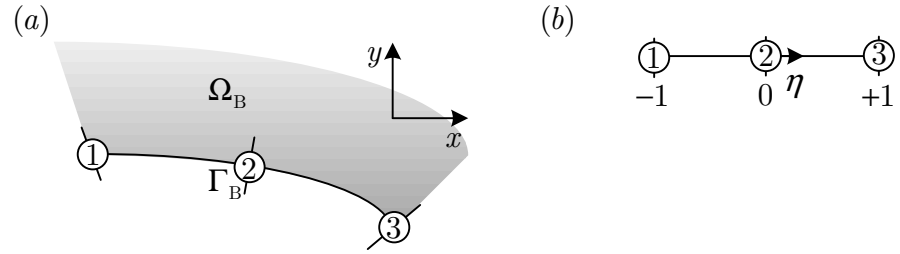

Figure 8. Boundary discretisation from (*a*) geometric continuous boundary element to (*b*) a mapped continuous boundary element

2.3.2 Discontinuous elements

Discontinuous boundary elements exhibit no nodal connectivity between neighbouring elements, thus

$$-1 < \eta_1 < \eta_2 < \eta_3 < 1 \tag{2.38}$$

Unlike conventional finite elements, discontinuous boundary elements extend beyond the extremities of the outermost nodes, as illustrated in Figure 9.

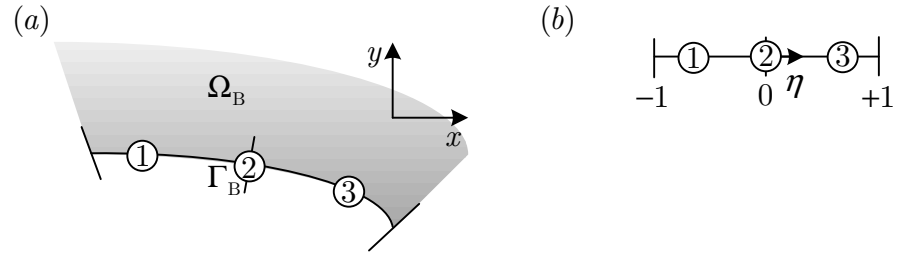

Figure 9. Boundary discretisation from (*a*) geometric discontinuous boundary element to (*b*) a mapped discontinuous boundary element

2.3.3 Semi-discontinuous elements

Semi-discontinuous boundary elements exhibit nodal connectivity with one of its neighbouring elements and no connectivity with the other, thus

$$-1 < \eta_1 < \eta_2 < \eta_3 = 1 \tag{2.39}$$

or

$$-1 = \eta_1 < \eta_2 < \eta_3 < 1 \tag{2.40}$$

as illustrated in Figure 10.

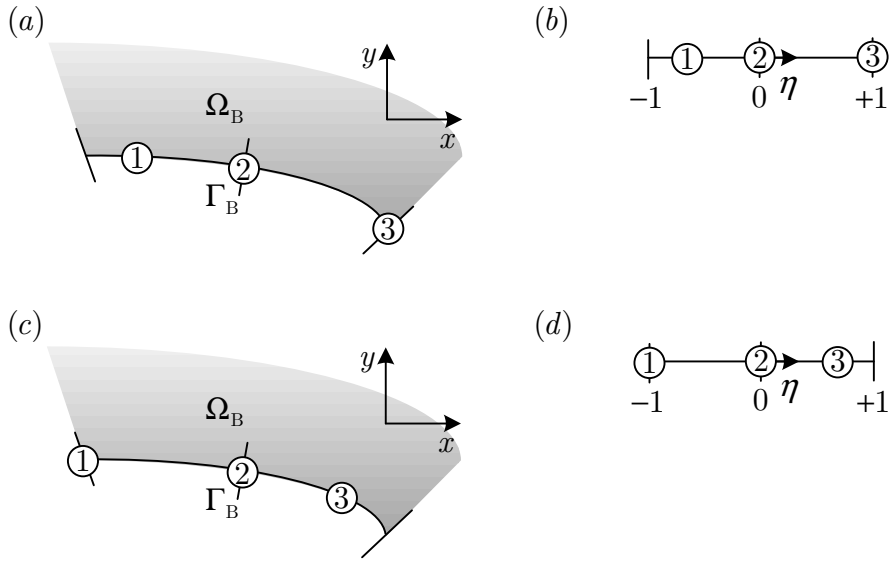

Figure 10. Boundary discretisation from (*a*) geometric semi-discontinuous boundary element to (*b*) a mapped semi-discontinuous boundary element of the first kind, and (*c*) geometric semi-discontinuous boundary element to (*d*) a mapped semi-discontinuous boundary element of the second kind

These elements can be used to provide a smooth transition between boundary sections modelled by continuous and discontinuous elements.

2.4 Shape functions

The quadratic shape functions required for discontinuous and semi-discontinuous element interpolation and extrapolation are modified from those for standard continuous elements used in methods such as the FEM. The vector of shape functions $\mathbf{N}$ for quadratic elements is given by

$$\mathbf{N} = \{ N_1(\eta) \quad N_2(\eta) \quad N_3(\eta) \} \tag{2.41}$$

where

$$N_k(\eta) = A_k(\eta^2 - B_k\eta + C_k) \tag{2.42}$$

where

$$A_k = \frac{1}{\prod_{j=1, j\neq k}^{3} (\eta_k - \eta_j)} \tag{2.43}$$

$$B_k = \sum_{j=1, j\neq k}^{3} \eta_j \tag{2.44}$$

$$C_k = \prod_{j=1, j\neq k}^{3} \eta_j \tag{2.45}$$

for $k = 1..3$. The form of equation (2.42) may not appear in the literature, but was devised as part of the present work in order to generalise the shape functions for the quadratic boundary element types illustrated in Figure 11.

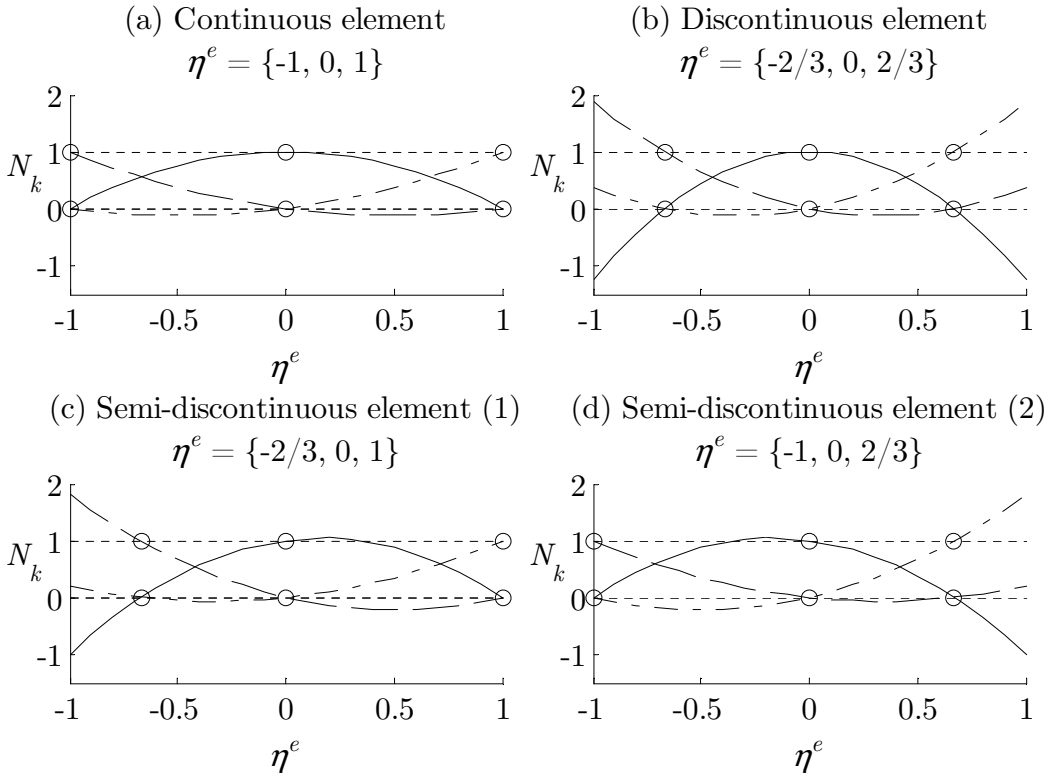

Figure 11. Set of three quadratic shape functions N_k for (*a*) continuous elements, (*b*) discontinuous elements, (*c*) semi-discontinuous elements of the first kind, and (*d*) semi-discontinuous elements of the second kind

Adjacent continuous elements share a common node and so C_0 will be observed. Such continuity is not guaranteed between adjacent elements offering no nodal connectivity. Although this may, at first, appear disadvantageous, this natural discontinuity can be expected to reduce with an improved mesh and thus may serve as an error indicator.

2.5 Integration

For quadratic elements in two dimensions, it is computationally convenient to compute submatrices of 2×2 terms corresponding to a single source node and field node pair, in each direction. With reference to Appendix A, it can be shown that these submatrices are given by

$$\hat{\mathbf{H}}^{ek}(P_s) = \begin{bmatrix} \hat{h}^{ek}_{xx}(P_s) & \hat{h}^{ek}_{xy}(P_s) \\ \hat{h}^{ek}_{yx}(P_s) & \hat{h}^{ek}_{yy}(P_s) \end{bmatrix} \tag{2.46}$$

$$\mathbf{G}^{ek}(P_s) = \begin{bmatrix} g^{ek}_{xx}(P_s) & g^{ek}_{xy}(P_s) \\ g^{ek}_{yx}(P_s) & g^{ek}_{yy}(P_s) \end{bmatrix} \tag{2.47}$$

$$\mathbf{H}'^{ek}(P_s) = \begin{bmatrix} h'^{ek}_{xx}(P_s) & h'^{ek}_{xy}(P_s) \\ h'^{ek}_{yx}(P_s) & h'^{ek}_{yy}(P_s) \end{bmatrix} \tag{2.48}$$

$$\hat{\mathbf{G}}'^{ek}(P_s) = \begin{bmatrix} \hat{g}'^{ek}_{xx}(P_s) & \hat{g}'^{ek}_{xy}(P_s) \\ \hat{g}'^{ek}_{yx}(P_s) & \hat{g}'^{ek}_{yy}(P_s) \end{bmatrix} \tag{2.49}$$

where $k = 1,2,3$ for quadratic elements, $i,j = x,y$ and

$$\hat{h}^{ek}_{ij}(P_s) = \int_{-1}^{+1} T^{e*}_{ij}(P_s) N_k(\boldsymbol{\eta}^e) J^e \mathrm{d}\boldsymbol{\eta}^e \tag{2.50}$$

$$g^{ek}_{ij}(P_s) = \int_{-1}^{+1} U^{e*}_{ij}(P_s) N_k(\boldsymbol{\eta}^e) J^e \mathrm{d}\boldsymbol{\eta}^e \tag{2.51}$$

$$h'^{ek}_{ij}(P_s) = \int_{-1}^{+1} D^{e*}_{ij}(P_s) N_k(\boldsymbol{\eta}^e) J^e \mathrm{d}\boldsymbol{\eta}^e \tag{2.52}$$

$$\hat{g}'^{ek}_{ij}(P_s) = \int_{-1}^{+1} S^{e*}_{ij}(P_s) N_k(\boldsymbol{\eta}^e) J^e \mathrm{d}\boldsymbol{\eta}^e \tag{2.53}$$

These terms are typically assembled into larger submatrices of size 2×6, corresponding to each source node and field element pair, before assembly into the BEM influence matrices.

2.5.1 Nature of singularity

As P_s approaches P_f, the BEM kernels may exhibit some form of singular behaviour and, depending on the nature of the singularity (if any), a suitable integration scheme must be employed over each respective portion of the boundary, as illustrated in Figure 12.

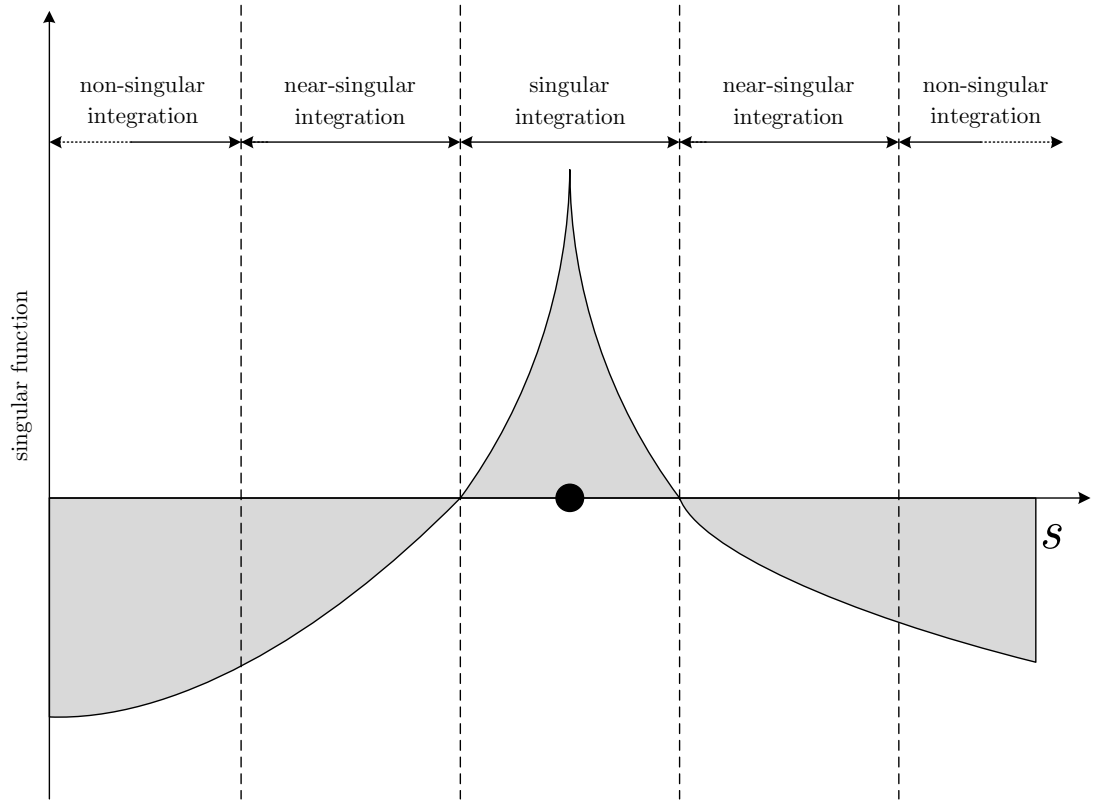

Figure 12. Illustration of the integration schemes required over the boundary for a kernel that exhibits singular behaviour close to the collocation point •, non-singular behaviour away from the collocation point, with a transition of near-singular behaviour elsewhere.

By using the piecewise polynomial elements and shape functions described

above, the element-wise integral of the DBIE and TBIE kernels over each boundary portion can be evaluated. The type of integration scheme required is determined on an element-by-element basis, depending on whether the function is non-singular, near-singular, weakly-singular, strongly-singular or hyper-singular, as categorised below.

2.5.2 Non-singular integration

These integrals can be approximated by standard methods, such as Gauss-Legendre quadrature, in which for a function $f(\eta)$

$$\int_{-1}^{+1} f(\eta)\mathrm{d}\eta \approx \sum_{\gamma=1}^{\gamma_{\max}} f(\eta_\gamma)w_\gamma \tag{2.54}$$

where η_γ and w_γ and the coordinates and weights of the $\gamma_{\max}$ quadrature points. Thus

$$\int_{-1}^{+1} T_{ij}^{e*}(P_s)N_k(\eta^e)J^e\mathrm{d}\eta^e \simeq \sum_{\gamma=1}^{\gamma_{\max}} T_{ij}^{e*}(P_s)N_k(\eta_\gamma^e)J^e w_\gamma \tag{2.55}$$

$$\int_{-1}^{+1} U_{ij}^{e*}(P_s)N_k(\eta^e)J^e\mathrm{d}\eta^e \simeq \sum_{\gamma=1}^{\gamma_{\max}} U_{ij}^{e*}(P_s)N_k(\eta_\gamma^e)J^e w_\gamma \tag{2.56}$$

$$\int_{-1}^{+1} S_{ij}^{e*}(P_s)N_k(\eta^e)J^e\mathrm{d}\eta^e \simeq \sum_{\gamma=1}^{\gamma_{\max}} S_{ij}^{e*}(P_s)N_k(\eta_\gamma^e)J^e w_\gamma \tag{2.57}$$

$$\int_{-1}^{+1} D_{ij}^{e*}(P_s)N_k(\eta^e)J^e\mathrm{d}\eta^e \simeq \sum_{\gamma=1}^{\gamma_{\max}} D_{ij}^{e*}(P_s)N_k(\eta_\gamma^e)J^e w_\gamma \tag{2.58}$$

2.5.3 Near- and weakly-singular integration

A popular method in this work for the approximation of weakly-singular functions is to map the element coordinate system η^e into another local coordinate $\tilde{\eta}^e$ (Telles, 1987), defined by

$$\tilde{\eta}_1 = \eta_1 \tag{2.59}$$

$$\frac{\partial \eta}{\partial \tilde{\eta}} = 0 \qquad \text{at} \qquad \tilde{\eta}_2 \tag{2.60}$$

$$\tilde{\eta}_3 = \eta_3 \tag{2.61}$$

as illustrated in Figure 13. Equation (2.54) is redefined

$$\int_{-1}^{+1} f(\eta) \mathrm{d}\eta = \int_{-1}^{+1} f(\tilde{\eta}) \frac{\partial \eta}{\partial \tilde{\eta}} \mathrm{d}\tilde{\eta} \tag{2.62}$$

such that

$$\text{as } f(\tilde{\eta}) \to \infty, \frac{\partial \eta}{\partial \tilde{\eta}} \to 0 \tag{2.63}$$

and the singularity is cancelled.

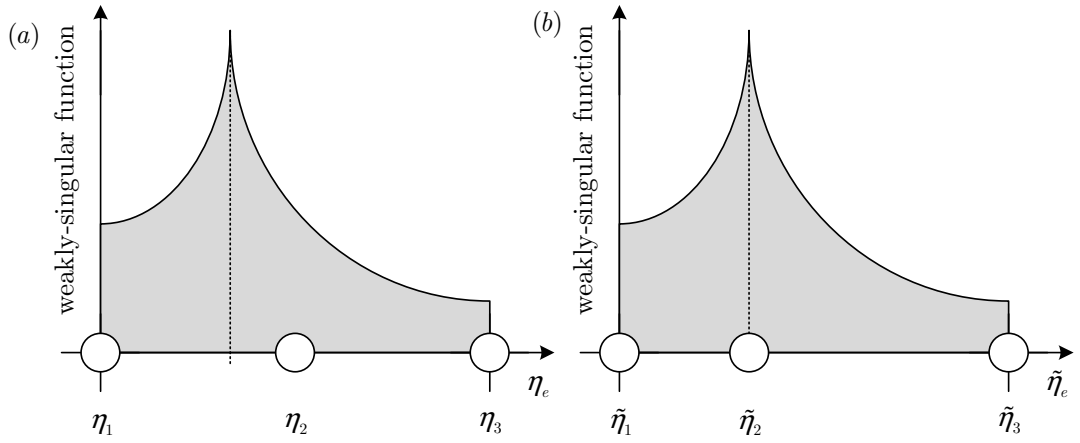

Figure 13. (*a*) The original element, and (*b*) the Telles transformation.

An additional effect of this scheme is the natural clustering of quadrature points towards the singularity, as illustrated by Figure 14, even if the singularity is not on that element. This makes the scheme appropriate for the near-singular integration as it offers an improved distribution of points over the Gauss-Legendre quadrature.

The transformation requires a modified Jacobian $\tilde{J}^e$ and weights $\tilde{w}_\gamma$, but

otherwise appears similar to the Gauss-Legendre quadrature.

$$\int_{-1}^{+1} T_{ij}^{e*}(P_s)N_k(\boldsymbol{\eta}^e)J^e \mathrm{d}\boldsymbol{\eta}^e \simeq \sum_{\gamma=1}^{\gamma_{\max}} T_{ij}^{e*}(P_s)N_k(\tilde{\boldsymbol{\eta}}_\gamma^e)\tilde{J}^e\tilde{w}_\gamma \tag{2.64}$$

$$\int_{-1}^{+1} U_{ij}^{e*}(P_s)N_k(\boldsymbol{\eta}^e)J^e \mathrm{d}\boldsymbol{\eta}^e \simeq \sum_{\gamma=1}^{\gamma_{\max}} U_{ij}^{e*}(P_s)N_k(\tilde{\boldsymbol{\eta}}_\gamma^e)\tilde{J}^e\tilde{w}_\gamma \tag{2.65}$$

$$\int_{-1}^{+1} S_{ij}^{e*}(P_s)N_k(\boldsymbol{\eta}^e)J^e \mathrm{d}\boldsymbol{\eta}^e \simeq \sum_{\gamma=1}^{\gamma_{\max}} S_{ij}^{e*}(P_s)N_k(\tilde{\boldsymbol{\eta}}_\gamma^e)\tilde{J}^e\tilde{w}_\gamma \tag{2.66}$$

$$\int_{-1}^{+1} D_{ij}^{e*}(P_s)N_k(\boldsymbol{\eta}^e)J^e \mathrm{d}\boldsymbol{\eta}^e \simeq \sum_{\gamma=1}^{\gamma_{\max}} D_{ij}^{e*}(P_s)N_k(\tilde{\boldsymbol{\eta}}_\gamma^e)\tilde{J}^e\tilde{w}_\gamma \tag{2.67}$$

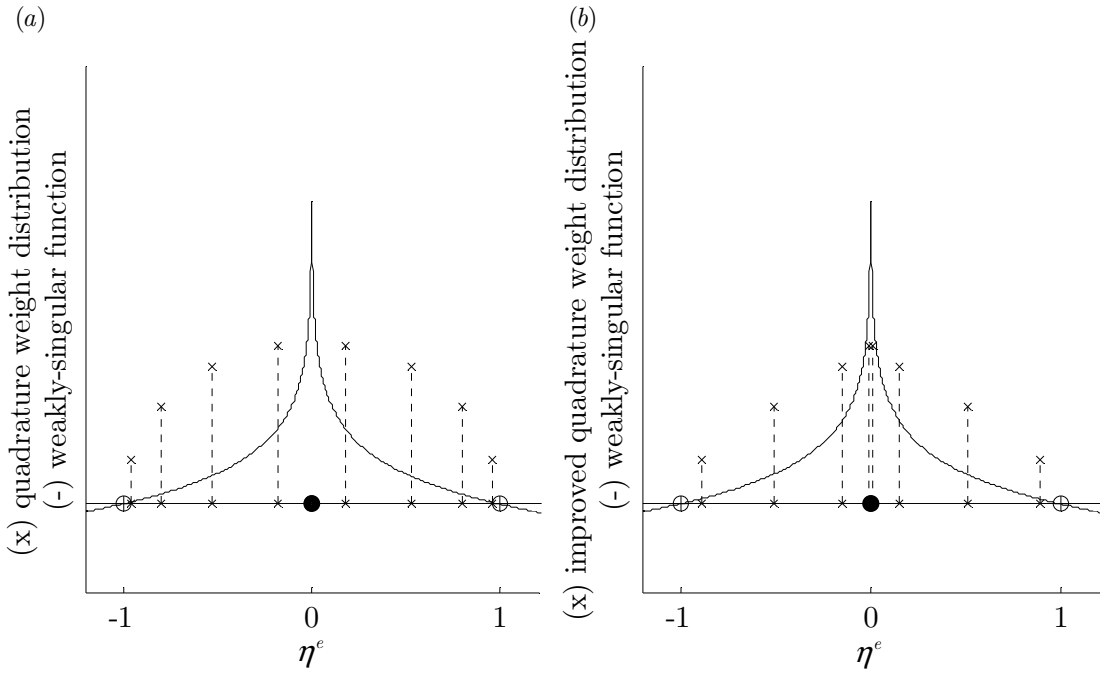

Figure 14. Quadrature points 'x' are naturally redistributed over element e from (a) a Gaussian distribution, (b) towards the singularity when using the Telles scheme. The comparative weights associated with each quadrature point is illustrated by '---'

2.5.4 Strongly-singular integration

For the functions that exhibit strongly-singular behaviour, the approach to the computation of the integral depends on the element type at the source point. A scheme of separating the singular function into its singular and non-

singular components is preferred (Guiggiani and Casalini, 1987), but can only be applied where the source node exhibits no nodal connectivity and lies upon a flat element. An alternative approach for continuous elements and non-flat elements follows later.

The singular integral exists as part of a *Cauchy principal value* (CPV), denoted by

$$\int_{-1}^{+1} f(\eta)\,\mathrm{d}\eta \underset{CPV}{=} \lim_{\delta\to 0}\left[\int_{-1}^{\eta'-\delta} f(\eta)\mathrm{d}\eta + \int_{\eta'+\delta}^{+1} f(\eta)\mathrm{d}\eta\right] \tag{2.68}$$

where f is an arbitrary function that exhibits strongly-singular behaviour at η', the local coordinate of the strong singularity where $-1 \le \eta' \le +1$ and δ is the radius of the CPV zone, illustrated in Figure 15.

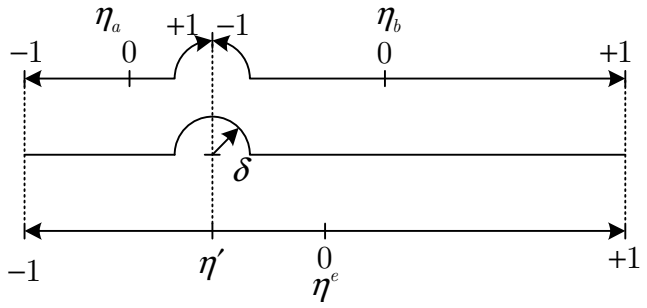

Figure 15. The Cauchy Principal Value zone and the subdivision of an element at the singularity

By subdividing the element at the singularity, two functions describing f in terms of the two local coordinates

$$f_a(\eta_a) = f(\eta)(1-\eta) \tag{2.69}$$
$$f_b(\eta_b) = f(\eta)(1+\eta) \tag{2.70}$$

are substituted into equation (2.68)

$$\int_{-1}^{+1} f(\eta)\,\mathrm{d}\eta \underset{CPV}{=} \lim_{\delta\to 0}\left[\int_{-1}^{+1}\frac{f_a(\eta)J_a(\eta)}{\eta-1}\,\mathrm{d}\eta + \int_{-1}^{+1}\frac{f_b(\eta)J_b(\eta)}{\eta+1}\,\mathrm{d}\eta\right] \tag{2.71}$$

where $J_a(\eta)$ and $J_b(\eta)$ are the Jacobians associated with element portions η_a and η_b. By simultaneously subtracting and expressions for the singularity existing at both $\eta_a = 1$ and $\eta_b = -1$

$$\int_{-1}^{+1} f(\eta)\,\mathrm{d}\eta \underset{CPV}{=} \lim_{\delta\to 0}\left\{\int_{-1}^{+1}\frac{f_a(\eta)J_a(\eta)-f_a(1)J_a(1)}{\eta-1}\,\mathrm{d}\eta + \int_{-1}^{+1}\frac{f_a(1)J_a(1)}{\eta-1}\,\mathrm{d}\eta + \ldots \right.$$
$$\left. \int_{-1}^{+1}\frac{f_b(\eta)J_b(\eta)-f_b(-1)J_b(-1)}{\eta+1}\,\mathrm{d}\eta + \int_{-1}^{+1}\frac{f_b(-1)J_b(-1)}{\eta+1}\,\mathrm{d}\eta\right\} \tag{2.72}$$

Since $f_a(\eta_a)J_a(\eta_a)\to\infty$ at $\eta_a = 1$, and $f_b(\eta_b)J_b(\eta_b)\to\infty$ at $\eta_b = -1$, the strongly singular part of the function is cancelled leaving two regular expressions to be evaluated.

$$\int_{-1}^{+1} f(\eta)\,\mathrm{d}\eta \underset{CPV}{=} \int_{-1}^{+1}\frac{f_a(\eta)J_a(\eta)-f_a(1)J_a(1)}{\eta-1}\,\mathrm{d}\eta + \int_{-1}^{+1}\frac{f_b(\eta)J_b(\eta)-f_b(-1)J_b(-1)}{\eta+1}\,\mathrm{d}\eta \ldots$$
$$-f_a(1)J_a(1)\ln\left|J_a(-1)\right| + f_b(-1)J_b(-1)\ln\left|J_b(1)\right| \tag{2.73}$$

When the arbitrary function f is replaced by the strongly-singular kernels used in the DBIE, by this separation and cancellation of the strongly singular part, the integral was shown to be computable for flat discontinuous elements (Portela *et al.*, 1992), given by

$$\hat{\mathbf{H}}^{ek}(P_s) = \frac{(1-2\nu)}{4\pi(1-\nu)}\mathbf{S}\int_{-1}^{+1}\left(\frac{N_k}{\eta-\eta'}\right)\mathrm{d}\eta_{\mathrm{CPV}} \tag{2.74}$$

or

$$\hat{\mathbf{H}}^{ek}(P_s) = \frac{E}{2\pi(1-\nu^2)l_e}\mathbf{S}\tilde{I}_i \tag{2.75}$$

where k is the index of the node on element e at which the singularity occurs, l_e is the geometric length of element e and

$$\mathbf{S} = \begin{bmatrix} 0 & -1 \\ +1 & 0 \end{bmatrix} \tag{2.76}$$

The singular integrals $\tilde{I}_k$ for discontinuous quadratic elements with local nodal coordinates $\boldsymbol{\eta}^e = \{-\frac{2}{3} \quad 0 \quad \frac{2}{3}\}$ are given by (Portela *et al.*, 1992)

$$\tilde{I}_1 = \int_{-1}^{+1}\left(\frac{N_1}{\eta-\eta'}\right)\mathrm{d}\eta_{\mathrm{CPV}} = \frac{3}{4}\left(\frac{\eta'(3\eta'-2)}{2}\ln\left|\frac{1-\eta'}{1+\eta'}\right| + 3\eta' - 2\right) \tag{2.77}$$

$$\tilde{I}_2 = \int_{-1}^{+1}\left(\frac{N_2}{\eta-\eta'}\right)\mathrm{d}\eta_{\mathrm{CPV}} = \frac{1}{2}\left(\frac{(3\eta'+2)(3\eta'-2)}{2}\ln\left|\frac{1+\eta'}{1-\eta'}\right| - 9\eta'\right) \tag{2.78}$$

$$\tilde{I}_3 = \int_{-1}^{+1}\left(\frac{N_3}{\eta-\eta'}\right)\mathrm{d}\eta_{\mathrm{CPV}} = \frac{3}{4}\left(\frac{\eta'(3\eta'+2)}{2}\ln\left|\frac{1-\eta'}{1+\eta'}\right| + 3\eta' + 2\right) \tag{2.79}$$

The applicability of these expressions has been extended as part of the present work by rewriting equations (2.77) to (2.79) for flat quadratic boundary elements with general local nodal coordinates $\boldsymbol{\eta}^e = \{\eta_1 \quad \eta_2 \quad \eta_3\}$ (Bird *et al.*, 2008b)

$$\tilde{I}_k = \int_{-1}^{+1}\left(\frac{N_k}{\eta-\eta'}\right)\mathrm{d}\eta_{\mathrm{CPV}} = A_k\left(2(\eta'-B_k) + (\eta'^2 - B_k\eta' + C_k)\ln\left|\frac{1-\eta'}{1+\eta'}\right|\right) \tag{2.80}$$

where A_k, B_k and C_k are defined in §2.4.

For non-flat elements, or elements with nodal continuity, the application of rigid body motion can be used to estimate the terms that otherwise require singular integration. Consider the analysis of a traction-free domain subject to

two independent boundary conditions, each a rigid body displacement in first the x-direction, then the y-direction. In each case, this displacement has a defined magnitude U_R, where typically

$$U_R = 1 \tag{2.81}$$

The nodal displacements and tractions of corresponding to each element $e = 1..L$ are thus given by

$$\mathbf{u}^{e\,\mathrm{T}} = \{U_R \quad 0 \quad U_R \quad 0 \quad U_R \quad 0\}^{\mathrm{T}} \tag{2.82}$$

$$\mathbf{t}^{e\,\mathrm{T}} = \{0 \quad 0 \quad 0 \quad 0 \quad 0 \quad 0\}^{\mathrm{T}} \tag{2.83}$$

in the first case and

$$\mathbf{u}_e{}^{\mathrm{T}} = \{0 \quad U_R \quad 0 \quad U_R \quad 0 \quad U_R\}^{\mathrm{T}} \tag{2.84}$$

$$\mathbf{t}_e{}^{\mathrm{T}} = \{0 \quad 0 \quad 0 \quad 0 \quad 0 \quad 0\}^{\mathrm{T}} \tag{2.85}$$

in the second. Using each rigid body displacement case in turn, equation (2.17) can thus be reduced to

$$C(P_s)U_R + \sum_{e=1}^{L}\sum_{k=1}^{3}\hat{h}_{xx}^{ek}U_R = 0 \tag{2.86}$$

$$C(P_s)U_R + \sum_{e=1}^{L}\sum_{k=1}^{3}\hat{h}_{xy}^{ek}U_R = 0 \tag{2.87}$$

and

$$C(P_s)U_R + \sum_{e=1}^{L}\sum_{k=1}^{3}\hat{h}_{yx}^{ek}U_R = 0 \tag{2.88}$$

$$C(P_s)U_R + \sum_{e=1}^{L}\sum_{k=1}^{3}\hat{h}_{yy}^{ek}U_R = 0 \tag{2.89}$$

respectively.

When using the DBIE, for each of the above equations there exists just one term that exhibits singular behaviour in its computation. Thus, by the integration of the regular (non-singular) terms, the singular term can be estimated by the difference of their sum and the jump term $C(P_s)$.

When using the TBIE, there may exist multiple terms that exhibit singular behaviour and so this scheme cannot be employed in this manner. It should also be noted that although the explicit computation of the singular integration is avoided, it is at the expense of the errors accumulated in the integration of each of the non-singular terms.

In the case of the TBIE, the strongly-singular integration required for the computation of equation (2.24) can be avoided by *a priori* knowledge of the application of the method. Within the scope of the present work, traction-free boundary conditions are assumed on elements that for which the TBIE is used

$$\mathbf{t}(P_s) = \begin{Bmatrix} 0 \\ 0 \end{Bmatrix} \tag{2.90}$$

Under this assumption, the computation of their coefficients, $\hat{\mathbf{G}}'^{ek}(P_s)$ in equation (2.49), is unnecessary..

2.5.5 Hyper-singular integration

Functions that exhibit hyper-singular behaviour are evaluated analytically. In a similar manner outlined above, the hyper-singular integral exists as part of a *Hadamard principal value* (HPV), denoted by

$$\int_{-1}^{+1} f(\eta)\, \mathrm{d}\eta \underset{HPV}{=} \lim_{\delta \to 0} \left[\int_{-1}^{\eta'-\delta} f(\eta)\mathrm{d}\eta + \int_{\eta'+\delta}^{+1} f(\eta)\mathrm{d}\eta \right] \tag{2.91}$$

where f is an arbitrary function that is exhibits hyper-singular behaviour at η', the local coordinate of the strong singularity where $-1 \le \eta' \le +1$ and δ is the radius of the HPV zone

When the arbitrary function f is replaced by the hyper-singular kernels used in the TBIE, the integral was shown to be computable for flat discontinuous elements (Portela *et al.*, 1992), given by

$$\mathbf{H}_k'^e(P_s) = \frac{E}{2\pi(1-\nu^2)l_e}\mathbf{S}'\int_{-1}^{+1}\left(\frac{\tilde{N}_k}{(\eta-\eta')^2}\right)\mathrm{d}\eta_{\mathrm{HPV}} \tag{2.92}$$

or

$$\mathbf{H}_k'^e(P_s) = \frac{E}{2\pi(1-\nu^2)l_e}\mathbf{S}'\tilde{I}_k \tag{2.93}$$

where k is the index of the node on element e at which the singularity occurs.

As part of the present work (Simpson and Bird, 2009), the matrix $\mathbf{S}'$, described fully in the reference (Portela *et al.*, 1992), was shown as to reduce to a more simplified expression relating the dot product of the normals at P_s and P_f

$$\mathbf{S}' = \begin{bmatrix} n_x(P_s)\bullet n_x(P_f) & n_x(P_s)\bullet n_y(P_f) \\ n_y(P_s)\bullet n_x(P_f) & n_y(P_s)\bullet n_y(P_f) \end{bmatrix} \tag{2.94}$$

The singular integrals $\tilde{I}_k'$ for discontinuous quadratic elements with local nodal coordinates $\boldsymbol{\eta}^e = \{-\frac{2}{3} \quad 0 \quad \frac{2}{3}\}$ are given by (Portela *et al.*, 1992)

$$\tilde{I}_1' = \int_{-1}^{+1}\left(\frac{N_1}{(\eta-\eta')^2}\right)\mathrm{d}\eta_{\mathrm{HPV}} = \frac{3}{4}\left((3\eta'-1)\ln\left|\frac{1-\eta'}{1+\eta'}\right| + \frac{6\eta'^2-2\eta'-3}{\eta'^2-1}\right) \tag{2.95}$$

$$\tilde{I}_2' = \int_{-1}^{+1}\left(\frac{N_2}{(\eta-\eta')^2}\right)\mathrm{d}\eta_{\mathrm{HPV}} = \frac{1}{2}\left(9\eta'\ln\left|\frac{1+\eta'}{1-\eta'}\right| - \frac{18\eta'^2-13}{\eta'^2-1}\right) \tag{2.96}$$

$$\tilde{I}_3' = \int_{-1}^{+1}\left(\frac{N_3}{(\eta-\eta')^2}\right)\mathrm{d}\eta_{\mathrm{HPV}} = \frac{3}{4}\left((3\eta'+1)\ln\left|\frac{1-\eta'}{1+\eta'}\right| + \frac{6\eta'^2+2\eta'-3}{\eta'^2-1}\right) \tag{2.97}$$

The applicability of these expressions has been extended as part of the present work by rewriting equations (2.95) to (2.97) for flat quadratic boundary elements with general local nodal coordinates $\boldsymbol{\eta}^e = \{\eta_1 \quad \eta_2 \quad \eta_3\}$ (Bird *et al.*, 2008b)

$$\tilde{I}_k = \int_{-1}^{+1}\left(\frac{N_k}{\eta-\eta'}\right)\mathrm{d}\eta_{\mathrm{HPV}} = 2A_k\left((\eta'-\frac{B_k}{2})\ln\left|\frac{1-\eta'}{1+\eta'}\right| + \frac{2\eta'^2-B_k\eta'+C_k-1}{\eta'^2-1}\right) \tag{2.98}$$

where A_k, B_k and C_k are defined in §2.4.

2.6 Submatrix assembly

Typically it is convenient to compute submatrices $\mathbf{H}^e(P_s)$ on a per-element/source point basis. Their assembly into $\mathbf{H}(P_s)$ for discontinuous elements is trivial, as illustrated in Figure 16(a), as each degree of freedom is associated with just one element, and thus with just one submatrix. However, if there is nodal connectivity between neighbouring elements e and $e+1$, through the use of continuous or semi-discontinuous elements, then their assembly into global system matrices $\mathbf{H}$ and $\mathbf{G}$ results in a non-square system. By the assimilation of the common displacement and traction coefficients in these matrices, these matrices can be made square.

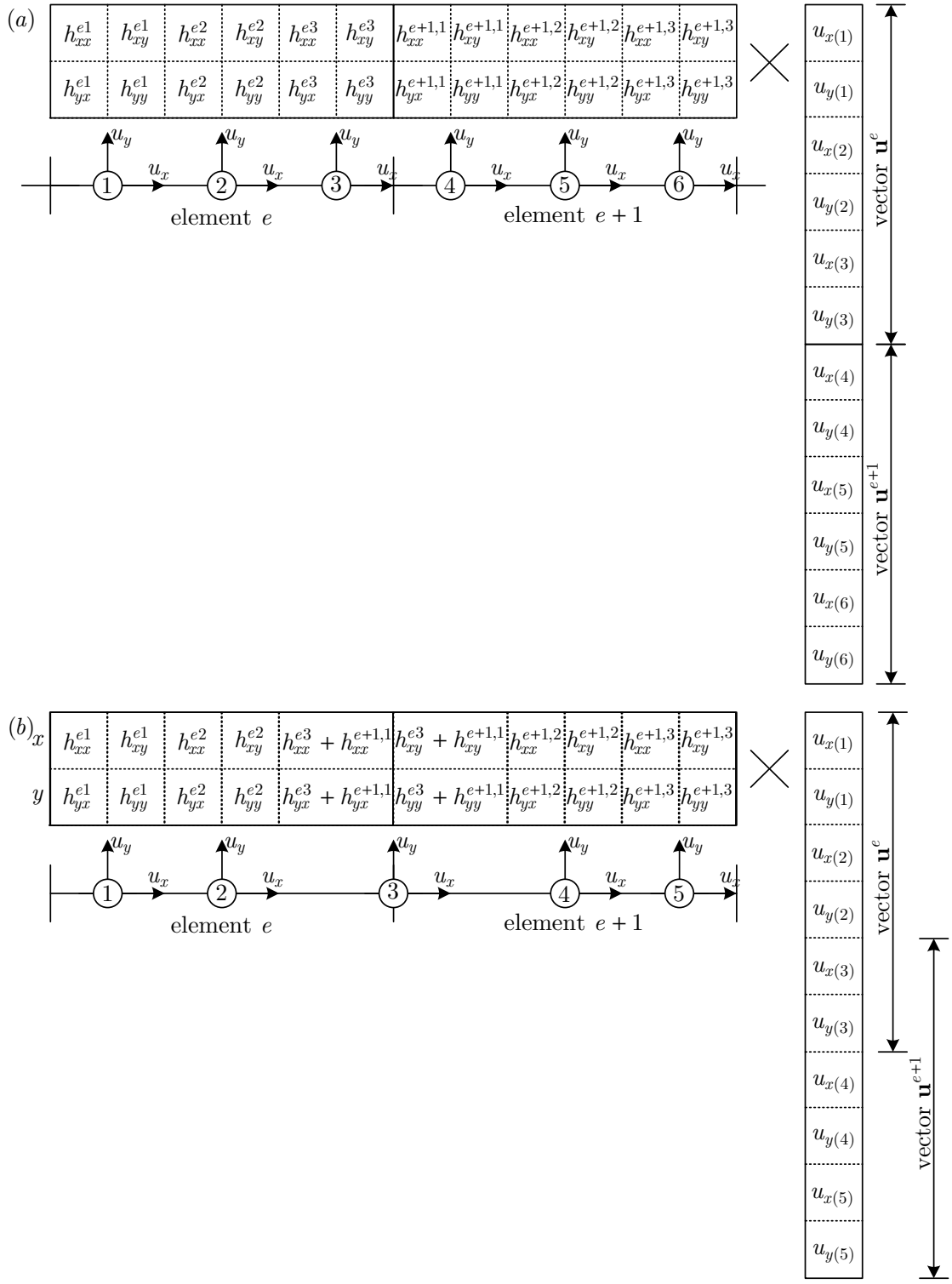

Figure 16. Submatrices $\mathbf{H}_e$ and $\mathbf{H}_{e+1}$ assembled into rows i and $i+1$, elements e and $e+1$ of $\mathbf{H}_{\mathrm{B}}$ for (a) discontinuous elements, and (b) semi-discontinuous elements

In the literature the means by which the system matrices are made square is not discussed. It may be simpler to assimilate these coefficients at a more local level, as illustrated in Figure 16, than attempt to fill global system matrices that retain their square structures during their construction. Such a local assimilation strategy was employed in the present work. This practice lends itself towards parallel computation where the elemental submatrices are built independently of their assembly into the global system matrices.

The local assembly of $\mathbf{G}_e(P_s)$ into $\mathbf{G}(P_s)$ for discontinuous elements follows that of $\mathbf{H}_e(P_s)$. However, if there is nodal connectivity between neighbouring elements e and $e+1$, it may be necessary to keep the traction components associated with both elements independent. If it is known *a priori* that there is continuity of the tractions over the shared node between elements, columns can be combined, like with the displacements, to form a single traction coefficient. However, if there is a discontinuity in traction at the shared node, then additional consideration is required. This discontinuity could be due to a discontinuity in boundary conditions, for example, or due to a non-smooth geometric feature, such as a corner, in which traction components on either side of the node will be formed using respective unit normals acting, by definition, in different directions.

Thus, in order to form the linear system in equation (2.32) using continuous elements, at a shared node, for each direction

- if both the contributions to the traction are unknown, then they are assumed continuous, and the corresponding displacement is known;
- if just one of the contributions to the traction is known, the corresponding displacement is also known; or

- if the displacement is unknown, the two contributions to the traction coefficient are both known,

otherwise the requirement of a known Dirichlet or Neumann boundary condition for each degree of freedom cannot be met.

As explained below, a discontinuous element assumption is made when using the TBIE and thus the assembly of $\mathbf{H}'_e(P_s)$ and $\mathbf{G}'_e(P_s)$ into $\mathbf{H}'(P_s)$ and $\mathbf{G}'(P_s)$ follows that of the discontinuous use of the DBIE described above.

2.7 Domain subdivision

The requirement of a known Dirichlet or Neumann boundary condition for each degree of freedom can be violated at interfaces of BEM subdomains. Consider the domain in Figure 17(a). The domain can be subdivided into that of Figure 17(b) by the introduction of the interior interface Γ_{I} common to both Ω_{B1} and Ω_{B2}

$$\Omega_{\mathrm{B}} = \Omega_{\mathrm{B1}} \cup \Omega_{\mathrm{B2}} \tag{2.99}$$

$$\Gamma_{\mathrm{B}} = \Gamma_{\mathrm{B1}} \cup \Gamma_{\mathrm{B2}} \tag{2.100}$$

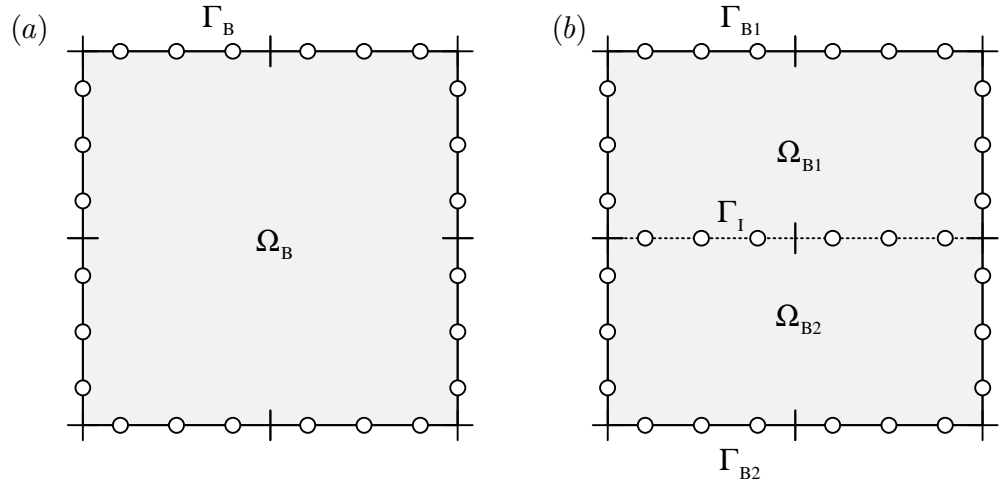

Figure 17. Subdivision of (*a*) Ω_{B} and Γ_{B} into (*b*) Ω_{B1}, Ω_{B2}, Γ_{B1}, Γ_{B2} and Γ_{I}

The formulation of the BEM equations can be performed on a subdomain by subdomain basis and assembled into the BEM system matrix. Boundary conditions are applied as with a single BEM domain, but with additional coupling conditions

$$\mathbf{u}_{\mathrm{I}1} = \mathbf{u}_{\mathrm{I}2} \tag{2.101}$$
$$\mathbf{t}_{\mathrm{I}1} = -\mathbf{t}_{\mathrm{I}2} \tag{2.102}$$

where the 'I' subscript denotes the interface degrees of freedom.

2.8 Dual BEM

The DBEM was developed primarily for applications to fracture mechanics and is summarised here. For further details, the reader is directed to Aliabadi (2002). Consider a domain Ω_{B}, bounded by external boundary Γ_{E}, and containing a crack whose upper and lower surfaces are Γ_{+} and Γ_{-} respectively, as illustrated in Figure 18.

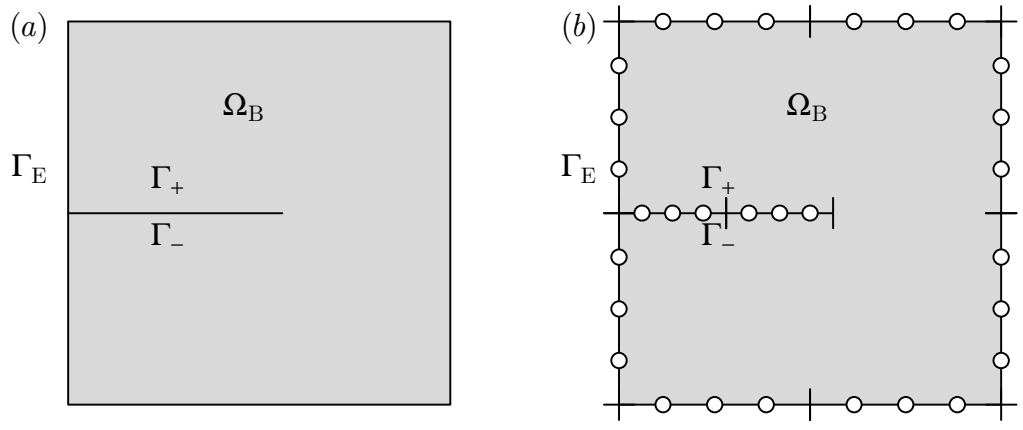

Figure 18. (*a*) A domain containing a crack, and (*b*) its BEM model

By introducing the subscripts '+' and '−', equation (2.30) can be partitioned

$$\begin{bmatrix} \mathbf{H}_{\mathrm{EE}} & \mathbf{H}_{\mathrm{E}+} & \mathbf{H}_{\mathrm{E}-} \\ \mathbf{H}_{+\mathrm{E}} & \mathbf{H}_{++} & \mathbf{H}_{+-} \\ \mathbf{H}_{-\mathrm{E}} & \mathbf{H}_{-+} & \mathbf{H}_{--} \end{bmatrix} \begin{Bmatrix} \mathbf{u}_{\mathrm{E}} \\ \mathbf{u}_{+} \\ \mathbf{u}_{-} \end{Bmatrix} = \begin{bmatrix} \mathbf{G}_{\mathrm{E}} & \mathbf{G}_{\mathrm{E}+} & \mathbf{G}_{\mathrm{E}-} \\ \mathbf{G}_{+\mathrm{E}} & \mathbf{G}_{++} & \mathbf{G}_{+-} \\ \mathbf{G}_{-\mathrm{E}} & \mathbf{G}_{-+} & \mathbf{G}_{--} \end{bmatrix} \begin{Bmatrix} \mathbf{t}_{\mathrm{E}} \\ \mathbf{t}_{+} \\ \mathbf{t}_{-} \end{Bmatrix} \tag{2.103}$$

Consider the collocation, first at P_{s+}, some source point on s on Γ_+, and second at P_{s-}, some coincident source point s on Γ_-, as illustrated in Figure 19. A drawback of the nature of the DBIE kernels is that when considered, for illustrative purposes, in terms of a polar separation (r,θ), there is no distinction between (r_+,θ_+) and (r_-,θ_-). Equation (2.103) becomes ill-conditioned owing to the repetition of terms caused by this apparent non-unique collocation.

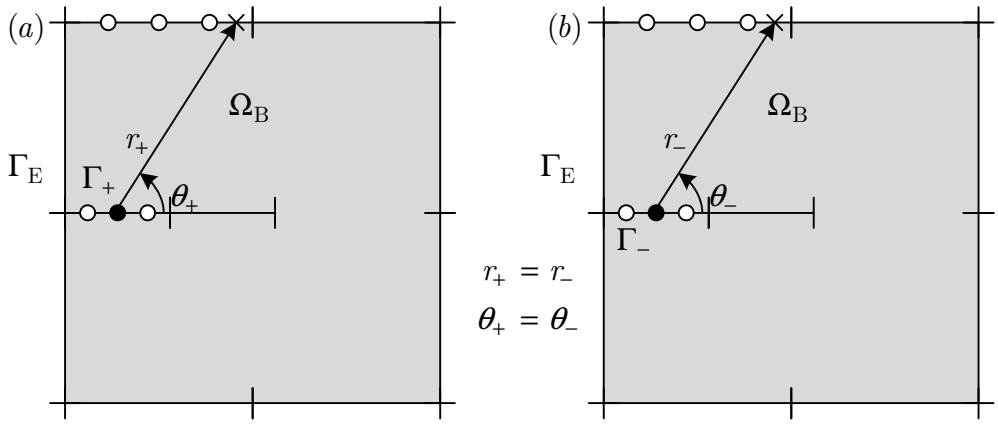

Figure 19. The BEM kernels make no distinction of the between collocation on (a) the upper crack surface and (b) the lower crack surface, as the separation r and angle θ from some source point • to Gauss Point × are the same

Using the TBIE, the DBEM offers a different set of equations when collocating on Γ_-, replacing the duplicated equations found using the BEM in (2.103), such that the partitioned equation is rewritten

$$\begin{bmatrix} \mathbf{H}_{\mathrm{EE}} & \mathbf{H}_{\mathrm{E}+} & \mathbf{H}_{\mathrm{E}-} \\ \mathbf{H}_{+\mathrm{E}} & \mathbf{H}_{++} & \mathbf{H}_{+-} \\ \mathbf{H}'_{-\mathrm{E}} & \mathbf{H}'_{-+} & \mathbf{H}'_{--} \end{bmatrix} \begin{Bmatrix} \mathbf{u}_{\mathrm{E}} \\ \mathbf{u}_{+} \\ \mathbf{u}_{-} \end{Bmatrix} = \begin{bmatrix} \mathbf{G}_{\mathrm{E}} & \mathbf{G}_{\mathrm{E}+} & \mathbf{G}_{\mathrm{E}-} \\ \mathbf{G}_{+\mathrm{E}} & \mathbf{G}_{++} & \mathbf{G}_{+-} \\ \mathbf{G}'_{-\mathrm{E}} & \mathbf{G}'_{-+} & \mathbf{G}'_{--} \end{bmatrix} \begin{Bmatrix} \mathbf{t}_{\mathrm{E}} \\ \mathbf{t}_{+} \\ \mathbf{t}_{-} \end{Bmatrix} \tag{2.104}$$

No further distinction between Γ_+ and Γ_- is required, so assimilating Γ_{E} and Γ_+ into Γ_{B}

$$\Gamma_{\mathrm{B}} = \Gamma_{\mathrm{E}} \cup \Gamma_+ \tag{2.105}$$

so rewriting Γ_- as Γ_D for clarity

$$\Gamma_D = \Gamma_- \tag{2.106}$$

equation (2.104) can be condensed into

$$\begin{bmatrix} \mathbf{H}_{BB} & \mathbf{H}_{BD} \\ \mathbf{H}_{DB} & \mathbf{H}_{DD} \end{bmatrix} \begin{Bmatrix} \mathbf{u}_B \\ \mathbf{u}_D \end{Bmatrix} = \begin{bmatrix} \mathbf{G}_{BB} & \mathbf{G}_{BD} \\ \mathbf{G}_{DB} & \mathbf{G}_{DD} \end{bmatrix} \begin{Bmatrix} \mathbf{t}_B \\ \mathbf{t}_D \end{Bmatrix} \tag{2.107}$$

where and the 'prime' superscript is dropped for brevity. Due to the nature of the TBIE, the DBEM is known to be a non-trivial extension to the BEM. Furthermore, although the choice of BEM element type is typically fairly arbitrary, in the case of the DBEM, the use of continuous elements presents computational complexities. The TBIE assumes C_1 continuity of tractions at the nodes, which cannot be guaranteed where there is a discontinuity in traction, such as at the crack tip illustrated in Figure 18(a). While efforts have been made to overcome this and to allow continuous elements in the DBEM, it may be more convenient to use discontinuous elements, as illustrated in Figure 18(b). However, as shown later in §5.2.1, the use of discontinuous elements can produce further complications of their own.

2.9 Adaptive integration

It should be noted that, unless otherwise stated, the remaining sections of this chapter follow as a direct result of work undertaken by the author.

2.9.1 Algorithm

In order to achieve acceptable levels of accuracy in the non-singular and weakly-singular integration of the BEM kernels, an iterative scheme was developed by the author. The integration of the kernels is computed using γ_t

quadrature points where ι is the iteration number, and $\gamma_1 = \gamma_{\min}$, the minimum number of quadrature points permitted by the algorithm.

The computation is repeated for $\iota + 1$ where

$$\gamma_{\iota+1} = \gamma_\iota + \Delta\gamma \tag{2.108}$$

and $\Delta\gamma$ is the quadrature point increment rate. The absolute differences between each of the twelve terms in $\hat{\mathbf{H}}^e(P_s)$ for iterations ι and $\iota + 1$ are given by

$$\left[\, \Delta\hat{H}^e_\iota(P_s)_{ij} \,\right] = \left| \left[\, \hat{H}^e_\iota(P_s)_{ij} \,\right]_\iota - \left[\, \hat{H}^e_{\iota+1}(P_s)_{ij} \,\right] \right|, \qquad \begin{matrix} i = 1,2 \\ j = 1..3 \end{matrix} \tag{2.109}$$

This process is repeated iteratively until

$$\max\left(\left[\, \Delta\hat{H}^e_\iota(P_s)_{ij} \,\right] \right) < \tau_{\hat{H}} \tag{2.110}$$

where $\tau_{\hat{H}}$ is the threshold of minimum numerical accuracy in $\hat{\mathbf{H}}^e(P_s)$ required by the algorithm, or until $\gamma_{\iota+1} \geq \gamma_{\max}$, the maximum number of quadrature points permitted by the algorithm. Complementarily, the absolute differences between each of the twelve terms in the traction coefficients

$$\left[\, \Delta G^e_\iota(P_s)_{ij} \,\right] = \left| \left[\, G^e_\iota(P_s)_{ij} \,\right]_\iota - \left[\, G^e_{\iota+1}(P_s)_{ij} \,\right] \right|, \qquad \begin{matrix} i = 1,2 \\ j = 1..3 \end{matrix} \tag{2.111}$$

are calculated iteratively until

$$\max\left(\left[\, \Delta G^e_\iota(P_s)_{ij} \,\right] \right) < \tau_G \tag{2.112}$$

where τ_G is the threshold of minimum numerical accuracy in $\mathbf{G}^e(P_s)$ required by the algorithm or until $\gamma_{\iota+1} \geq \gamma_{\max}$. Similar adaptive schemes are used in the integration of the DBEM kernels in producing $\mathbf{H}'^e(P_s)$ and $\hat{\mathbf{G}}'^e(P_s)$ with

thresholds of $\tau_{H'}$ and $\tau_{\hat{G}'}$ respectively.

Absolute errors are appropriate as the order of magnitude of the terms in the submatrices is such that normalised errors rapidly approach thresholds of computation accuracy.

2.9.2 Verification

In order both to verify the adaptive integration and to establish suitable values for the parameters used in the algorithm, convergence rates were tested. Convergence was found to be problem-dependent, so in order to estimate suitable parameters for general domains, convergence rates were based on the results of a range of semi-random domains.

A circular domain as discretised with a random distribution of boundary elements, which are then subject to further random perturbations, as illustrated in Figure 20. The convergence of the terms in the submatrices with γ for each of the collocation/numerical integration pairs for 10 such semi-random domains was analysed.

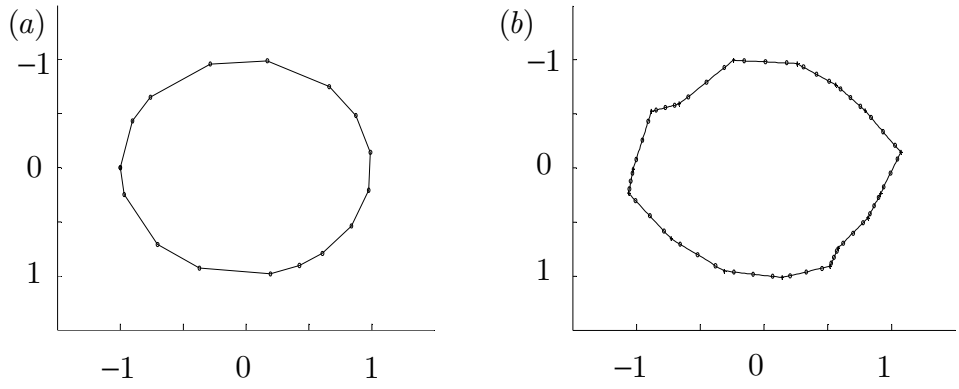

Figure 20. Example of the semi-random domain defined by (a) a discretised circular domain, (b) subject to perturbations and discretised further with discontinuous boundary elements

The thresholds of accuracy beyond which increases in γ made no significant difference were found to be

$$\tau_{\hat{H}} = 10^{-12} \tag{2.113}$$

$$\tau_{G} = 10^{-17} \tag{2.114}$$

$$\tau_{H'} = 10^{-6} \tag{2.115}$$

$$\tau_{\hat{G}'} = 10^{-11} \tag{2.116}$$

Repeated analyses in this manner confirmed the suitability of these tolerances. Depending on the rate of convergence towards these tolerances, the adaptive integration scheme may significantly increase computation times. However, this increase in computation times for the domains is less than those of post-analysis adaptive mesh refinement-based solution to reducing errors. An efficient, hierarchical approach to mesh refinement (Charafi *et al.*, 1995) in conjunction with the presented algorithm may provide a more suitable balance between solution accuracy and computation time.

2.10 Example applications to fracture mechanics

The DBEM is considered well-suited to fracture mechanics in which crack faces are assumed to be infinitesimally separated. Limitations of the displacement accuracy are well-known, but are presented in the following examples both to demonstrate code flexibility, robustness and reliability and to provide a means for comparison with later examples, and should not be considered a new application of this method.

The following benchmark problem is presented for the comparison of each of the numerical methods in this thesis. With reference to Figure 21, a finite domain Ω models the immediate vicinity of the tip of a crack of length $2a$ central to an infinite domain Ω_∞ subject to a uniaxial load of σ such that the

section of crack face modelled is of length $\overline{a}$ and $\overline{a} << a$. Some *a priori* knowledge may be used about the symmetrical nature of the crack face and its effect on a suitable model. The boundary is subdivided into portions of boundary $\Gamma_{\tilde{u}}$ with known displacement boundary conditions, and portions of boundary Γ_u with displacements to be found as part of the solution:

$$\Gamma = \Gamma_{\tilde{u}} \cup \Gamma_u \tag{2.117}$$

The displacement boundary conditions are defined by Williams expansion describing displacements around a crack tip in an infinite plate (Williams, 1957), converted to the boundary coordinate system

$$\mathbf{u}_W(s) = \mathbf{u}_W(r,\theta) \tag{2.118}$$

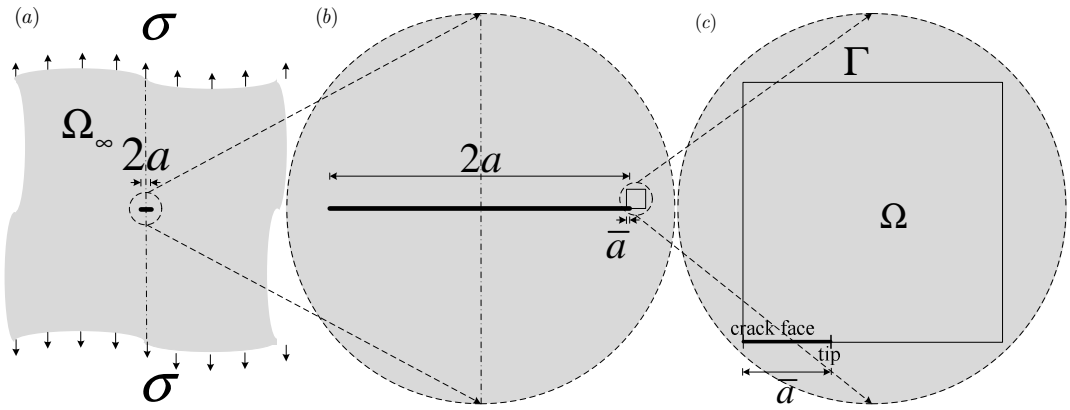

Figure 21. (*a*) Through crack in an infinite plate, (*b*) the section of the domain modelled, and (*c*) the portion of the crack face and its vicinity to be modelled

Traction free boundary conditions are applied to Γ_u.

An indication of the average global errors in the solution can be estimated by means of L^2-based error norms of the displacement solution on Γ_u given by

$$\varepsilon_{L^2k} = \sqrt{\frac{\sum_s \left(u_k(s) - u_{Wk}(s)\right)^2}{\sigma}}, \qquad s \in \Gamma_u, \sigma \neq 0 \tag{2.119}$$

where $k = x, y$. The mesh is uniformly subdivided and the analysis repeated order to assess the convergence characteristics of these displacements. While only one problem is presented for comparison, multiple variants of the same problem (with different boundary conditions, material properties, crack lengths etc.) have demonstrated that the following results are indicative of this method.

For the examples in this chapter

$$\Omega = \Omega_{\mathrm{B}} \tag{2.120}$$

2.10.1 Through crack in an infinite plate example 1

The BEM is used to model the crack tip described in §2.10. With reference to Figure 22(c), the dimensions of Ω_{B} are $b \times h$, and Γ_{B} is subdivided into portions of boundary $\Gamma_{\tilde{u}}$ with known displacement boundary conditions (red nodes), and portions of boundary Γ_u with displacements to be found as part of the solution (white nodes). In this case

$$\Gamma = \Gamma_{\mathrm{B}} \tag{2.121}$$

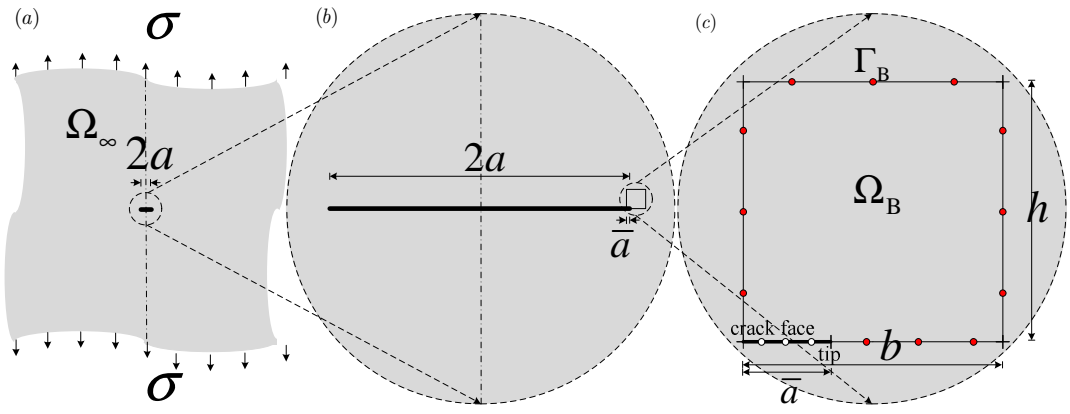

Figure 22. BEM analysis of (a) through crack in an infinite plate, (b) the section of the domain modelled, and (c) the mesh where red and white nodes indicate $\Gamma_{\tilde{u}}$ and Γ_u

The displacements of the domain and boundary portion Γ_u are illustrated in Figure 23(a) and Figure 24 respectively. Convergence characteristics of the BEM are illustrated in Figure 25 using the uniform mesh refinement indicated in Figure 23(b) where n is the number of degrees of freedom.

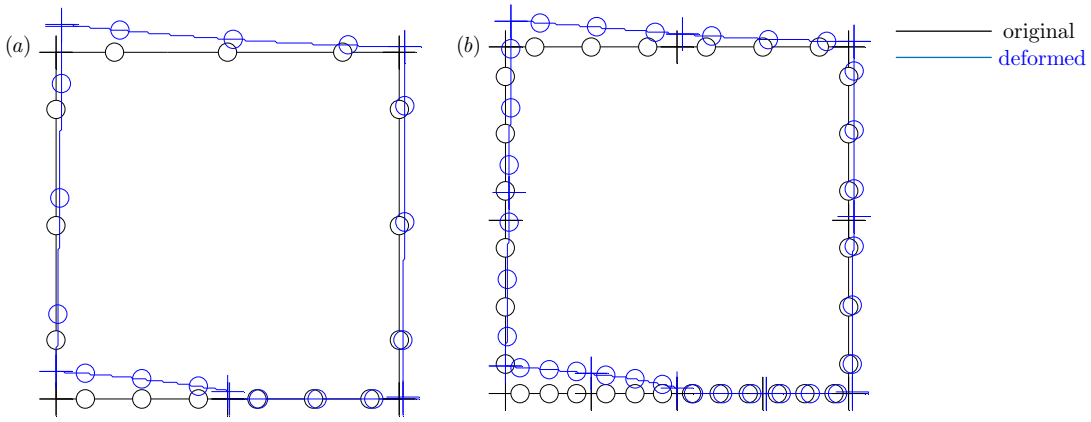

Figure 23. To-scale deformation of (a) initial mesh and (b) uniformly-refined mesh

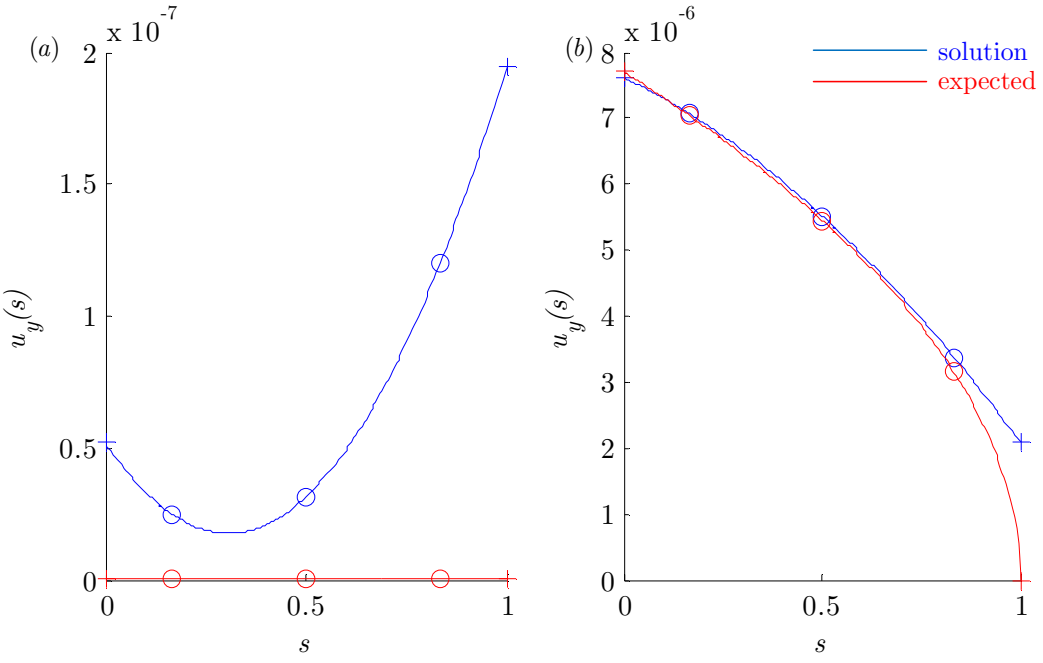

Figure 24. (a) x- and (b) y-direction displacement results on Γ_u

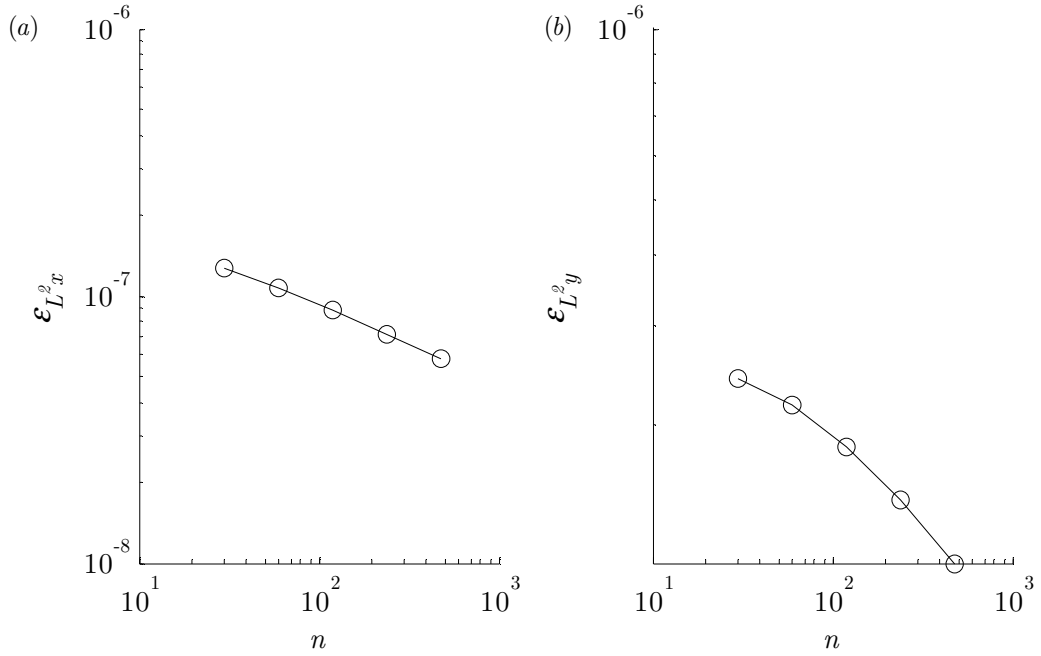

Figure 25. Convergence characteristics of global error estimators $(a)\,\varepsilon_{L^2x}$ and $(b)\,\varepsilon_{L^2y}$

2.10.2 Through crack in an infinite plate example 2

The BEM is again used to model the crack tip described in §2.10, but the assumption of symmetry is removed by domain subdivision. With reference to Figure 26(c), Ω_{B} (of dimensions $b \times 2h$) is divided into subdomains Ω_{B1} and Ω_{B1}, separated by interface portion Γ_{I} such that

$$\Gamma = \Gamma_{\mathrm{B1}} \cup \Gamma_{\mathrm{B2}} \cup \Gamma_{\mathrm{I}} \tag{2.122}$$

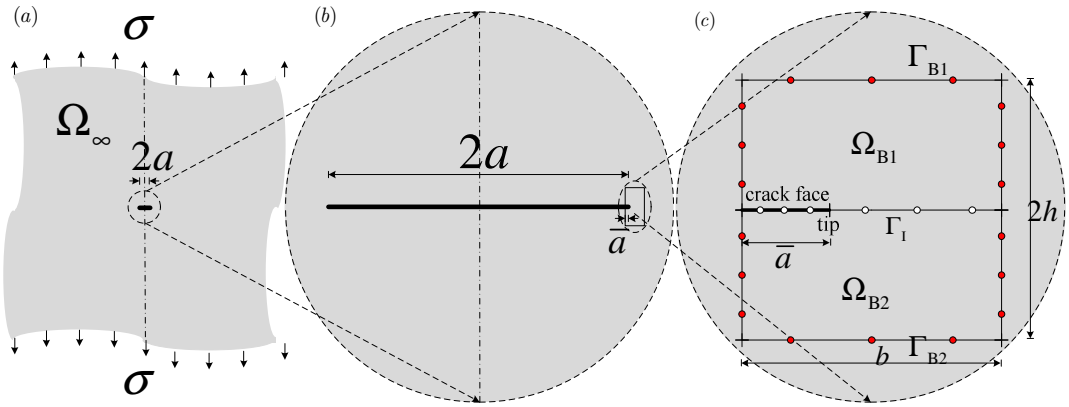

Figure 26. Multizone BEM analysis of (a) through crack in an infinite plate, (b) the section of the domain modelled, and (c) the mesh where red and white nodes indicate $\Gamma_{\tilde{u}}$ and Γ_u

The displacements of the domain and boundary portion Γ_u are illustrated in Figure 27(a) and Figure 28 respectively. Convergence characteristics of the multizone BEM are illustrated in Figure 29 using the uniform mesh refinement indicated in Figure 27(b).

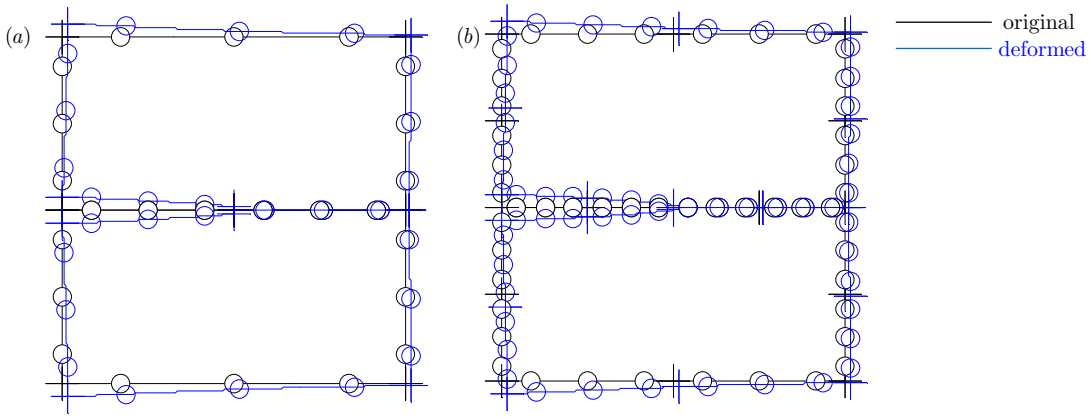

Figure 27. To-scale deformation of (a) initial mesh and (b) uniformly-refined mesh

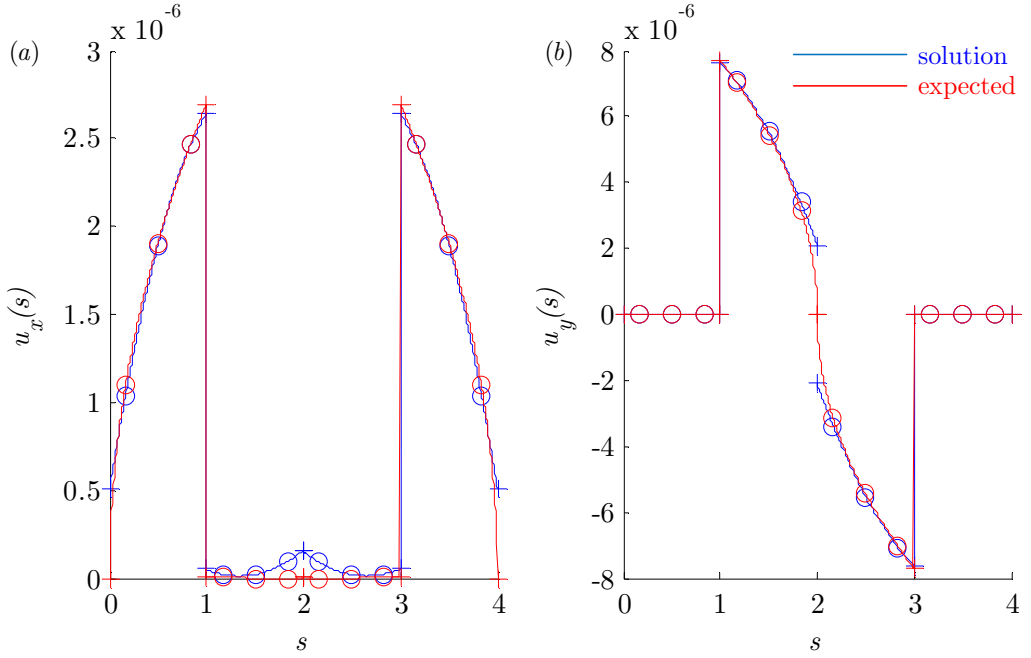

Figure 28. (a) x- and (b) y-direction displacement results on Γ_u

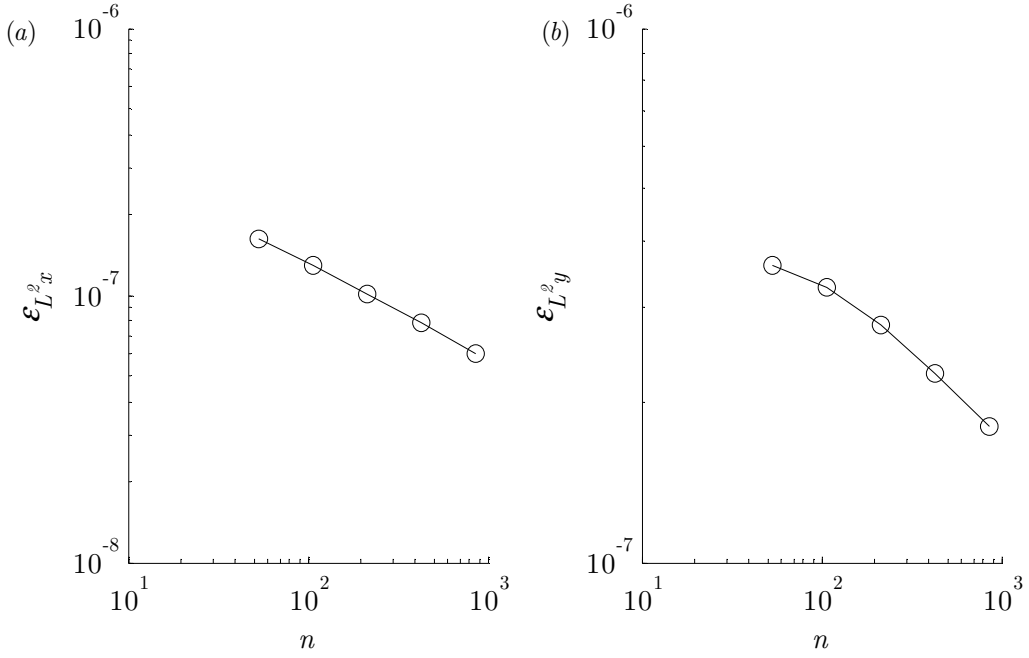

Figure 29. Convergence characteristics of global error estimators $(a)\,\varepsilon_{L^2x}$ and $(b)\,\varepsilon_{L^2y}$

2.10.3 Through crack in an infinite plate example 3

The BEM is again used to model the crack tip described in §2.10, but the assumption of symmetry is removed by the use of the DBEM. With reference

to Figure 30(c), the elements on the upper and lower crack surfaces are coincident and their finite separation is for illustrative purposes only, and

$$\Gamma = \Gamma_B \cup \Gamma_D \tag{2.123}$$

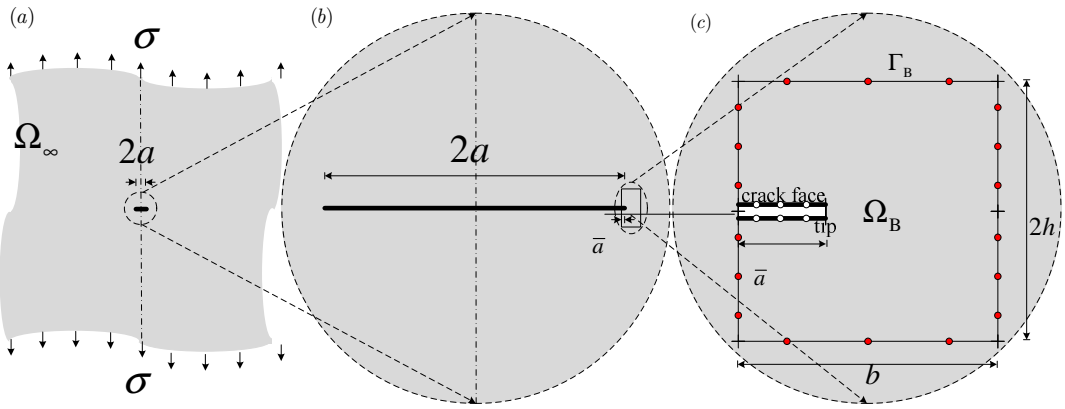

Figure 30. DBEM analysis of (a) through crack in an infinite plate, (b) the section of the domain modelled, and (c) the mesh where red and white nodes indicate $\Gamma_{\bar{u}}$ and Γ_u

The displacements of the domain and boundary portion Γ_u are illustrated in Figure 27(a) and Figure 28 respectively. Convergence characteristics of the DBEM are illustrated in Figure 29 using the uniform mesh refinement indicated in Figure 27(b).

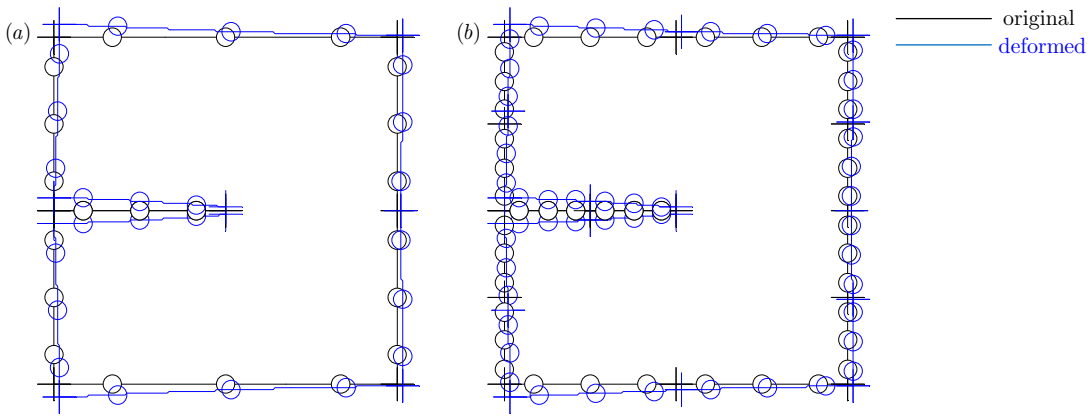

Figure 31. To-scale deformation of (a) initial mesh and (b) uniformly-refined mesh

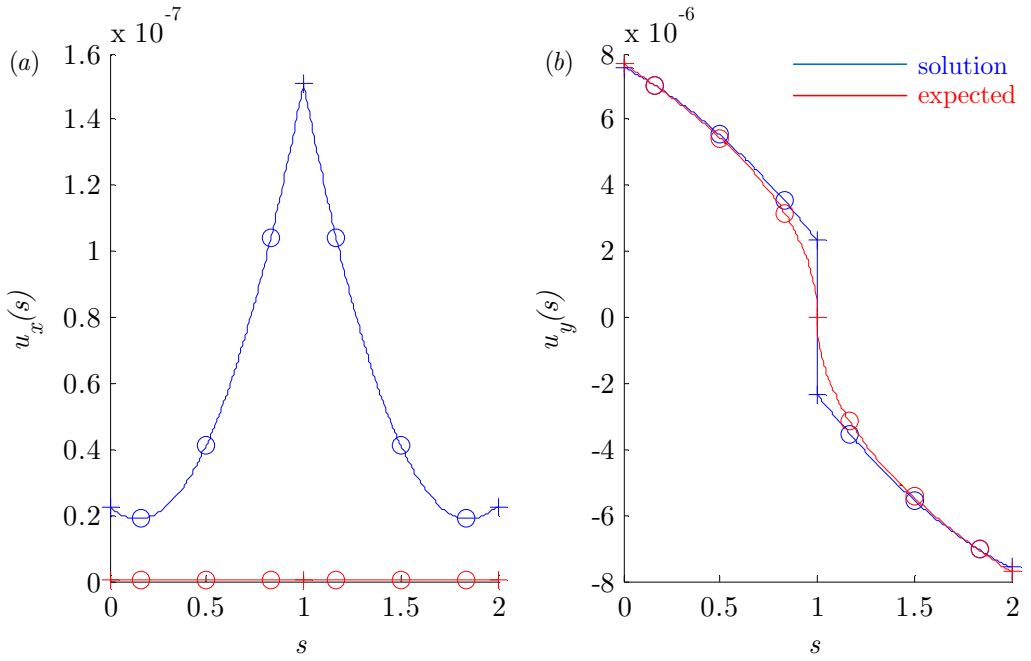

Figure 32. (a) x- and (b) y-direction displacement results on Γ_u

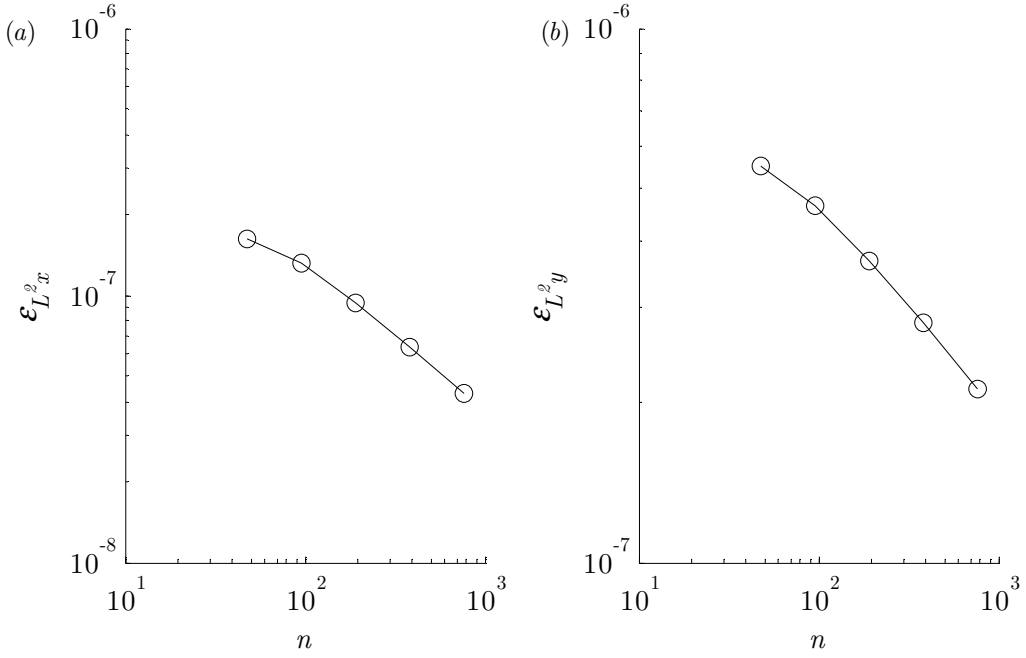

Figure 33. Convergence characteristics of global error estimators $(a)\,\varepsilon_{L^2x}$ and $(b)\,\varepsilon_{L^2y}$

2.11 Boundary element local nodal distribution

A working assumption drawn from the literature, such as , (Aliabadi, 1997) and (Portela *et al.*, 1992), about the discontinuous boundary elements

described in §2.3 is that the local nodal distribution

$$\boldsymbol{\eta}^e = \left\{-\tfrac{2}{3} \quad 0 \quad +\tfrac{2}{3}\right\} \tag{2.124}$$

is preferred. When applied to a mesh of uniform element size, it produces an evenly-spaced global nodal distribution, as illustrated in Figure 34(a). This maximises the separation all nodes, and in turn, increases the dissimilarities between each row in the BEM system matrices. This may contribute to the assumption that equation (2.124) offers an optimum solution.

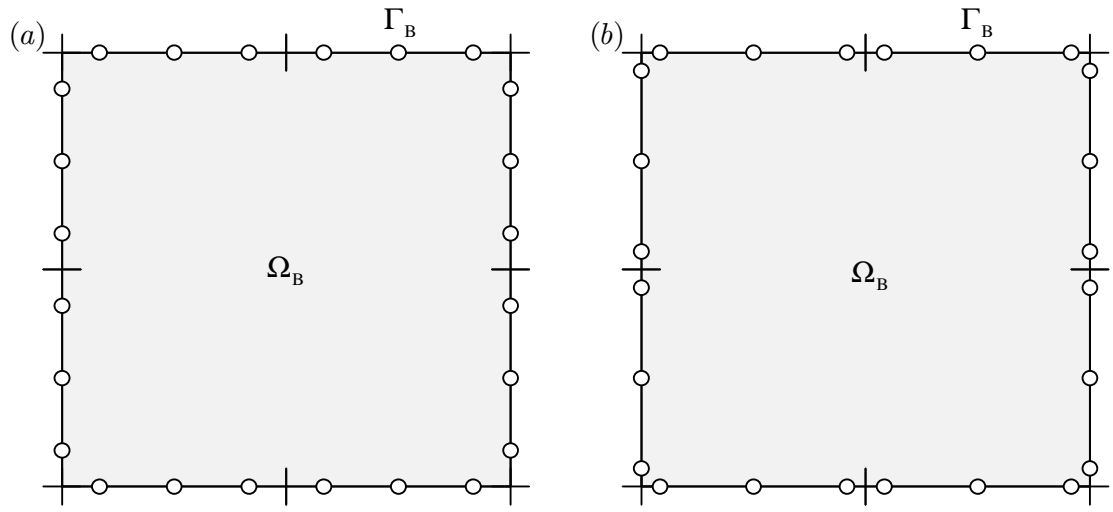

Figure 34. Example local nodal distributions where $(a)\,\boldsymbol{\eta}^e = \{-\tfrac{2}{3} \quad 0 \quad +\tfrac{2}{3}\}$ and $(b)\,\boldsymbol{\eta}^e = \{-\tfrac{5}{6} \quad 0 \quad +\tfrac{5}{6}\}$

However, the motivation for this assumption appears anecdotal and the suggestion that an unevenly-distributed nodal configuration, such as illustrated in Figure 34(b), produces a less reliable mesh is not necessarily true. It is well-known that the major drawback of the configuration in equation (2.124) is the increased discontinuity between neighbouring elements. But the effect this has on the global solution has not been demonstrated in the literature and as part of the present work is now illustrated by example.

Consider a domain in which the model in §2.10.3 is an example of the general case

$$\boldsymbol{\eta}^e = \{-\eta \quad 0 \quad +\eta\} \tag{2.125}$$

where $\eta = \frac{2}{3}$ for all e. By varying η such that $0 < \eta < 1$, the effect of the local nodal element distribution and element size can be observed. The effect of is examined by two stages of uniform refinement. This analysis was only made possible by the present work in which general expressions for the analytical integration of strongly-singular (§2.5.4) and hyper-singular functions (§2.5.5) were developed. These results are summarised in Figure 35 and discussed in §2.12.3.

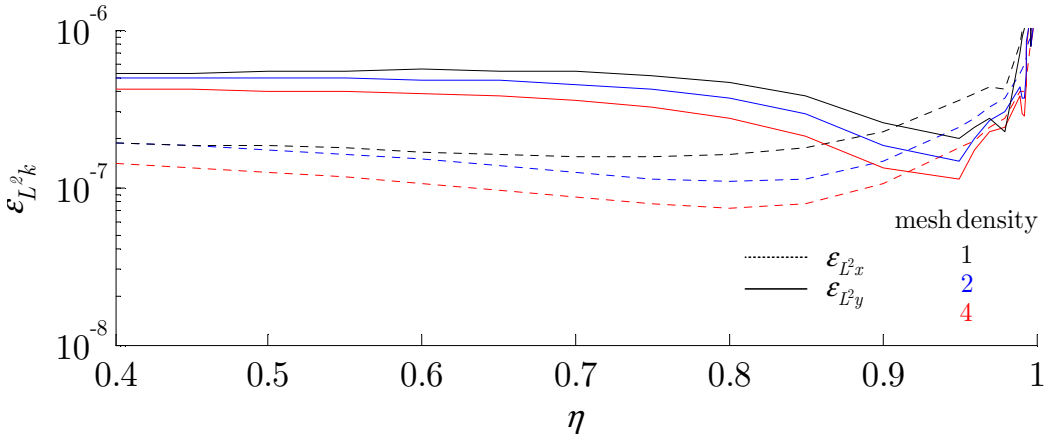

Figure 35. x- and y-displacement errors for example §2.10.3 with varying η

2.12 Discussion

2.12.1 Applications to fracture mechanics

Recalling that $\overline{a} << a$, in each of the three applications to fracture mechanics the BEM is seen to model the vicinity of the crack face well. However, the tip itself suffers relatively high displacement errors owing to the boundary element's poor quadratic approximation to a non-quadratic solution. Mesh

refinement merely shifts the problem closer to the crack tip without ever eradicating it. This is a known trait of the BEM and other polynomial-based approaches such as the FEM. Derived quantities, such as stress intensity factors, will therefore also be subject to errors in the same way. So, in terms of engineering applications, using the BEM displacement solution to estimate stress intensity factors, should be undertaken with this note of caution.

The displacement discontinuities present in all three examples are due to the discontinuous boundary elements used here. The analytical computation of the singular functions in §2.5 requires discontinuous boundary elements be used with the DBEM, so were used in the BEM in order to provide a basis for comparison. Moreover, continuous boundary elements only provide continuity in displacement, and the traction that is based on its derivative. Thus, the replacing of discontinuous elements with continuous elements is not only restricted to the BEM, but does not yield the continuous tractions at the node common to neighbouring continuous elements, as assumed in the application of boundary conditions.

Compared to the BEM, the multizone BEM and DBEM models yield a greater number of displacement degrees of freedom in the solution. This improves the error estimation in equation (2.119) by increasing the number of terms in the error norm. Furthermore, by removing the assumption of symmetry, they increase the applicability of the method. However, the BEM was selected for its versatility and ease of meshing which is made more involved by the multizone BEM approach. The DBEM does not suffer such meshing complications, but is hampered by boundary condition limitations and the integration of hyper-singular functions.

2.12.2 Consistent error definition

Due to the nature of the problem analysed and its effect on the x- and y-direction displacement solution, the components of the global averaging of errors was separated into its x- and y-direction components. The y-displacement solution suffers from the form of the expected solution in that

$$u_{Wy}(r,\theta) \to 0 \qquad \text{as} \qquad r \to 0 \tag{2.126}$$

So in the direct vicinity of the crack tip, the small, but finite y-direction displacement may be masked by the computational errors associated with dealing with values in the region of 10^{-15}, in addition to the inadequacies of its polynomial approximation. The x-displacement solution suffers in a similar way, but over the entire length of the crack face, not just near the tip, as

$$u_{Wx}(r,\theta = \pm\pi) = 0 \tag{2.127}$$

Perhaps a more attractive way to present results is to demonstrate the rate of convergence of the displacement error on the crack face as far from the crack tip as model can accommodate. This way, the effects of the polynomial approximation to the non-polynomial displacement field on the crack face would be minimised. Further, the relative error would be more favourable on a computational level as the expected y-direction displacements have a greater finite value. This yields both lower initial errors and a faster rate of convergence, as illustrated for the DBEM in Figure 36. However, the decision has been taken not to present only the applications at which the algorithm excels, or even offers marginal improvement over other available methods. Such a manner risks disguising the method's relative merits and drawbacks. Thus a more consistent basis for comparable results later is preferred, and so 'cherry-picked' results, such as those in Figure 36 are included for

demonstration purposes only and will not be replicated for other examples.

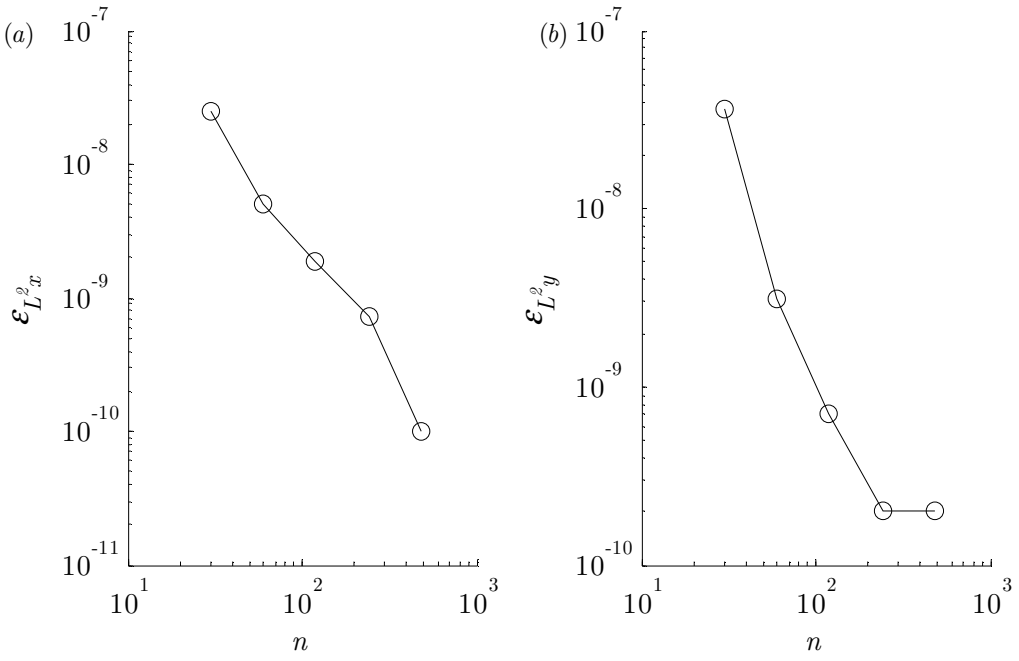

Figure 36. Convergence of 'cherry-picked' DBEM error estimators (a) ε_{L^2x} and (b) ε_{L^2y}

2.12.3 Boundary element local nodal distribution

As to be expected, as η approaches $\eta = 1$, the errors rise sharply as the rows in the BEM system matrices lose uniqueness and conditioning worsens. However, it can also be seen that $\eta = \frac{2}{3}$ is among the worst performing local nodal distributions and $\eta \approx 0.92$ offers the lowest errors when both x- and y-direction displacements are considered. Indeed, a crude initial mesh where $\eta = 0.91$ outperforms its counterpart where $\eta = \frac{2}{3}$ even after two levels of mesh refinement.

Error characteristics vary in direction owing to the problem-dependency of this effect, verified by further examples not presented here in which the optimum value of η also varies considerably. As such, it is beyond the scope of the present work to offer a strategy for *a priori* local nodal distribution

optimisation, but simply to deliver a note of caution about the form of the discontinuous elements used in the DBEM in the literature.

In order to facilitate comparisons with the results in the literature, the boundary element local nodal distribution in equation (2.124) is used for the results presented in this thesis.

2.13 Literature review

The roots of the BEM can be traced back to Green's identities and beyond (Cheng and Cheng, 2005), and as such the method is well-published in the literature. The method has been adopted for many applications and the author recommends Beer (Beer, 2001) for more tips for the practical implementation of the BEM in stress analysis code, and Aliabadi (Aliabadi, 2002) and Becker (Becker, 1992) more details on the fundamental solutions. There are many sources available for the implementation of the BEM, and owing to the trigonometric properties of the fundamental solutions, they are presented in many different ways. The decision to present them more explicitly in this thesis was made in order to narrow the scope for transcrption errors.

The DBEM is less well-known although in essence is formed simply through the derivative of the DBIE with respect to the outward normal. Following the first presentation of the boundary integral equations used in the DBEM and this subsequent derivation (Hong and Chen, 1988), the method became more widely used over the multi-zone approach (Blandford *et al.*, 1981) in applications with domain discontinuities. Several publications appeared in which the DBEM was applied to fracture mechanics, general implementation strategies of the method (Portela *et al.*, 1992) and the use of reanalysis in

crack propagation (Portela *et al.*, 1993).

Typically, when using the DBEM to model a fractured domain, the stress intensity factors are estimated by means of the *J*-integral method (Portela *et al.*, 1993), which is assumed path-independent. The accuracy of the method in calculating the stress intensity factors is dependent on the boundary displacement solution and the ability to define a path around crack tip. Inaccuracies may occur with internal point calculations for which the ratio of the distance between the internal point the closest point on the boundary, and the length of the element at that point on the boundary, is too small. This is in addition to the contribution to the integral by the displacements found on the crack faces where the discontinuous quadratic elements fail to capture the asymptotic behaviour of the boundary displacement in the immediate vicinity of the crack tip, as in Figure 31. This, albeit small, path dependency was observed in the extension of the DBEM with enrichment functions (Simpson, 2010), an extension to using the partition of unity in much the same way it extends the FEM to XFEM. A strategy for guaranteed avoidance of this path dependency suitable in the analysis of general engineering domains without some form of *a posteriori* analysis remains elusive.

The DBEM is not limited to the examples illustrated in this chapter where some *a priori* knowledge of symmetric geometry is used or where discontinuities extend to a boundary. Discontinuities found within a domain can be modelled using the DBEM, such as interior cracks (Portela *et al.*, 1992), and like the BEM, in applications outside of fracture mechanics, such as modelling infinitely-thin, degenerate boundaries within an electrostatic problem (Liao *et al.*, 2004). This vastly reduces the number of elements required to model such internal discontinuities than a finite element method

equivalent where the lack of symmetry would necessitate many additional domain elements.

An underlying implication that the nodes of the coincident boundary elements used in describing the geometry of the upper and lower crack surfaces are also coincident has been a working assumption through the DBEM literature. Consequentially Portela *et al.* concluded that because of the resulting non-unique equations in the BEM system matrix, the solution of general crack problems cannot be achieved with the direct application of the BEM, in a single-region analysis (Portela *et al.*, 1993). This working limitation of nodal coincidence is overcome in §6 of the present work.

2.14 Conclusion

The well-known BEM and its extension the DBEM have been assessed. Standard techniques for their implementation have been presented alongside complementary additions developed by the author, and by the author *et al.* as a direct part of this work. A general adaptive integration scheme has been presented that offers greater confidence in the numerical integration of BEM and DBEM kernels than a more arbitrary approach to determining the number of Gaussian integration points.

Expressions for the analytical integration of strongly-singular and hyper-singular functions for general boundary element local nodal distributions have been developed. Although motivated by their need in the coupled method discussed in later chapters, these new formulations have been applied in the reconfiguration of elements with redistributed local nodal coordinates. The resulting analysis revealed the distribution used in models, well-publicised in the literature, are far from optimum.

Results in this thesis have been presented with emphasis focused on consistency and comparability; methods demonstrated to improve only the accuracy of specific problems by fine-tuning their configurations, such as local nodal distributions, are not applied to the general use of the BEM throughout the present work.

3 Scaled boundary finite element method

3.1 Introduction

In this chapter, the *scaled boundary finite element method* (SBFEM) is introduced. First, the concept of *modal superposition*, on which the SBFEM is based, is described. A detailed numerical formulation of the SBFEM follows, with examples, demonstrating its suitability for applications to fracture mechanics. Its other strengths and limitations are assessed.

Concepts new to the SBFEM are discussed and the motivation for their development by the author is then presented. A new semi-discontinuous scaled boundary finite element is defined and verified by example results.

The method's historical development is discussed in a literature review, detailing its introduction as a method for use in applications to unbounded domain modelling, to its more recent application to fracture mechanics. The use of the SBFEM in coupled numerical methods is also discussed.

The data in numerical examples in this chapter are obtained by the development of the author's own code.

3.2 Modal superposition

Consider a domain subject to a displacement field. The deformation of the domain can be described by the combination of displacement modes $\tilde{\mathbf{u}}_j$, such as those illustrated in Figure 37. The minimum number of displacement modes required to define the deformation of the domain by the superposition of displacement modes is defined as $M_{\min}$ and is problem-specific. A displacement mode $\tilde{\mathbf{u}}_j$ describes the form of the deformation, but neither the magnitude nor direction. In example 1 the deformation of the domain can be described by a single displacement mode; examples 2 requires multiple displacement modes.

A sample of displacement modes associated with the deformation of the domain illustrated in Figure 37 can be found in Appendix B, where it can be seen that some displacement modes have an obvious physical interpretation, such as translation, rotation, skew etc. Some displacement modes are less-well described and differ only subtly from other modes. The effect of these displacement modes differs from domain to domain, as illustrated by the sample in Appendix C.

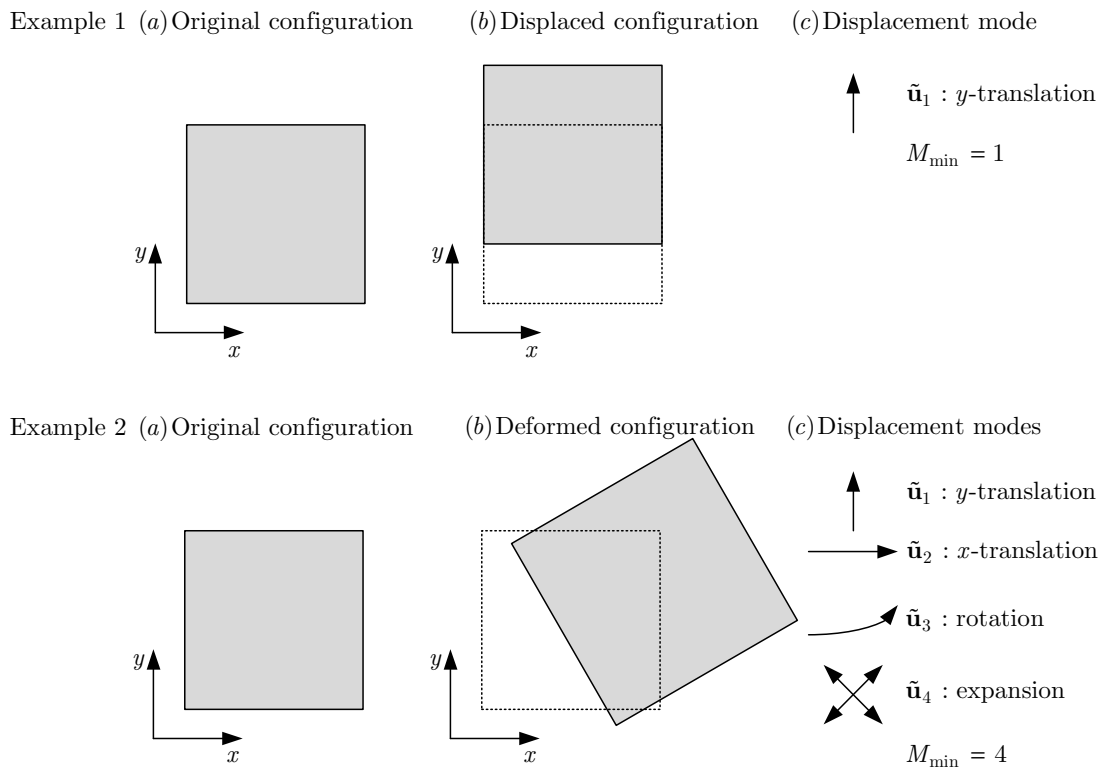

Figure 37. Two examples of: (1) the displacement of a bounded domain due to one displacement mode and (2) the deformation of a bounded domain due to multiple displacement modes

The superposition of m displacement modes can be used to estimate the deformation of the domain. It is necessary to determine which of the infinite range of displacement modes contribute to the deformation of the domain and by how much. If the appropriate m displacement modes are selected and $m \geq M_{\min}$, then the estimation will be exact, else the estimation will remain an approximation.

For a domain with n degrees of freedom, the i^{th} displacement degree of freedom, u_i, where $i = 1..n$, can each be described by

$$u_i = \sum_{j=1}^{m} \tilde{c}_j \tilde{u}_{ij} \tag{3.1}$$

where each of the m terms in this series is considered the product of a displacement mode *component* $\tilde{u}_{ij}$, contributing to each degree of freedom u_i by some corresponding factor $\tilde{c}_j$. It should be noted that the term $\tilde{u}_{ij}$ refers to the i^{th} term in the column vector $\tilde{\mathbf{u}}_j$ describing mode j, and is not a tensor.

For each displacement mode $\tilde{\mathbf{u}}_j$ there exists a complementary force mode $\tilde{\mathbf{p}}_j$, describing the force required to induce its corresponding displacement mode. The force p_i, where $i = 1...n$, can be described by

$$p_i = \sum_{j=1}^{m} \tilde{c}_j \tilde{p}_{ij} \tag{3.2}$$

where each of the m terms in this series is considered the product of a force mode *component* $\tilde{p}_{ij}$, contributing to each degree of freedom p_i by some corresponding factor $\tilde{c}_j$. It should be noted that the term $\tilde{p}_{ij}$ refers to the i^{th} term in the column vector $\tilde{\mathbf{p}}_i$ describing mode j, and is not a tensor.

The aim of the SBFEM is to estimate u_i and p_i by numerically determining $\tilde{\mathbf{c}}$ (the vector of m contribution factors $\tilde{c}_j$, and the $n \times m$ displacement mode components $\tilde{u}_{ij}$ and $n \times m$ force mode components $\tilde{p}_{ij}$ that define vectors $\tilde{\mathbf{u}}_j$ and $\tilde{\mathbf{p}}_j$ respectively.

3.3 Numerical formulation

3.3.1 Method introduction

Like the BEM, by modelling the boundary only, the SBFEM can be used to model both finite and infinite domains. Indeed, the modelling of the finite domain results in the modelling infinite domain as a by-product, and *vice-versa*. In doing so, the efficiency of the SBFEM may be called into question.

However, the SBFEM does not require the elemental discretisation of the volume, thus comparing favourably with the FEM, nor does it require the computation of weakly or strongly singular integrals, thus comparing favourably with the BEM.

For the purpose of disambiguity, it should be stated that the numerical method described here is available in the literature. However, along with the overview of modal superposition, the following derivation offers a fresh perspective with the intention of providing a clearer and easier understanding of a method that is far less daunting than its reputation suggests. Efforts have been made to address the practical implementation of the method in code, rather than the more general overviews offered in the literature. Some aspects of the derivation are borrowed from that of Deeks and Wolf (Deeks and Wolf, 2002a), and Yang (Yang, 2006).

Further details of the contributions made to the method and its development by the author and others can be found in §3.12. Following the convention found throughout this work, the subscript 'S' is used to denote the SBFEM to allow distinction from, and comparison with, terms relating to other numerical methods.

3.3.2 Scaled boundary coordinate system

A domain Ω_S modelled using the SBFEM requires conversion from a Cartesian coordinate system to a *scaled boundary* coordinate system. A geometrically-specific coordinate s is defined as acting in the circumferential direction, running parallel to the boundary Γ_S. The s-axis is scaled about a geometric *scaling centre* (x_0, y_0), by a radial coordinate ξ, defined such that $\xi = 0$ at (x_0, y_0) and $\xi = 1$ at Γ_S, as shown in Figure 38.

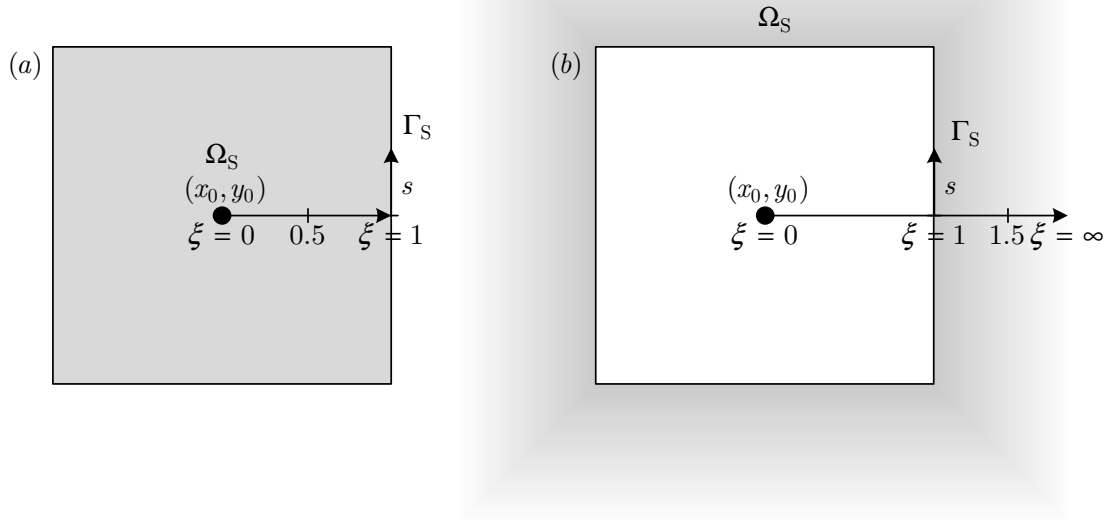

Figure 38. The boundary Γ_S follows s, scaled about the scaling centre (x_0, y_0), modelling a domain Ω_S that is (a) bounded and (b) unbounded

A function is sought that describes the i^{th} displacement of degree of freedom $u_i(\xi, s)$ for values of ξ within a bounded range. This bounded range depends on the location of (x_0, y_0). In the finite domain case, (x_0, y_0) is located internally such that the domain is bounded by $0 \leq \xi \leq 1$. For the infinite domain case, (x_0, y_0) may be located externally such that the domain is bounded by $1 \leq \xi \leq \infty$.

Defining the Cartesian origin as coincident with (x_0, y_0), the coordinate transformation is given by

$$x = x_0 + \xi x(s) \tag{3.3}$$
$$y = y_0 + \xi y(s) \tag{3.4}$$

where $x(s)$ and $y(s)$ describe the Cartesian coordinates as functions of the boundary coordinate, and equations (3.1) and (3.2) are transformed into

$$u_i(\xi, s) = \sum_{j=1}^{n} \tilde{c}_j \tilde{u}_{ij}(\xi, s) \tag{3.5}$$

$$p_i(\xi, s) = \sum_{j=1}^{n} \tilde{c}_j \tilde{p}_{ij}(\xi, s) \tag{3.6}$$

These terms are used to define a statement of the principle of virtual work (Deeks and Wolf, 2002a), transformed from

$$\int_{\Gamma_S} \delta u(x,y)^T t(x,y) \mathrm{d}\Gamma_S - \int_{\Omega_S} \delta\varepsilon(x,y)^T \sigma(x,y) \mathrm{d}\Omega_S = 0 \tag{3.7}$$

into

$$\int_{\Gamma_S} \delta u(s)^T t(s) \mathrm{d}\Gamma_S - \int_{\Omega_S} \delta\varepsilon(\xi,s)^T \sigma(\xi,s) \mathrm{d}\Omega_S = 0 \tag{3.8}$$

where body loads have been neglected for simplicity, and

$$u_i(x,y) = u_i(\xi,s) \tag{3.9}$$
$$t_i(x,y) = t_i(\xi,s) \tag{3.10}$$
$$\sigma_i(x,y) = \sigma_i(\xi,s) \tag{3.11}$$
$$\varepsilon_i(x,y) = \varepsilon_i(\xi,s) \tag{3.12}$$
$$p_i(x,y) = p_i(\xi,s) \tag{3.13}$$

or in vector form

$$\mathbf{u}(x,y) = \mathbf{u}(\xi,s) \tag{3.14}$$
$$\mathbf{t}(x,y) = \mathbf{t}(\xi,s) \tag{3.15}$$
$$\boldsymbol{\sigma}(x,y) = \boldsymbol{\sigma}(\xi,s) \tag{3.16}$$
$$\boldsymbol{\varepsilon}(x,y) = \boldsymbol{\varepsilon}(\xi,s) \tag{3.17}$$
$$\mathbf{p}(x,y) = \mathbf{p}(\xi,s) \tag{3.18}$$

3.3.3 Boundary integration

The boundary Γ_S is discretised in the usual manner by means of a piecewise polynomial isoparametric continuous finite element approximation as described in §2.3.1. Nodal interpolation can be used to estimate displacements,

tractions, strains, stresses, and forces in the in the s-direction using the continuous shape functions $\mathbf{N}(s)$ described in §2.4. Equations (3.14) to (3.18) are modified to reflect the discretisation in s.

$$\mathbf{u}(\xi, s) = \mathbf{N}(s)\mathbf{u}(\xi) \tag{3.19}$$
$$\mathbf{t}(\xi, s) = \mathbf{N}(s)\mathbf{t}(\xi) \tag{3.20}$$
$$\boldsymbol{\sigma}(\xi, s) = \mathbf{N}(s)\boldsymbol{\sigma}(\xi) \tag{3.21}$$
$$\boldsymbol{\varepsilon}(\xi, s) = \mathbf{N}(s)\boldsymbol{\varepsilon}(\xi) \tag{3.22}$$
$$\mathbf{p}(\xi, s) = \mathbf{N}(s)\mathbf{p}(\xi) \tag{3.23}$$

and so it follows the discretised form of equations (3.5) and (3.6) are

$$u_i(\xi, s) = \mathbf{N}(s)u_i(\xi) \tag{3.24}$$
$$p_i(\xi, s) = \mathbf{N}(s)p_i(\xi) \tag{3.25}$$

where

$$u_i(\xi) = \sum_{j=1}^{m} \tilde{c}_j \tilde{u}_{ij}(\xi) \tag{3.26}$$
$$p_i(\xi) = \sum_{j=1}^{m} \tilde{c}_j \tilde{p}_{ij}(\xi) \tag{3.27}$$

and the vectors of displacement and force degrees of freedom are given by

$$\mathbf{u}(\xi, s) = \mathbf{N}(s)\mathbf{u}(\xi) \tag{3.28}$$
$$\mathbf{p}(\xi, s) = \mathbf{N}(s)\mathbf{p}(\xi) \tag{3.29}$$

where

$$\mathbf{u}(\xi) = \sum_{j=1}^{m} \tilde{c}_j \tilde{\mathbf{u}}_j(\xi) \tag{3.30}$$
$$\mathbf{p}(\xi) = \sum_{j=1}^{m} \tilde{c}_j \tilde{\mathbf{p}}_j(\xi) \tag{3.31}$$

With reference to Appendix D, the discretised form of the principle of virtual

work is found by substituting expressions for the nodal strains, forces, displacements and tractions resulting in

$$\begin{aligned}&\delta\mathbf{u}(\xi_\Gamma)^{\mathrm{T}}\int_S \mathbf{t}(s)\mathrm{d}s - \\ &\int_S\int_0^1\left[\mathbf{B}^1(s)\delta\mathbf{u}(\xi)_{,\xi}+\frac{1}{\xi}\mathbf{B}^2(s)\delta\mathbf{u}(\xi)\right]^{\mathrm{T}}\left[\mathbf{D}\mathbf{B}^1(s)\mathbf{u}(\xi)_{,\xi}+\mathbf{D}\mathbf{B}^2(s)\frac{1}{\xi}\mathbf{u}(\xi)\right]|\mathbf{J}(s)|\xi\mathrm{d}\xi\mathrm{d}s \\ &\qquad = 0\end{aligned} \tag{3.32}$$

which, can be rewritten

$$\begin{aligned}&\delta\mathbf{u}(\xi_\Gamma)^{\mathrm{T}}\left(\mathbf{E}_0\mathbf{u}(\xi_\Gamma)_{,\xi}+\mathbf{E}_1{}^{\mathrm{T}}\mathbf{u}(\xi_\Gamma)-\mathbf{p}(\xi_\Gamma)\right) \\ &\qquad -\int_0^1\delta\mathbf{u}(\xi)^{\mathrm{T}}\left(\mathbf{E}_0\xi\mathbf{u}(\xi)_{,\xi\xi}+\left(\mathbf{E}_0+\mathbf{E}_1{}^{\mathrm{T}}-\mathbf{E}_1\right)\mathbf{u}(\xi)_{,\xi}-\frac{1}{\xi}\mathbf{E}_2\mathbf{u}(\xi)\right)\mathrm{d}\xi \\ &\qquad = 0\end{aligned} \tag{3.33}$$

where $\mathbf{u}(\xi_\Gamma)$ and $\mathbf{p}(\xi_\Gamma)$ are the vectors of nodal displacements and forces at the boundary (denoted by ξ_Γ where $\xi = 1$), and $\mathbf{E}_0$, $\mathbf{E}_1$ and $\mathbf{E}_2$ are boundary integrals given by

$$\mathbf{E}_0 = \int_S \mathbf{B}_1(s)^{\mathrm{T}}\mathbf{D}\mathbf{B}_1(s)|\mathbf{J}(s)|\mathrm{d}s \tag{3.34}$$

$$\mathbf{E}_1 = \int_S \mathbf{B}_2(s)^{\mathrm{T}}\mathbf{D}\mathbf{B}_1(s)|\mathbf{J}(s)|\mathrm{d}s \tag{3.35}$$

$$\mathbf{E}_2 = \int_S \mathbf{B}_2(s)^{\mathrm{T}}\mathbf{D}\mathbf{B}_2(s)|\mathbf{J}(s)|\mathrm{d}s \tag{3.36}$$

and $\mathbf{J}(s)$ is the Jacobian matrix. In a manner similar to that of discretising the boundary element method, these boundary functions, equations (3.34) to (3.36) are approximated by

$$\mathbf{E}_0 \simeq \sum_{e=1}^{L}\mathbf{E}_0^e \tag{3.37}$$

$$\mathbf{E}_1 \simeq \sum_{e=1}^{L} \mathbf{E}_1^e \tag{3.38}$$

$$\mathbf{E}_2 \simeq \sum_{e=1}^{L} \mathbf{E}_2^e \tag{3.39}$$

where

$$\mathbf{E}_0^e = \int_{-1}^{+1} \mathbf{B}_1(\eta^e)^{\mathrm{T}} \mathbf{D} \mathbf{B}_1(\eta^e) J^e \mathrm{d}\eta^e \tag{3.40}$$

$$\mathbf{E}_1^e = \int_{-1}^{+1} \mathbf{B}_2(\eta^e)^{\mathrm{T}} \mathbf{D} \mathbf{B}_1(\eta^e) J^e \mathrm{d}\eta^e \tag{3.41}$$

$$\mathbf{E}_2^e = \int_{-1}^{+1} \mathbf{B}_2(\eta^e)^{\mathrm{T}} \mathbf{D} \mathbf{B}_2(\eta^e) J^e \mathrm{d}\eta^e \tag{3.42}$$

and L is the number of elements on boundary Γ_{S}. Unlike the BEM, these construction matrices are not generally full and asymmetric. Only the neighbouring elements that share common nodes with element e contribute to each row in these matrices resulting in banding with overlapping elemental submatrices, much like the appearance of a FEM stiffness matrix.

In solving equation (3.33) for $\mathbf{u}$, to dismiss the trivial solutions ($\boldsymbol{\delta}\mathbf{u}(\xi_\Gamma) = 0$ and $\boldsymbol{\delta}\mathbf{u}(\xi) = 0$), both their coefficients must simultaneously be zero. Thus the following conditions must be satisfied.

$$\mathbf{E}_0 \xi_\Gamma \mathbf{u}(\xi_\Gamma)_{,\xi} + \mathbf{E}_1{}^{\mathrm{T}} \mathbf{u}(\xi_\Gamma) - \mathbf{p}(\xi_\Gamma) = 0 \tag{3.43}$$

$$\mathbf{E}_0 \xi \mathbf{u}(\xi)_{,\xi\xi} + \left(\mathbf{E}_0 + \mathbf{E}_1{}^{\mathrm{T}} - \mathbf{E}_1 \right) \mathbf{u}(\xi)_{,\xi} - \frac{1}{\xi} \mathbf{E}_2 \mathbf{u}(\xi) = 0 \tag{3.44}$$

In order to provide simpler manipulation later equation (3.44) is rewritten

$$\mathbf{E}_0 \xi^2 \mathbf{u}(\xi)_{,\xi\xi} + \left(\mathbf{E}_0 + \mathbf{E}_1{}^{\mathrm{T}} - \mathbf{E}_1 \right) \xi \mathbf{u}(\xi)_{,\xi} - \mathbf{E}_2 \mathbf{u}(\xi) = 0 \tag{3.45}$$

As equation (3.45) is a set of second order partial differential equations of the

Euler-Cauchy type in the form

$$f_2(\xi^2)\mathbf{u}(\xi)_{,\xi\xi} + f_1(\xi^1)\mathbf{u}(\xi)_{,\xi} + f_0(\xi^0)\mathbf{u}(\xi) = 0 \tag{3.46}$$

its solution is known to take the form

$$\mathbf{u}(\xi) = \sum_{j=1}^{m} c_j \xi^{-\lambda_j} \boldsymbol{\varphi}_j \tag{3.47}$$

By the evaluation of coefficients of equation (3.30), repeated below,

$$\mathbf{u}(\xi) = \sum_{j=1}^{m} \tilde{c}_j \tilde{\mathbf{u}}_j(\xi) \tag{3.48}$$

the displacement mode j can be defined

$$\tilde{\mathbf{u}}_j(\xi) = \xi^{-\lambda_j} \boldsymbol{\varphi}_j \tag{3.49}$$

and

$$\tilde{\mathbf{c}} = \mathbf{c} \tag{3.50}$$

The vectors $\boldsymbol{\varphi}_j$ are the *unscaled* displacement modes, vectors comprising n unscaled displacement mode *components* φ_{ij}, contributing to each (scaled) displacement mode $\tilde{\mathbf{u}}_j$ by some corresponding factor $\xi^{-\lambda_j}$, where the exponent λ_j is to be found later.

Similarly, the force mode j can be defined

$$\tilde{\mathbf{p}}_j(\xi) = \xi^{-\lambda_j} \mathbf{q}_j \tag{3.51}$$

The vectors $\mathbf{q}_j$ are the *unscaled* force modes, vectors comprising n unscaled force mode *components* q_{ij}, contributing to each (scaled) force mode $\tilde{\mathbf{p}}_j$ by some corresponding factor $\xi^{-\lambda_j}$. It should be noted that the terms φ_{ij} and q_{ij}

refer to the i^{th} term in column vectors $\boldsymbol{\varphi}_j$ and $\mathbf{q}_j$ describing unscaled mode j, and are not tensors.

These scaled displacement and force modes $\tilde{\mathbf{u}}_j$ are $\tilde{\mathbf{q}}_j$ are products of the geometric and material properties of the domain under analysis. Their scaling at this point is only by their respective factor $\xi^{-\lambda_j}$. While these factors are problem-specific, they remain independent of the boundary conditions. The extent of the contribution of each mode to the solution of this problem under a particular set of specific boundary conditions will be determined by the further scaling of these modes by their corresponding contribution factor in $\tilde{\mathbf{c}}$, discussed later.

As the modal definition ($\boldsymbol{\varphi}_j$, $\mathbf{q}_j$ and $\boldsymbol{\lambda}$) is independent of boundary conditions, an arbitrary set of contribution factors can be assumed in order to proceed. Thus, for convenience, a set of contribution factors are prescribed by

$$c_j = 1, \qquad j = 1..m \tag{3.52}$$

3.3.4 Eigenvalue problem

Consider the contribution of mode j to the i^{th} displacement degree of freedom $u_i(\xi)$. Selecting the terms corresponding to mode j and recalling that $c_j = 1$, this contribution and its first and second order derivatives are given by

$$u_i(\xi)\big|_j = \xi^{-\lambda_j}\varphi_{ij} \tag{3.53}$$

$$u_i(\xi)_{,\xi}\big|_j = -\lambda_j\xi^{-\lambda_j-1}\varphi_{ij} \tag{3.54}$$

$$u_i(\xi)_{,\xi\xi}\big|_j = \lambda_j(\lambda_j+1)\xi^{-\lambda_j-2}\varphi_{ij} \tag{3.55}$$

Similarly, the contribution of mode j to the i^{th} force degree of freedom $p_i(\xi)$. is given by

$$p_i(\xi)\big|_j = \xi^{-\lambda_j} q_{ij}(\xi) \tag{3.56}$$

Extracting mode j from sets of equations (3.43) and (3.45)

$$\mathbf{E}_0 \xi_\Gamma \, \mathbf{u}(\xi_\Gamma)_{,\xi}\big|_j + \mathbf{E}_1{}^{\mathrm{T}} \, \mathbf{u}(\xi_\Gamma)\big|_j - \mathbf{p}(\xi_\Gamma)\big|_j = 0 \tag{3.57}$$

$$\mathbf{E}_0 \xi \, \mathbf{u}(\xi)_{,\xi\xi}\big|_j + \left(\mathbf{E}_0 + \mathbf{E}_1{}^{\mathrm{T}} - \mathbf{E}_1 \right) \mathbf{u}(\xi)_{,\xi}\big|_j - \frac{1}{\xi} \mathbf{E}_2 \, \mathbf{u}(\xi)\big|_j = 0 \tag{3.58}$$

and substituting them with equations (3.53) to (3.56) gives

$$\mathbf{E}_0 \xi \lambda_j (\lambda_j + 1) \xi^{-\lambda_j - 2} \varphi_{ij}(\xi) - \left(\mathbf{E}_0 + \mathbf{E}_1{}^{\mathrm{T}} - \mathbf{E}_1 \right) \lambda_j \xi^{-\lambda_j - 1} \varphi_{ij}(\xi) - \frac{1}{\xi} \mathbf{E}_2 \xi^{-\lambda_j} \varphi_{ij}(\xi) = 0 \tag{3.59}$$

$$-\mathbf{E}_0 \xi_\Gamma \lambda_j \xi^{-\lambda_j - 1} \varphi_{ij}(\xi) + \mathbf{E}_1{}^{\mathrm{T}} \xi^{-\lambda_j} \varphi_{ij}(\xi) - \xi^{-\lambda_j} q_{ij}(\xi) = 0 \tag{3.60}$$

or

$$\left(\mathbf{E}_0{}^{-1} \mathbf{E}_1{}^{\mathrm{T}} \varphi_{ij}(\xi) - \mathbf{E}_0{}^{-1} q_{ij}(\xi) \right) = \lambda_j \varphi_{ij}(\xi) \tag{3.61}$$

$$\left((\mathbf{E}_0 \lambda) \lambda \varphi_{ij}(\xi) - \mathbf{E}_1{}^{\mathrm{T}} \lambda \varphi_{ij}(\xi) + \mathbf{E}_1 \lambda \varphi_{ij}(\xi) - \mathbf{E}_2 \varphi_{ij}(\xi) \right) = 0 \tag{3.62}$$

Substituting equation (3.61) into the first and third terms of equation (3.62) yields

$$\left((\mathbf{E}_1 \mathbf{E}_0{}^{-1} \mathbf{E}_1{}^{\mathrm{T}} - \mathbf{E}_2) \varphi_{ij}(\xi) - \mathbf{E}_1 \mathbf{E}_0{}^{-1} q_{ij}(\xi) \right) = \lambda q_{ij}(\xi) \tag{3.63}$$

or in matrix form

$$\begin{bmatrix} \mathbf{E}_0{}^{-1} \mathbf{E}_1{}^{\mathrm{T}} & -\mathbf{E}_0{}^{-1} \\ \mathbf{E}_1 \mathbf{E}_0{}^{-1} \mathbf{E}_1{}^{\mathrm{T}} - \mathbf{E}_2 & -\mathbf{E}_1 \mathbf{E}_0{}^{-1} \end{bmatrix} \begin{Bmatrix} \begin{Bmatrix} \varphi_{1j}(\xi) \\ \vdots \\ \varphi_{nj}(\xi) \end{Bmatrix} \\ \begin{Bmatrix} q_{1j}(\xi) \\ \vdots \\ q_{nj}(\xi) \end{Bmatrix} \end{Bmatrix} = \lambda_j \begin{Bmatrix} \begin{Bmatrix} \varphi_{1j}(\xi) \\ \vdots \\ \varphi_{nj}(\xi) \end{Bmatrix} \\ \begin{Bmatrix} q_{1j}(\xi) \\ \vdots \\ q_{nj}(\xi) \end{Bmatrix} \end{Bmatrix} \tag{3.64}$$

or

$$\begin{bmatrix} \mathbf{E}_0^{-1}\mathbf{E}_1^{\mathrm{T}} & -\mathbf{E}_0^{-1} \\ \mathbf{E}_1\mathbf{E}_0^{-1}\mathbf{E}_1^{\mathrm{T}} - \mathbf{E}_2 & -\mathbf{E}_1\mathbf{E}_0^{-1} \end{bmatrix} \begin{Bmatrix} \varphi_j(\xi) \\ \mathbf{q}_j(\xi) \end{Bmatrix} = \lambda_j \begin{Bmatrix} \varphi_j(\xi) \\ \mathbf{q}_j(\xi) \end{Bmatrix} \tag{3.65}$$

Assembling equations (3.61) and (3.63) for all n degrees of freedom and m modes yields a system

$$\mathbf{Z}\boldsymbol{\Psi} = \boldsymbol{\Psi}\boldsymbol{\Lambda} \tag{3.66}$$

where

$$\mathbf{Z} = \begin{bmatrix} \mathbf{E}_0^{-1}\mathbf{E}_1^{\mathrm{T}} & -\mathbf{E}_0^{-1} \\ \mathbf{E}_1\mathbf{E}_0^{-1}\mathbf{E}_1^{\mathrm{T}} - \mathbf{E}_2 & -\mathbf{E}_1\mathbf{E}_0^{-1} \end{bmatrix} \tag{3.67}$$

$$\boldsymbol{\Psi} = \begin{bmatrix} \varphi_1(\xi) & \cdots & \varphi_m(\xi) \\ \mathbf{q}_1(\xi) & \cdots & \mathbf{q}_m(\xi) \end{bmatrix} \tag{3.68}$$

$$\boldsymbol{\Lambda} = \begin{bmatrix} \lambda_1 & 0 & 0 & 0 & 0 & 0 \\ 0 & \ddots & 0 & 0 & 0 & 0 \\ 0 & 0 & \ddots & 0 & 0 & 0 \\ 0 & 0 & 0 & \ddots & 0 & 0 \\ 0 & 0 & 0 & 0 & \ddots & 0 \\ 0 & 0 & 0 & 0 & 0 & \lambda_{2n} \end{bmatrix} \tag{3.69}$$

In order to solve the eigenvalue problem, $\mathbf{Z}$ must be a square matrix, and so

$$m = 2n \tag{3.70}$$

3.3.5 Eigenvalue solution

A vector of length $2n$ comprising the diagonal terms of $\boldsymbol{\Lambda}$ is defined as

$$\tilde{\boldsymbol{\lambda}} = diag(\boldsymbol{\Lambda}) \tag{3.71}$$

and recalling that the SBFEM models both bounded and unbounded domains simultaneously, $\tilde{\boldsymbol{\lambda}}$ is subdivided into two vectors of length n

$$\tilde{\boldsymbol{\lambda}} = \begin{Bmatrix} \tilde{\boldsymbol{\lambda}}_K \\ \tilde{\boldsymbol{\lambda}}_\infty \end{Bmatrix} \tag{3.72}$$

where $\tilde{\boldsymbol{\lambda}}_K$ contains the n eigenvalues λ_j whose real parts are negative and are used in the solution to the bounded (or finite) domain case, and $\tilde{\boldsymbol{\lambda}}_\infty$ contains the n eigenvalues whose real parts are positive and are used in the solution to the unbounded (or infinite) domain case.

The matrix of corresponding eigenvectors is divided into 4 submatrices of size $n \times n$

$$\boldsymbol{\Psi} = \begin{bmatrix} \tilde{\boldsymbol{\Phi}}_K & \tilde{\boldsymbol{\Phi}}_\infty \\ \tilde{\mathbf{Q}}_K & \tilde{\mathbf{Q}}_\infty \end{bmatrix} \tag{3.73}$$

For the bounded (or finite domain case), the eigenvalues and matrices of modal displacement column vectors and modal force column vectors are given by

$$\boldsymbol{\lambda} = \tilde{\boldsymbol{\lambda}}_K \tag{3.74}$$
$$\boldsymbol{\Phi} = \tilde{\boldsymbol{\Phi}}_K \tag{3.75}$$
$$\mathbf{Q} = \tilde{\mathbf{Q}}_K \tag{3.76}$$

For the unbounded (or infinite domain case), the eigenvalues and matrices of modal displacement column vectors and modal force column vectors are given by

$$\boldsymbol{\lambda} = \tilde{\boldsymbol{\lambda}}_\infty \tag{3.77}$$
$$\boldsymbol{\Phi} = \tilde{\boldsymbol{\Phi}}_\infty \tag{3.78}$$
$$\mathbf{Q} = \tilde{\mathbf{Q}}_\infty \tag{3.79}$$

3.3.6 Stiffness matrix

By assembling m sets of equations (3.26) and (3.27), the matrices of displacement and force mode column vectors $\boldsymbol{\Phi}$ and $\mathbf{Q}$ can be seen to be related to the nodal displacements and forces by

$$\mathbf{u}(\xi) = \mathbf{\Phi F c} \tag{3.80}$$
$$\mathbf{p}(\xi) = \mathbf{Q F c} \tag{3.81}$$

where $\mathbf{F}$ is a diagonal matrix that scales the modal displacement and force matrices and is given by

$$\mathbf{F} = \begin{bmatrix} \xi^{-\lambda_1} & 0 & 0 \\ 0 & \ddots & 0 \\ 0 & 0 & \xi^{-\lambda_m} \end{bmatrix} \tag{3.82}$$

Equations (3.80) and (3.81) are rewritten

$$\mathbf{\Phi}^{-1}\mathbf{u}(\xi) = \mathbf{\Phi}^{-1}\mathbf{\Phi F c} \tag{3.83}$$
$$\mathbf{Q}^{-1}\mathbf{p}(\xi) = \mathbf{Q}^{-1}\mathbf{Q F c} \tag{3.84}$$

and combined to form

$$\mathbf{Q\Phi}^{-1}\mathbf{u}(\xi) = \mathbf{p}(\xi) \tag{3.85}$$

which, when evaluated at the boundary, forms the stiffness equation

$$\mathbf{Q\Phi}^{-1}\mathbf{u}(\xi_\Gamma) = \mathbf{p}(\xi_\Gamma) \tag{3.86}$$

in which the absence of $\mathbf{c}$ shows the arbitrary nature of the contribution factors in the formation of the displacement and force nodes and confirms the independence of the boundary conditions to the modal definition. The SBFEM stiffness matrix $\mathbf{K}_\mathrm{S}$ is the product of the matrix of force mode contributions $\mathbf{Q}$ and the inverse of the matrix of displacement mode contributions $\mathbf{\Phi}$.

$$\mathbf{K}_\mathrm{S}\mathbf{u}(\xi_\Gamma) = \mathbf{p}(\xi_\Gamma) \tag{3.87}$$

Like the FEM for linear elasticity and infinitesimal strains, $\mathbf{K}_\mathrm{S}$ is symmetric. However, unlike the FEM, $\mathbf{K}_\mathrm{S}$ contains only boundary degrees of freedom and is fully populated. This linear system of equations can be solved in the usual

manner by the application of nodal displacement and force boundary conditions.

3.3.7 Contribution factors

With the boundary problem solved, it is possible to solve the domain problem. First, the contribution factors $\mathbf{c}$ must be found (replacing the vector of arbitrary boundary conditions used to compute the mode shapes) such that equations (3.24) and (3.25) can be solved for $\mathbf{u}(\xi \neq 1)$.

The equation for the domain displacement (for lines of constant s)

$$u_i(\xi) = \sum_{j=1}^{m} c_j \xi^{-\lambda_j} \varphi_{ij}(\xi) \tag{3.88}$$

can be rewritten using equation(3.70)

$$u_i(\xi) = \sum_{j=1}^{n} c_j \xi^{-\lambda_j} \varphi_{ij}(\xi) \tag{3.89}$$

replacing the number of terms in the summation from m to n reflecting the discarding of the n modes depending on whether the domain is bounded or unbounded. At the boundary where $\xi = 1$, this is rewritten

$$u_i(\xi_\Gamma) = \sum_{j=1}^{n} c_j \varphi_{ij}(\xi_\Gamma) \tag{3.90}$$

and thus $\mathbf{c}$ can be found by the product of the nodal displacements at the boundary $\mathbf{u}(\xi_\Gamma)$ and the inverse of the matrix of modal displacement column vectors $\mathbf{\Phi}^{-1}$

$$\mathbf{c} = \mathbf{u}(\xi_\Gamma)\mathbf{\Phi}^{-1} \tag{3.91}$$

3.3.8 Stress recovery

The stress field over Ω_S, given in the principle of virtual work, is extracted from equation (3.32) as

$$\boldsymbol{\sigma}(\xi,s) = \mathbf{D}\mathbf{B}_1(s)\mathbf{u}(\xi)_{,\xi} + \mathbf{D}\mathbf{B}_2(s)\frac{1}{\xi}\mathbf{u}(\xi) \tag{3.92}$$

and can be recovered using the modal displacements and contribution factors

$$\boldsymbol{\sigma}(\xi,s) = \mathbf{D}\sum_{j=1}^{n} c_j \xi^{-\lambda_j - 1}\left(-\lambda_j \mathbf{B}_1(s) + \mathbf{B}_2(s)\right)\boldsymbol{\varphi}_j \tag{3.93}$$

The inter-element discontinuity of stresses at shared nodes, due to the discontinuity of the derivatives of the shape functions in $\mathbf{B}_2(s)$, is a known problem that manifests itself in a way similar to that of the FEM. As with the FEM, raw nodal stresses can be smoothed by means such as simple averaging of stresses, or by superconvergent patch stress recovery techniques (Deeks and Wolf, 2002b).

A critical evaluation of stress recovery using the SBFEM is made as part of the present work, illustrated by example in §3.10.

3.3.9 Boundary mesh

In this section the discretisation of the model is explained by means of an example. Consider the domains in Figure 38. The boundary Γ_S is discretised in the usual manner by means of a piecewise polynomial isoparametric continuous finite element approximation. One mesh can be used to model both the bounded and unbounded domains, as illustrated in Figure 39. As in the conventional FEM, the mesh requires nodal connectivity between the

elements, although it will be shown in §3.8 that this requirement can be overcome in limited circumstances.

In the present work, the boundary is discretised using quadratic elements with equal nodal spacing, unless otherwise stated. This discretisation allows the element-by-element integration of equations (3.34) to (3.36) in much the same manner as the FEM, but unlike the FEM, is performed over the boundary only. As with the BEM, described in §2.5, the integration is performed using Gaussian quadrature. Unlike the BEM, however, the functions in the SBFEM are not singular in nature and integration can be performed using Gauss points distributed in the standard manner.

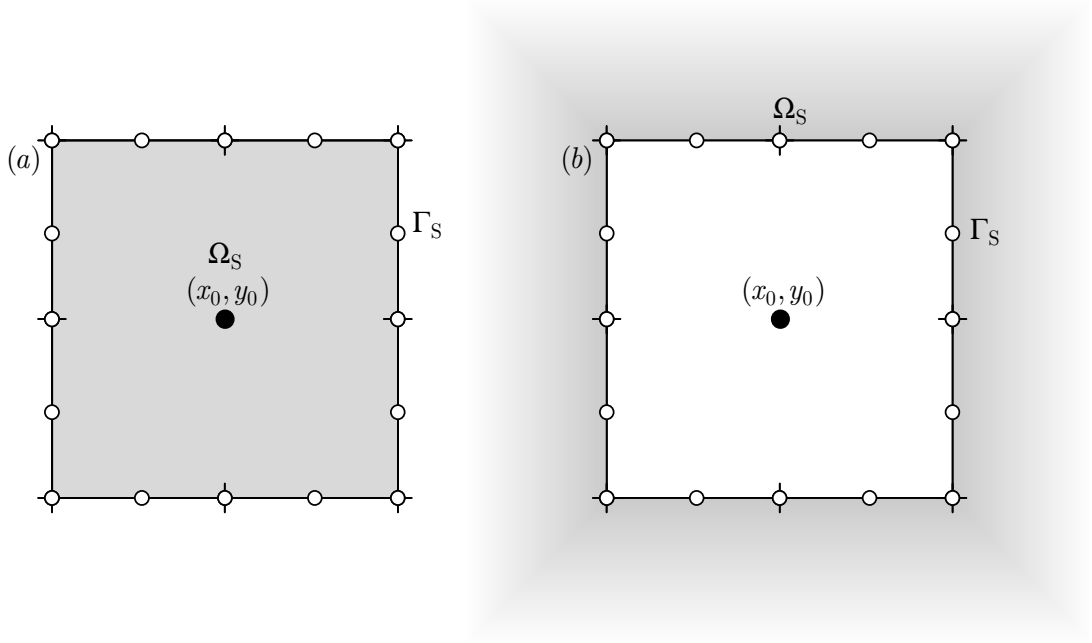

Figure 39. The same boundary mesh can be used in either the (*a*) bounded or (*b*) unbounded domain cases

3.3.10 Boundary 'line of sight' requirement

The SBFEM is not without its limitations. Aside from a linear elastic assumption, other geometric factors limit the method's applicability. The

location of the scaling centre (x_0, y_0) is both important and subject to geometric limitations. The functions describing the displacement and force degrees of freedom $\mathbf{u}(\xi)$ and $\mathbf{p}(\xi)$ are continuous in ξ. Thus, no discontinuities may be permitted in the ξ-direction[iv]. This is commonly referred to as the *boundary line of sight requirement* and is illustrated in Figure 40 where it is illustrated that sections of Ω_S cannot be 'seen' from (x_0, y_0) without crossing Γ_S. By moving (x_0, y_0), a valid scaling centre can be found from which all sections Ω_S can be 'seen' without crossing Γ_S.

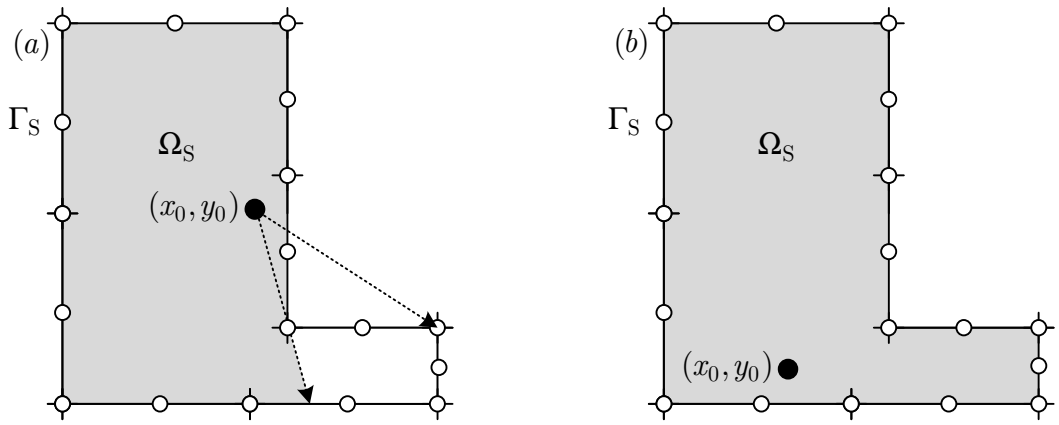

Figure 40. Boundary line of sight requirement: (a) not satisfied (white) and (b) fully satisfied

In some instances, this may not be achievable due to geometric restrictions, such as in Figure 41, in which case the domain can be substructured into subdomains 1 and 2, with scaling centres that satisfy the boundary line of sight requirements for their respective subdomains. Figure 41 is supplied for completeness, however, as in the work presented in this thesis, no such substructuring is required.

[iv] with the exception of unbounded domains with side faces, described in §3.4, examples of which do not appear in this work.

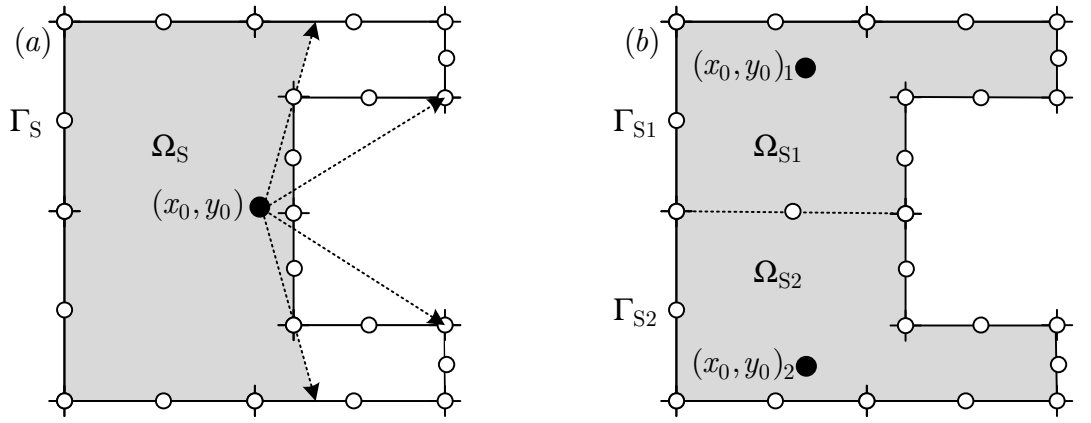

Figure 41. Boundary line of sight requirement (a) cannot be satisfied without (b) multiple subdomains

3.4 Side faces

The method as described above is sufficient for the modelling any suitable domain using the SBFEM. However, this in itself offers limited advantages over other numerical methods. The advantage of the method of most use and interest in this work is *side faces*.

3.4.1 Definition

Provided the boundary line of sight requirement is adhered to, the scaling centre (x_0, y_0) may be located anywhere within a finite domain, or anywhere in the void within an infinite domain. It is also possible for (x_0, y_0) to lie *on* the boundary at $\xi = 1$.

If (x_0, y_0) lies on the boundary, two ξ axes each overlap a section of boundary, and the solutions relating to the displacements of these axes (and the sections of boundary they lie upon) can be found without the numerical interpolation required by other sections of boundary described by equation (3.24). These two sections of boundary are known as *side faces*, and the side faces to the left and right of the scaling centre are labelled A_L and A_R

respectively.

With reference to Figure 42, the formation of side faces is sometimes referred to in the literature as the *case of the missing triangles*, or *pyramids* in three dimensions (Wolf and Song, 2000). It should also be noted that in the cited reference, the term *interface* is used in a context not relevant to the present work and it should be noted, unless otherwise stated, the term *interface* will relate to the frontier between coupled numerical methods.

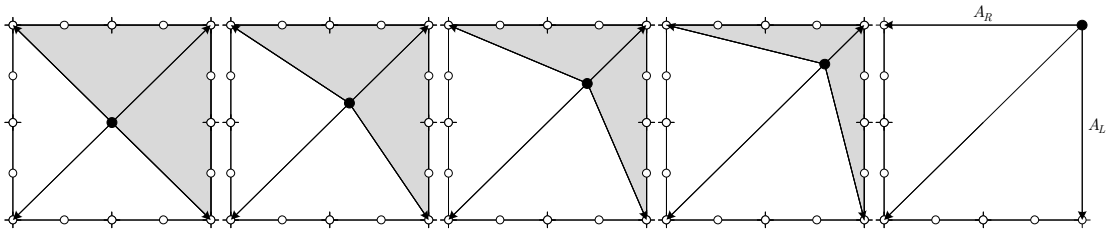

Figure 42. Schematic illustration of the formation of side faces A_L and A_R. As the scaling centre is drawn to the boundary, the shaded triangular regions disappear. Sections of the boundary are overlaid by axes in ξ

The side face property of the SBFEM has desirable applications. Sections of boundary that are known *a priori* to have solutions deemed inappropriate for a polynomial-based approximation, such as singularities and discontinuities, can be modelled more accurately by the modal superposition described by the method's solution in the radial direction.

The use of side faces in the numerical modelling of cracks forms the fundamental basis of the work in this thesis. By placing of the scaling centre coincidentally with a crack tip, the singular behaviour exhibited along the crack faces is captured using modal superposition rather than by an alternative polynomial-based method.

The implications of side faces on the modelling of a domain using the SBFEM are in boundary integration leading to the construction of $\mathbf{E}_0$, $\mathbf{E}_1$ and $\mathbf{E}_2$, and the application of boundary conditions. Otherwise, the formulation of the SBFEM remains the same.

3.5 Boundary integration

The implications of the presence of side faces on the computation of boundary integrals $\mathbf{E}_0$, $\mathbf{E}_1$ and $\mathbf{E}_2$, are illustrated by an example. Consider the finite domain Ω_S, bounded by a discretised boundary Γ_S, with scaled boundary elements labelled locally and according to respective sections of Γ_S. Domains with an internal and boundary scaling centre are illustrated in Figure 43.

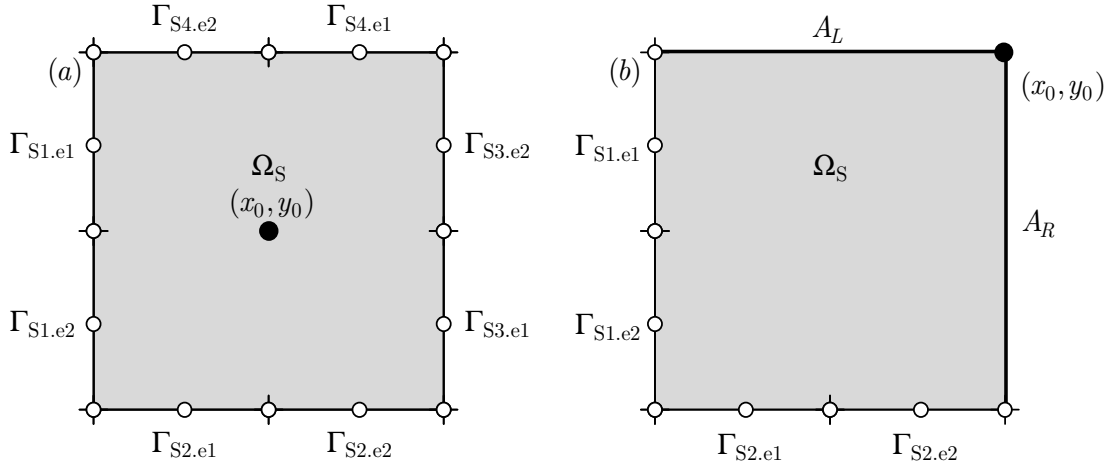

Figure 43. Locally element labelling of the discretised boundary Γ_S of a domain Ω_S with (a) an internal scaling centre and (b) a boundary scaling centre

Matrices $\mathbf{E}_0$, $\mathbf{E}_1$ and $\mathbf{E}_2$ are banded and symmetric, exhibiting the local connectivity of elements in much the same way as a one-dimensional FEM stiffness matrix. Element connectivity can be observed where sections of the matrices overlap at adjoining nodes. The existence of side faces A_L and A_R reduces the extent of the discretisation, and thus the size of matrices $\mathbf{E}_0$, $\mathbf{E}_1$

and $\mathbf{E}_2$, and results in an *open boundary.* These effects are illustrated in the form of matrix block representations in Figure 44, where it should be noted that as the discretisation is no longer a closed loop the overlapping of elemental blocks does not wrap about each end of the diagonal.

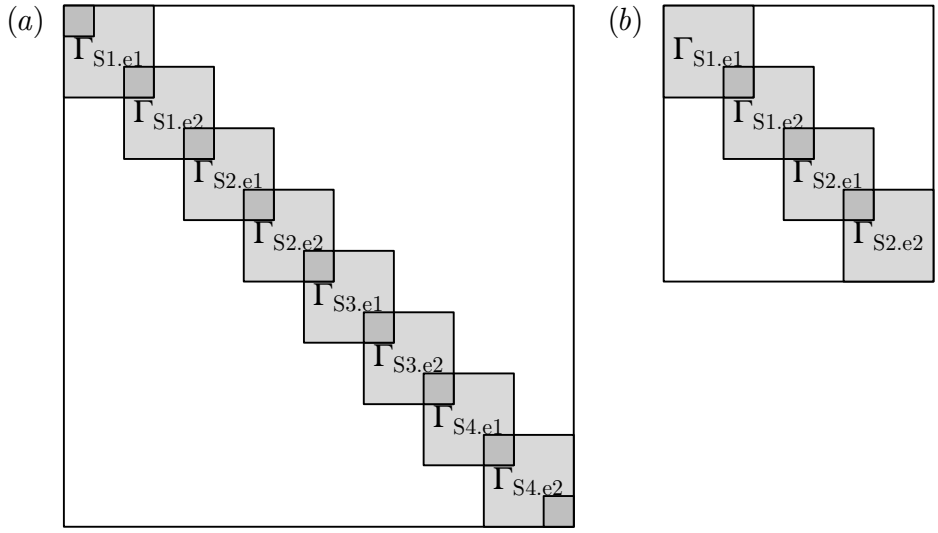

Figure 44. Block representation of banded, symmetric matrices $\mathbf{E}_0$, $\mathbf{E}_1$ and $\mathbf{E}_2$, with elemental connectivity at the adjoining nodes for domain with (a) an internal scaling centre and (b) a boundary scaling centre

3.6 Mode identification

It can be shown, that the terms in $\tilde{\boldsymbol{\lambda}}$ comprise integer multiples of $^{-1}/_{2}$ and $^{1}/_{2}$ respectively. For each integer multiple of $^{\pm 1}/_{2}$ there are two eigenvalues, one with a negative imaginary part and one with a positive imaginary part. In practice, the eigenvalues are unlikely to be exact integer multiple of $^{\pm 1}/_{2}$, but with increased n, the real part will converge towards integer multiples of $^{\pm 1}/_{2}$. The identification of the modes, where $\lambda_j = {}^{-1}/_{2}$, is important in this work. These are the *crack opening* and *crack shearing* modes and so are labelled modes $j = j_{K_{\mathrm{I}}}$ and $j = j_{K_{\mathrm{II}}}$ respectively for future reference.

3.6.1 Translation modes

Some other modes have clear and more obvious physical interpretations, as illustrated in Appendix B. Two such modes are the x- and y-translation modes, denoted $j = j_x$ and $j = j_y$ respectively for future reference. As translation modes are displacement modes independent of ξ, as illustrated in Figure 45,

$$c_j \xi^{-\lambda_j} \varphi_{ij}(\xi) = c_j \varphi_{ij} \tag{3.94}$$

or where $\lambda_j = 0$.

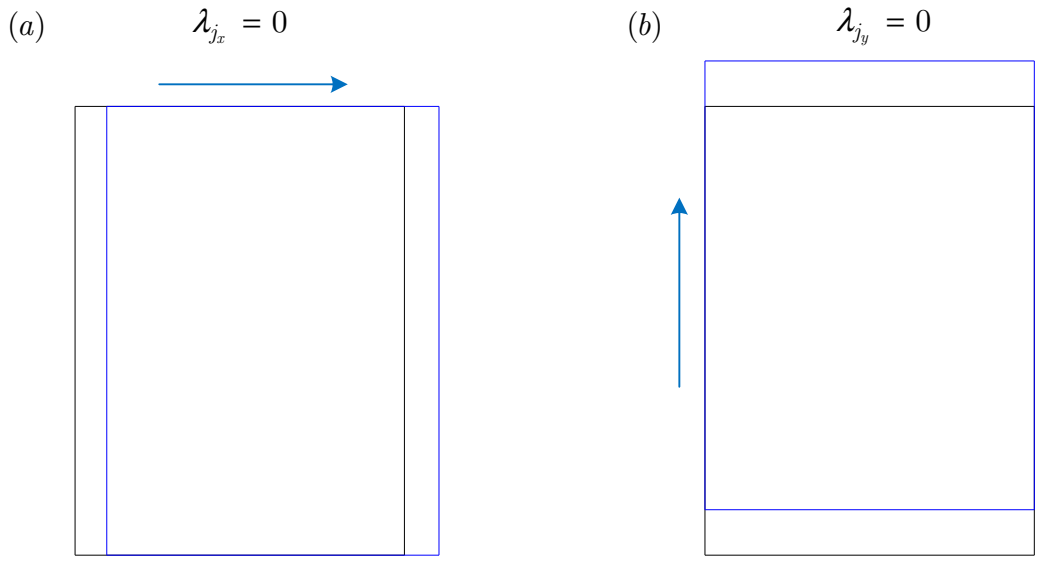

Figure 45. The x- and y-translation modes (a) j_x and (b) j_y are independent of ξ

As there are four such eigenvalues (two for each of the unbounded and bounded domain cases), and as zero-value terms, their distinction cannot be made by the sign of their corresponding eigenvalues. Even though the calculation of the eigenvalues is unlikely to result in exact zero values for these modes, it cannot be assumed that the two bounded x- and y-translation

modes will have a negative finite value, or that the two unbounded x- and y-translation modes will have a positive finite value.

Thus, the two missing translation modes are omitted from $\hat{\boldsymbol{\lambda}}$, a subset of $\boldsymbol{\lambda}$ for which the appropriate bounded or unbounded modes have been identified

$$\boldsymbol{\lambda} = \begin{Bmatrix} \hat{\boldsymbol{\lambda}} \\ \lambda_{j_x} \\ \lambda_{j_y} \end{Bmatrix} \tag{3.95}$$

Similarly, $\boldsymbol{\Phi}$ and $\mathbf{Q}$ are truncated and denoted $\hat{\boldsymbol{\Phi}}$ and $\hat{\mathbf{Q}}$

$$\boldsymbol{\Phi} = \begin{bmatrix} \hat{\boldsymbol{\Phi}} & \varphi_{j_x} & \varphi_{j_y} \end{bmatrix} \tag{3.96}$$

$$\mathbf{Q} = \begin{bmatrix} \hat{\mathbf{Q}} & \mathbf{q}_{j_x} & \mathbf{q}_{j_y} \end{bmatrix} \tag{3.97}$$

3.6.2 Reconstruction of translation modes

Consider a domain constrained in both the x- and y-directions, as illustrated in Figure 46(a). With *a priori* knowledge of the nature of the lost displacement modes ($\lambda_{j_x} = 0$ and $\lambda_{j_y} = 0$), these lost translation modes can be re-inserted in order to complete $\boldsymbol{\lambda}$

$$\boldsymbol{\lambda} = \begin{Bmatrix} \hat{\boldsymbol{\lambda}} \\ 0 \\ 0 \end{Bmatrix} \tag{3.98}$$

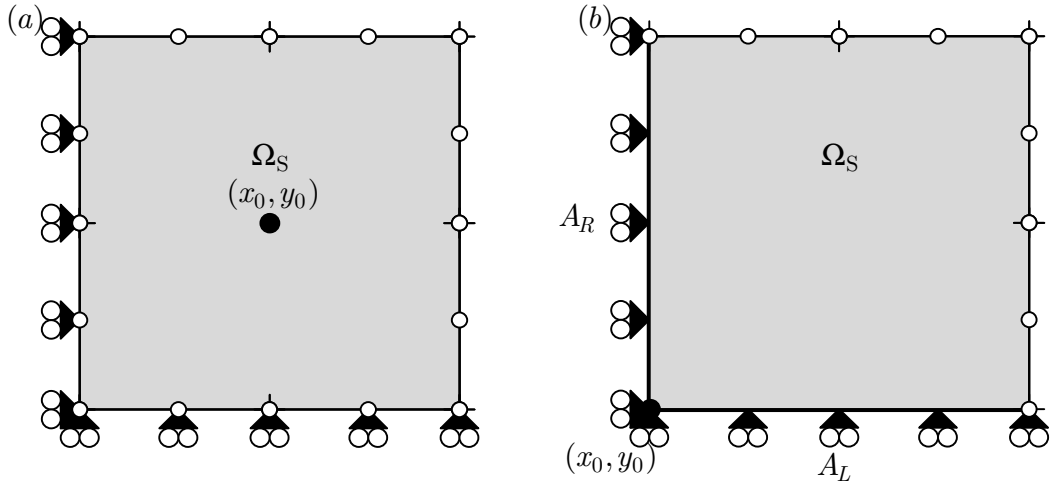

Figure 46. Constraining x- and y-direction of Ω_S by constraint of (a) boundary nodes, and (b) side faces

The corresponding column vectors $\boldsymbol{\varphi}_{j_x}$ and $\boldsymbol{\varphi}_{j_y}$, the unscaled displacement modes, are defined to ensure rigid-body translation independent of $\boldsymbol{\xi}$

$$\boldsymbol{\Phi} = \begin{bmatrix} \begin{bmatrix} \\ \hat{\boldsymbol{\Phi}} \\ \\ \end{bmatrix} & \begin{Bmatrix} 1 \\ 0 \\ \vdots \\ 1 \\ 0 \end{Bmatrix} & \begin{Bmatrix} 0 \\ 1 \\ \vdots \\ 0 \\ 1 \end{Bmatrix} \end{bmatrix} \tag{3.99}$$

These rigid-body translation modes, require no reaction forces, so equilibrium is ensured by defining the corresponding force column vectors $\mathbf{q}_{j_x}$ and $\mathbf{q}_{j_y}$

$$\mathbf{Q} = \begin{bmatrix} \begin{bmatrix} \\ \hat{\mathbf{Q}} \\ \\ \end{bmatrix} & \begin{Bmatrix} 0 \\ 0 \\ \vdots \\ 0 \\ 0 \end{Bmatrix} & \begin{Bmatrix} 0 \\ 0 \\ \vdots \\ 0 \\ 0 \end{Bmatrix} \end{bmatrix} \tag{3.100}$$

3.6.3 Reconstruction of translation modes with side faces

Zero-displacement boundary condition constraints can be applied to side faces, as illustrated in Figure 46(b), but with additional considerations (Deeks and

Wolf, 2002a). The constraint of side faces results in the omission of rows and columns from $\mathbf{E}_0$, $\mathbf{E}_1$ and $\mathbf{E}_2$, and in addition to defining modes j_x and j_y as above, each column vector $\boldsymbol{\varphi}_j$ and $\mathbf{q}_j$ will omit terms relating to i_x and i_y, the constrained displacement degrees of freedom.

$$\boldsymbol{\Phi} = \begin{bmatrix} [& \hat{\boldsymbol{\Phi}} &] & \{\hat{\boldsymbol{\varphi}}_{j_x}\} & \{\hat{\boldsymbol{\varphi}}_{j_y}\} \\ \{\varphi_{i_x 1} & \cdots & \varphi_{i_x (n-2)}\} & \varphi_{i_x j_x} & \varphi_{i_x j_y} \\ \{\varphi_{i_y 1} & \cdots & \varphi_{i_y (n-2)}\} & \varphi_{i_y j_y} & \varphi_{i_y j_y} \end{bmatrix} \tag{3.101}$$

$$\mathbf{Q} = \begin{bmatrix} [& \hat{\mathbf{Q}} &] & \{\hat{\mathbf{q}}_{j_x}\} & \{\hat{\mathbf{q}}_{j_y}\} \\ \{q_{i_x 1} & \cdots & q_{i_x (n-2)}\} & q_{i_x j_x} & q_{i_x j_y} \\ \{q_{i_y 1} & \cdots & q_{i_y (n-2)}\} & q_{i_y j_y} & q_{i_y j_y} \end{bmatrix} \tag{3.102}$$

The missing terms from $\boldsymbol{\Phi}$ corresponding to rows i_x and i_y can be inserted

$$\boldsymbol{\Phi} = \begin{bmatrix} [& \hat{\boldsymbol{\Phi}} &] & \{\hat{\boldsymbol{\varphi}}_{j_x}\} & \{\hat{\boldsymbol{\varphi}}_{j_y}\} \\ \{0 & \cdots & 0\} & 1 & 0 \\ \{0 & \cdots & 0\} & 0 & 1 \end{bmatrix} \tag{3.103}$$

The missing terms from $\mathbf{Q}$ are the forces reacting the total x- and y-direction forces for each mode, which can be found by ensuring force equilibrium for each mode, i.e.

$$q_{i_x j} = -\sum_{i=1}^{n} q_{ij} \qquad \text{where } i \neq j_x \tag{3.104}$$

$$q_{i_y j} = -\sum_{i=1}^{n} q_{ij} \qquad \text{where } i \neq j_y \tag{3.105}$$

Neither the application of zero-displacement boundary conditions in orientations other than parallel to the Cartesian axes, nor the application of non-zero-displacement boundary conditions to side faces (Deeks, 2004), are required in the present work and are not described here.

3.7 Applications to fracture mechanics

As the form of the solution in the radial direction is the modal superposition of an exponent series, including those on side faces, the SBFEM is considered analytical in ξ. However, as the solution is interpolated numerically in s, the method is often referred in the literature as semi-analytical.

The semi-analytical form of the solution is desirable in modelling problems whose solution is known *a priori* to be modelled better by an analytical series using a finite number of modes than a polynomial-based alternative. If there is one principal or dominating stress field to be modelled, the SBFEM may be a good choice if the scaling centre can be placed such that the variation in this stress field is aligned with the radial axes, without violating the line of sight requirement. By coinciding the scaling centre with a crack tip, j_{K_I} and j_{K_II} may be identified and used in the estimation of the associated stress intensity factors (Yang, 2006). Rewriting equation (3.93)

$$\boldsymbol{\sigma}(\xi, s) = \sum_{j=1}^{n} c_j \xi^{-\lambda_j - 1} \boldsymbol{\psi}(s)_j \tag{3.106}$$

where

$$\boldsymbol{\psi}(s)_j = \mathbf{D}\left[\mathbf{B}_2(s) - \lambda_j \mathbf{B}_1(s)\right]\boldsymbol{\varphi}_j \tag{3.107}$$

and $\boldsymbol{\psi}(s)_j$ is the mode j vector of contributory stresses at s

$$\boldsymbol{\psi}(s)_j = \begin{Bmatrix} \boldsymbol{\psi}_{xx}(s)_j \\ \boldsymbol{\psi}_{yy}(s)_j \\ \boldsymbol{\psi}_{xy}(s)_j \end{Bmatrix} \tag{3.108}$$

3.7.1 Stress intensity factors

It is possible to define generally $r(\xi,s)$, the distance from the crack tip r, as a function of radial and boundary coordinates ξ and s. With reference to Figure 47, in which side faces are omitted for clarity (but without loss of generality), it can be seen that $r(\xi,s)$ simplifies to $\xi r(s)$.

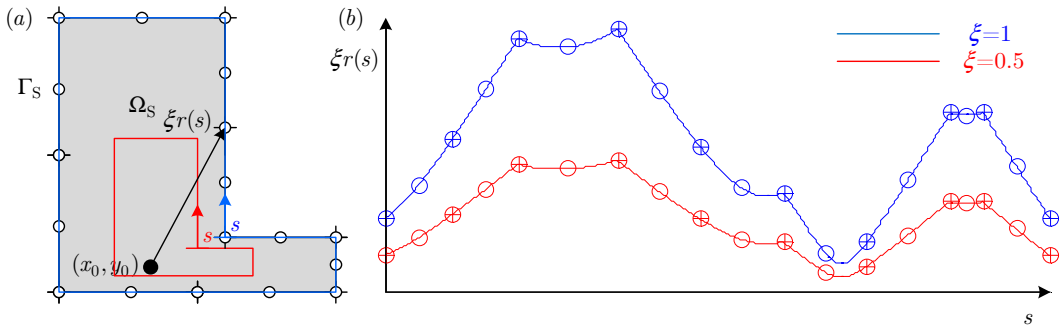

Figure 47. An example SBFEM domain with (a) geometrically-scaled boundaries and (b) the resulting functions $r(\xi,s) = \xi r(s)$

More specifically ξr_0 is then defined as the distance (scaled by ξ) from a crack tip to s_0, the point on s coinciding with $\theta_p = 0$, where θ_p is the local crack angle defined in §1.4. The substitution of ξr_0 and equation (3.106) into equations (1.1) and (1.2) yields

$$K_{\mathrm{I}} = \lim_{r\to 0} \sum_{j=1}^{n} c_i \xi^{-\lambda_j - 1} \psi_{yy}(s_0)_j \sqrt{2\pi\xi r_0} \tag{3.109}$$

$$K_{\mathrm{II}} = \lim_{r\to 0} \sum_{j=1}^{n} c_i \xi^{-\lambda_j - 1} \psi_{xy}(s_0)_j \sqrt{2\pi\xi r_0} \tag{3.110}$$

and or

$$K_{\mathrm{I}} = \lim_{\xi\to 0} \sum_{j=1}^{n} c_i \xi^{-\lambda_j - 1/2} \psi_{yy}(s_0)_j \sqrt{2\pi r_0} \tag{3.111}$$

$$K_{\mathrm{II}} = \lim_{\xi \to 0} \sum_{j=1}^{n} c_i \xi^{-\lambda_j - 1/2} \psi_{xy}(s_0)_j \sqrt{2\pi r_0} \tag{3.112}$$

The relationships between these terms in a generally-oriented crack are illustrated in Figure 48.

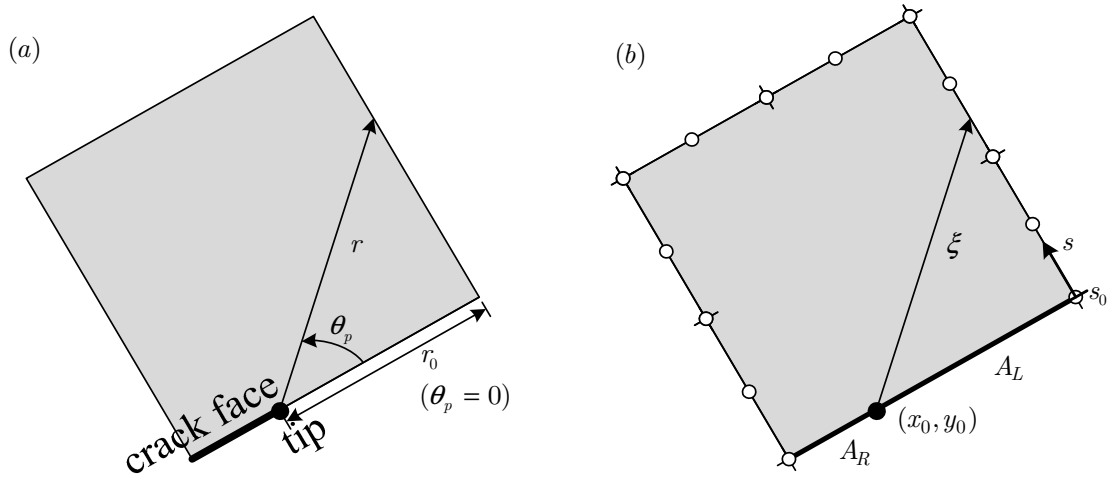

Figure 48. Relationship between (*a*) stress intensity factor parameters and (*b*) SBFEM parameters

Because as $\xi \to 0$

$$\xi^{-\lambda_j - 1/2} \to \begin{cases} 1 & \lambda_j = -1/2 \\ 0 & \text{otherwise} \end{cases} \tag{3.113}$$

the stress intensity factors arising as $r \to 0$ (as $\xi \to 0$), are estimated by

$$K_{\mathrm{I}_h} = c_{j_{K_I}} \psi_{yy}(s_0)_{j_{K_I}} \sqrt{2\pi r_0} \tag{3.114}$$

$$K_{\mathrm{II}_h} = c_{j_{K_{II}}} \psi_{xy}(s_0)_{j_{K_{II}}} \sqrt{2\pi r_0} \tag{3.115}$$

where $j_{K_{\mathrm{I}}}$ and $j_{K_{\mathrm{II}}}$ are the crack modes for which $\lambda_j = -1/2$ and the 'h' subscript indicates a numerical approximation expected to improve with an *h*-adaptive mesh refinement strategy.

This represents an important result in the application of SBFEM to fracture mechanics as the stress intensity factors can be found by the direct extraction of the stresses associated with crack modes $j_{K_{\mathrm{I}}}$ and $j_{K_{\mathrm{II}}}$. Further, if the domain is meshed such that s_0 coincides with a node, these modal stresses are extracted without the need for numerical interpolation in the s-direction. It is this analytical form of the stress intensity factors that makes the SBFEM such a suitable method for use in modelling the singular functions in associated with fracture mechanics.

3.8 Semi-discontinuous SBFEM

For the purposes of disambiguity, it should be noted that, unless otherwise stated, the remaining sections follow as a direct result of work undertaken by the author.

In order to facilitate the coupling of the SBFEM and DBEM, a new semi-discontinuous SBFEM was developed (Bird *et al.*, 2009b). The motivation for the development is discussed in §5.2.1, but as it is directly related to the SBFEM, it is more appropriate for its formulation and analysis to be included in this chapter.

As described in §3.5, the matrices $\mathbf{E}_0$, $\mathbf{E}_1$ and $\mathbf{E}_2$ formed in the construction of the $\mathbf{K}_{\mathrm{S}}$ exhibit a banded overlapping of submatrices similar to that of a typical FEM stiffness matrix. Unlike in the BEM, where adjacent elements do not require common nodes, nodal discontinuity in the SBFEM results in a discontinuity of the overlapping regions in the matrices $\mathbf{E}_0$, $\mathbf{E}_1$ and $\mathbf{E}_2$. With reference to Figure 43 and Figure 44, the effect of element discontinuities is illustrated in Figure 49. In such a case, additional constraint equations may be required to render $\mathbf{K}_{\mathrm{S}}$ non-singular.

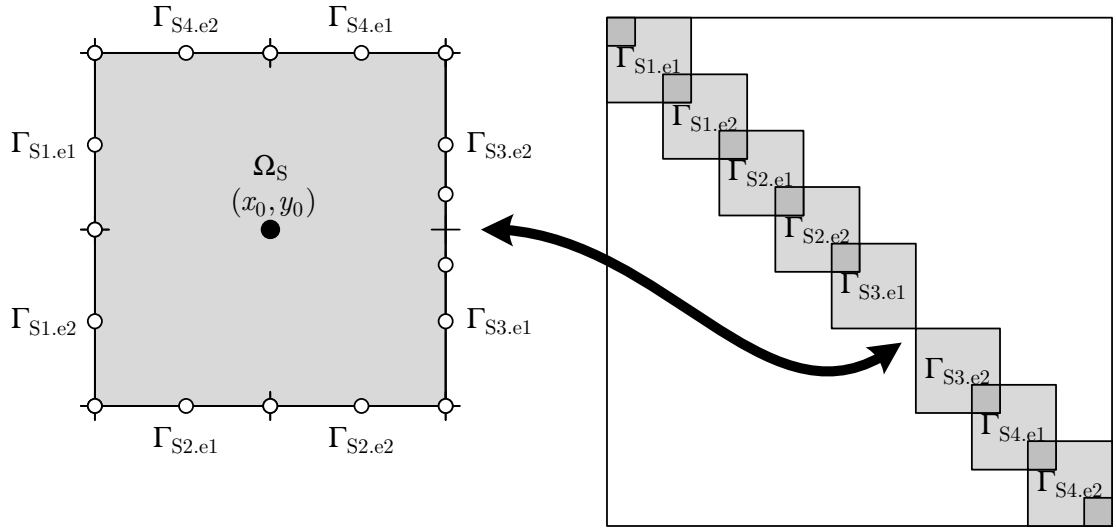

Figure 49. Elemental connectivity is lost if discontinuous elements are used to discretise Γ_S

However, with the scaling centre on the boundary, a natural discontinuity in the s-direction can be found as the discretised boundary meets the side faces. This facilitates the possibility of replacing the continuous elements that connect the discretised sections of the boundary with the side faces with semi-discontinuous elements, while maintaining the overlapping structure of matrices $\mathbf{E}_0$, $\mathbf{E}_1$ and $\mathbf{E}_2$. This is illustrated in Figure 50.

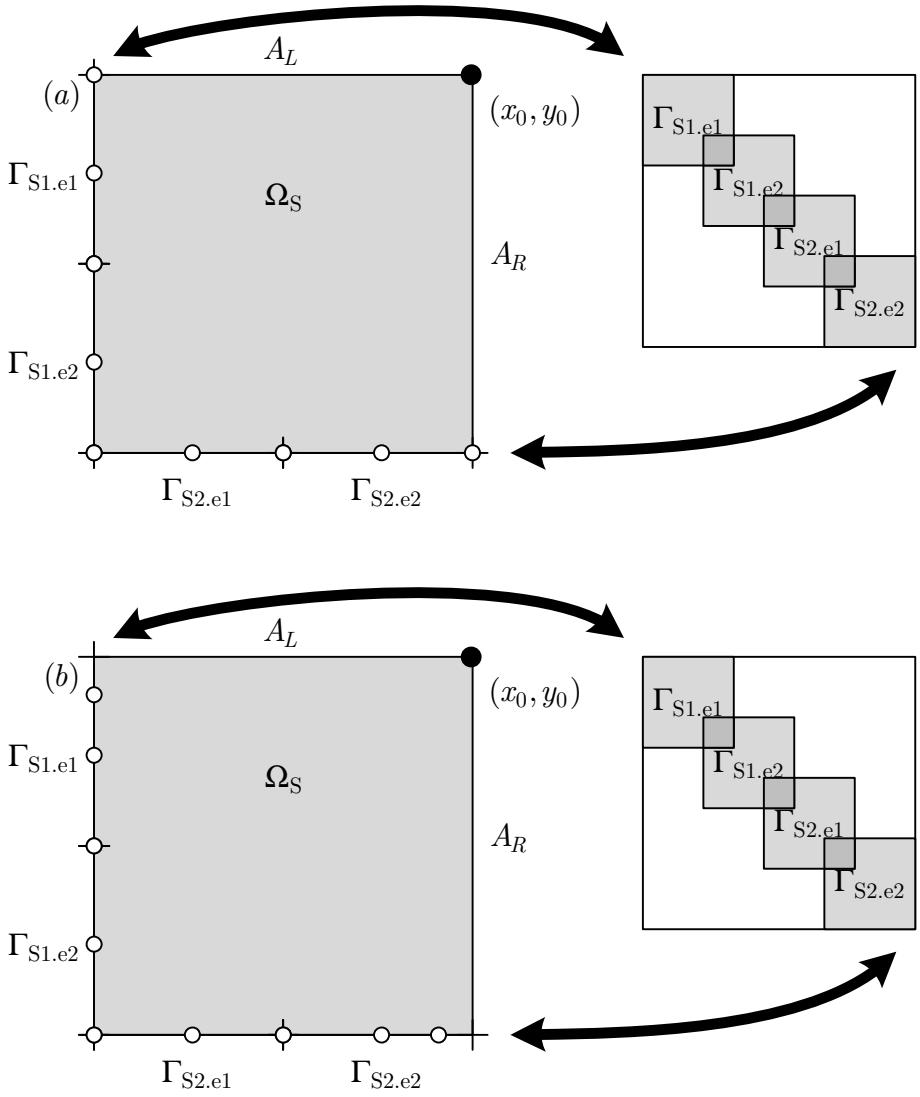

Figure 50. (a) Side faces cause a natural discontinuity in the discretisation of Γ_{S}, facilitating (b) the introduction of semi-discontinuous scaled boundary finite elements adjacent to side faces, without altering the structure of the overlapping submatrix connectivity

The boundary integration of the SBFEM undertaken in forming $\mathbf{E}_0$, $\mathbf{E}_1$ and $\mathbf{E}_2$ requires the use of (quadratic) shape functions, modified in the same manner as conventional semi-discontinuous boundary elements used in the BEM. The construction of $\mathbf{K}_{\mathrm{S}}$ then follows that of the conventional (continuous) SBFEM.

It should also be noted that because there is no nodal degree of freedom on

the side face, the conventional application of boundary conditions on the side faces is not trivial and may require the use of additional constraint equations. This is beyond the scope of the current work where all side faces are assumed traction-free.

An advantage of (and the motivation for) the discontinuous scaled boundary finite element is its readiness for coupling with the DBEM in which it is advantageous for there to be no nodal connectivity between the boundary elements.

3.9 Example applications to fracture mechanics

The SBFEM is applied to the same benchmark problem used in §2.10. A notable difference between the methods is that without nodes on the undiscretised sideface portions of Γ_S, there may be fewer contributory terms to equation (2.119). So in addition to the displacement solution at the nodes, contributions to the error estimate are made by the displacement solution at sample locations along the side faces (where $\xi = \{0.1 \quad 0.2 \quad \cdots \quad 1.0\}$).

In addition to a displacement-based error indicator, the stress intensity factor may be extracted directly by the identification of modes j_{K_I} and $j_{K_{II}}$, and an additional error indicator is defined for each crack mode

$$\varepsilon_{K_I} = \frac{\left| K_I - K_{I_h} \right|}{K_I} \tag{3.116}$$

$$\varepsilon_{K_{II}} = \left| K_{II} - K_{II_h} \right| \tag{3.117}$$

The error $\varepsilon_{K_{II}}$ is defined in absolute terms as in this example, where $K_{II} = 0$, it is inappropriate to normalise by the expected value.

It should be noted that permutations of the following example have been published before (Chidgzey and Deeks, 2005), but are reproduced here using the author's code to provide means for comparison of numerical methods later and should not be considered a new application of this method. The use of the author's code also provides alternative visualisation of the results.

For the examples in this chapter

$$\Omega = \Omega_S \tag{3.118}$$

$$\Gamma = \Gamma_S \cup A_R \cup A_L \tag{3.119}$$

and the scaling centre is co-incident with the crack tip.

3.9.1 Through crack in an infinite plate example 1

The SBFEM is used to model the crack tip described in §2.10. With reference to Figure 51(c), the dimensions of Ω_S are $b \times h$, and Γ_S is subdivided into portions of boundary $\Gamma_{\tilde{u}}$ with known displacement boundary conditions (red nodes), and portions of boundary Γ_u with displacements to be found as part of the solution (white nodes). As there are no nodes at which the boundary conditions are to be found in the solution

$$\Gamma_u = A_R \tag{3.120}$$

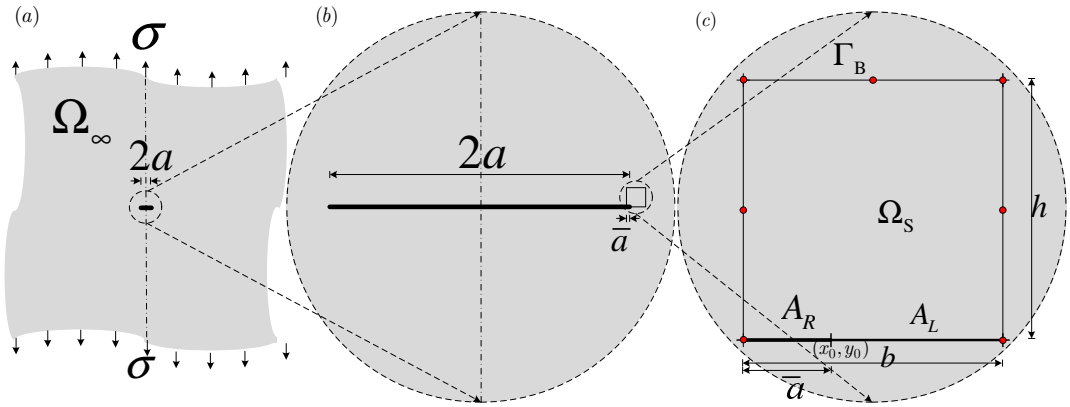

Figure 51. SBFEM analysis of (a) through crack in an infinite plate, (b) the section of the domain modelled, and (c) the mesh where red and white nodes indicate $\Gamma_{\tilde{u}}$ and Γ_u

The displacements of the domain and boundary portion Γ_u are illustrated in Figure 52(a) and Figure 53 respectively. Figure 54 illustrates the sample locations on the side faces used as an addition to the nodal displacements in equation (2.119). Convergence characteristics of the SBFEM displacement and stress intensity factor errors are illustrated in Figure 55 and Figure 56 respectively, using the uniform mesh refinement indicated in Figure 52(b).

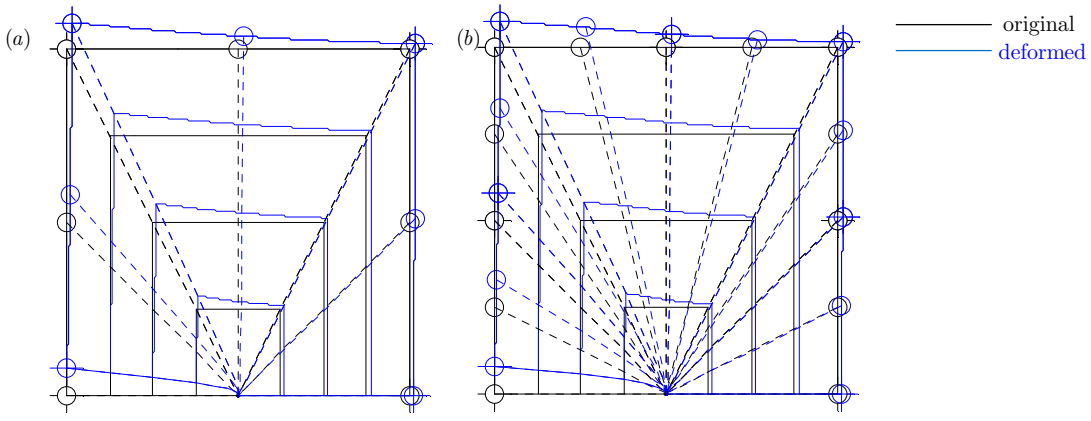

Figure 52. To-scale deformation of (a) initial mesh and (b) uniformly-refined mesh

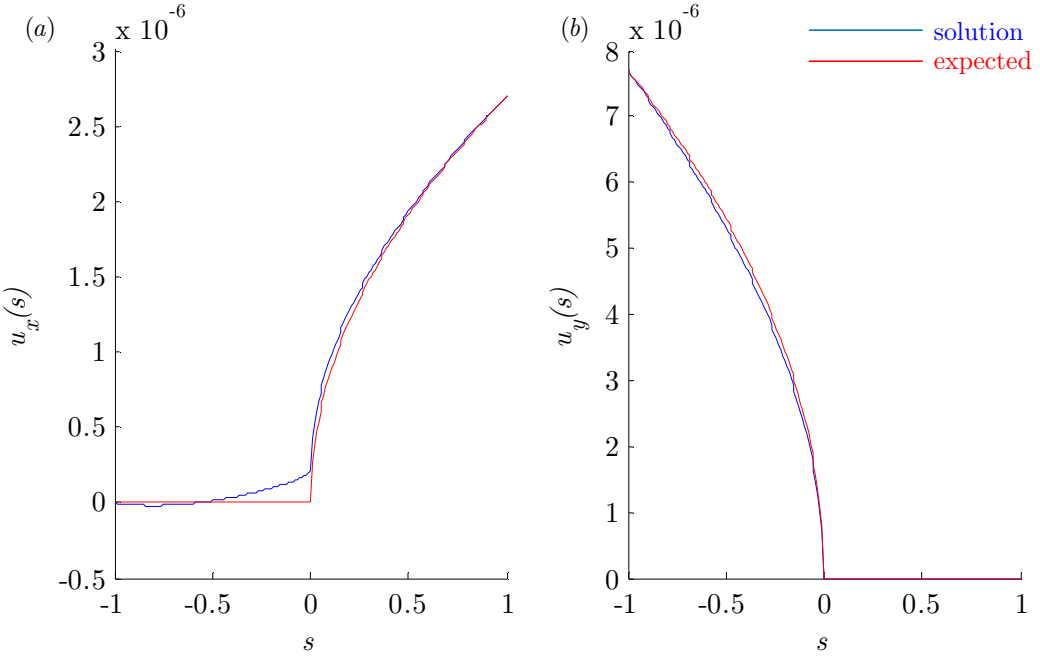

Figure 53. (a) x- and (b) y-direction displacement results on Γ_u

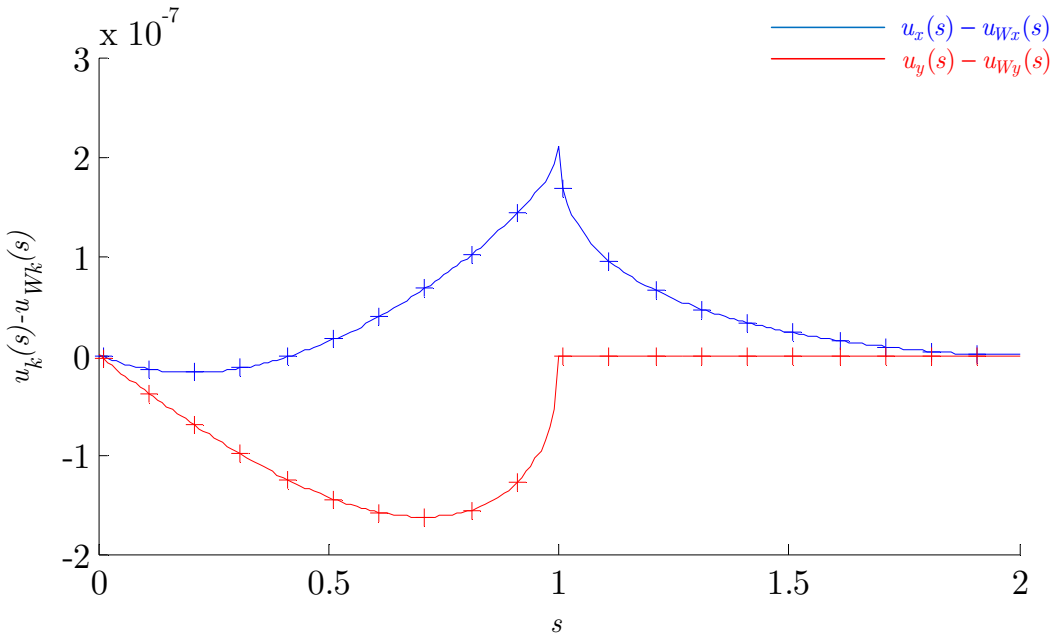

Figure 54. x- and y-direction displacement errors on Γ_u and the sample points used in the estimation of $\boldsymbol{\varepsilon}_{L^2x}$ and $\boldsymbol{\varepsilon}_{L^2y}$

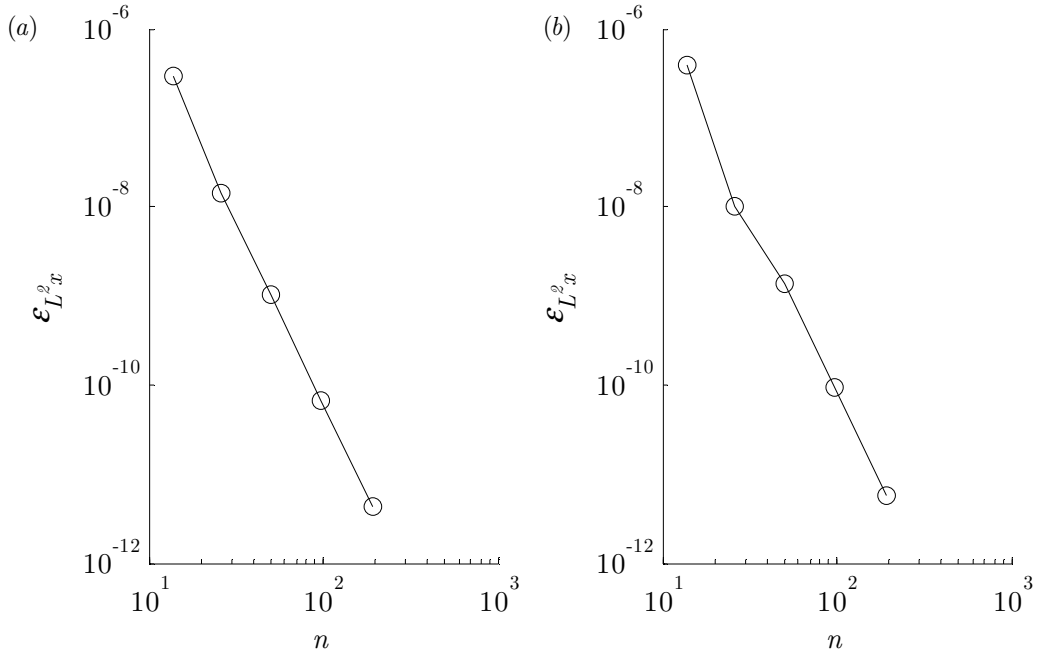

Figure 55. Convergence characteristics of global error estimators $(a)\,\varepsilon_{L^2x}$ and $(b)\,\varepsilon_{L^2y}$

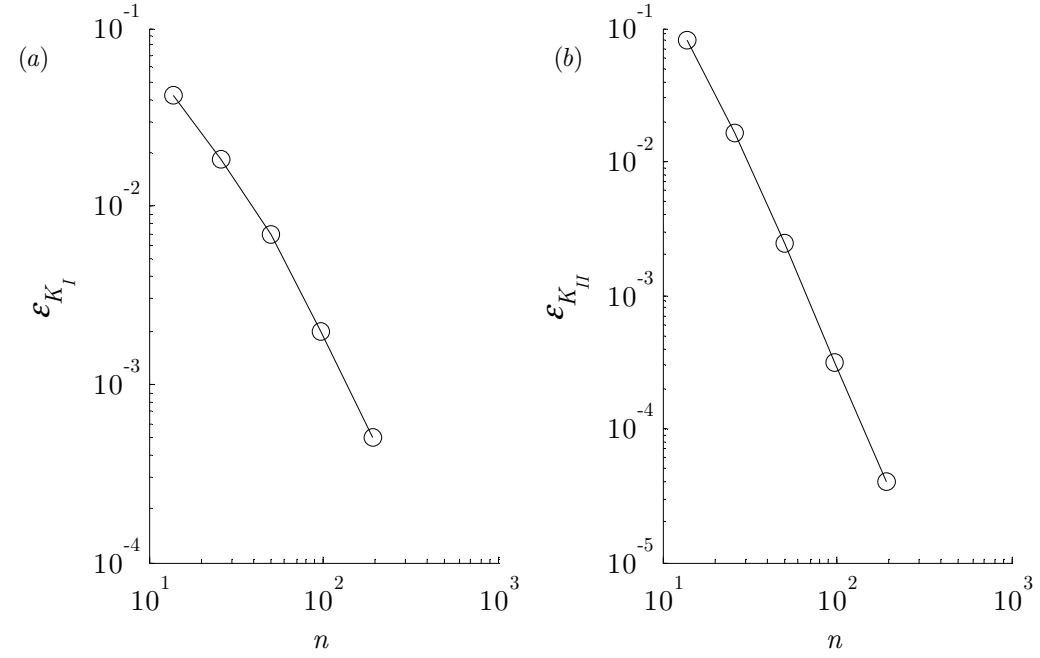

Figure 56. Convergence characteristics of global error estimators $(a)\ \varepsilon_{K_I}$ and $(b)\,\varepsilon_{K_{II}}$

3.9.2 Through crack in an infinite plate example 2

The SBFEM is again used to model the crack tip described in §2.10, but the assumption of symmetry is removed by modelling both crack faces with side

faces. With reference to Figure 57(c), the dimensions of Ω_S is doubled ($b \times 2h$) and

$$\Gamma_u = A_L \cup A_R \tag{3.121}$$

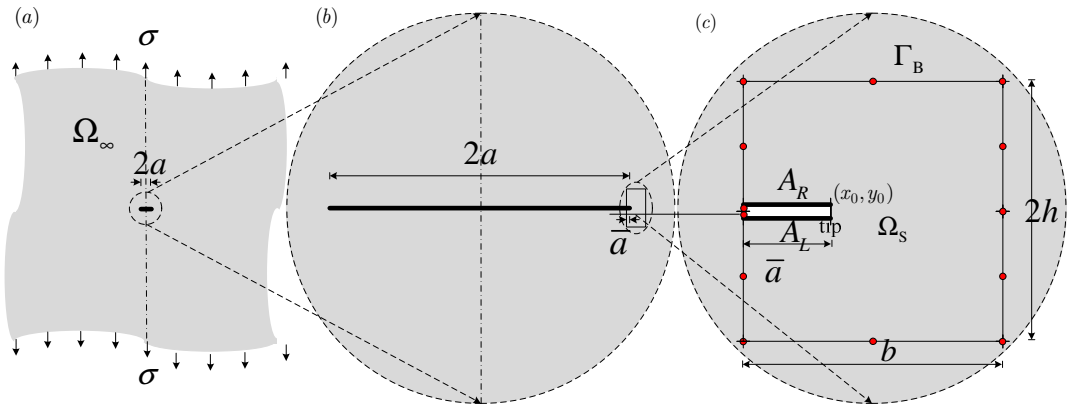

Figure 57. SBFEM analysis of (a) through crack in an infinite plate, (b) the section of the domain modelled, and (c) the mesh where red and white nodes indicate $\Gamma_{\bar{u}}$ and Γ_u

The displacements of the domain and boundary portion Γ_u are illustrated in Figure 58(a) and Figure 59 respectively. Convergence characteristics of the SBFEM displacement and stress intensity factor errors are illustrated in Figure 60 and Figure 61 respectively, using the uniform mesh refinement indicated in Figure 58(b).

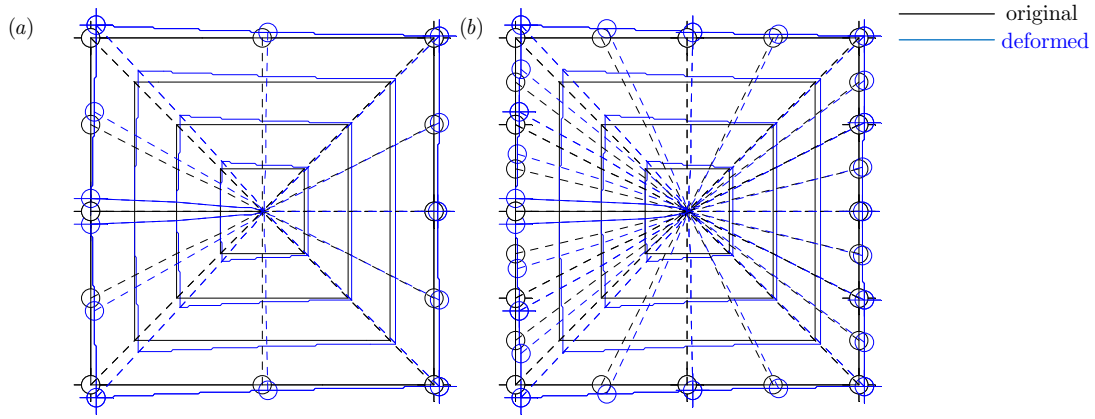

Figure 58. To-scale deformation of (a) initial mesh and (b) uniformly-refined mesh

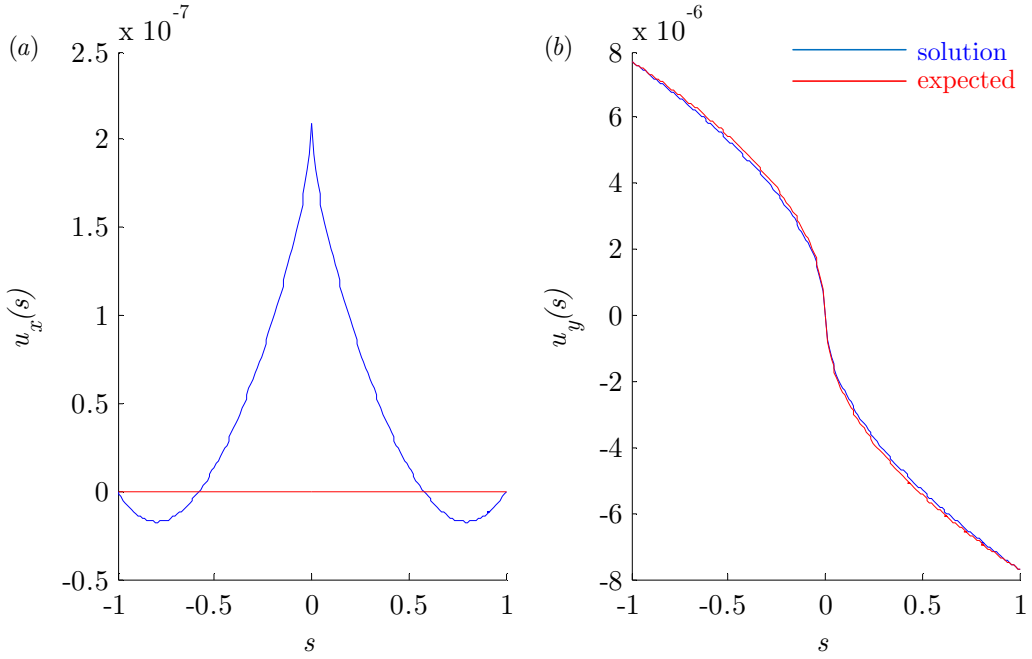

Figure 59. (a) x- and (b) y-direction displacement results on Γ_u

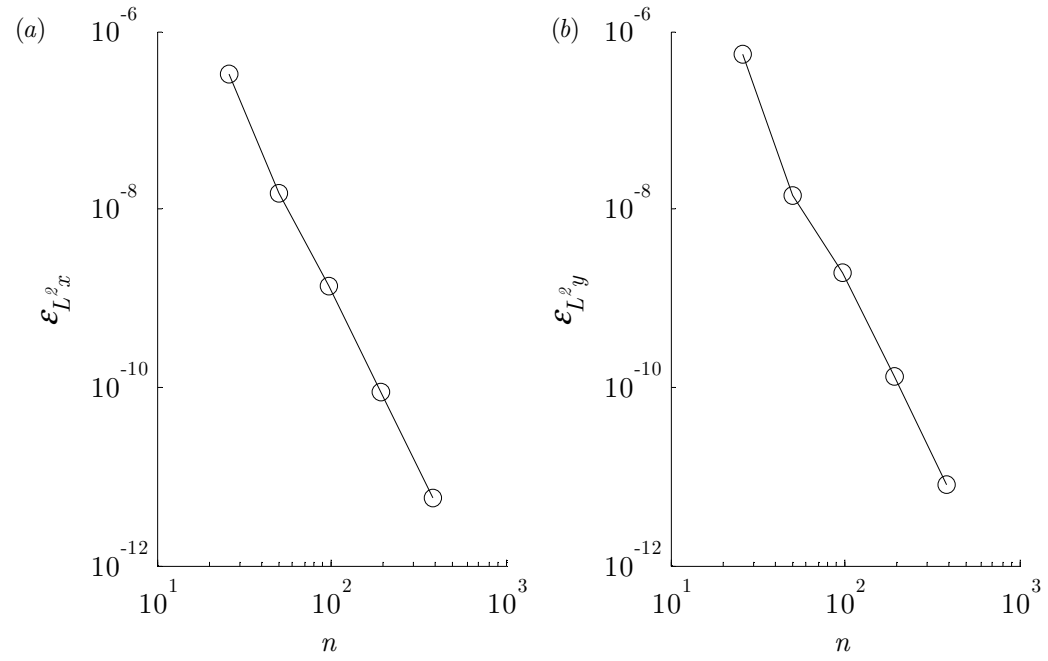

Figure 60. Convergence characteristics of global error estimators (a) ε_{K_I} and (b) $\varepsilon_{K_{II}}$

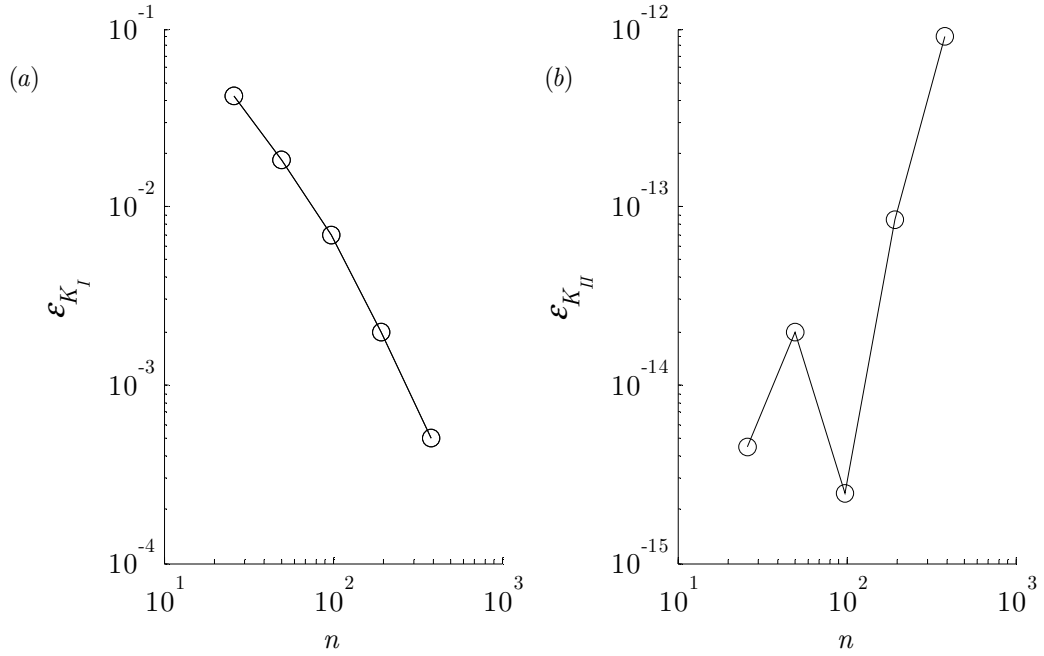

Figure 61. Convergence characteristics of global error estimators (a) ε_{K_I} and (b) $\varepsilon_{K_{II}}$

3.9.3 Through crack in an infinite plate example 3

The SBFEM is again used to model the crack tip described in §2.10, but in addition to removing the assumption of symmetry, the effect of the semi-discontinuous elements of §3.8 is evaluated, as illustrated in Figure 62(c).

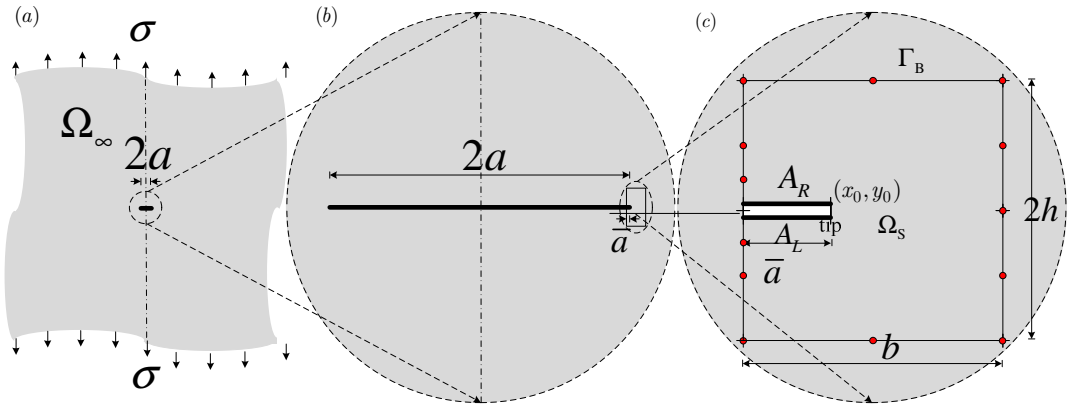

Figure 62. SBFEM analysis of (a) through crack in an infinite plate, (b) the section of the domain modelled, and (c) the mesh where red and white nodes indicate $\Gamma_{\tilde{u}}$ and Γ_u

The displacements of the domain and boundary portion Γ_u are illustrated in Figure 63(a) and Figure 64 respectively. Convergence characteristics of the SBFEM displacement and stress intensity factor errors are illustrated in Figure 65 and Figure 66 respectively, using the uniform mesh refinement indicated in Figure 63(b).

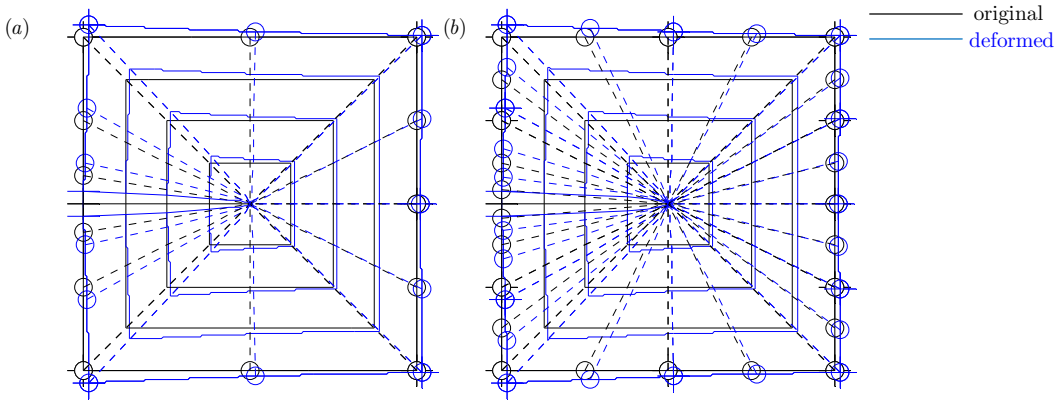

Figure 63. To-scale deformation of (a) initial mesh and (b) uniformly-refined mesh

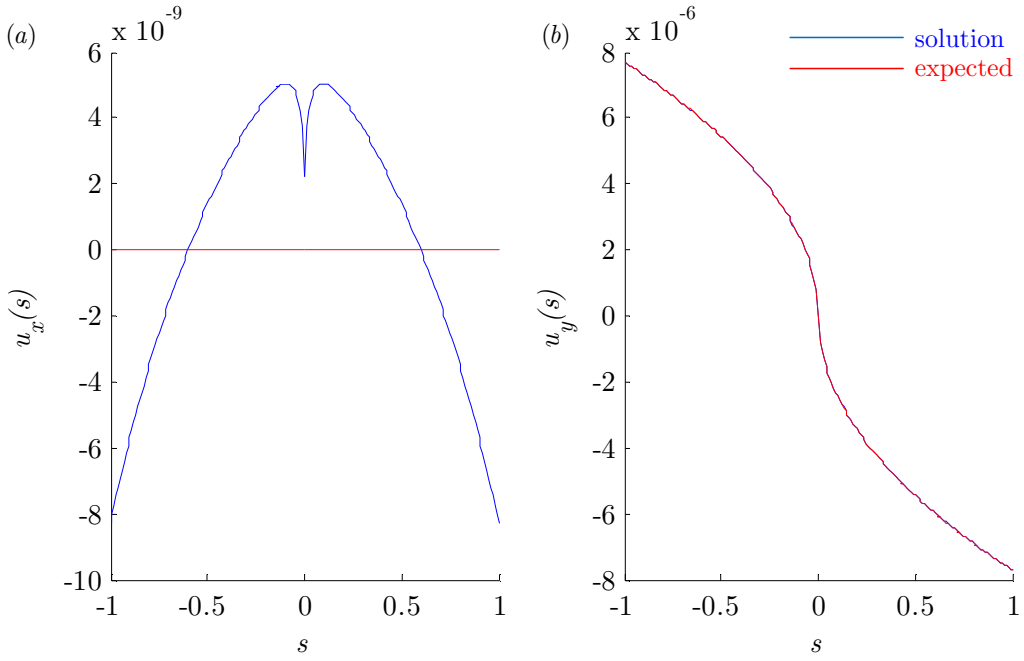

Figure 64. (a) x- and (b) y-direction displacement results on Γ_u

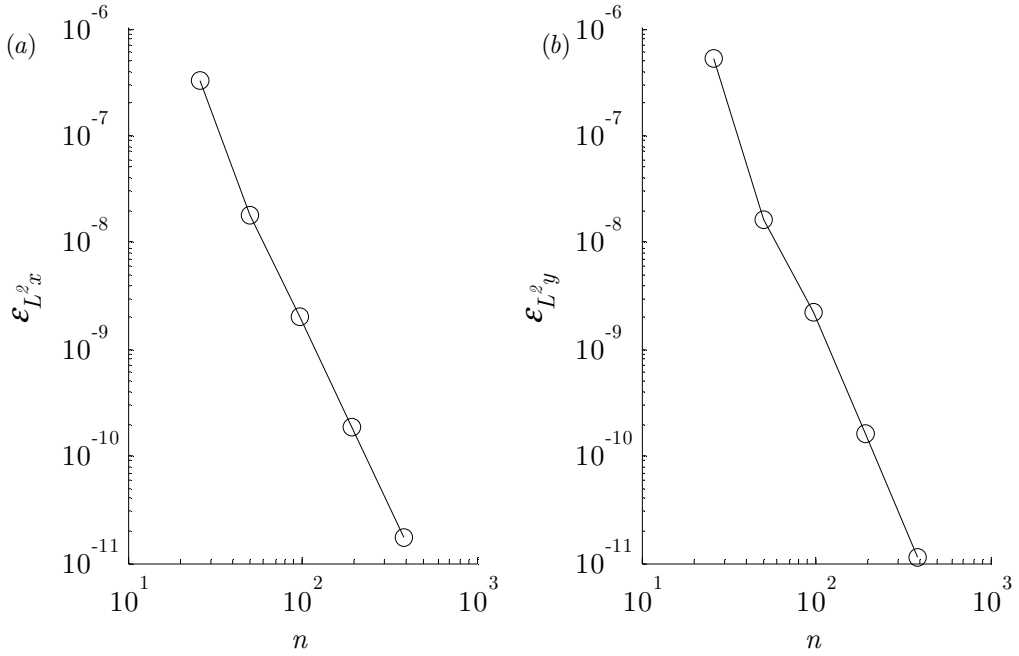

Figure 65. Convergence characteristics of global error estimators $(a)\,\varepsilon_{L^2x}$ and $(b)\,\varepsilon_{L^2y}$

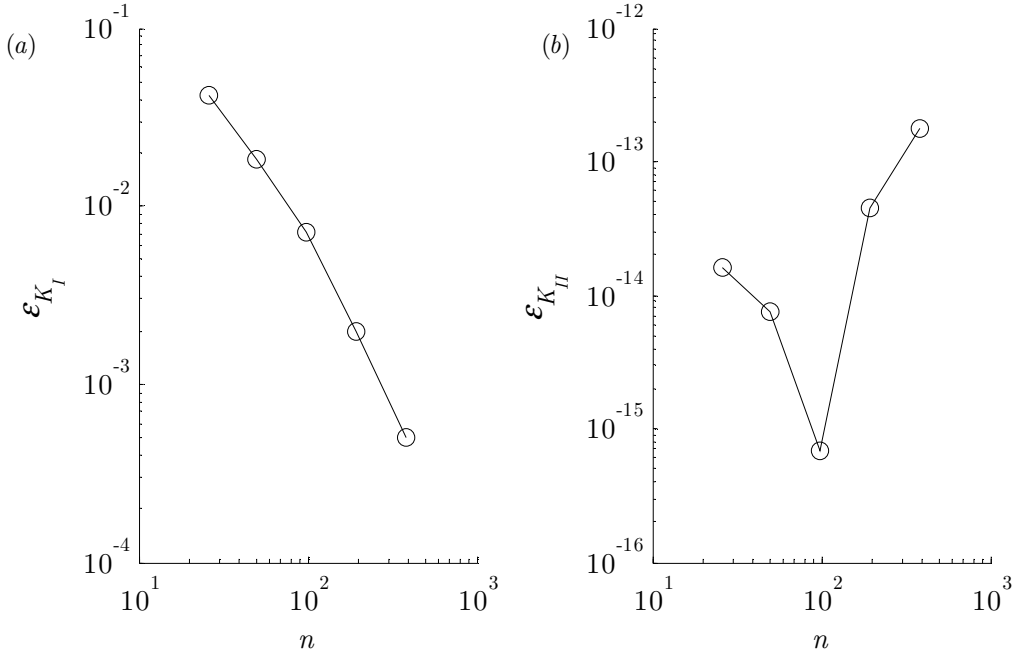

Figure 66. Convergence characteristics of global error estimators $(a)\,\varepsilon_{K_{\mathrm{I}}}$ and $(b)\,\varepsilon_{K_{\mathrm{II}}}$

3.10 Significance of imaginary components

Although the eigenvalue problem in equation (3.66) contains only real numbers, the matrices of modal displacements $\mathbf{\Phi}$ and modal forces $\mathbf{Q}$, and

vector of eigenvalues $\boldsymbol{\lambda}$ found in its solution may contain imaginary parts, which in turn induce imaginary parts to the vector of contribution factors $\mathbf{c}$. In the calculation of $\mathbf{u}(\boldsymbol{\xi}, s)$, the imaginary component of each term contributing to its respective series is assumed negligible (Chidgzey, 2007).

The following indicator is defined in order to quantify the significance of the imaginary component of c_j

$$F_j^c = \mathrm{Re}(c_j) \times \mathrm{Im}(c_j) \tag{3.122}$$

and is considered more satisfactory than a normalised indicator[v]. Consequences of neglecting imaginary terms been observed as part of the present work on both displacement and recovered stress results. Examples are now presented.

3.10.1 Displacement results and domain regularity

In addition to restrictions in domain shape imposed on the SBFEM by the line of sight requirement, anecdotal observations suggest that the method's performance is improved with the regularity of the domain geometry (Deeks, 2009). It is known that the uniqueness of the eigenvalues degrades as their

[v] A normalised indicator such as $F_j^c = \dfrac{\mathrm{Re}(c_j) - \mathrm{Im}(c_j)}{\mathrm{Re}(c_j)}$ may inflate the significance of $\mathrm{Im}(c_j)$ when $\mathrm{Re}(c_j)$ is low. Modes for which $\mathrm{Re}(c_j)$ is relatively low contribute little to $\mathbf{u}(\boldsymbol{\xi}, s)$ and so are less important than modes for which $\mathrm{Re}(c_j)$ is relatively high. Thus, it is more important to estimate the significance of $\mathrm{Im}(c_j)$ where $\mathrm{Re}(c_j)$ is relatively high. This is achieved through the indicator described in equation (3.122)

corresponding eigenvectors become near parallel. However, here it is postulated that similar effects shall be observed with the reduction of regularity of the domain.

A wide range of models was used in the acceptance testing of the computer code used to develop the SBFEM used in the present work. Models included uniaxial tension tests, both with and without the inclusion of circular holes, simply supported beams and cantilevered beams etc. However, by varying the geometry of Ω_S in addition to the mesh density, the effect of domain regularity was investigated. The following example demonstrates results representative of these tests.

A uniformly-distributed load is applied to a cantilevered beam, as illustrated in Figure 67, and is modelled using the SBFEM. The effect of domain regularity is investigated by varying aspect ratio $b:h$ and is compared to the effect of variations in mesh density with 1, 5, 10, 15 and 20 elements per line. The acceptance tests were based on boundary results (maximum tip deflection) and in all cases were satisfactory. However the effect of domain geometry on the interior results are largely ignored. Sample results are illustrated in Figure 68 and Figure 69.

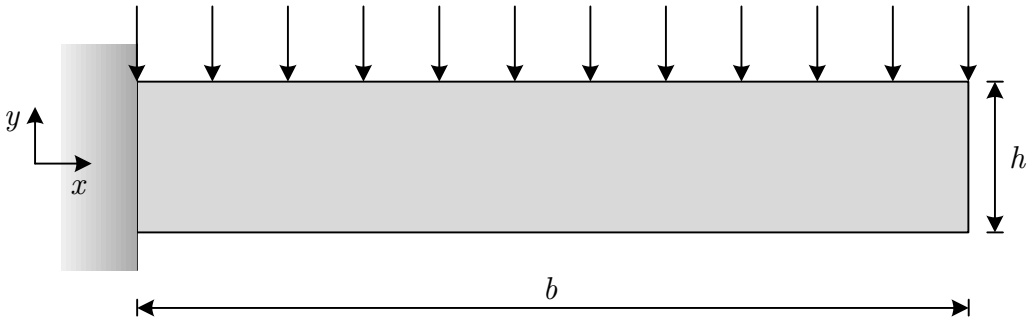

Figure 67. Cantilevered beam

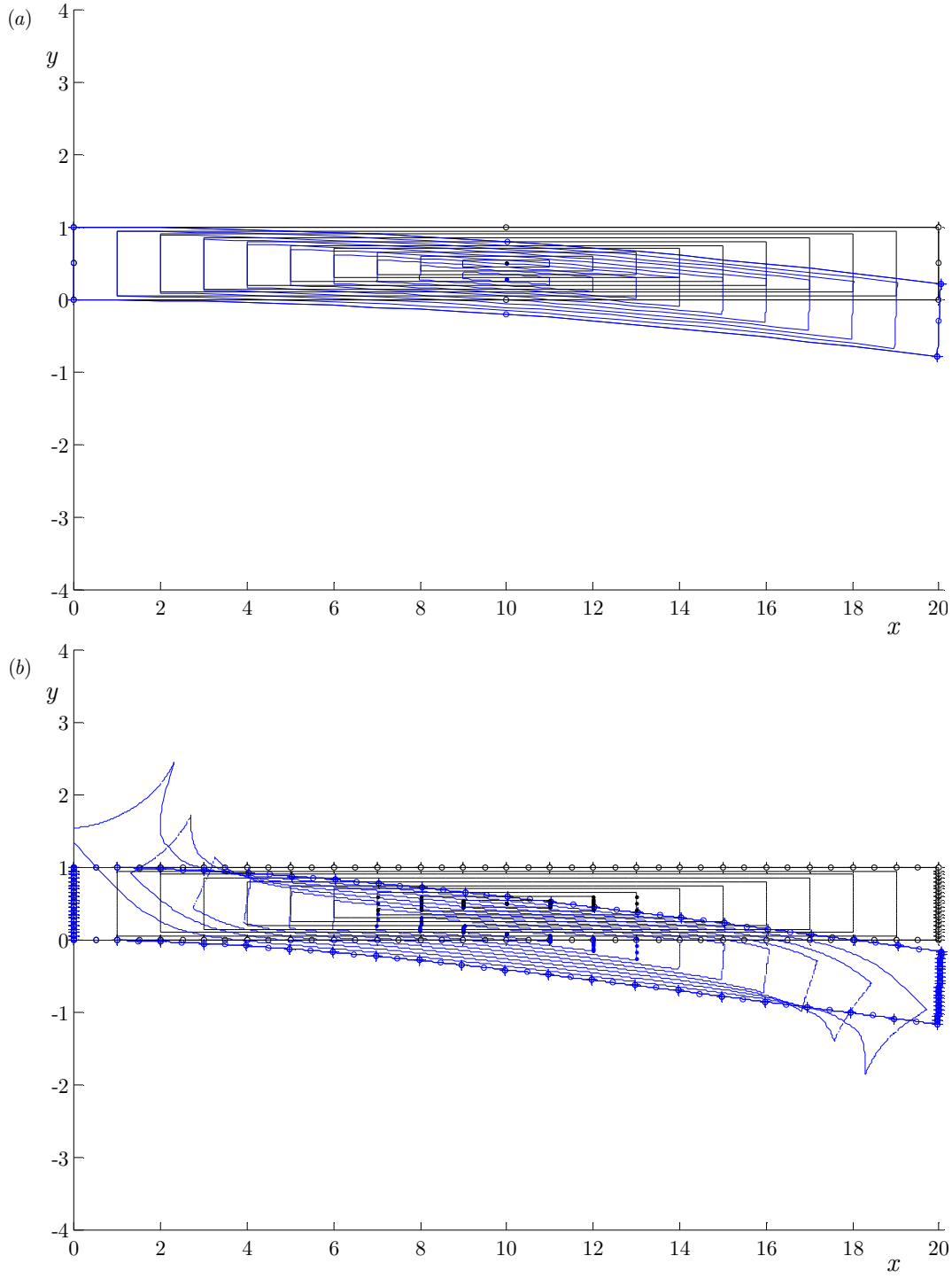

Figure 68. With reference to Figure 67, effect of increasing mesh density from (*a*) initial density to (*b*) 20x initial density upon interior displacement results with aspect ratio of 20:1

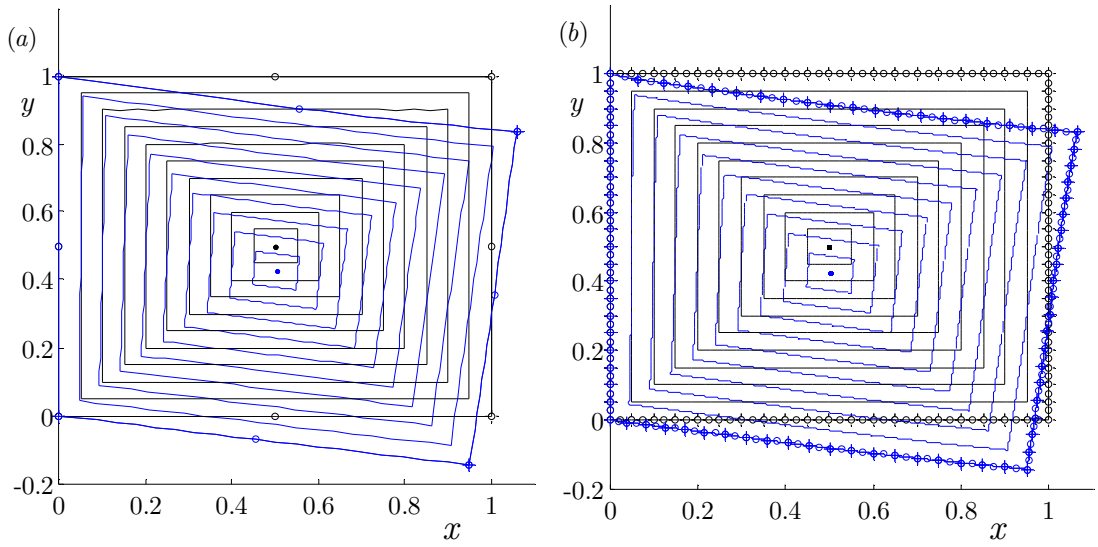

Figure 69. With reference to Figure 67, effect of increasing mesh density from (*a*) initial density to (*b*) 20x initial density upon interior displacement results with aspect ratio of 1:1

The variation of the indicator described in equation (3.122) is illustrated in Figure 70 for the 25 combinations of mesh density and aspect ratio. The square point represents the sum of all the indicators for respective mesh density/aspect ratio combinations. The solid line that connects them is included to highlight that these totals tend to increase with aspect ratio.

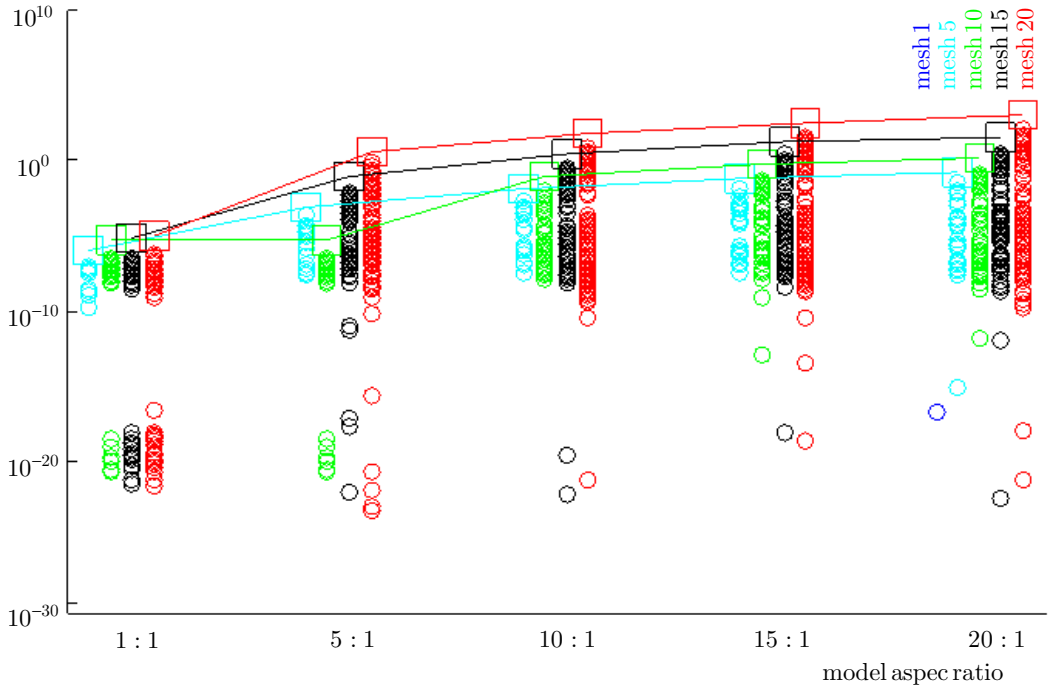

Figure 70. Indication of the significance of $\mathrm{Im}(c_j)$ for 25 model combinations of 5x mesh densities and 5x aspect ratios. Each circular point represents an individual mode j. Note that Zero-values of F_j^c do not appear on the logarithm axis.

3.10.2 Stress recovery

Further to errors in domain displacement, the secondary calculation of $\mathbf{c}$ may result in poor recovered stresses. Moreover, observations of poor stress results have been made even when the corresponding domain displacements are adequate.

Consider a linear elastic domain of dimensions $b \times h$ subject to a uniaxial stress and boundary constraints illustrated in Figure 71, modelled using the SBFEM by two side faces and two sections of discretised boundary labelled Γ_{S1} and Γ_{S2}. The results in terms of nodal displacements and stresses can be calculated for arbitrary domain and model parameters, and are given by

$$u_x(x) = x\frac{\sigma_x}{E},\ 0 \le x \le b \tag{3.123}$$

where Young's modulus $E = 207\text{GPa}$, $\sigma_x = 1\text{MPa}$ and $b = h = 1\text{m}$. The x-direction displacement thus varies linearly with x to a maximum of $u_x(b) = 4.8309\text{mm}$ with a uniform stress distribution over the domain of $\sigma_x(x) = 1\text{MPa}$. Defining error estimates ε_u and ε_σ

$$\varepsilon_u = \frac{|u_x(x) - u_{hx}(x)|}{u_x(x)} \tag{3.124}$$

$$\varepsilon_\sigma = \frac{|\sigma_x(x) - \sigma_{hx}(x)|}{\sigma_x(x)} \tag{3.125}$$

where the 'h' subscript indicates the solution, an approximation to the exact value which is expected to improve with h-adaptive mesh refinement.

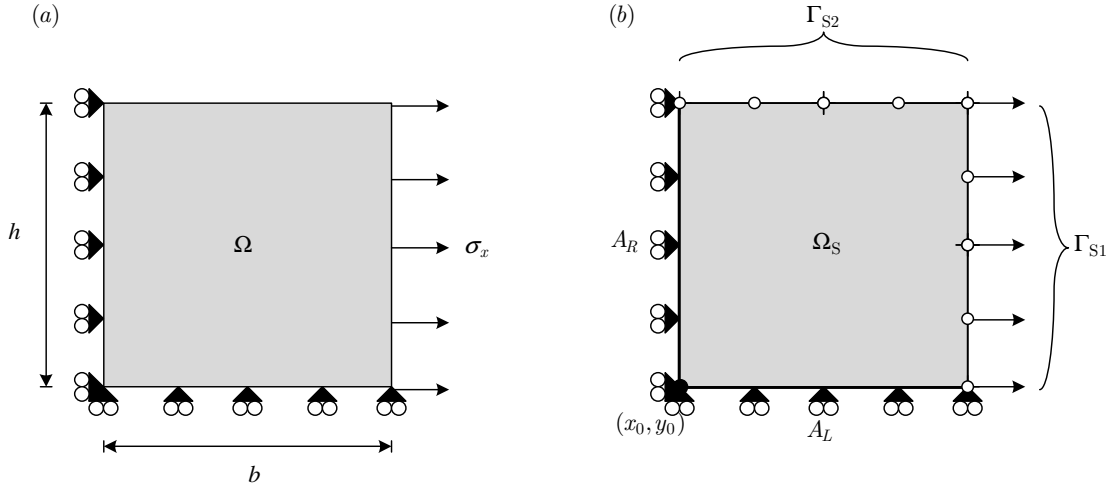

Figure 71. (a) Domain subject to uniaxial stress and (b) the SBFEM model

The discretised portions of the mesh are defined by configuration of elements on Γ_{S1} and Γ_{S2} ranging from 1 to 5 elements each. Representative samples of $u_{hx}(a)$ and $u_{hx}(b)$ are selected to illustrate the effect of the neglecting of the imaginary component in the solution. The errors for selected mesh configurations are illustrated in Figure 72 along with results of the indicator described in equation (3.122).

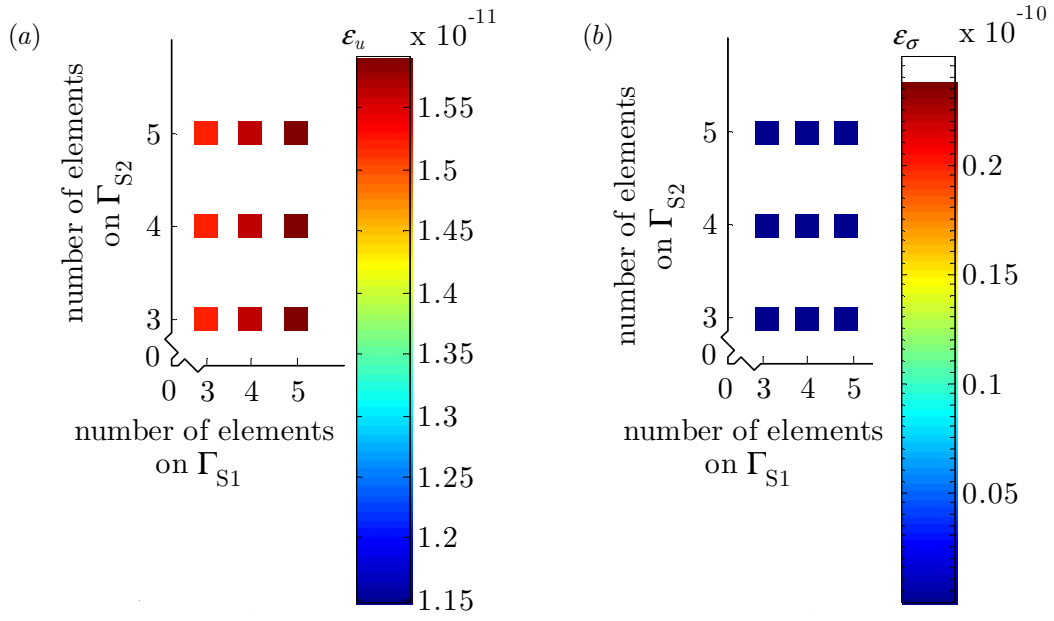

Figure 72. Representative errors (*a*) ε_u and (*b*) ε_σ for sample mesh configurations

3.11 Discussion

3.11.1 Nodal and modal co-dependency

Although not recognised specifically in the literature, equation (3.70) is an important observation as either:

1. the number of modes available in describing the deformation of the domain by modal superposition is restricted by the number of degrees of freedom, rather than, say, because the difference between m and M_{min} is approaching some threshold of numerical accuracy; or

2. the number of degrees of freedom is restricted by the number of modes made available in defining the deformation of the domain by modal superposition, rather than, say, being defined by a mesh generation algorithm dictating a specific number of degrees of freedom.

This may be problematic if the geometry can be described by sufficiently few

degrees of freedom. Typically $n \geq 6$ as the geometry must be defined by a minimum of three geometric lines, which themselves must be modelled by a minimum of one linear element with four degrees of freedom each, as illustrated by Figure 73.

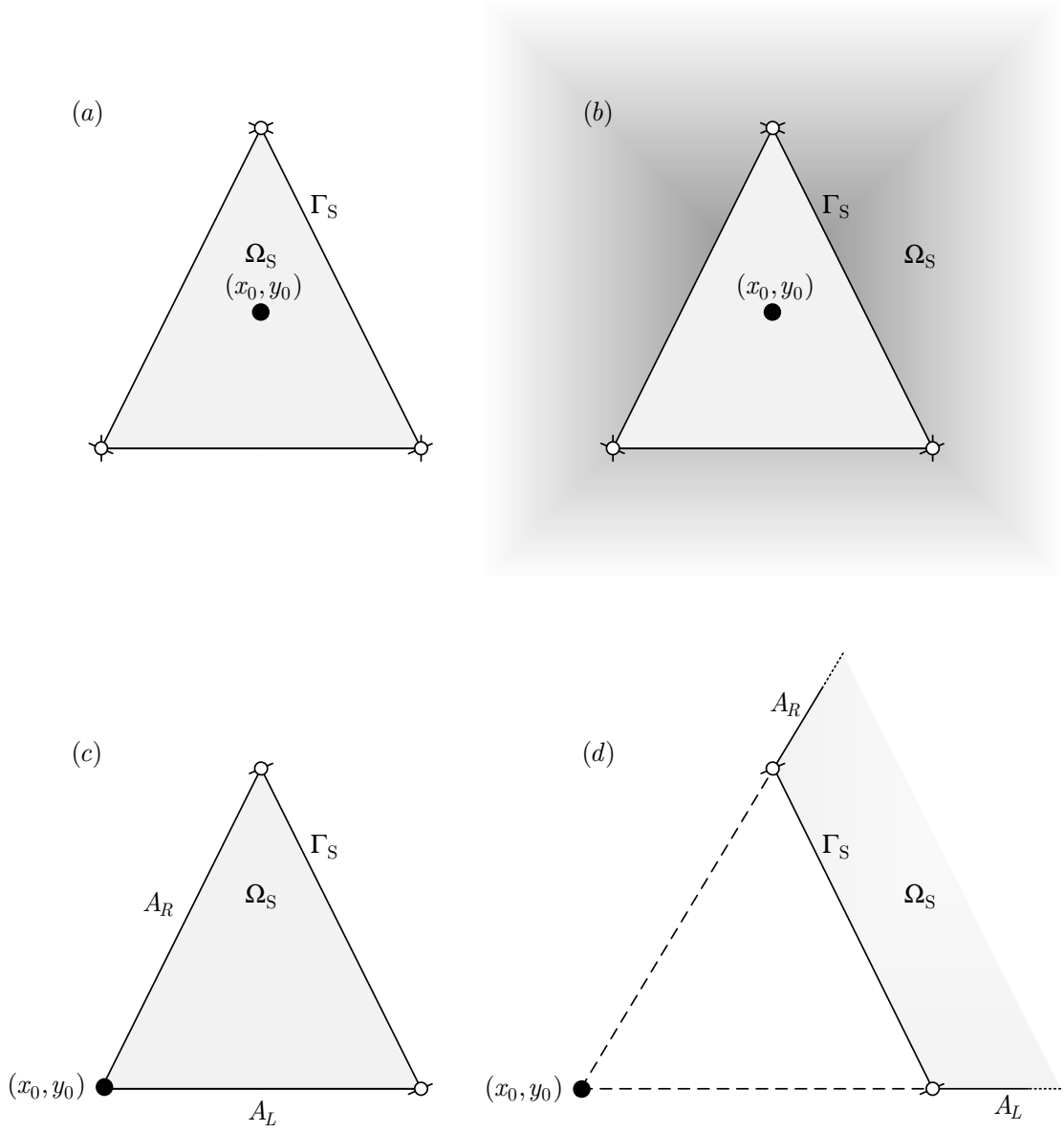

Figure 73. (a) Bounded and (b) unbounded domains with $n = 6$; (c) Bounded and (d) unbounded domains with side faces with $n = 4$

However, with the use of side faces, it is possible to define domains in which

$n = 4$. As an *a priori* knowledge of $M_{\min}$ is unlikely, for small n, it cannot be assumed that n modes are sufficient to model the solution by modal superposition. One solution to this problem is to adaptively refine the mesh (Deeks and Wolf, 2005), introducing additional degrees of freedom and thus increasing the number of modes contributing to the solution. This approach should be undertaken with caution as it should be noted that while the local refinement of the mesh may improve the geometric representation of the domain, if n increases greatly, then the distinction between the modes reduces (Appendix B) as the eigenvectors defining the mode shapes approach becoming parallel.

3.11.2 Applications of the SBFEM

This assessment of the SBFEM confirms its suitability to applications to fracture mechanics. The ability of the method to capture the dominating crack-opening mode facilitates its improved accuracy over the BEM. The accuracy of the new semi-discontinuous scaled boundary finite element has been verified as its impact on the quality of results is of the order of magnitude associated with computer error. Thus, this element is available for use in later work in which the semi-discontinuous property is required.

The results in Figure 68 confirm the known issues relating to the parallelisation of the eigenvectors due to increased mesh refinements may result in poor interior displacements. However, as demonstrated in Figure 69, increased mesh denisity alone does not dictate poor results. Figure 69(b) shows that even for a fine mesh where $n = 240$, good boundary and interior displacements can be achieved. Thus, the poor results in this case may be attributed more towards the slender aspect ratio of the problem than its high

mesh density, as shown in Figure 68(b). So, as expected, the trends in Figure 70 illustrate the effects of both mesh density and aspect ratio on $\mathbf{c}$.

This is likely to be caused by the ill-conditioning of $\mathbf{\Phi}$ as used in the calculation of $\mathbf{c}$ in equation (3.91) owing to the numerical difficulties in representing the necessary displacement in exactly n modes. Preliminary analysis suggests that significant imaginary components of c_j occur where the condition number $\kappa(\mathbf{\Phi}) \approx 10^6$ or greater, although a high condition number is not necessarily indicative of significant imaginary components in $\mathbf{c}$.

In Figure 72 it can be seen that displacement and stress errors are acceptably low ($\sim 10^{-11}$ and $\sim 10^{-10}$ respectively). However, results not shown here for low element configurations (with fewer than 3 elements on each discretised edge) resulted in poor recovered stresses ($\sim 10^{-1}$). Further examination of this point is recommended.

3.12 Literature review

The SBFEM was predated by the infinitesimal finite-element cell method (Wolf and Song, 1995), and later the consistent infinitesimal finite-element cell method (Wolf and Song, 1995), although all are evolutions of the same method. However, the involved mathematics behind the original mechanical-based derivation of the SBFEM in these publications may have contributed to its slow uptake by other engineering researchers. In efforts to raise its awareness and to demonstrate its versatility as a tool for computing the dynamic stiffness of an unbounded domain, the method was re-derived. By means of a weighted residual approach, a displacement formulation in the frequency domain was derived for general problems in elastodynamics in three dimensions (Song and Wolf, 1998). The inclusion of body loads was then

addressed and the two derivations summarised for the SBFEM in two and three dimensions for bounded and unbounded domains (Song and Wolf, 1998).

Two 'primer papers' consolidated the progress of the SBFEM, describing in detail the method by the comparison of both derivations with an example application and solution. First, the method was formulated using a weighted residual approach, and then re-derived using a mechanical-based approach to reproduce the same governing equation (Wolf and Song, 2000). (This is the equivalent of equation (3.45) here, although in the present (static) work, there are no terms relating to a dynamic mass matrix.) This preceded a summary of solution procedures (Song and Wolf, 2000), illustrated by a four-degree of freedom worked example using side faces, similar to that illustrated in Figure 73(d), geometrically the simplest problem possible for the SBFEM to model.

A third derivation of the method was presented (Deeks and Wolf, 2002a). This formulation took a virtual work-based approach, comparing the formulation of the SBFEM in with that of an accompanying formulation of the FEM. Highlighting their similarities, this increased the accessibility of the method to researchers with a background in solid mechanics. Axisymmetric modelling and the application of Neumann boundary conditions on side faces were also addressed, along with the use of domain substructuring and multiple scaling centres. A method of prescribing Dirichlet boundary conditions on side faces followed (Deeks, 2004) . For examples such as those found in the present work in which displacement constraints are restricted to $u_x = 0$ or $u_y = 0$, it was demonstrated that a displacement constraint could be applied to a side face in much the same way as other nodal displacement constraints by removing the appropriate degree of freedom from the stiffness matrix. In addition, the appropriate mode, corresponding to the x- or y-direction rigid

body translation, must be removed too. Non-zero displacement boundary conditions were also addressed.

Some aspects of the virtual work approach by Deeks and Wolf are borrowed in the present work. However, here, there is a greater emphasis on both the form of the solution in terms of modal superposition, and the limitations of such a form.

The SBFEM offers C_0 displacement continuity between neighbouring elements as the solution uses the continuous shape functions for element interpolation. However, as the stress recovery requires the derivative of the shape functions, continuity of stresses is not maintained between neighbouring elements. The application of the *superconvergent patch recovery* technique (Zienkiewicz and Zhu, 1992a) (Zienkiewicz and Zhu, 1992b) was introduced (Deeks and Wolf, 2002b), offering an improvement over simple averaging of nodal stresses for inter-element stress smoothing. This helped facilitate the accompanying error estimator based on the 'Z^2' error estimator found commonly in finite element analysis (Zienkiewicz and Zhu, 1987), allowing, for the first time, a direct comparison of the accuracy of stresses recovered by the FEM and SBFEM. The results demonstrated the high accuracy of the SBFEM in the applications combining linear elasticity and semi-infinite domains. This stress recovery technique and error estimator was used to develop a simple *h*-adaptive mesh refinement strategy (Deeks and Wolf, 2005). A *h*-adaptive mesh refinement strategy using a strain energy-based error estimator was demonstrated for use in elastodynamics (Yang *et al.*, 2011). A *p*-adaptive refinement procedure was developed to increase the polynomial order of the elements identified for mesh refinement (Vu and Deeks, 2006).

The convenient modal superposition form of the SBFEM demonstrated its suitability to fracture mechanics (Chidgzey and Deeks, 2005). It was shown that if the scaling centre was coincident with a crack tip the coefficients of modal superposition of the displacement solution and recovered stresses converge to give the coefficients of the Williams expansion (Williams, 1957) estimating the displacements and stresses in its vicinity. The first modes, $j_{K_{\mathrm{I}}}$ and $j_{K_{\mathrm{II}}}$, in the superposition series of the SBFEM solution were identified as crack opening modes which can be used directly to estimate the mode I and mode II stress intensity factors. The next modes j_x and j_y, were identified as rigid body translation modes which can be used directly to estimate the T-stresses. The remaining modes could be used directly to estimate the higher order terms in the expansion. An application to electromagnetism demonstrated similar use of the superposition nature of the solution (Rajan and Raju, 2002).

By introducing an automated method of substructuring around the crack tip modelled by the SBFEM, the remeshing complications often associated with crack propagation in some other numerical methods, such as the FEM, were reduced (Yang, 2006), and was extended to include cohesive cracks (Yang and Deeks, 2007). Dynamic stress intensity factors were calculated using the SBFEM as part of a series in which the static stress intensity factor forms the first term (Yang, 2006).

The SBFEM has been used in coupled methods with different motivations. For example, a coupled FE-SBFEM used the FEM to model a subdomain in the vicinity of a load, with the SBFEM modelling the unbounded far-field (Doherty and Deeks, 2005). As the load increments, the algorithm detects plasticity as it approaches the interface and the FEM subdomain increases in

size at the expense of the SBFEM subdomain, such that the elastic assumption of the far-field can be maintained. With similar motivation, the SBFEM was coupled to a meshless method (Deeks and Augarde, 2007), for applications to geotechnical analysis. A meshless domain models the plastic behaviour of a geotechnical problem, coupled to an SBFEM modelling the far-field as an infinite domain with a linear-elasticity assumption.

With similar motivation to Yang *et al*, but limited to linear elastic fracture mechanics, the SBFEM was coupled to the BEM (Chidgzey *et al.*, 2008). The geometric flexibility of the BEM was used to model a relatively large domain, using the SBFEM to estimate the stress intensity factor and T-stresses. However, results were limited to empirical comparisons and assumptions were made that limit the application of their scheme to certain sets of boundary conditions. As part of the present work, it was found that modelling problems with displacement constraints to the nodes at the junction of the interface and exterior boundary would result in a singular system.

This was addressed by making the system square for such problems and increasing the applicability of the coupled method. Additional equations were computed by extra, non-nodal collocation on the BEM boundary (Bird *et al.*, 2007), and external to the boundary (Bird *et al.*, 2008a). However, the accuracy of the results was shown to be sensitive to the location of the additional BEM collocation points (Bird *et al.*, 2008b), and had a considerable, adverse effect on the condition number of the system. The coupled method was reworked with special consideration of the junction nodes (Bird *et al.*, 2009a). This new formulation ensured the coupled system was square, providing the means for analytical evaluation of the BE-SBFEM rather than empirical evaluation, without the need for additional equations,

negating the ill-effects of additional BEM collocation (Bird *et al.*, 2010). The conditioning of the system was improved by the introduction of a scaling parameter. This work is presented in §4.5.

The coupled BE-SBFEM in its presented form restricts fracture mechanics analysis to problems that offer symmetry about infinitely thin crack faces, or problems in which the entire crack is modelled by the SBFEM. While this may offer solutions to academic problems, the BE-SBFEM was extended to use a BEM domain that uses the DBEM in order to model more general engineering problems. To date, the effects of coupled DBE-SBFEM are described as part of the present work in §5, including the need for a semi-discontinuous scaled boundary finite element (Bird *et al.*, 2009b).

3.13 Conclusion

This chapter has presented a summary of the SBFEM whose novel and desirable semi-analytical properties have been used to model the rapidly-varying stress singularities in the region of a crack tip with great accuracy. Its historical development and that made subsequently by the author has been presented. A new overview of the method's formulation has been presented here with a focus on modal superposition, offering a different and more complete perspective to those found in the literature.

Results in this thesis have been presented with emphasis focused on consistency and comparability; methods demonstrated to improve only the accuracy of specific problems by fine-tuning their configurations are not applied to the general use of the SBFEM throughout the present work.

As part of the present work, the method has been assessed. The necessary

relationship between the number of modes contributing to the solution and the number of degrees of freedom defining the geometry has been highlighted. The impact of neglecting imaginary components from the solution to the eigenvalue problem has been quantified, and has been shown to affect both interior displacements and recovered stresses for cases with fewer than 3 elements per discretised face. The analysis offers scope for further work in which it is expected to relate to the conditioning of the matrix of modal displacement vectors.

Extensions to the SBFEM have been demonstrated and verified. A semi-discontinuous element has been introduced, motivated by the work to be presented in §5.

4 Boundary element-scaled boundary finite element method

4.1 Introduction

In this chapter, the coupled *boundary element-scaled boundary finite element method* (BE-SBFEM) is introduced. As described in earlier chapters, the motivation behind the this coupling is in combining the SBFEM's ability to model crack tip displacements within a loaded system with the BEM's geometric flexibility, providing a tool for analysis of real engineering problems. After a general overview of the strategies behind combining boundary and finite element-based methods, the original derivation of the coupled method is presented. As part of the present work, this method is reformulated to increase its applicability. Further improvements to the numerical stability of the method are presented. The strengths and weaknesses of the BE-SBFEM are assessed.

4.2 Coupling the BEM and FEM

Although based on a boundary integral method, the form of the SBFEM system matrices is more akin to the FEM than the BEM, and the approaches

to their coupling follows that of the coupling the BEM and FEM (BE-FEM), a coupled method well-established in the literature. The displacements and forces at the interface between the BEM and FEM subdomains require consideration. For a homogenous, linear elastic material, such as those considered in the present work, the interface does not describe a physical boundary between two regions within a domain of differing material properties but an artificial boundary introduced merely to separate the subdomains. A physical separation of the two domains cannot, therefore, be permitted and the BEM interface displacement degrees of freedom are coupled to those of the FEM interface, such that there is one unknown displacement per interface degree of freedom. Similarly, the tractions and forces across the interface are assumed continuous and the respective BEM and FEM degrees of freedom are coupled, subject to a direction sign convention. Coupling the BEM and FEM requires the conversion of BEM interface tractions into equivalent FEM nodal forces, or *vice versa*, details of which can be found in Appendix E.

A weakly-coupled, iterative approach is to solve each of the subdomains independently (Elleithy *et al.*, 2001). The BEM subdomain is analysed using its respective method with estimated interface displacements estimated and imposed as boundary conditions. The interface tractions found from its solution are converted into equivalent nodal forces and used in the solution of the FEM subdomain. The interface displacements found in the solution to the FEM used as boundary conditions in the following iteration for the BEM and the process is repeated until convergence. This approach is flexible in its applicability to many a wide range of problems, such as modelling non-homogenous material interfaces. However, for meshes in which the number of BEM degrees of freedom significantly outnumbers those of the FEM subdomain, as found in the present work, this flexibility is achieved at a high

computational cost in which several hundred iterations may be necessary for convergence, and this form of coupling is rejected.

An alternative is the direct coupling of the BEM and FEM displacement degrees of freedom and their respective tractions and forces. The influence matrices described in equation (2.30) can be used to define an equivalent BEM stiffness matrix relating boundary displacements and forces, such as described by the SBFEM stiffness matrix in (3.87). This stiffness matrix can then be coupled directly to that of the FEM subdomain (Leung *et al.*, 1995). However, this approach has two significant drawbacks when applied to the coupled BE-SBFEM. Again, in the present work and in the examples to which it can be applied, the size of the BEM subdomain may, generally, be larger than that of the SBFEM. Thus, the conversion of the BEM tractions into forces will take a significant proportion of computational effort. Secondly, the motivation of the present work includes the use of reanalysis, described in §5.4, in which it is beneficial to maintain the BEM influence matrices rather than convert them into stiffness matrices.

The approach favoured here is to transform the relatively few interface force degrees of freedom into equivalent interface element tractions, which can be done independently of the force degrees of freedom that appear in the rest of the SBFEM subdomain. As it will be shown, the result is a simple coupling with minimal additional computation that lends itself to reanalysis.

With all the approaches outlined in this section, it is important that the forces and tractions across the interface are converted with appropriate consideration of both the internal and external forces acting on a boundary element (Cruse and Osias, 1991). With this in mind, the reformulation of the BE-SBFEM as

part of the present work has been demonstrated to increase the applicability of the method.

4.3 Numerical formulation

4.3.1 Method introduction

The SBFEM is gaining more acknowledgement as a useful numerical method, albeit with some undesirable limitations. The method's ability to model the solution by modal superposition, rather than by some polynomial approximation, makes it suitable for problems with discontinuities and singularities. The BEM is known for its geometric flexibility and suitability to applications to linear elasticity.

The motivation for the coupling of the methods lies in applications to fracture mechanics. By modelling a crack using the SBFEM, the rapidly varying stress fields around the tip (leading to the prediction of crack growth) can be modelled efficiently. However, real engineering domains are unlikely to be as trivial as the examples illustrated in the previous chapter. Rather than use a potentially awkward meshing procedure for the subdivision of domain, the more flexible BEM is used to model the remainder of the problem (Chidgzey *et al.*, 2008). This formulation is repeated here.

As part of the present work, it was identified that the method, as formulated originally in the reference, was limited to certain boundary condition sets. A new formulation is then presented, demonstrating the increase in the applicability of the coupled method, and allowing for the first time, the coupled method to be assessed by its analysis of problems for which there is a known, analytical solution.

4.3.2 Method coupling

The following overview briefly describes the original derivation of coupled BE-SBFEM (Chidgzey *et al.*, 2008). Consistent with previous chapters, subscripts 'B' and 'S' are used to denote the BEM and SBFEM subdomains respectively. Furthermore, the subscript 'I' denotes the interface between subdomains. For simplicity, the derivation focuses on the coupling of two subdomains in two dimensions where a domain Ω is divided into Ω_B and Ω_S, bounded by Γ_B and Γ_S and Γ_I, as illustrated in Figure 74.

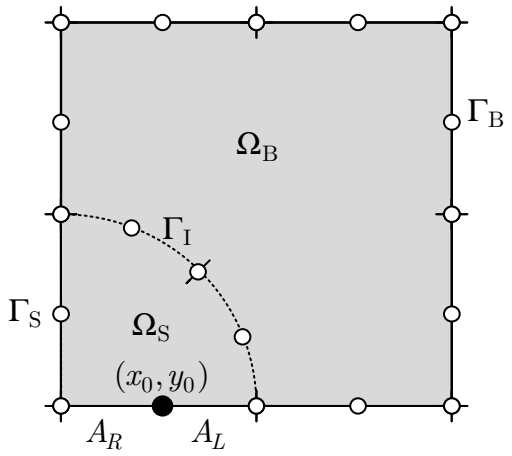

Figure 74. An example domain subdivided into BEM and SBFEM subdomains

Equations (2.30) and (3.87), describing the solutions to Γ_B and Γ_S, can be partitioned into their I, B and S components

$$\begin{bmatrix} \mathbf{H}_{\mathrm{II}} & \mathbf{H}_{\mathrm{IB}} & -\mathbf{G}_{\mathrm{II}} & -\mathbf{G}_{\mathrm{IB}} \\ \mathbf{H}_{\mathrm{BI}} & \mathbf{H}_{\mathrm{BB}} & -\mathbf{G}_{\mathrm{BI}} & -\mathbf{G}_{\mathrm{BB}} \end{bmatrix} \begin{Bmatrix} \mathbf{u}_\mathrm{I} \\ \mathbf{u}_\mathrm{B} \\ \mathbf{t}_\mathrm{I} \\ \mathbf{t}_\mathrm{B} \end{Bmatrix} = \begin{Bmatrix} \mathbf{0} \\ \mathbf{0} \end{Bmatrix} \tag{4.1}$$

$$\begin{bmatrix} \mathbf{K}_{\mathrm{II}} & \mathbf{K}_{\mathrm{IS}} \\ \mathbf{K}_{\mathrm{SI}} & \mathbf{K}_{\mathrm{SS}} \end{bmatrix} \begin{Bmatrix} \mathbf{u}_\mathrm{I} \\ \mathbf{u}_\mathrm{S} \end{Bmatrix} = \begin{Bmatrix} \mathbf{p}_\mathrm{I} \\ \mathbf{p}_\mathrm{S} \end{Bmatrix} \tag{4.2}$$

As explained in Appendix E, the transformation matrix $\mathbf{M}$ relating nodal forces and tractions is introduced

$$\mathbf{M}_\mathrm{I}\mathbf{t}_\mathrm{I} = -\mathbf{p}_\mathrm{I} \tag{4.3}$$

where the negative sign is introduced to ensure compatibility across the interface (Becker, 1992). Combining equations (4.1) to (4.3) gives the system of linear equations

$$\begin{bmatrix} \mathbf{K}_\mathrm{II} & \mathbf{K}_\mathrm{IS} & \mathbf{M}_\mathrm{I} & \mathbf{0} & \mathbf{0} \\ \mathbf{K}_\mathrm{SI} & \mathbf{K}_\mathrm{SS} & \mathbf{0} & \mathbf{0} & \mathbf{0} \\ \mathbf{H}_\mathrm{II} & \mathbf{0} & -\mathbf{G}_\mathrm{II} & \mathbf{H}_\mathrm{IB} & -\mathbf{G}_\mathrm{IB} \\ \mathbf{H}_\mathrm{BI} & \mathbf{0} & -\mathbf{G}_\mathrm{BI} & \mathbf{H}_\mathrm{BB} & -\mathbf{G}_\mathrm{IB} \end{bmatrix} \begin{Bmatrix} \mathbf{u}_\mathrm{I} \\ \mathbf{u}_\mathrm{S} \\ \mathbf{t}_\mathrm{I} \\ \mathbf{u}_\mathrm{B} \\ \mathbf{t}_\mathrm{B} \end{Bmatrix} = \begin{Bmatrix} \mathbf{0} \\ \mathbf{p}_\mathrm{S} \\ \mathbf{0} \\ \mathbf{0} \\ \mathbf{0} \end{Bmatrix} \tag{4.4}$$

Boundary conditions are applied, and then by separating known and unknown terms in the usual manner, equation (4.4) can be rearranged to yield a square system of linear equations in the form

$$\mathbf{A}\mathbf{x} = \mathbf{b} \tag{4.5}$$

4.4 Formulation assessment

For the purposes of disambiguity, it should be noted that, unless otherwise stated, the following assessments of and extensions to the BE-SBFEM detailed in the remainder of this chapter are as direct result of work undertaken by the author.

4.4.1 Limited boundary conditions

One limiting factor in this approach is the lack of distinction between forces acting on the *junction* nodes, the nodes that exist on both the interface and the boundary (Cruse and Osias, 1991), as illustrated in Figure 75. The forces acting on these nodes are given by the external nodal forces acting on the adjoining SBFEM elements (or side faces), and the contributions to the nodal tractions from each of the adjoining BEM and interface elements. In forming

the coupled BE-SBFEM in this manner, an assumption is made that there are no external forces or tractions acting on the junction nodes (Bird *et al.*, 2007), i.e. the forces acting on those nodes can be defined fully by the transformed tractions acting internally through the interface only.

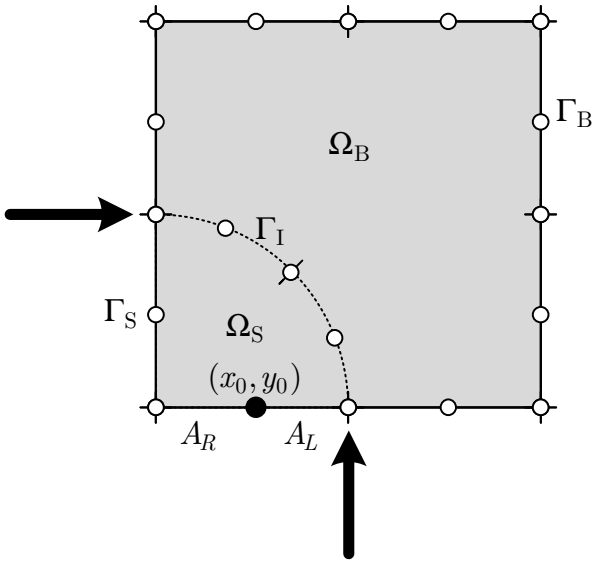

Figure 75. Boundary conditions imposed on the junction nodes are restricted

4.4.2 Matrix conditioning

In almost all mechanical problems using typical engineering materials, it is likely that the traction coefficients $\mathbf{t}$ will be several orders of magnitude larger than the displacement coefficients $\mathbf{u}$ when using conventional SI units. Without taking this into consideration, the general approach outlined above may lead to conditioning problems of $\mathbf{A}$.

4.5 New numerical formulation

The following overview briefly describes a new derivation of coupled BE-SBFEM (Bird *et al.*, 2010), formulated as part of the current work, providing means to analyse problems with boundary condition sets restricted by the

original formulation (Chidgzey *et al.*, 2008), without the need for additional collocation points (Bird *et al.*, 2008b). The additional subscript 'J' denotes *junction* degrees of freedom, i.e. those associated with the nodes found at the junction nodes, denoted by Γ_{J}, as in Figure 76. In the illustrated example, Γ_{B} includes use of discontinuous boundary elements in order to highlight later the additional considerations required when using these elements over those necessary when using just continuous boundary elements.

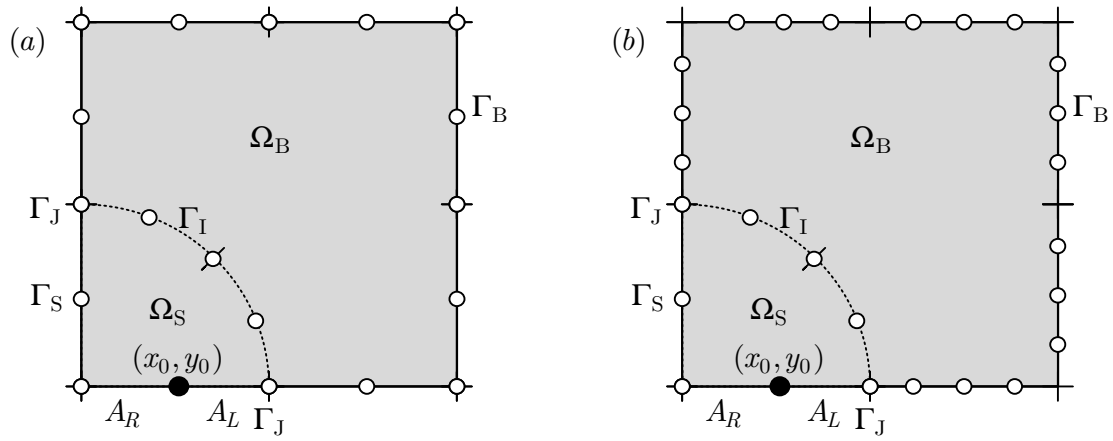

Figure 76. An example domain subdivided into BEM and SBFEM subdomains using (a) continuous boundary elements and (b) discontinuous boundary elements

As before, equations (2.30) and (3.87) are be partitioned into their I, B and S components, but this time includes partitioning of their J components too

$$\begin{bmatrix} \mathbf{H}_{\mathrm{JJ}} & \mathbf{H}_{\mathrm{JI}} & \mathbf{H}_{\mathrm{JB}} \\ \mathbf{H}_{\mathrm{IJ}} & \mathbf{H}_{\mathrm{II}} & \mathbf{H}_{\mathrm{IB}} \\ \mathbf{H}_{\mathrm{BJ}} & \mathbf{H}_{\mathrm{BI}} & \mathbf{H}_{\mathrm{BB}} \end{bmatrix} \begin{Bmatrix} \mathbf{u}_{\mathrm{J}} \\ \mathbf{u}_{\mathrm{I}} \\ \mathbf{u}_{\mathrm{B}} \end{Bmatrix} = \begin{bmatrix} \mathbf{G}_{\mathrm{JJ}} & \mathbf{G}_{\mathrm{JI}} & \mathbf{G}_{\mathrm{JB}} \\ \mathbf{G}_{\mathrm{IJ}} & \mathbf{G}_{\mathrm{II}} & \mathbf{G}_{\mathrm{IB}} \\ \mathbf{G}_{\mathrm{BJ}} & \mathbf{G}_{\mathrm{BI}} & \mathbf{G}_{\mathrm{BB}} \end{bmatrix} \begin{Bmatrix} \mathbf{t}_{\mathrm{J}} \\ \mathbf{t}_{\mathrm{I}} \\ \mathbf{t}_{\mathrm{B}} \end{Bmatrix} \tag{4.6}$$

$$\begin{bmatrix} \mathbf{K}_{\mathrm{JJ}} & \mathbf{K}_{\mathrm{JI}} & \mathbf{K}_{\mathrm{JS}} \\ \mathbf{K}_{\mathrm{IJ}} & \mathbf{K}_{\mathrm{II}} & \mathbf{K}_{\mathrm{IS}} \\ \mathbf{K}_{\mathrm{SJ}} & \mathbf{K}_{\mathrm{SI}} & \mathbf{K}_{\mathrm{SS}} \end{bmatrix} \begin{Bmatrix} \mathbf{u}_{\mathrm{J}} \\ \mathbf{u}_{\mathrm{I}} \\ \mathbf{u}_{\mathrm{S}} \end{Bmatrix} = \begin{Bmatrix} \mathbf{P}_{\mathrm{J}} \\ \mathbf{P}_{\mathrm{I}} \\ \mathbf{P}_{\mathrm{S}} \end{Bmatrix} \tag{4.7}$$

The nodal forces on Γ_{S}, Γ_{I} and Γ_{J} are decomposed into their internal and external components

$$\begin{aligned}\mathbf{P}_{\mathrm{J}} &= \mathbf{P}_{\mathrm{Jint}} + \mathbf{P}_{\mathrm{Jext}} \\ \mathbf{P}_{\mathrm{I}} &= \mathbf{P}_{\mathrm{Iint}} + \mathbf{P}_{\mathrm{Iext}} \\ \mathbf{P}_{\mathrm{S}} &= \mathbf{P}_{\mathrm{Sint}} + \mathbf{P}_{\mathrm{Sext}}\end{aligned} \tag{4.8}$$

As the interface Γ_{I} is defined *exclusive* of the junction nodes and therefore is entirely internal, there are no external forces so

$$\mathbf{P}_{\mathrm{Iext}} = \mathbf{0} \tag{4.9}$$

As Γ_{S} is also defined *exclusive* of the junction nodes and therefore is entirely external (on the boundary), there are no internal forces so

$$\mathbf{P}_{\mathrm{Sint}} = \mathbf{0} \tag{4.10}$$

The transformation matrix $\mathbf{M}_{\mathrm{I}}$ is also partitioned and is given by

$$\begin{bmatrix} \mathbf{M}_{\mathrm{JJ}} & \mathbf{M}_{\mathrm{JI}} \\ \mathbf{M}_{\mathrm{IJ}} & \mathbf{M}_{\mathrm{II}} \end{bmatrix} \begin{Bmatrix} \mathbf{t}_{\mathrm{J}} \\ \mathbf{t}_{\mathrm{I}} \end{Bmatrix} = \begin{Bmatrix} -\mathbf{P}_{\mathrm{Jint}} \\ -\mathbf{P}_{\mathrm{Iint}} \end{Bmatrix} \tag{4.11}$$

The coupled BE-SBFEM is therefore given by

$$\begin{bmatrix} \mathbf{K}_{\mathrm{JJ}} & \mathbf{K}_{\mathrm{JI}} & \mathbf{K}_{\mathrm{JS}} & \mathbf{M}_{\mathrm{JJ}} & \mathbf{M}_{\mathrm{JI}} & \mathbf{0} & \mathbf{0} \\ \mathbf{K}_{\mathrm{IJ}} & \mathbf{K}_{\mathrm{II}} & \mathbf{K}_{\mathrm{IS}} & \mathbf{M}_{\mathrm{IJ}} & \mathbf{M}_{\mathrm{II}} & \mathbf{0} & \mathbf{0} \\ \mathbf{K}_{\mathrm{SJ}} & \mathbf{K}_{\mathrm{SI}} & \mathbf{K}_{\mathrm{SS}} & \mathbf{0} & \mathbf{0} & \mathbf{0} & \mathbf{0} \\ \mathbf{H}_{\mathrm{JJ}} & \mathbf{H}_{\mathrm{JI}} & \mathbf{0} & -\mathbf{G}_{\mathrm{JJ}} & -\mathbf{G}_{\mathrm{JI}} & \mathbf{H}_{\mathrm{JB}} & -\mathbf{G}_{\mathrm{JB}} \\ \mathbf{H}_{\mathrm{IJ}} & \mathbf{H}_{\mathrm{II}} & \mathbf{0} & -\mathbf{G}_{\mathrm{IJ}} & -\mathbf{G}_{\mathrm{II}} & \mathbf{H}_{\mathrm{IB}} & -\mathbf{G}_{\mathrm{IB}} \\ \mathbf{H}_{\mathrm{BJ}} & \mathbf{H}_{\mathrm{BI}} & \mathbf{0} & -\mathbf{G}_{\mathrm{BJ}} & -\mathbf{G}_{\mathrm{BI}} & \mathbf{H}_{\mathrm{BB}} & -\mathbf{G}_{\mathrm{BB}} \end{bmatrix} \begin{Bmatrix} \mathbf{u}_{\mathrm{J}} \\ \mathbf{u}_{\mathrm{I}} \\ \mathbf{u}_{\mathrm{S}} \\ \mathbf{t}_{\mathrm{J}} \\ \mathbf{t}_{\mathrm{I}} \\ \mathbf{u}_{\mathrm{B}} \\ \mathbf{t}_{\mathrm{B}} \end{Bmatrix} = \begin{Bmatrix} \mathbf{P}_{\mathrm{Jext}} \\ \mathbf{0} \\ \mathbf{P}_{\mathrm{Sext}} \\ \mathbf{0} \\ \mathbf{0} \\ \mathbf{0} \end{Bmatrix} \tag{4.12}$$

Once again, boundary conditions are applied, and then by separating known and unknown terms in the usual manner, equation (4.12) can be rearranged to yield a square system of linear equations in the form

$$\mathbf{A}\mathbf{x} = \mathbf{b} \tag{4.13}$$

where $\mathbf{x}$ is the vector of unknown displacements and tractions.

4.6 Matrix scaling

By selecting an appropriate value for a scale factor Ψ_1, and introducing it into the BEM system matrix

$$\mathbf{Hu} = \Psi_1 \mathbf{G} \frac{\mathbf{t}}{\Psi_1} \tag{4.14}$$

it has been shown that the displacement and scaled traction influence matrices, $\mathbf{H}$ and $\Psi_1\mathbf{G}$, are of the same order (Bird *et al.*, 2009a), improving matrix conditioning. Thus, equation (4.12) is rewritten

$$\begin{bmatrix} \mathbf{K}_{JJ} & \mathbf{K}_{JI} & \mathbf{K}_{JS} & \Psi_1\mathbf{M}_{JJ} & \Psi_1\mathbf{M}_{JI} & \mathbf{0} & \mathbf{0} \\ \mathbf{K}_{IJ} & \mathbf{K}_{II} & \mathbf{K}_{IS} & \Psi_1\mathbf{M}_{IJ} & \Psi_1\mathbf{M}_{II} & \mathbf{0} & \mathbf{0} \\ \mathbf{K}_{SJ} & \mathbf{K}_{SI} & \mathbf{K}_{SS} & \mathbf{0} & \mathbf{0} & \mathbf{0} & \mathbf{0} \\ \mathbf{H}_{JJ} & \mathbf{H}_{JI} & \mathbf{0} & -\Psi_1\mathbf{G}_{JJ} & -\Psi_1\mathbf{G}_{JI} & \mathbf{H}_{JB} & -\Psi_1\mathbf{G}_{JB} \\ \mathbf{H}_{IJ} & \mathbf{H}_{II} & \mathbf{0} & -\Psi_1\mathbf{G}_{IJ} & -\Psi_1\mathbf{G}_{II} & \mathbf{H}_{IB} & -\Psi_1\mathbf{G}_{IB} \\ \mathbf{H}_{BJ} & \mathbf{H}_{BI} & \mathbf{0} & -\Psi_1\mathbf{G}_{BJ} & -\Psi_1\mathbf{G}_{BI} & \mathbf{H}_{BB} & -\Psi_1\mathbf{G}_{BB} \end{bmatrix} \begin{Bmatrix} \mathbf{u}_J \\ \mathbf{u}_I \\ \mathbf{u}_S \\ \frac{\mathbf{t}_J}{\Psi_1} \\ \frac{\mathbf{t}_I}{\Psi_1} \\ \mathbf{u}_B \\ \frac{\mathbf{t}_B}{\Psi_1} \end{Bmatrix} = \begin{Bmatrix} \mathbf{P}_J \\ \mathbf{0} \\ \mathbf{P}_S \\ \mathbf{0} \\ \mathbf{0} \\ \mathbf{0} \end{Bmatrix} \tag{4.15}$$

where the 'ext' subscripts have been dropped for brevity, and by the application of boundary conditions, reduces once more to equation (4.13), but now $\mathbf{x}$ is the vector of unknown displacements and *scaled* tractions.

A range of test problems were analysed, including fracture mechanics examples described later in this chapter, and other suitable applications of the coupled method (Appendix G). The impact of Ψ_1 is problem and parametric-specific, but the trend illustrated in Figure 77 is indicative for these examples. Thus, throughout the work presented here $\Psi_1 = 10^6$.

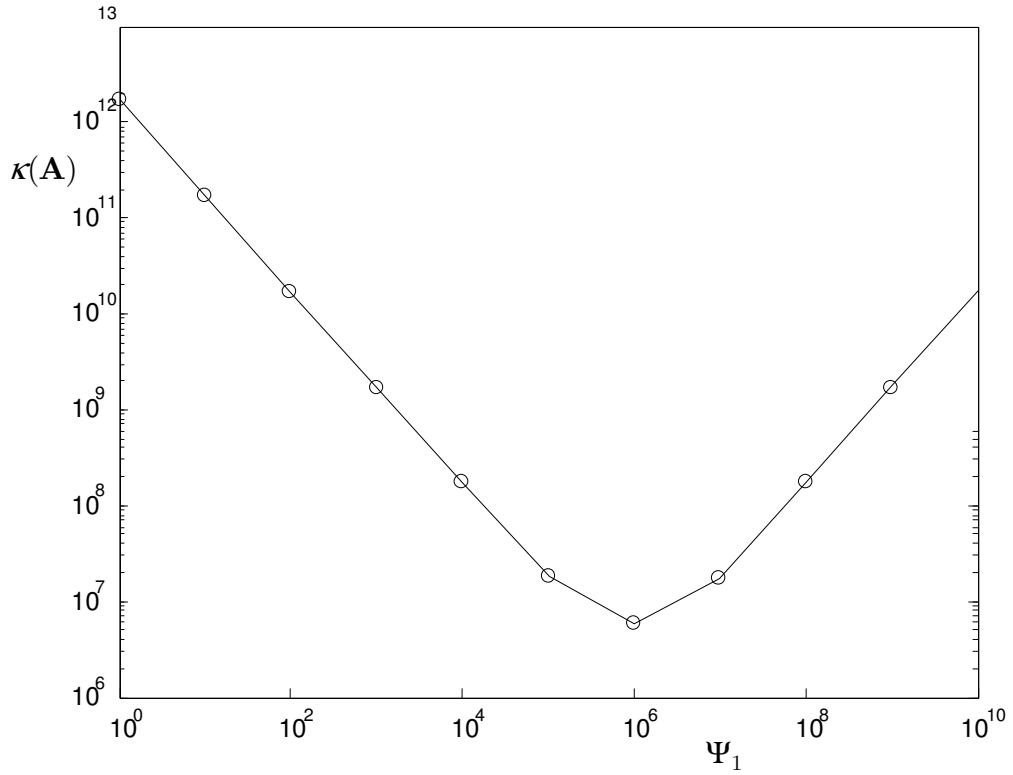

Figure 77. Illustration of the trend found by varying the scaling factor Ψ_1 on system matrix condition number $\kappa(\mathbf{A})$ for fracture mechanics examples in §4.7

4.7 Example applications to fracture mechanics

The approach outlined in §4.5 differs from the original formulation (Chidgzey *et al.*, 2008), in that it can now be seen $\mathbf{P}_{\text{Jext}}$ is not restricted to $\mathbf{0}$. Consequentially, the BE-SBFEM can now be applied to the same benchmark problem used in §2.10 and contributions to the error include the sample points on the sidefaces used in §3.9.

For the examples in this chapter

$$\Omega = \Omega_{\text{B}} \cup \Omega_{\text{S}} \tag{4.16}$$

$$\Gamma = \Gamma_{\text{B}} \cup \Gamma_{\text{S}} \cup \Gamma_{\text{I}} \cup A_{\text{R}} \cup A_{\text{L}} \tag{4.17}$$

and the scaling centre of Ω_{S} is coincident with the crack tip.

4.7.1 Through crack in an infinite plate example 1

The BE-SBFEM is used to model the crack tip described in §2.10. With reference to Figure 51(c), the dimensions of Ω are $b \times h$, and the boundary is subdivided into portions of boundary $\Gamma_{\tilde{u}}$ with known displacement boundary conditions (red nodes), and portions of boundary Γ_u with displacements to be found as part of the solution (white nodes). This example is adapted from results published by Bird *et al.* (Bird *et al.*, 2010).

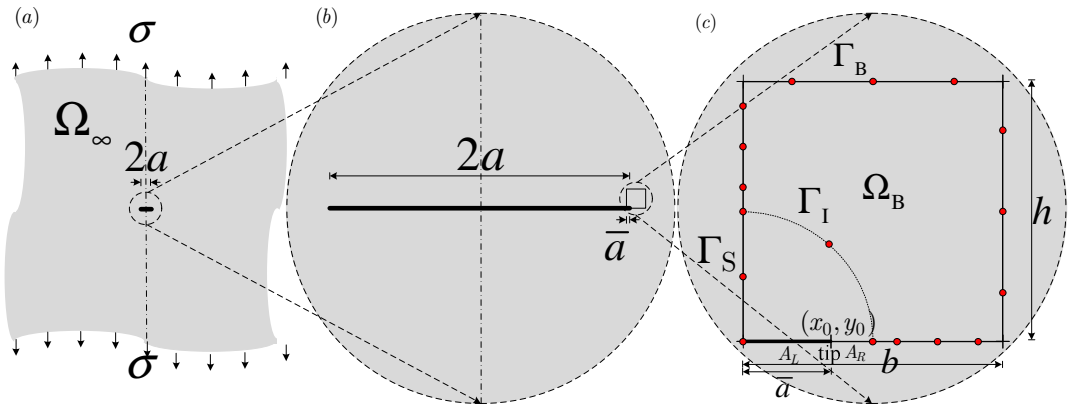

Figure 78. BE-SBFEM analysis of (a) through crack in an infinite plate, (b) the section of the domain modelled, and (c) the mesh where red and white nodes indicate $\Gamma_{\tilde{u}}$ and Γ_u

Convergence characteristics of the SBFEM stress intensity factor errors are illustrated in Figure 79 using the same uniform mesh refinement strategy as in previous chapters.

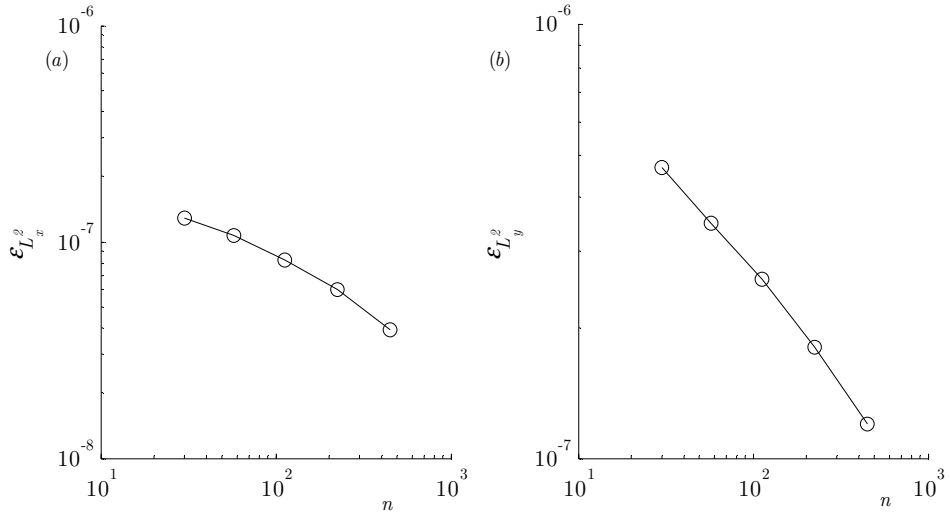

Figure 79 Convergence characteristics of global error estimators $(a)\,\boldsymbol{\varepsilon}_{L^2x}$ and $(b)\,\boldsymbol{\varepsilon}_{L^2y}$; these results are adapted from those first published by Bird *et al* (Bird *et al.*, 2010)

4.7.2 Through crack in an infinite plate example 2

The trivial examples used to illustrate the accuracy and efficiency of the methods described in this and previous chapters are selected for consistency and ease of comparison with other published results. However, the meshing requirements of a complex domain (such as those with voids and notches) proves more arduous for the SBFEM than an equivalent BEM mesh requirement. The line-of-sight requirement in real engineering domains may necessitate subdivision and introduction of many interior interface elements, and the slender aspect ratios of the subdomains may reduce the uniqueness of the eigenvalue solution and thus introduce computational errors.

But because the domains of these benchmark problems exist within a continuous medium, their boundaries do not represent traction-free or exposed surfaces. Thus, while the domains have been defined regularly, allowing comparison with literature results, their respective domain geometries have been largely arbitrary. With reference to Figure 80, the considerably irregular

shape of the example prevents its comparison with literature results, but demonstrates the robustness of the coupled method and its versatile applicability. As before, the boundary is subdivided into portions of boundary $\Gamma_{\tilde{u}}$ with known displacement boundary conditions (red nodes), and portions of boundary Γ_u with displacements to be found as part of the solution (white nodes). This example is adapted from results published by Bird *et al.* (Bird *et al.*, 2010).

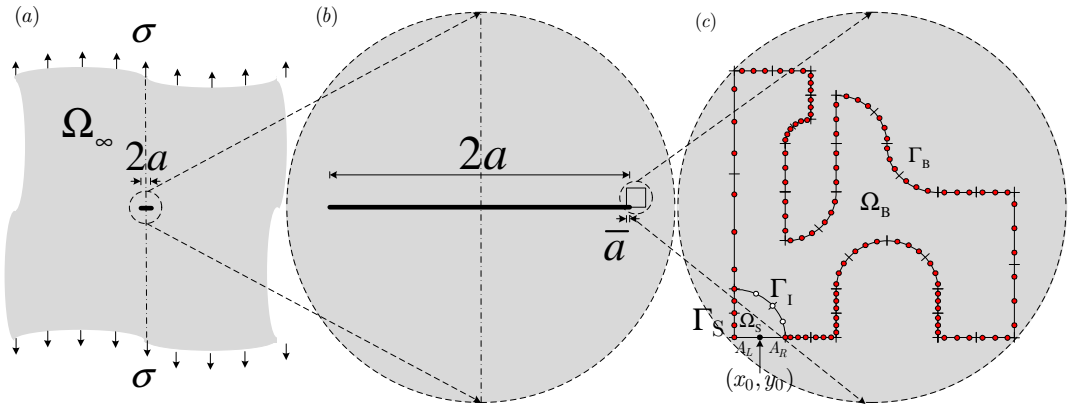

Figure 80. BE-SBFEM of (a) through crack in an infinite plate, (b) the section of the domain modelled, and (c) the mesh where red and white nodes indicate $\Gamma_{\tilde{u}}$ and Γ_u

Convergence characteristics of the SBFEM stress intensity factor errors are illustrated in Figure 81 using the same uniform mesh refinement strategy as in previous chapters.

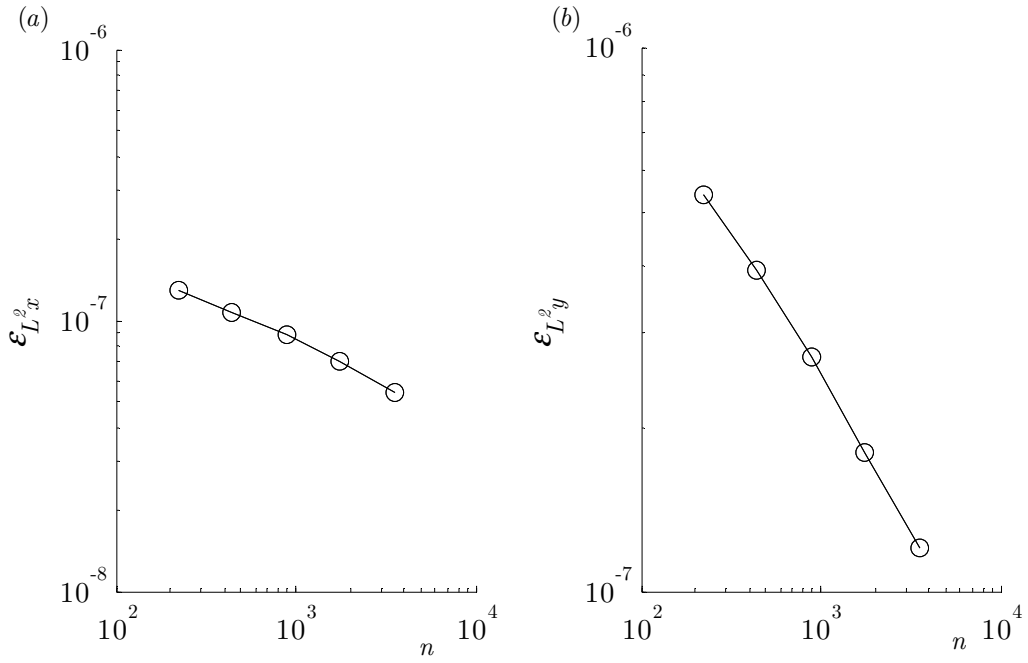

Figure 81 Convergence characteristics of BE-SBFEM; these results are adapted from those first published by Bird *et al* (Bird *et al.*, 2010)

4.8 Discussion

4.8.1 Discontinuous junction elements

It should be noted that if a discontinuous BEM mesh is used, such as illustrated in Figure 76(b), then additional considerations must be made. There exists a collocation point (the junction node) upon an element to which it does not contribute to any geometric definition. Just as can be observed when non-nodal collocation points are used, such as in providing additional equations to form a square system (Bird *et al.*, 2008b), when integrating from the junction node over this element, the singular integrals discussed in §2.5.3 and §2.5.4 are present. In the example illustrated in Figure 82, singularities would be observed when collocating at the junction node at the local coordinate $\eta_{\mathrm{J}} = 1$, in addition to those observed when collocating at η_1, η_2 and η_3.

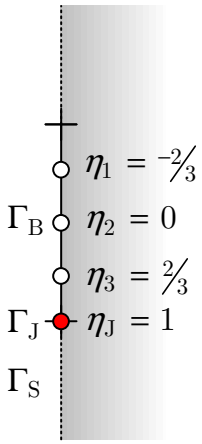

Figure 82. Junction node on a discontinuous boundary element

4.8.2 Original method formulation limitations

The original formulation of the BE-SBFEM (Chidgzey *et al.*, 2008) demonstrated a proof of concept. As part of present work, method limitations were identified (in addition to limitations in its implementation and a poor approach to testing[vi]). For applications of the BE-SBFEM to problems requiring displacement constraints on the junction nodes, the resulting system matrix was shown to be under-defined.

As an intermediate solution, additional equations were added to the system until the matrix was square (Bird *et al.*, 2008b). These additional equations were computed by further collocation of the boundary integral equation at non-nodal points around Γ_B ensuring uniqueness, and with each collocation point, up to two new equations could be computed. However, the method was shown to exhibit strong instability issues depending on the location of the additional collocation point or points resulting in poor-conditioning of the

[vi] Not discussed here. Further discussions of the original formulation can be found in the more general discussion of the approach to method implementation in §7

system and a consequent effect on the numerical accuracy.

4.8.3 New method formulation

The new approach presented here has overcome this issue by the distinction of boundary conditions at the junction nodes. In conjunction with the consideration of a discontinuous BEM mesh, this new approach provides the means to model the same benchmark problems used throughout this thesis.

As expected, the SBFEM subdomain provides accurate displacement results in the vicinity of the crack tip. The coupled method does not converge at the same rate as the SBFEM alone owing to consistent employment of the uniform mesh refinement used elsewhere. This is more evident in §4.7.2, but to be expected as many of the subdivided BEM elements serve more to increase n than they do to reduce $\boldsymbol{\varepsilon}_{K_{\mathrm{I}}}$ and $\boldsymbol{\varepsilon}_{K_{\mathrm{II}}}$. An improved mesh refinement technique can improve convergence considerably, but is not included here for reasons discussed in 2.12.2.

While the coupled BE-SBFEM has demonstrated its suitability to fracture mechanics, a major limiting factor is its reliance on symmetry, a property that cannot be assumed for general engineering domains. This can be overcome by domain subdivision in a way similar to that demonstrated in §2.10.2. But, as with the BEM, while more interface nodes provides more degrees of freedom for the errors analysis characterising the method, they provide little benefit as an analysis tool, rather a hindrance in terms of meshing requirements and so an alternative strategy is sought for problems where symmetry cannot be assumed.

4.8.4 Scaling factor

The effect of Ψ_1 is problem-specific, varying with parametric permutations, particularly with varying magnitude of applied loads and domain properties. This is to be expected as it is precisely this variation within real engineering problems that motivates the need for the scaling factor. An optimum value for Ψ_1 may not be known *a priori*, but an appropriate value can be based on the Young's modulus and the size and type of the domain under analysis. The impact of an improved condition number depends on the implementation of the method.

4.9 Conclusion

This chapter has presented a summary of the coupled BE-SBFEM. What began as a partially-explored proof of concept has, through the present work, been assessed and reworked. The evolved method offers greater flexibility and with this increasing in applicability provides greater confidence in the results obtained.

By introducing a scaling parameter, the conditioning of the system matrix has been shown to reduce by several orders of magnitude, allowing its solution without the need for routines to solve ill-conditioned matrixes.

As an intermediate step towards the coupling of the Dual BEM with the SBFEM, these extensions to the BE-SBFEM have been demonstrated and verified by examples, both here and in other publications by the author. For the first time, the evaluation of the BE-SBFEM has been made by comparison with analytical solutions, rather than by empirical examples and have shown little deviation from the single-domain SBFEM equivalents. Thus it has been

demonstrated any inaccuracies of a BEM subdomain have little bearing of the high accuracy of its coupled SBFEM counterpart and that the benefits of each method's respective properties can be explored for use in an efficient and accurate coupled algorithm. The BE-SBFEM has also been shown to model domains, representative of real engineering problems, to which the SBFEM alone may not be suited.

5 Dual boundary element-scaled boundary finite element method

5.1 Introduction

In this chapter, the coupled *dual boundary element-scaled boundary finite element method* (DBE-SBFEM) is introduced and assessed. The DBE-SBFEM has been developed with the same motivation as for the BE-SBFEM. By modelling a crack using the SBFEM, the rapidly varying stress fields around the tip can be estimated efficiently, leaving the more flexible BEM to model the remainder of the problem. By introducing the DBEM into the coupled method, its applicability increases. Unlike the BE-SBFEM, the DBE-SBFEM can model multi-faceted cracks using the SBFEM to model just the crack tip; using the DBE-SBFEM, modelling is no longer restricted to symmetry about the crack face.

For purposes of disambiguity, the DBE-SBFEM has been developed in its entirely as part of the present work, the data in the examples in this chapter are obtained by the development of the author's own code.

5.2 Numerical formulation

The formulation of the DBE-SBFEM shares similarities with that of the BE-SBFEM. For simplicity, the derivation focuses on the coupling of two subdomains in two dimensions such as in Figure 83, where a domain Ω is divided into Ω_B and Ω_S, bounded by Γ_B, Γ_D and Γ_I as illustrated in Figure 83. Like the BE-SBFEM, the scaling centre of Ω_S is placed on the crack tip. The upper crack surface is modelled by Γ_B and A_R; the lower crack surface is modelled by Γ_D and A_L. Unlike the BE-SBFEM, $\Gamma_S = \Gamma_I$ and there are no junction degrees of freedom.

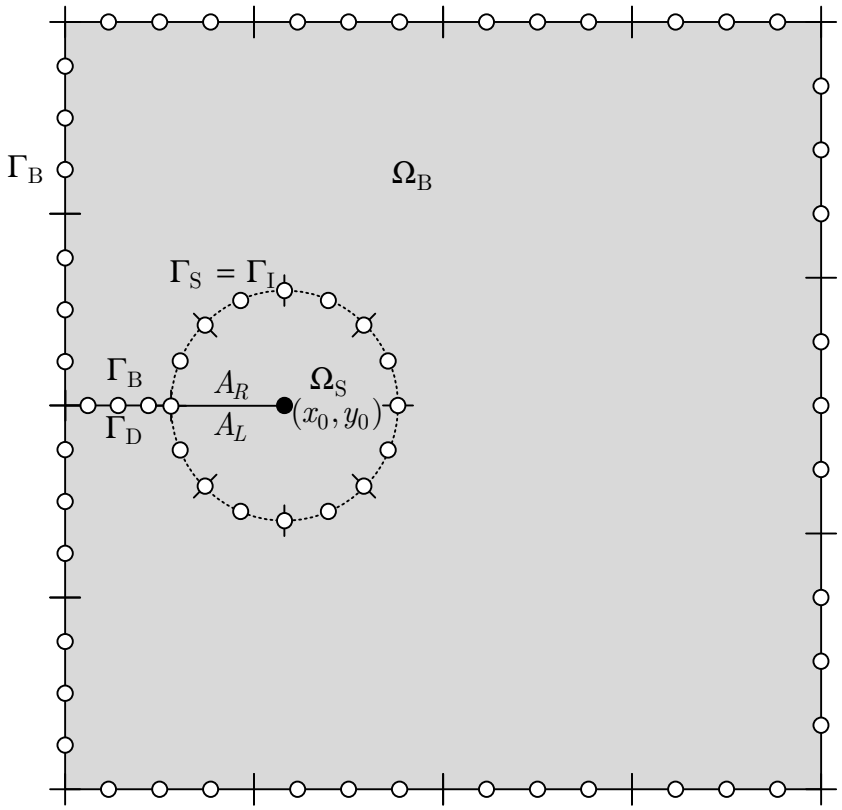

Figure 83. An example domain subdivided into BEM and SBFEM subdomains. The BEM portion of the lower crack is modelled using the DBEM

The coupled DBE-SBFEM is formed in the same manner as the BE-SBFEM, with the introduction of further partitioning relating to the DBEM (denoted

by the subscript 'D'). As there are no pure SBFEM terms $\mathbf{K}_{SS}$, these are omitted resulting in

$$\begin{bmatrix} \mathbf{K}_{JJ} & \mathbf{K}_{JI} & \mathbf{M}_{JJ} & \mathbf{M}_{JI} & \mathbf{0} & \mathbf{0} & \mathbf{0} & \mathbf{0} \\ \mathbf{K}_{IJ} & \mathbf{K}_{II} & \mathbf{M}_{IJ} & \mathbf{M}_{II} & \mathbf{0} & \mathbf{0} & \mathbf{0} & \mathbf{0} \\ \mathbf{H}_{JJ} & \mathbf{H}_{JI} & -\Psi_1\mathbf{G}_{JJ} & -\Psi_1\mathbf{G}_{JI} & \mathbf{H}_{JB} & \mathbf{H}_{JD} & -\Psi_1\mathbf{G}_{JB} & -\Psi_1\mathbf{G}_{JD} \\ \mathbf{H}_{IJ} & \mathbf{H}_{II} & -\Psi_1\mathbf{G}_{IJ} & -\Psi_1\mathbf{G}_{II} & \mathbf{H}_{IB} & \mathbf{H}_{ID} & -\Psi_1\mathbf{G}_{IB} & -\Psi_1\mathbf{G}_{ID} \\ \mathbf{H}_{BJ} & \mathbf{H}_{BI} & -\Psi_1\mathbf{G}_{BJ} & -\Psi_1\mathbf{G}_{BI} & \mathbf{H}_{BB} & \mathbf{H}_{BD} & -\Psi_1\mathbf{G}_{BB} & -\Psi_1\mathbf{G}_{BD} \\ \mathbf{H}_{DJ} & \mathbf{H}_{DI} & -\Psi_1\mathbf{G}_{DJ} & -\Psi_1\mathbf{G}_{DI} & \mathbf{H}_{DB} & \mathbf{H}_{DD} & -\Psi_1\mathbf{G}_{DB} & -\Psi_1\mathbf{G}_{DD} \end{bmatrix} \begin{Bmatrix} \mathbf{u}_J \\ \mathbf{u}_I \\ \dfrac{\mathbf{t}_J}{\Psi_1} \\ \dfrac{\mathbf{t}_I}{\Psi_1} \\ \mathbf{u}_B \\ \mathbf{u}_D \\ \dfrac{\mathbf{t}_B}{\Psi} \\ \dfrac{\mathbf{t}_D}{\Psi_1} \end{Bmatrix} = \begin{Bmatrix} \mathbf{P}_{Jext} \\ \mathbf{0} \\ \mathbf{0} \\ \mathbf{0} \\ \mathbf{0} \\ \mathbf{0} \end{Bmatrix} \tag{5.1}$$

If it is assumed $\mathbf{t}_D = \mathbf{0}$, then

$$\begin{bmatrix} \mathbf{K}_{JJ} & \mathbf{K}_{JI} & \mathbf{M}_{JJ} & \mathbf{M}_{JI} & \mathbf{0} & \mathbf{0} & \mathbf{0} \\ \mathbf{K}_{IJ} & \mathbf{K}_{II} & \mathbf{M}_{IJ} & \mathbf{M}_{II} & \mathbf{0} & \mathbf{0} & \mathbf{0} \\ \mathbf{H}_{JJ} & \mathbf{H}_{JI} & -\Psi_1\mathbf{G}_{JJ} & -\Psi_1\mathbf{G}_{JI} & \mathbf{H}_{JB} & \mathbf{H}_{JD} & -\Psi_1\mathbf{G}_{JB} \\ \mathbf{H}_{IJ} & \mathbf{H}_{II} & -\Psi_1\mathbf{G}_{IJ} & -\Psi_1\mathbf{G}_{II} & \mathbf{H}_{IB} & \mathbf{H}_{ID} & -\Psi_1\mathbf{G}_{IB} \\ \mathbf{H}_{BJ} & \mathbf{H}_{BI} & -\Psi_1\mathbf{G}_{BJ} & -\Psi_1\mathbf{G}_{BI} & \mathbf{H}_{BB} & \mathbf{H}_{BD} & -\Psi_1\mathbf{G}_{BB} \\ \mathbf{H}_{DJ} & \mathbf{H}_{DI} & -\Psi_1\mathbf{G}_{DJ} & -\Psi_1\mathbf{G}_{DI} & \mathbf{H}_{DB} & \mathbf{H}_{DD} & -\Psi_1\mathbf{G}_{DB} \end{bmatrix} \begin{Bmatrix} \mathbf{u}_J \\ \mathbf{u}_I \\ \dfrac{\mathbf{t}_J}{\Psi_1} \\ \dfrac{\mathbf{t}_I}{\Psi_1} \\ \mathbf{u}_B \\ \mathbf{u}_D \\ \dfrac{\mathbf{t}_B}{\Psi} \end{Bmatrix} = \begin{Bmatrix} \mathbf{P}_{Jext} \\ \mathbf{0} \\ \mathbf{0} \\ \mathbf{0} \\ \mathbf{0} \\ \mathbf{0} \end{Bmatrix} \tag{5.2}$$

which, by the application of boundary conditions and separating known and unknown terms in the usual manner, can be rearranged to yield a square system of linear equations in the form

$$\mathbf{A}\mathbf{x} = \mathbf{b} \tag{5.3}$$

5.2.1 Semi-discontinuous SBFEM motivation

The motivation for the semi-discontinuous SBFEM introduced in §3.8 as part of the current work is highlighted by the example in Figure 83. As described in §4.8.1, the existence of degrees of freedom at the junction of Γ_B , Γ_D and Γ_I causes complications in the computation of the integral of singular BEM kernels in the formation of $\mathbf{G}_{DD}$. By moving the node from this junction along the interface (illustrated in Figure 84), and thus introducing semi-discontinuous interface elements, the integration is no longer singular, merely near-singular, which can be computed with greater ease.

As there are no junction terms, these are omitted from the system resulting in

$$\begin{bmatrix} \mathbf{K}_{II} & \mathbf{M}_{II} & \mathbf{0} & \mathbf{0} & \mathbf{0} \\ \mathbf{H}_{II} & -\Psi_1\mathbf{G}_{II} & \mathbf{H}_{IB} & \mathbf{H}_{ID} & -\Psi_1\mathbf{G}_{IB} \\ \mathbf{H}_{BI} & -\Psi_1\mathbf{G}_{BI} & \mathbf{H}_{BB} & \mathbf{H}_{BD} & -\Psi_1\mathbf{G}_{BB} \\ \mathbf{H}_{DI} & -\Psi_1\mathbf{G}_{DI} & \mathbf{H}_{DB} & \mathbf{H}_{DD} & -\Psi_1\mathbf{G}_{DB} \end{bmatrix} \begin{Bmatrix} \mathbf{u}_I \\ \frac{\mathbf{t}_I}{\Psi_1} \\ \mathbf{u}_B \\ \mathbf{u}_D \\ \frac{\mathbf{t}_B}{\Psi} \end{Bmatrix} = \begin{Bmatrix} \mathbf{0} \\ \mathbf{0} \\ \mathbf{0} \\ \mathbf{0} \end{Bmatrix} \tag{5.4}$$

The remainder of the formulation follows as with the DBE-SBFEM above.

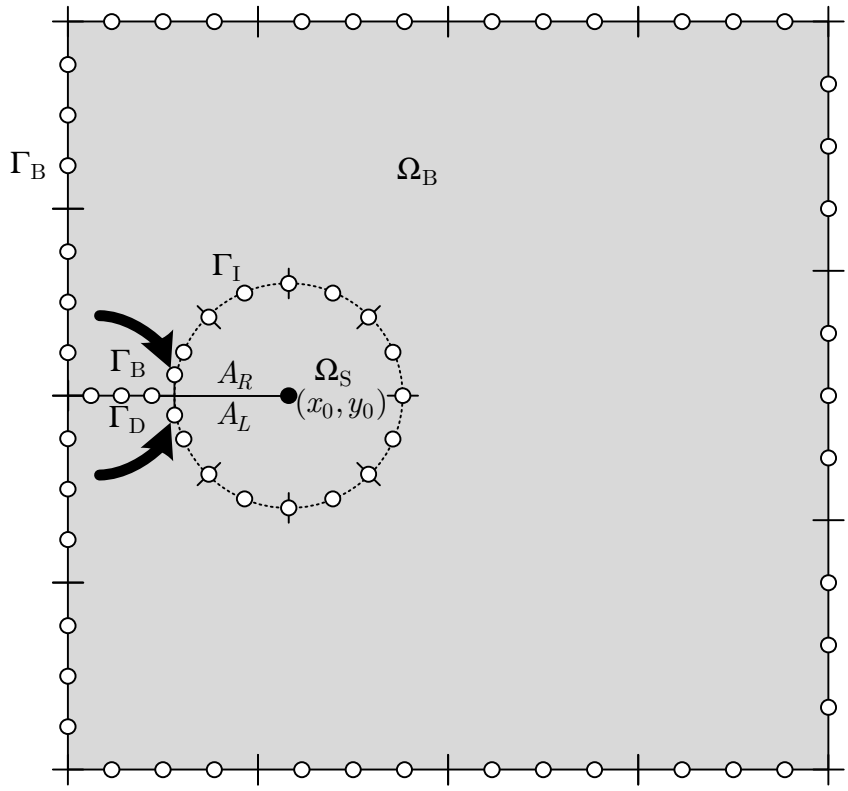

Figure 84. An example domain modelled using the DBE-SBFEM with semi-discontinuous SBFEM

5.3 Matrix scaling

Further to the scaling introduced in §4.6, by selecting an appropriate value for scale factors Ψ_2 and Ψ_3, and by introducing them into the DBE-SBFEM system matrix, equation (5.4) is rewritten

$$\begin{bmatrix} \Psi_2\Psi_3\mathbf{K}_{\mathrm{II}} & \Psi_1\Psi_2\mathbf{M}_{\mathrm{II}} & \mathbf{0} & \mathbf{0} & \mathbf{0} \\ \Psi_3\mathbf{H}_{\mathrm{II}} & -\Psi_1\mathbf{G}_{\mathrm{II}} & \Psi_3\mathbf{H}_{\mathrm{IB}} & \Psi_3\mathbf{H}_{\mathrm{ID}} & -\Psi_1\mathbf{G}_{\mathrm{IB}} \\ \Psi_3\mathbf{H}_{\mathrm{BI}} & -\Psi_1\mathbf{G}_{\mathrm{BI}} & \Psi_3\mathbf{H}_{\mathrm{BB}} & \Psi_3\mathbf{H}_{\mathrm{BD}} & -\Psi_1\mathbf{G}_{\mathrm{BB}} \\ \Psi_3\mathbf{H}_{\mathrm{DI}} & -\Psi_1\mathbf{G}_{\mathrm{DI}} & \Psi_3\mathbf{H}_{\mathrm{DB}} & \Psi_3\mathbf{H}_{\mathrm{DD}} & -\Psi_1\mathbf{G}_{\mathrm{DB}} \end{bmatrix} \begin{Bmatrix} \dfrac{\mathbf{u}_{\mathrm{I}}}{\Psi_3} \\ \dfrac{\mathbf{t}_{\mathrm{I}}}{\Psi_1} \\ \dfrac{\mathbf{u}_{\mathrm{B}}}{\Psi_3} \\ \dfrac{\mathbf{u}_{\mathrm{D}}}{\Psi_3} \\ \dfrac{\mathbf{t}_{\mathrm{B}}}{\Psi_1} \end{Bmatrix} = \begin{Bmatrix} \mathbf{0} \\ \mathbf{0} \\ \mathbf{0} \\ \mathbf{0} \end{Bmatrix} \quad (5.5)$$

5.4 DBE-SBFEM with reanalysis for crack growth

Consider a crack of length a propagated by a length Δa, as illustrated in Figure 85, in which the transition from the original state to the new state is a single iteration in a series defining the full propagation. If the DBE-SBFEM is used to model the original state, then the advantages of the method over other crack-modelling methods becomes apparent.

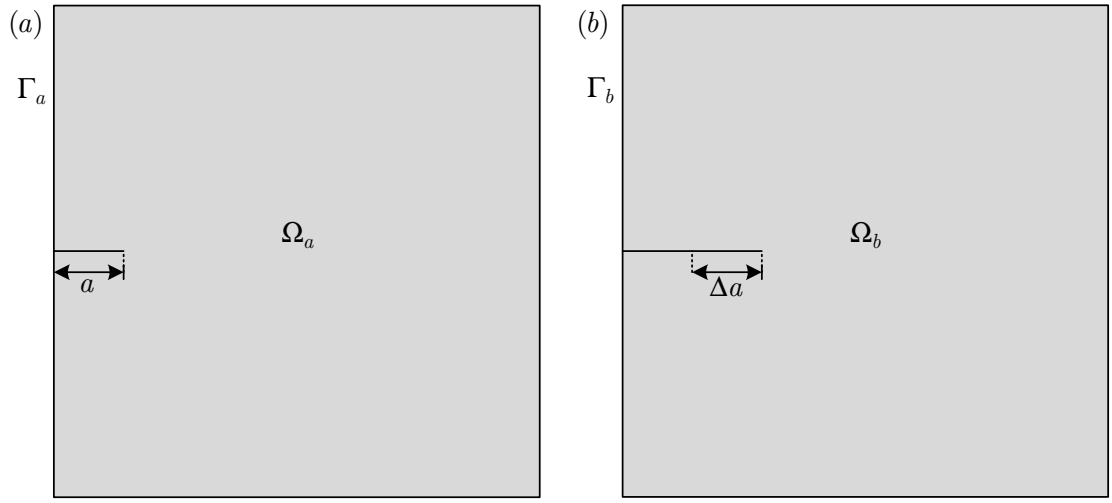

Figure 85. Crack propagation from (a) an original state to (b) a new state

It can be seen from comparison of Figure 84 (the original state model) and Figure 86 (the new state model), the crack propagation analysis is undertaken with minimal remeshing. In identifying which computations are common to sequential iterations, reanalysis can be employed to great effect for an efficient propagation algorithm. Subdomain Ω_S is translated in the direction of propagation, interface boundary $\Gamma_{\tilde{I}}$ replaces Γ_I, and boundary portions $\Gamma_{\tilde{B}}$ and $\Gamma_{\tilde{D}}$ are added. The subscripts $\tilde{I}$, $\tilde{B}$ and $\tilde{D}$ are also used in the partitioning of the BEM and SBFEM matrices.

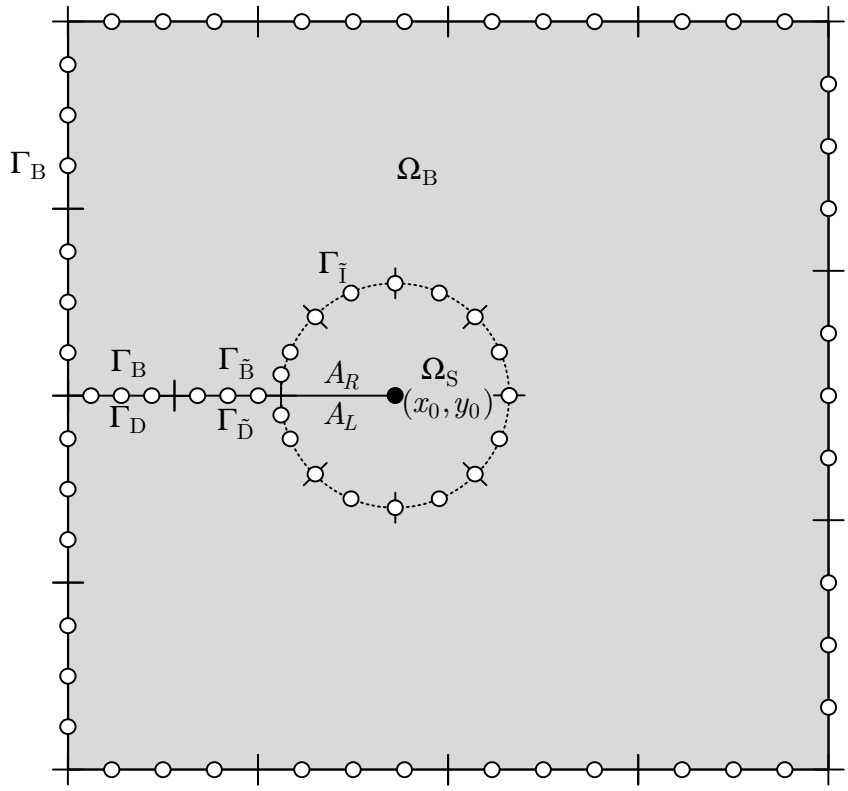

Figure 86. The DBE-SBFEM model for new state, using reanalysis with translation of Ω_{S}

In the BEM subdomain, the computations in which the collocation point and field elements are unchanged are common to both analyses. Thus, any submatrices $\mathbf{H}_{ij}$ and $\mathbf{G}_{ij}$ where $i, j = \mathrm{B}, \mathrm{D}, \mathrm{I}$, in which neither subscript 'i' nor 'j' contains a tilde '~', correspond to repeated computations in which the collocation point and the field elements are common to both the original and new models. The remaining submatrices correspond to new computations in which the collocation point and/or the field elements are different from the original.

Although the interface has undergone translation, and any collocation at the interface and corresponding integration over the boundary differs between analyses, the integration over the interface can be reused as there is no *relative* difference between the interface collocation points and the interface field elements. Similarly, Ω_{S} is static relative to the scaling centre (x_0, y_0) and

equations (3.3) and (3.4) defining the scaled boundary coordinate system are preserved. Thus, computations made in forming the stiffness matrices $\mathbf{K}_{\text{II}}$ and $\mathbf{K}_{\tilde{\text{I}}\tilde{\text{I}}}$, and their respective constituents $\mathbf{Q}_{\text{II}}$, $\mathbf{\Phi}_{\text{II}}$, $\mathbf{Q}_{\tilde{\text{I}}\tilde{\text{I}}}$ and $\mathbf{\Phi}_{\tilde{\text{I}}\tilde{\text{I}}}$ are common to both the models in Figure 84 and Figure 86 and can be reused, along with the old matrix of eigenvalues $\mathbf{\Lambda}$.

Equation (5.5) can be partitioned into reflect this reused data

$$\begin{bmatrix}
\Psi_2\Psi_3\mathbf{K}_{\tilde{\text{I}}\tilde{\text{I}}} & \Psi_1\Psi_2\mathbf{M}_{\tilde{\text{I}}\tilde{\text{I}}} & \mathbf{0} & \mathbf{0} & \mathbf{0} & \mathbf{0} & \mathbf{0} & \mathbf{0} \\
\Psi_3\mathbf{H}_{\tilde{\text{I}}\tilde{\text{I}}} & -\Psi_1\mathbf{G}_{\tilde{\text{I}}\tilde{\text{I}}} & \Psi_3\mathbf{H}_{\tilde{\text{I}}\text{B}} & \Psi_3\mathbf{H}_{\tilde{\text{I}}\tilde{\text{B}}} & \Psi_3\mathbf{H}_{\tilde{\text{I}}\text{D}} & \Psi_3\mathbf{H}_{\text{I}\tilde{\text{D}}} & -\Psi_1\mathbf{G}_{\tilde{\text{I}}\text{B}} & -\Psi\mathbf{G}_{\tilde{\text{I}}\tilde{\text{B}}} \\
\Psi_3\mathbf{H}_{\text{B}\tilde{\text{I}}} & -\Psi_1\mathbf{G}_{\text{B}\tilde{\text{I}}} & \Psi_3\mathbf{H}_{\text{BB}} & \Psi_3\mathbf{H}_{\text{B}\tilde{\text{B}}} & \Psi_3\mathbf{H}_{\text{BD}} & \Psi_3\mathbf{H}_{\text{BD}} & -\Psi_1\mathbf{G}_{\text{BB}} & -\Psi\mathbf{G}_{\text{B}\tilde{\text{B}}} \\
\Psi_3\mathbf{H}_{\tilde{\text{B}}\tilde{\text{I}}} & -\Psi_1\mathbf{G}_{\tilde{\text{B}}\tilde{\text{I}}} & \Psi_3\mathbf{H}_{\tilde{\text{B}}\text{B}} & \Psi_3\mathbf{H}_{\tilde{\text{B}}\tilde{\text{B}}} & \Psi_3\mathbf{H}_{\text{BD}} & \Psi_3\mathbf{H}_{\text{BD}} & -\Psi_1\mathbf{G}_{\tilde{\text{B}}\text{B}} & -\Psi\mathbf{G}_{\tilde{\text{B}}\tilde{\text{B}}} \\
\Psi_3\mathbf{H}_{\text{D}\tilde{\text{I}}} & -\Psi_1\mathbf{G}_{\text{D}\tilde{\text{I}}} & \Psi_3\mathbf{H}_{\text{DB}} & \Psi_3\mathbf{H}_{\text{D}\tilde{\text{B}}} & \Psi_3\mathbf{H}_{\text{DD}} & \Psi_3\mathbf{H}_{\text{D}\tilde{\text{D}}} & -\Psi_1\mathbf{G}_{\text{DB}} & -\Psi\mathbf{G}_{\text{D}\tilde{\text{B}}} \\
\Psi_3\mathbf{H}_{\tilde{\text{D}}\tilde{\text{I}}} & -\Psi_1\mathbf{G}_{\tilde{\text{D}}\tilde{\text{I}}} & \Psi_3\mathbf{H}_{\tilde{\text{D}}\text{B}} & \Psi_3\mathbf{H}_{\tilde{\text{D}}\tilde{\text{B}}} & \Psi_3\mathbf{H}_{\tilde{\text{D}}\text{D}} & \Psi_3\mathbf{H}_{\tilde{\text{D}}\tilde{\text{D}}} & -\Psi_1\mathbf{G}_{\tilde{\text{D}}\text{B}} & -\Psi_1\mathbf{G}_{\tilde{\text{D}}\tilde{\text{B}}}
\end{bmatrix}
\begin{Bmatrix}
\frac{\mathbf{u}_{\tilde{\text{I}}}}{\Psi_3} \\
\frac{\mathbf{t}_{\tilde{\text{I}}}}{\Psi_1} \\
\frac{\mathbf{u}_{\text{B}}}{\Psi_3} \\
\frac{\mathbf{u}_{\tilde{\text{B}}}}{\Psi_3} \\
\frac{\mathbf{u}_{\text{D}}}{\Psi_3} \\
\frac{\mathbf{u}_{\tilde{\text{D}}}}{\Psi_3} \\
\frac{\mathbf{t}_{\text{B}}}{\Psi_1} \\
\frac{\mathbf{t}_{\tilde{\text{B}}}}{\Psi_1}
\end{Bmatrix} =
\begin{Bmatrix}
\mathbf{0} \\ \mathbf{0} \\ \mathbf{0} \\ \mathbf{0} \\ \mathbf{0} \\ \mathbf{0} \\ \mathbf{0} \\ \mathbf{0}
\end{Bmatrix} \tag{5.6}$$

Figure 87 illustrates the relative sizes of each of the terms in the matrix in equation (5.6) in this example. Much of the data is reusable due to *a priori* knowledge of duplicate calculations or blocks of zeros.

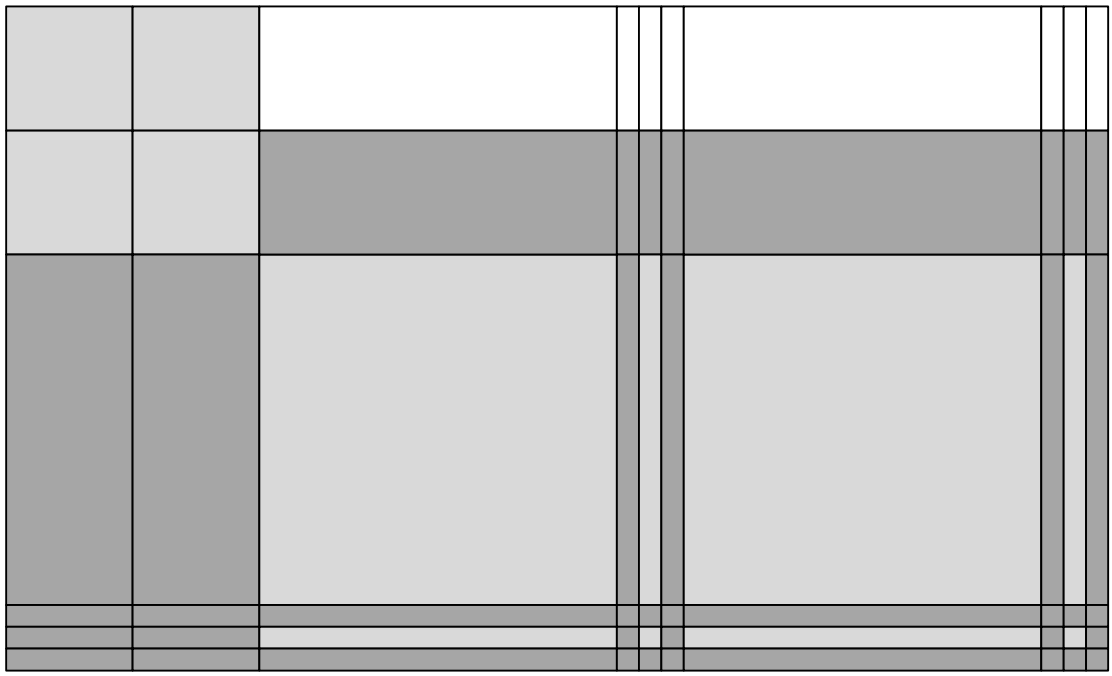

Figure 87. A block representation (drawn to scale) of terms in the matrix in equation (5.6) for the new state in the propagation algorithm. The dark regions represent terms requiring new computations, the light regions represent reused data and white regions are blocks of zeros

In this trivial example, the effects are less obvious than those associated with a more complicated model with a more involved mesh. In practice, the effects of reanalysis on the system size will be problem-dependent, but in the applications intended for this coupled method, $\mathbf{H}_{\mathrm{BB}}$ and $\mathbf{G}_{\mathrm{BB}}$ will dominate the matrix and the effects of reanalysis are more noticeable, as illustrated in Figure 88.

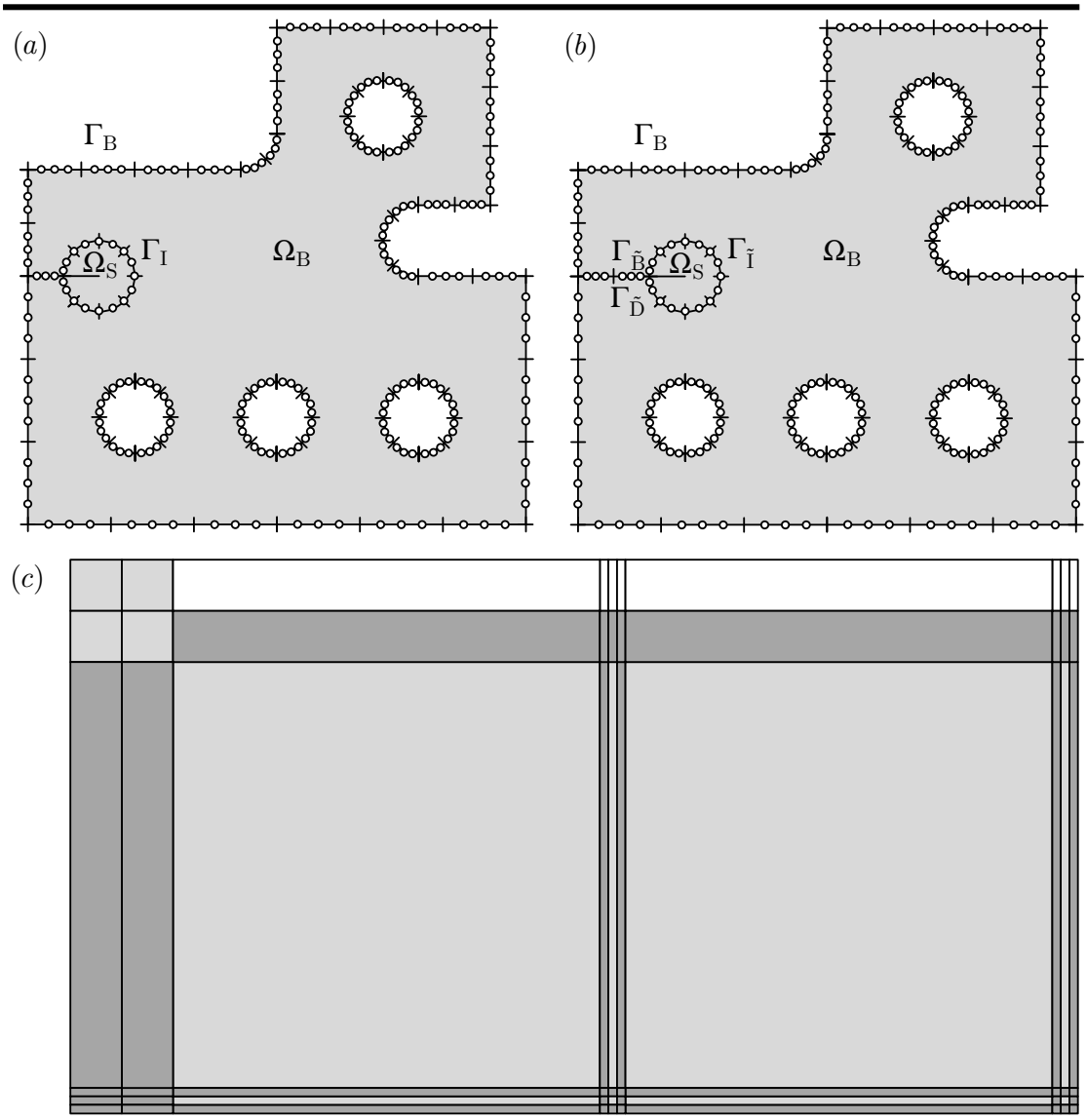

Figure 88. Crack propagation from (a) original state to (b) new state in a non-trivial domain, demonstrating (c) the major reuse of data through reanalysis (drawn to scale)

5.5 Reanalysis for non-planar crack growth

Consider the reanalysis situation where Ω_{S} undergoes a rotation of θ about (x_0, y_0) and x- and y-direction translation, as illustrated in Figure 89. Unlike the translation-only propagation, $\mathbf{K}_{\tilde{\mathrm{II}}} \neq \mathbf{K}_{\mathrm{II}}$. However a transformation matrix $\mathbf{T}_\theta$ comprising repeated diagonal submatrices $\mathbf{t}_\theta$ where

$$\mathbf{t}_\theta = \begin{bmatrix} \cos\theta & -\sin\theta \\ \sin\theta & \cos\theta \end{bmatrix} \tag{5.7}$$

is introduced such that

$$\mathbf{K}_{\tilde{\mathrm{II}}} = \mathbf{T}_\theta{}^{\mathrm{T}} \mathbf{K}_{\mathrm{II}} \mathbf{T}_\theta \tag{5.8}$$

and so

$$\mathbf{K}_\theta = \mathbf{T}_\theta{}^{\mathrm{T}} \mathbf{Q}_{\mathrm{S}} \boldsymbol{\Phi}_{\mathrm{S}}{}^{-1} \mathbf{T}_\theta \tag{5.9}$$

$$\mathbf{Q}_\theta = \mathbf{T}_\theta{}^{\mathrm{T}} \mathbf{Q}_{\mathrm{S}} \tag{5.10}$$

$$\boldsymbol{\Phi}_\theta = \mathbf{T}_\theta{}^{-1} \boldsymbol{\Phi}_{\mathrm{S}} \tag{5.11}$$

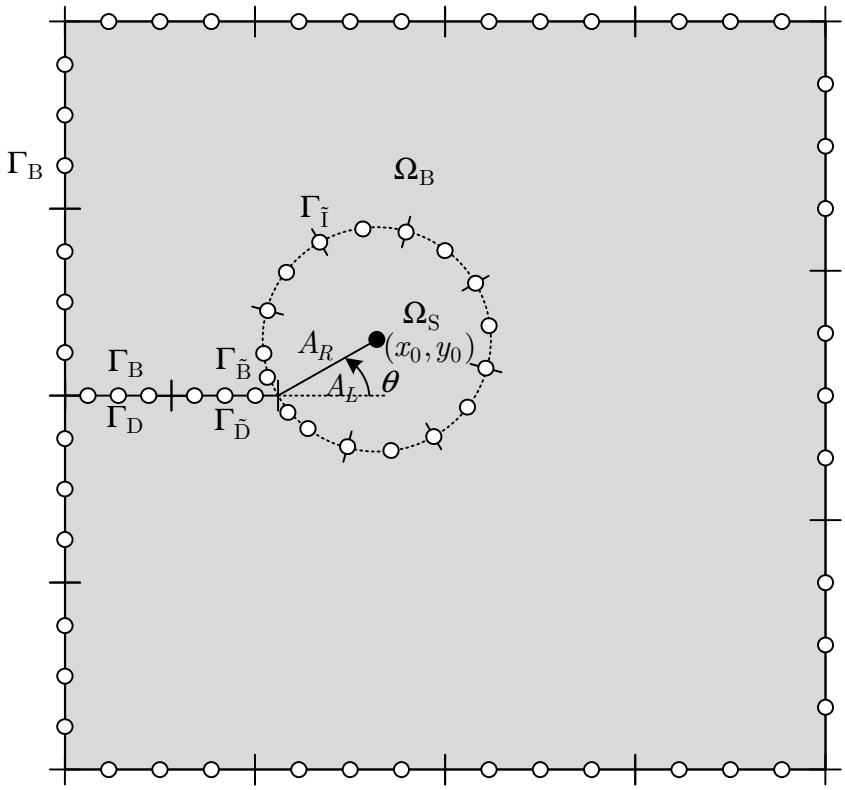

Figure 89. Reanalysis with translation and rotation of Ω_{S}

5.5.1 Verification

In order to assess the errors associated with a general rotated stiffness matrix $\mathbf{K}_{\tilde{\mathrm{S}}}$, a comparison with $\mathbf{K}_{\mathrm{S}}$ is made by analysing an example domain, rotated by θ, where $0 \le \theta \le \pi/4$, illustrated in Figure 90.

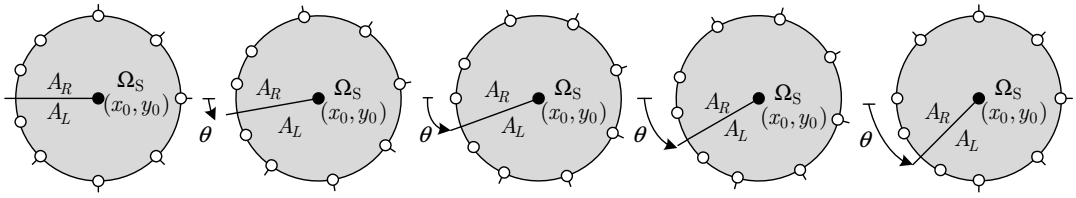

Figure 90. Rotational perturbation of Ω_S

An error indicator is defined

$$\varepsilon_K = \frac{\text{median}\left[\Delta K_{ij}\right]}{\text{median}\left[K_{Sij}\right]} \qquad i,j = 1..n \tag{5.12}$$

where $\mathbf{\Delta K}$ is determined on a term-by-term basis

$$\mathbf{\Delta K} = \begin{bmatrix} K_{11} & \cdots & K_{1n} \\ \vdots & \ddots & \vdots \\ K_{n1} & \cdots & K_{nn} \end{bmatrix} \tag{5.13}$$

where

$$K_{ij=}\left|\frac{K_{\tilde{S}ij} - K_{Sij}}{K_{Sij}}\right|, \qquad i,j = 1..n \tag{5.14}$$

The median is used in order to reduce the impact of the near-zero denominators that would otherwise be present in equation (5.12)** which cause extreme and spurious outliers that exhibit unrepresentative and distorted error profiles. The analysis is repeated with uniform mesh refinement. The results the impact of this rotation on the condition number of the system matrix $\kappa(\mathbf{K}_S)$ are shown in Figure 91.

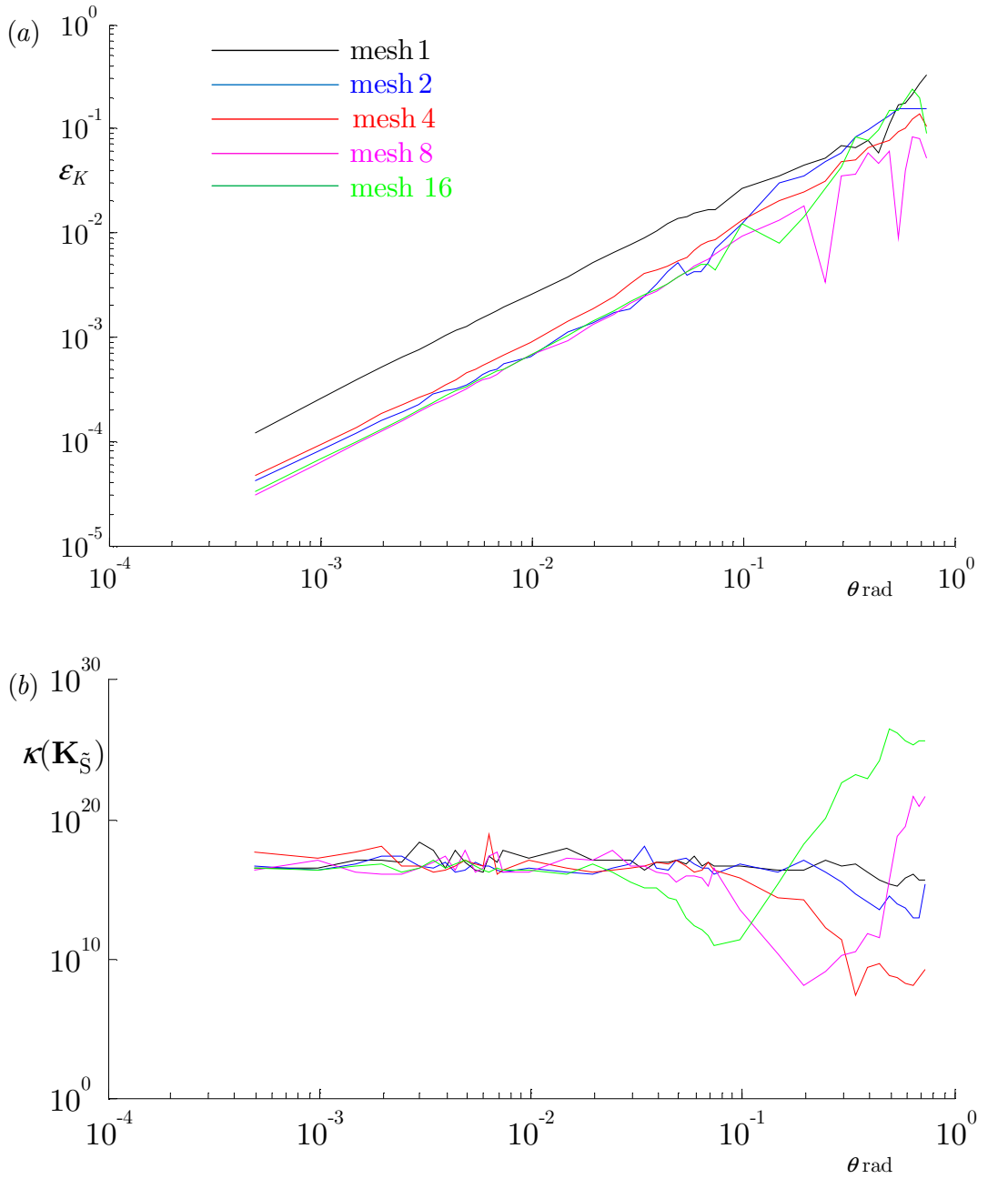

Figure 91. (*a*) Error in reanalysed SBFEM stiffness matrix $\Delta\mathbf{K}$ with angular perturbation θ and (*b*) corresponding condition number $\kappa(\mathbf{K}_S)$. Each 'mesh' corresponds to the initial mesh density on the model, varying from 1 to 16 elements per line. The log scale θ is chosen to show that numerical stability is observer until around $\theta = 0.1$ rad

5.6 Example applications to fracture mechanics

The same benchmark problem used in §2.10 is used to validate the coupled

DBE-SBFEM and contributions to the error include the sample points on the sidefaces used in §3.9.

For the examples in this chapter

$$\Omega = \Omega_B \cup \Omega_S \tag{5.15}$$

and the scaling centre of Ω_S is coincident with the crack tip.

In order to assess the impact of reanalysis, results obtained through reanalysis are compared with a model analysed using the DBE-SBFEM without reanalysis, i.e. a model of the same geometry (including domain propagation), analysed in full.

First, the analysis times are compared using ε_{ti} defined

$$\varepsilon_{ti} = \frac{t_{fi} - t_{ri}}{t_0} \tag{5.16}$$

where t_{ri} $(i = 1..4)$ and t_{fi} $(i = 1..4)$ are the times taken for each of the 4 reanalysis and equivalent full analysis iterations, and t_0 is the time taken for the first (base) analysis that is common to both, such that ε_{ti} indicates how much time is saved through reanalysis. Each of the duration times presented are based on the mean averaging of three analyses.

Second, because the purpose of the reanalysis is its efficiency, it is not expected to demonstrate any improvement in accuracy over a full analysis. A more interesting measure of its accuracy is in its difference relative to a full analysis, rather than against the analytical solution. Thus, the errors are redefined

$$\varepsilon_{L^2 k} = \sqrt{\frac{\sum_s \left(u_k(s) - u_{\tilde{k}}(s) \right)^2}{\sigma}},\ s \in \Gamma_u, \sigma \neq 0 \tag{5.17}$$

where $u_k(s)$ and $u_{\tilde{k}}(s)$ are the approximations to the displacements found in corresponding full analysis and reanalysis solutions respectively.

5.6.1 Through crack in an infinite plate example 1

The DBE-SBFEM is used to model the crack tip described in §2.10. With reference to Figure 92(c), the dimensions of Ω are $b \times 2h$, and the boundary is subdivided into portions of boundary $\Gamma_{\tilde{u}}$ with known displacement boundary conditions (red nodes), and portions of boundary Γ_u with displacements to be found as part of the solution (white nodes). In this case

$$\Gamma = \Gamma_{\mathrm{B}} \cup \Gamma_{\mathrm{D}} \cup \Gamma_{\mathrm{I}} \cup \Gamma_{\mathrm{S}} \cup A_R \cup A_L \tag{5.18}$$

where Γ_{S} is omitted as there are no pure SBFEM degrees of freedom, only those that appear on Γ_{I}. The displacement results of the coupled domains are illustrated in Figure 93, and for $\mathbf{u}(s)$, where s lies on Γ_u are summarised in Figure 94. This crude initial mesh is uniformly subdivided and the analysis repeated in order to assess the convergence characteristics. The convergence characteristics of the coupled DBE-SBFEM are illustrated in Figure 95.

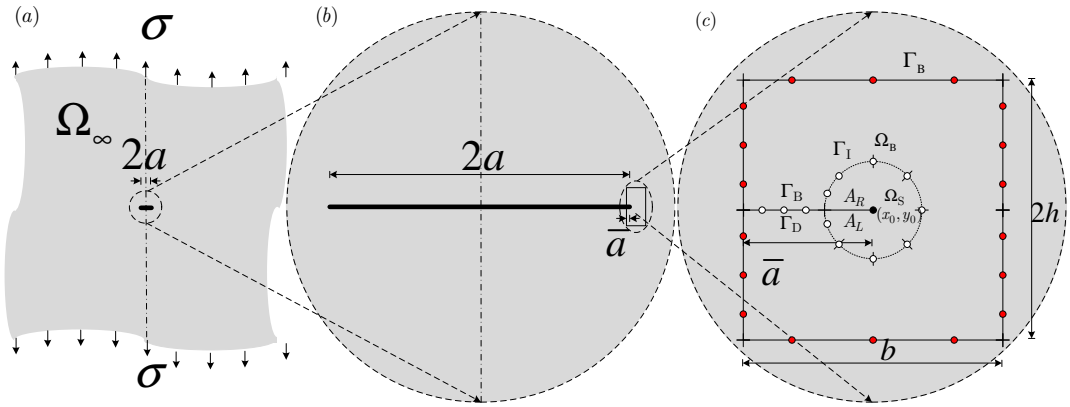

Figure 92. DBE-SBFEM analysis of (a) through crack in an infinite plate, (b) the section of the domain modelled, and (c) the mesh where red and white nodes indicate $\Gamma_{\tilde{u}}$ and Γ_u

The displacements of the domain and boundary portion Γ_u are illustrated in Figure 93(a) and Figure 94 respectively. Convergence characteristics of the DBE-SBFEM displacement and stress intensity factor errors are illustrated in Figure 95, using the uniform mesh refinement indicated in Figure 93(b).

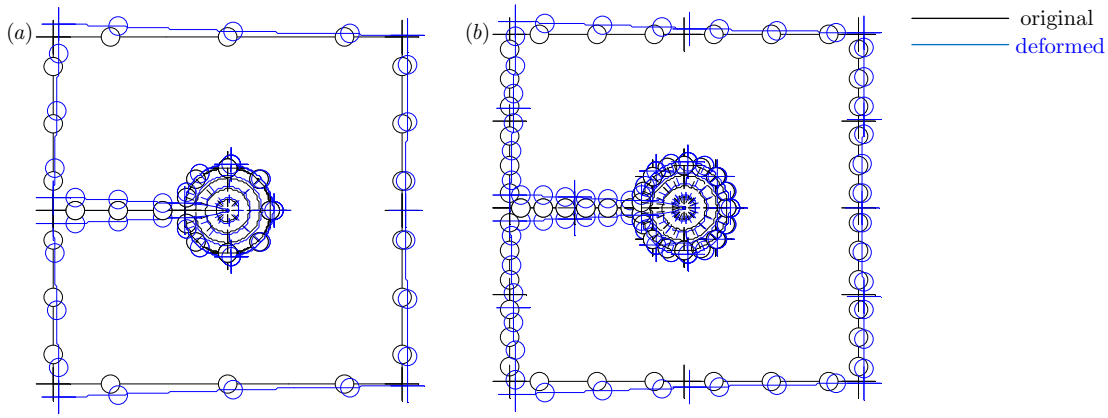

Figure 93. To-scale deformation of (a) initial mesh and (b) uniformly-refined mesh

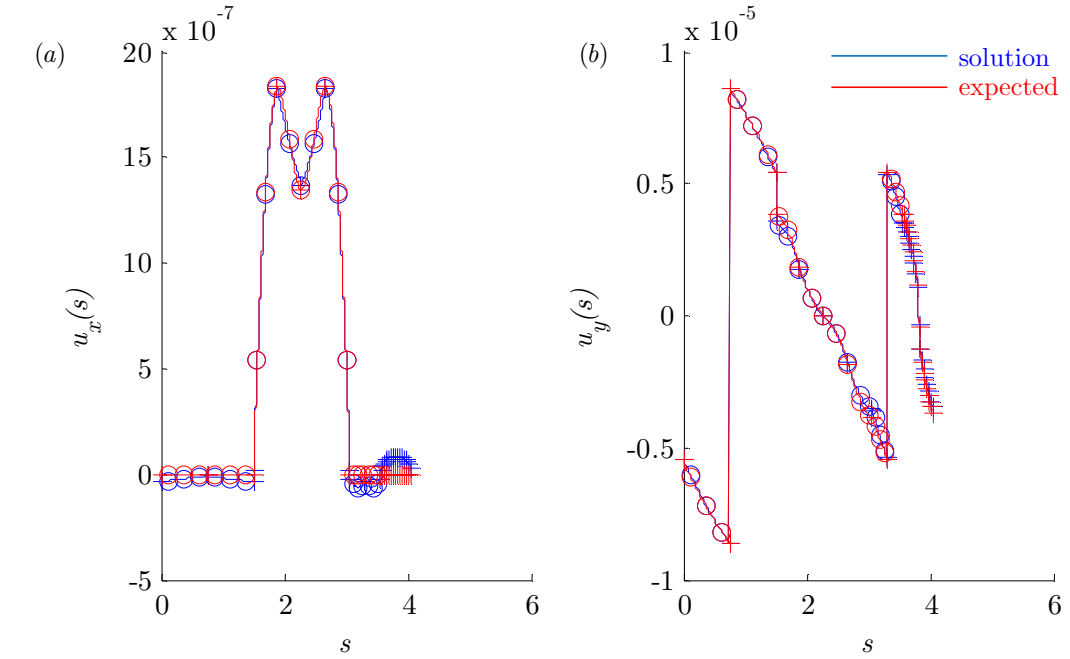

Figure 94. (*a*) *x*- and (*b*) *y*-direction displacement results on Γ_u

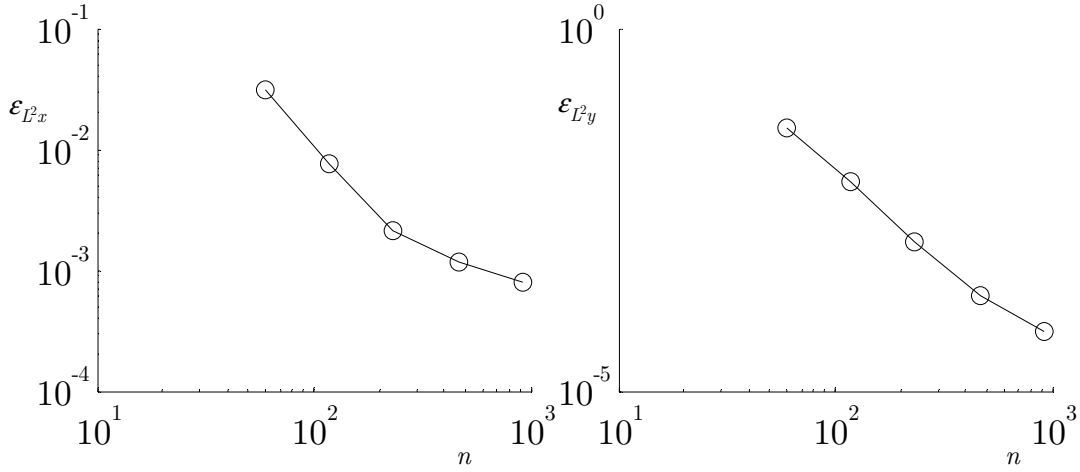

Figure 95. Convergence characteristics of DBE-SBFEM

5.6.2 Through crack in an infinite plate example 2

The benefits of reanalysis in the coupled DBE-SBFEM are illustrated in an example similar to that above. The basis of the reanalysed data is the system matrices formed in the previous example with the angle of propagation θ determined using equation (1.3). By propagating Ω_S and introducing $\Gamma_{\tilde{B}}$ and $\Gamma_{\tilde{D}}$

$$\Gamma = \Gamma_{\mathrm{B}} \cup \Gamma_{\tilde{\mathrm{B}}} \cup \Gamma_{\mathrm{D}} \cup \Gamma_{\tilde{\mathrm{D}}} \cup \Gamma_{\mathrm{I}} \cup A_R \cup A_L \tag{5.19}$$

The displacements of the domain and boundary portion Γ_u are illustrated in Figure 96(a) and Figure 97 respectively. The analysis times and displacement errors of the each reanalysis iteration compared with that an equivalent full analysis are illustrated in Figure 98. Convergence characteristics of the DBE-SBFEM with reanalysis using the uniform mesh refinement indicated in Figure 96(b) are omitted as the differences with Figure 95 are indiscernible.

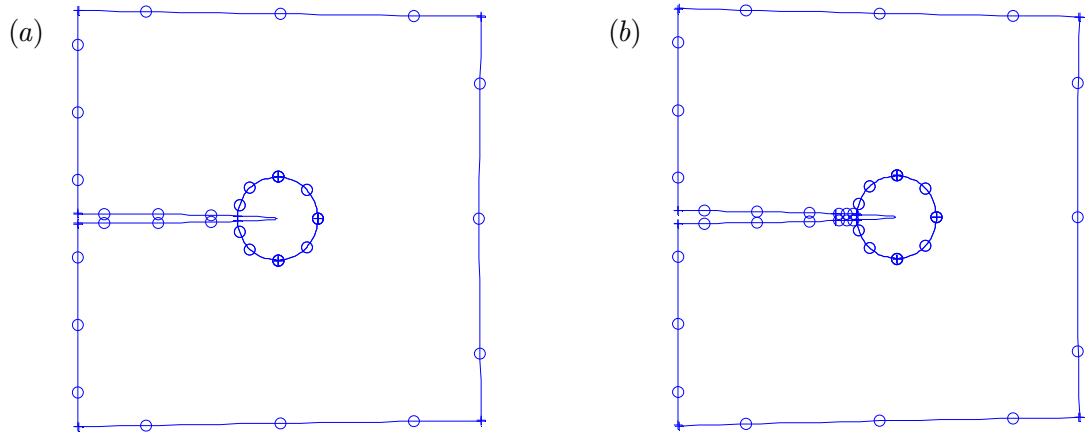

Figure 96. To-scale deformation of (a) initial mesh and (b) reanalysed mesh

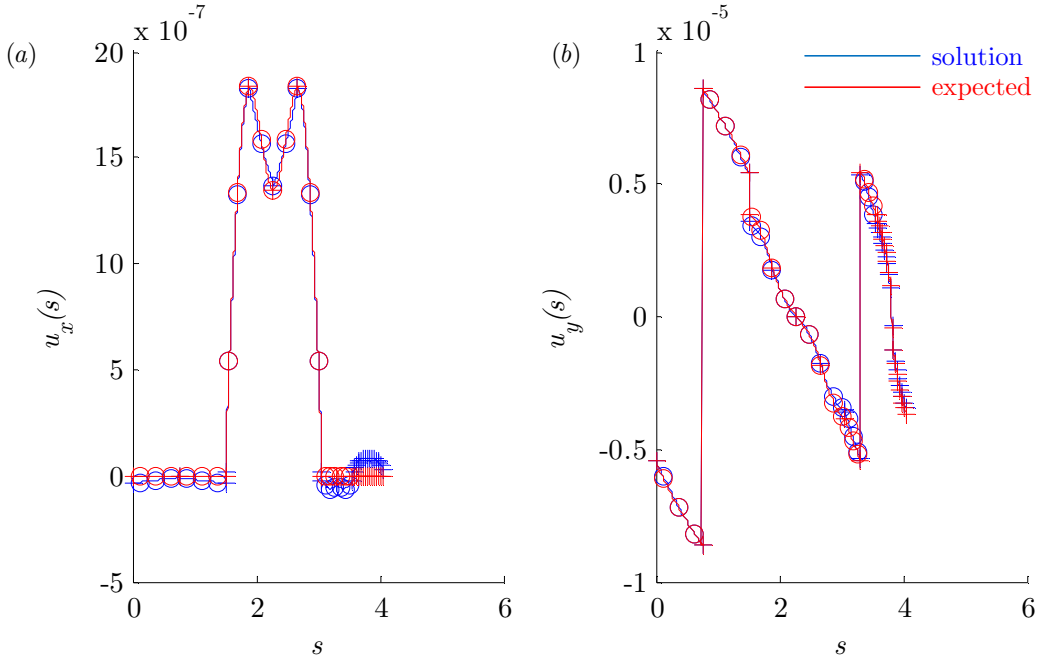

Figure 97. (*a*) *x*- and (*b*) *y*-direction displacement results on Γ_u

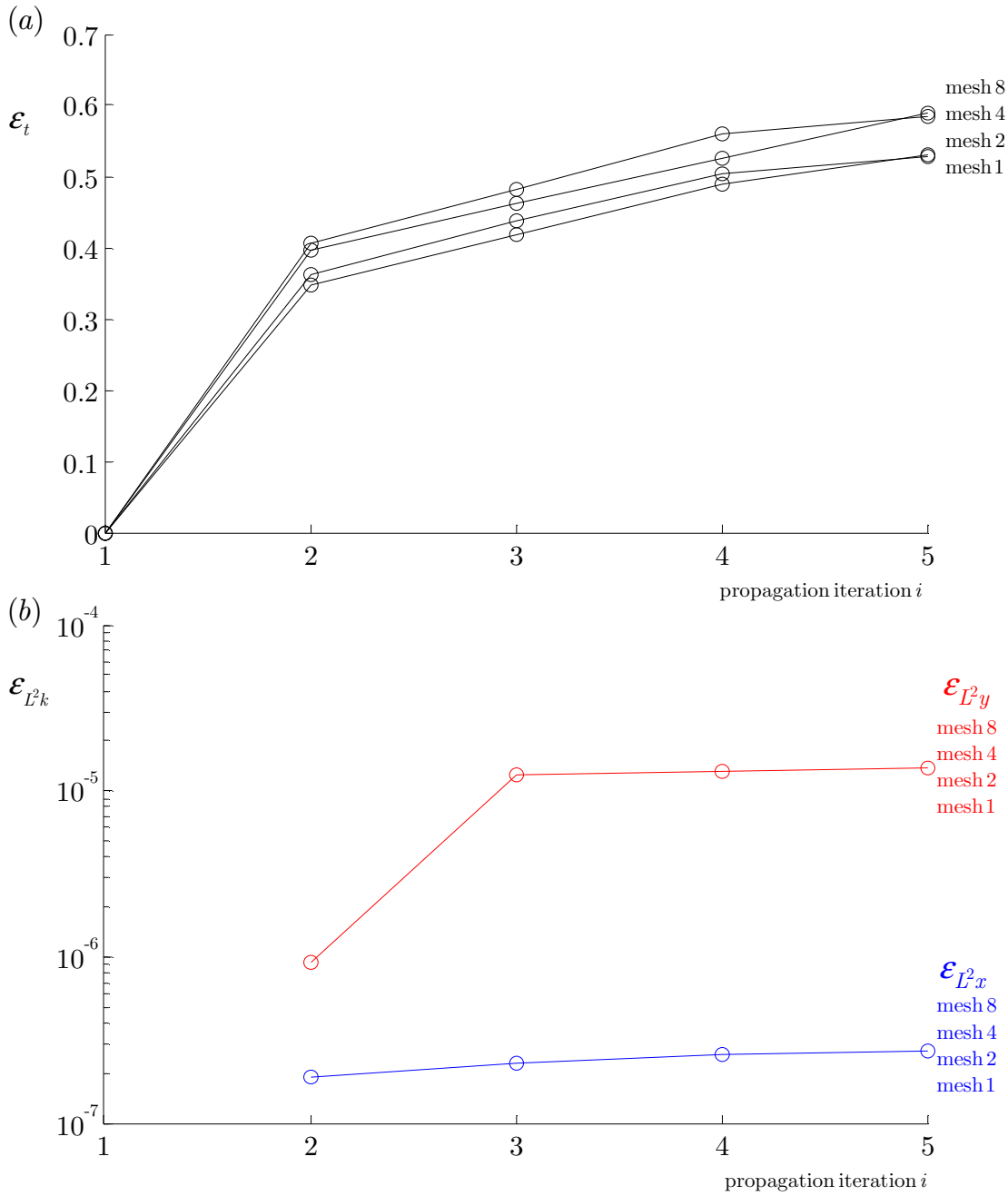

Figure 98. Comparison of reanalysis and full analysis (a) computation times and (b) displacement errors

5.6.3 Through crack in an infinite plate example 3

The same approach used to demonstrate the accuracy and flexibility of the coupled BE-SBFEM is now presented using the DBE-SBFEM with reanalysis.

The mesh used in Figure 88 may be used in the usual infinite plate problem, although it should be noted that the holes illustrated in the mesh must be replaced with continuous media, as illustrated in Figure 99.

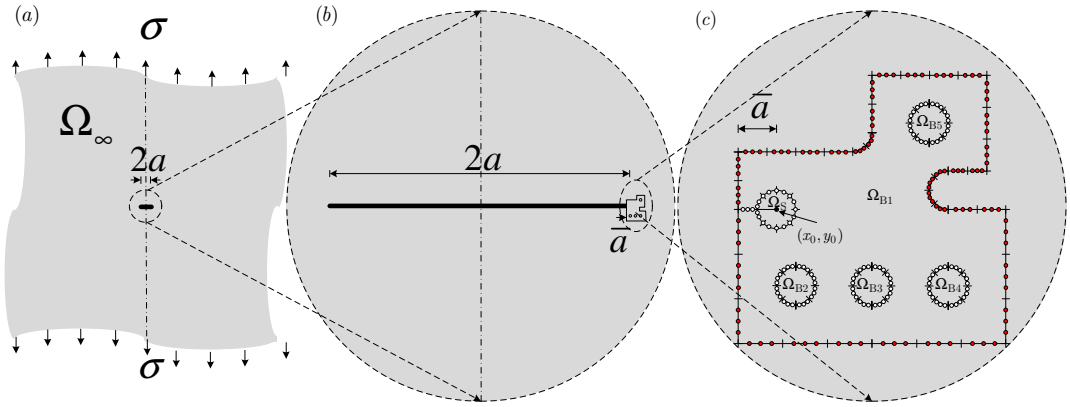

Figure 99. DBE-SBFEM reanalysis of (a) through crack in an infinite plate, (b) the section of the domain modelled, and (c) the mesh where red and white nodes indicate $\Gamma_{\tilde{u}}$ and Γ_u

The displacements of the domain are illustrated in Figure 100(a). Reanalysis is used during subsequent iterations of crack growth through the domain and compared with iterations based on an equivalent full analysis.

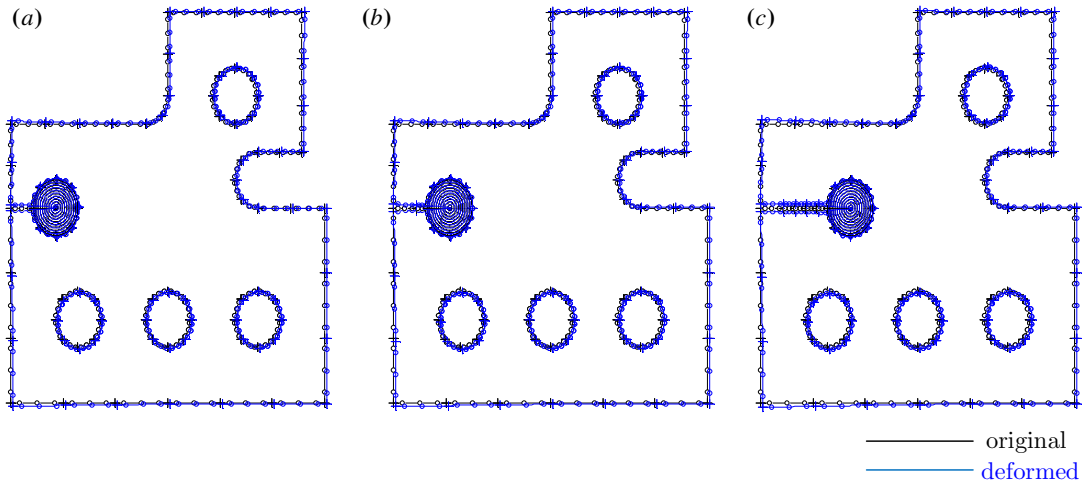

Figure 100. To-scale deformation of (a) initial mesh and (b) 1st and (c) 5th reanalysed meshes

The reanalysis and full analysis iterations are repeated using the uniform mesh refinement indicated in Figure 93(b). The analysis times and displacement errors of the each reanalysis iteration are illustrated in Figure 101.

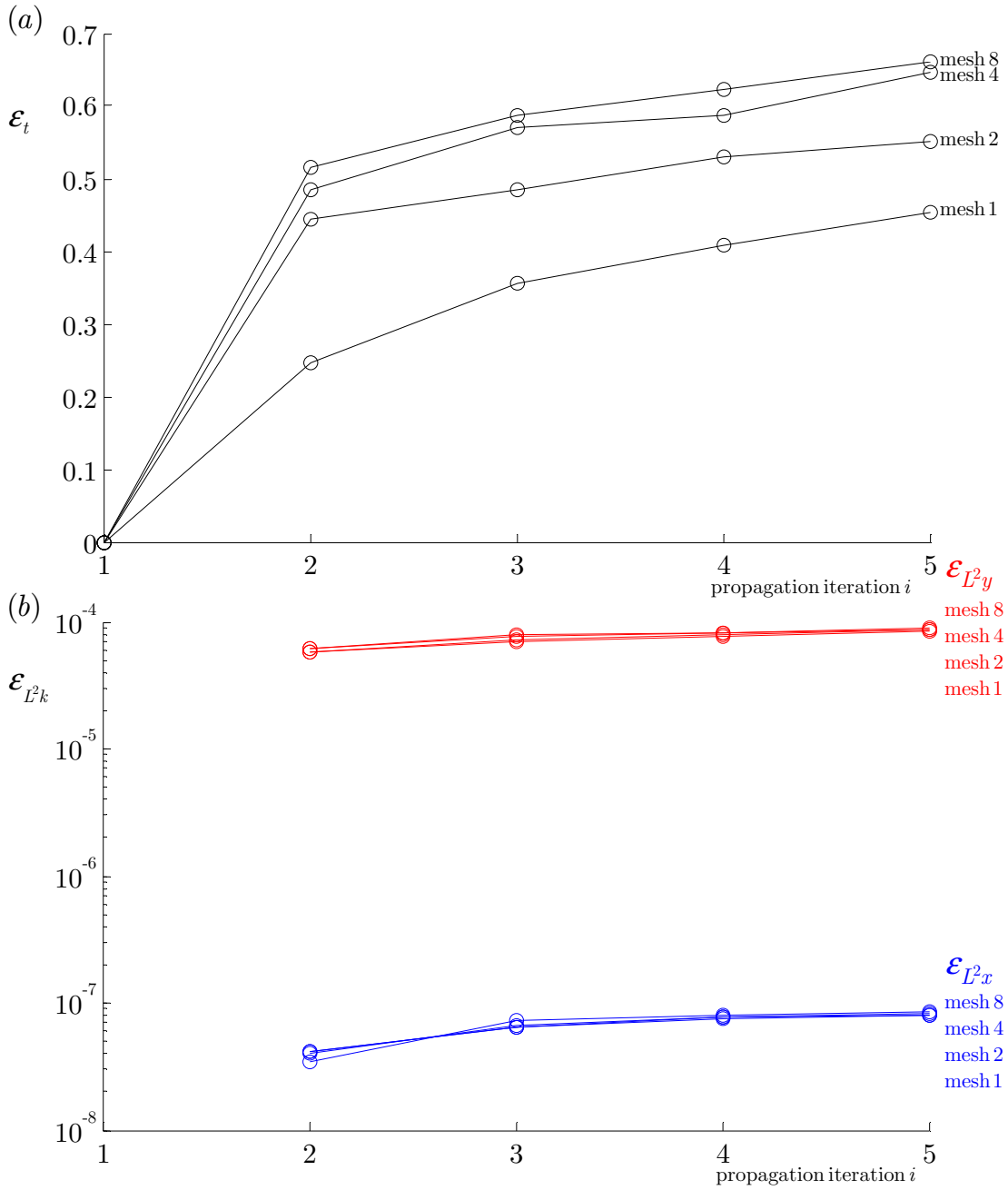

Figure 101. Comparison of reanalysis and full analysis (a) computation times and (b) displacement errors

5.6.4 Crack propagation with mixed-mode propagation

The same approach is used demonstrating the DBE-SBFEM with reanalysis where a rotation of Ω_S is expected. Consider a finite domain Ω of dimensions $b \times h$ with a central, through-crack subject to asymmetric boundary conditions, as illustrated in Figure 102(a). A DBE-SBFEM model of dimensions $b \times h$ is defined to model this domain, making use of the symmetric geometry. The prescribed asymmetric boundary conditions are applied, as illustrated in Figure 102(b). After an initial full DBE-SBFEM analysis, the crack is propagated in the direction determined by equation (1.3) , the model remeshed and progressive iterations of reanalysis are employed.

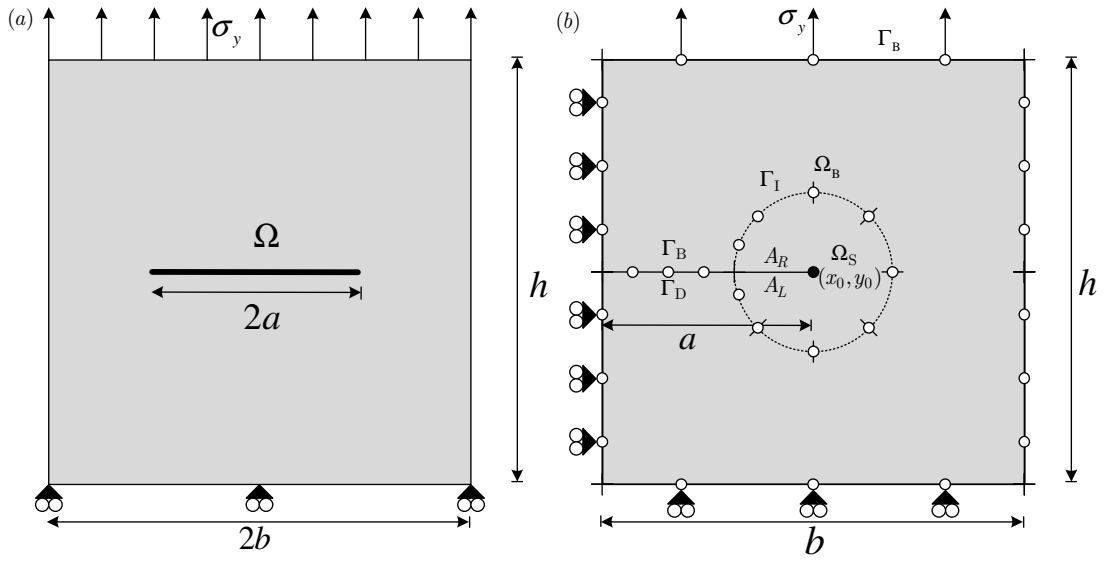

Figure 102. (a) An asymmetrically-loaded crack and (a) the DBE-SBFEM model

The deformation of the domains for each increment using reanalysis are illustrated in Figure 103 and are comparable to the equivalent full analyses found in Figure 104. The resulting propagation paths are illustrated in Figure 105 and Figure 106 respectively. The mesh is refined uniformly and the analyses repeated. The effect of reanalysis on analysis times is illustrated in Figure 107(a). It is assumed that the full analysis presents a more accurate

solution than that obtained using reanalysis. Thus, the error is estimated by the difference in stress intensity factors defined in equations (3.116) and (3.117) where K_I and K_{I_h} are the stress intensity factors recovered using full analyses and reanalyses respectively, and are illustrated in Figure 107(b).

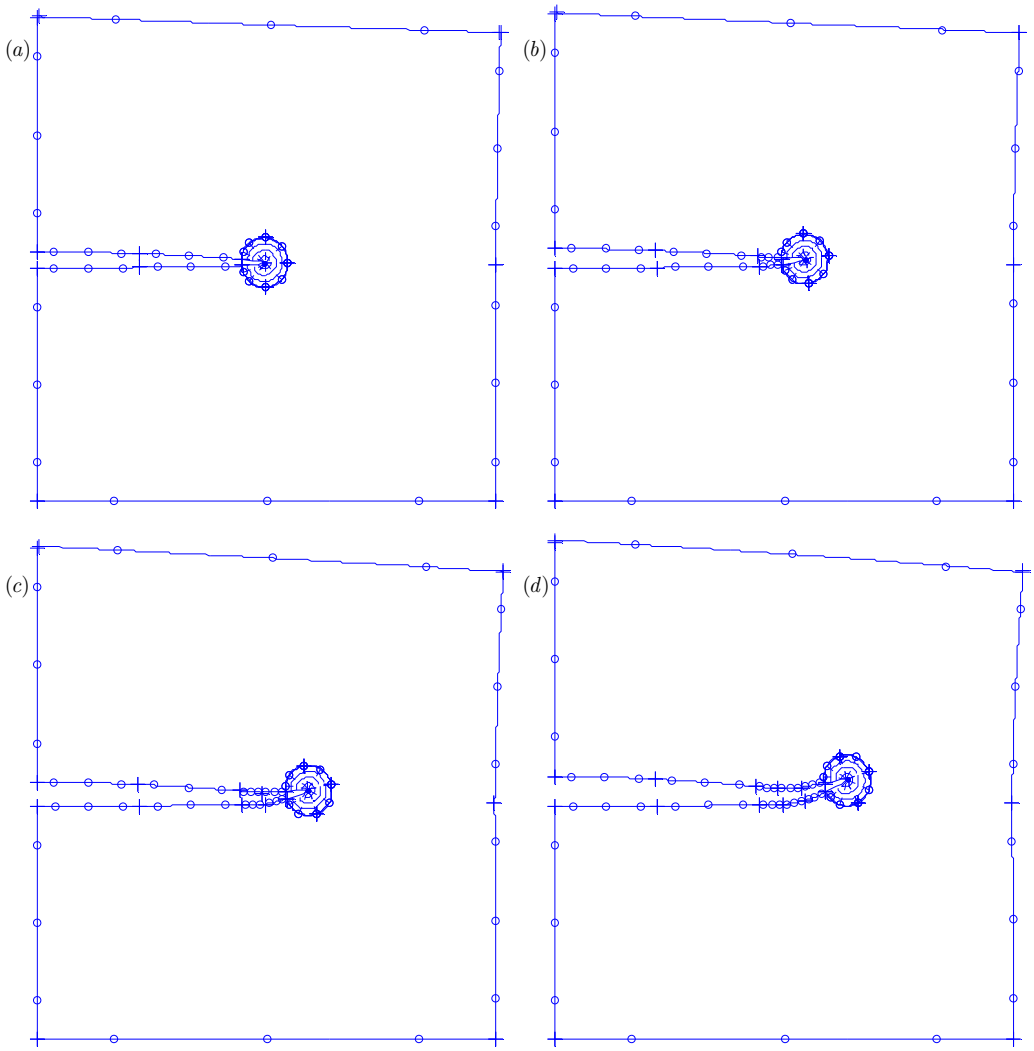

Figure 103. To-scale deformations of DBE-SBFEM reanalysis crack propagation iterations

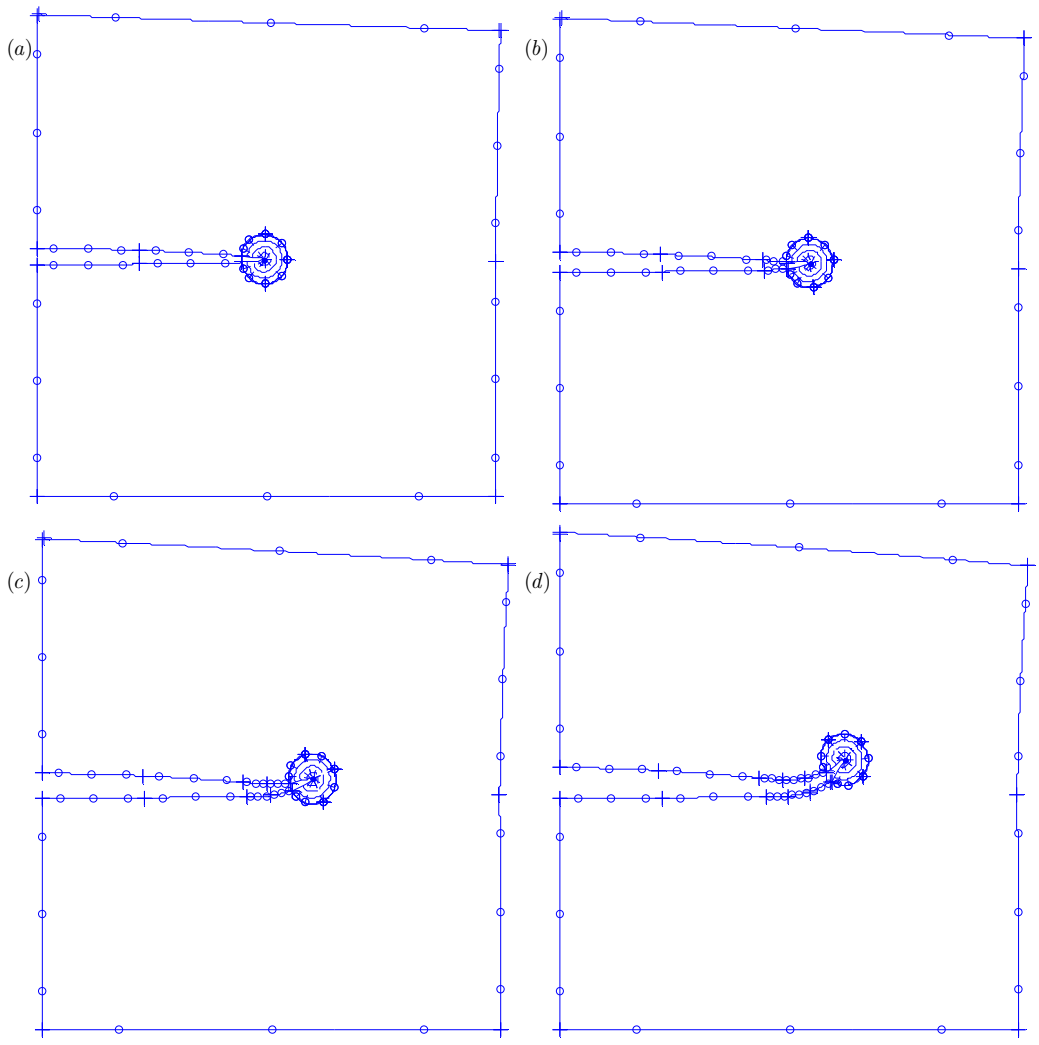

Figure 104. To-scale deformations of DBE-SBFEM full analysis crack propagation iterations

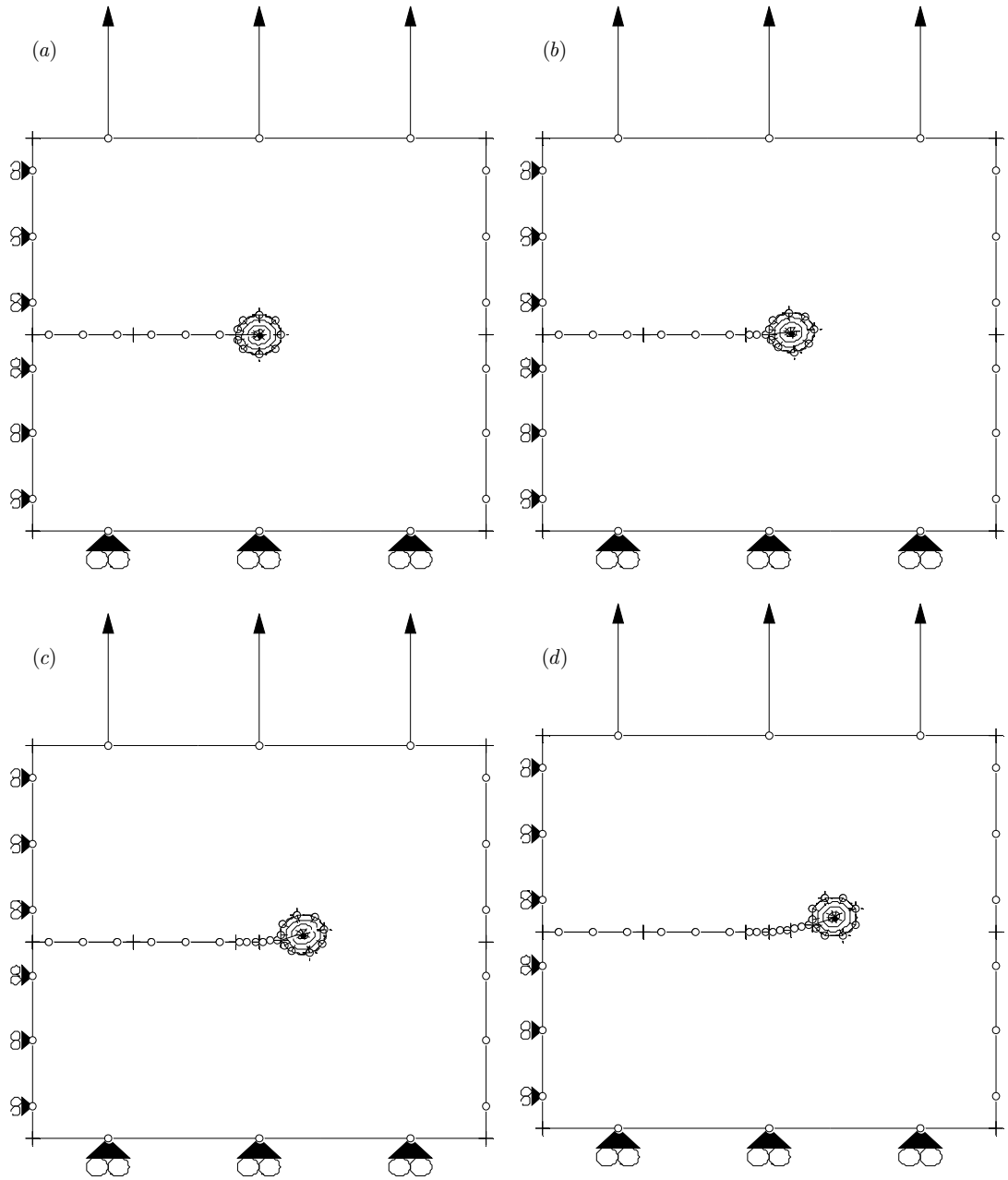

Figure 105. DBE-SBFEM reanalysis crack propagation paths

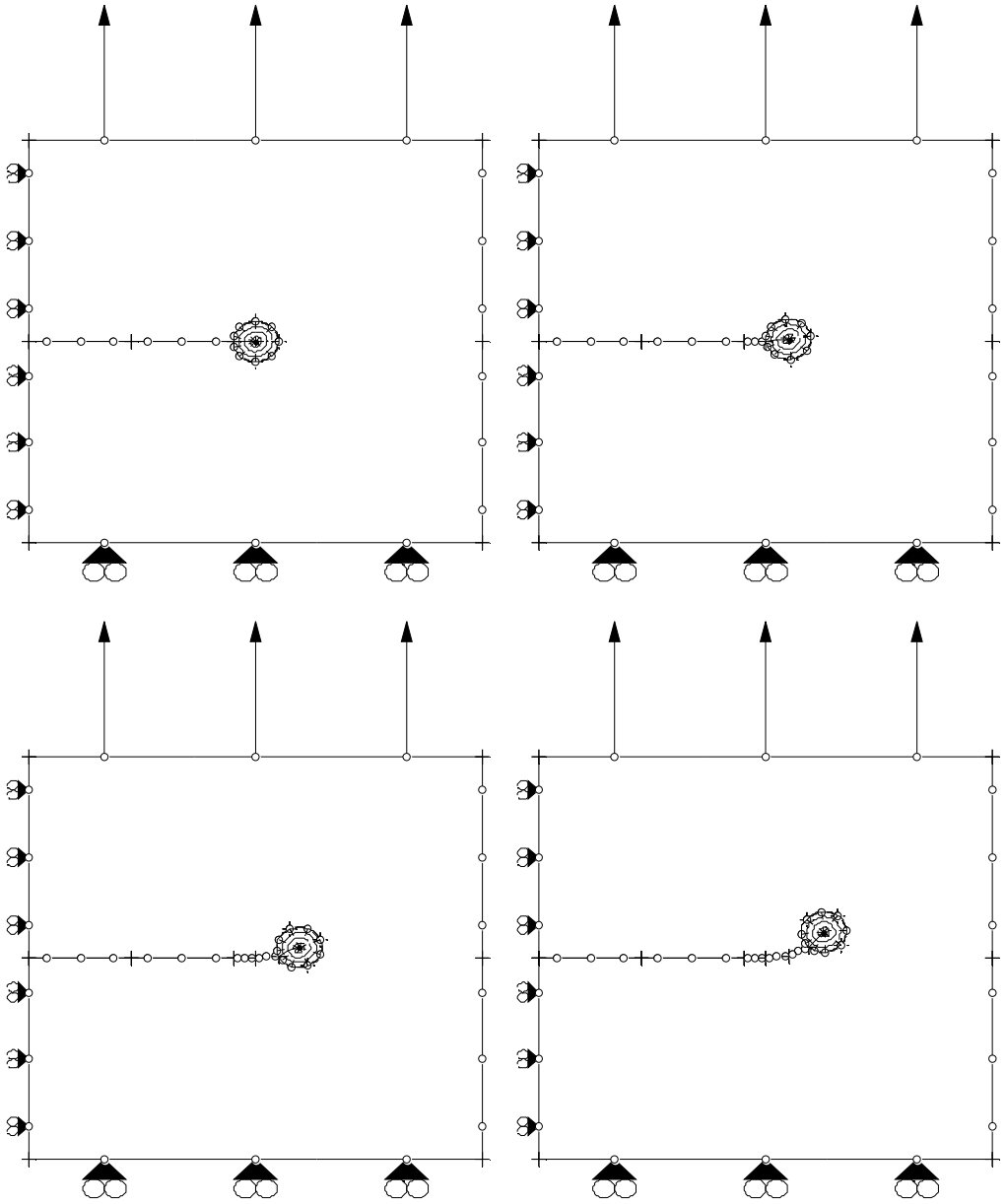

Figure 106. Full DBE-SBFEM analysis crack propagation paths

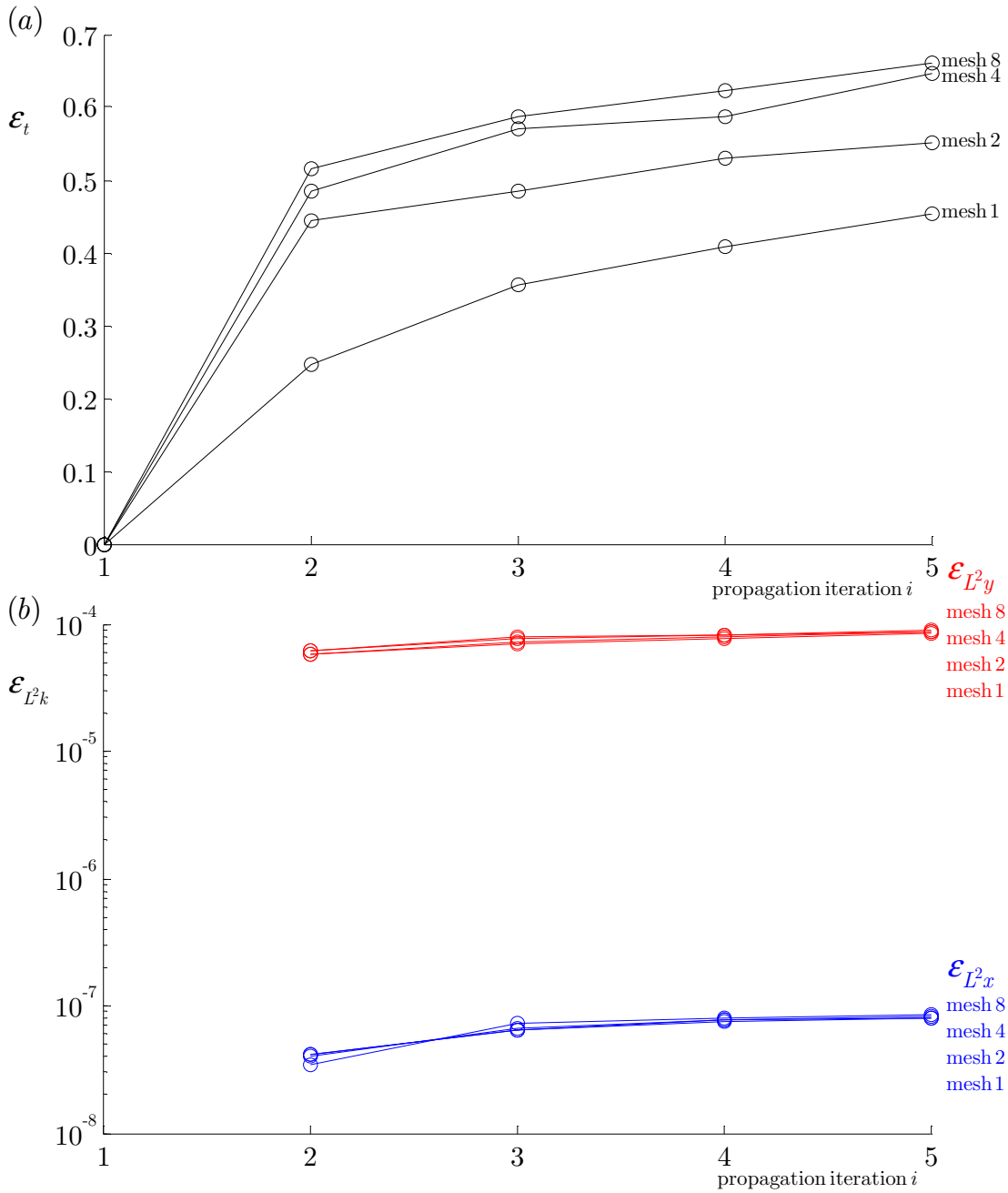

Figure 107. Comparison of reanalysis and full analysis of (a) normalised computation times and (b) accuracy.

5.7 Discussion

5.7.1 Optimisation of method parameters

It is not the intention to present the DBE-SBFEM as a coupled method that is optimised for specific fracture mechanics problems. However, it is of interest to investigate permutations of method parameters that may offer an improved strategy for its application to more *general* fracture mechanics problems. To this end, the observed and expected effects of some varying some method parameters is discussed.

The couple methods' constituents have their own parametric optimisation strategies for increasing their respective performance. For example, the BEM is known to be hampered by the poor quadratic approximation to the circular arcs that define the element geometry on the interface Γ_I. It can be shown that for an equivalent DBEM-DBEM model (in which the crack tip is modelled within a DBEM subdomain), the performance may be improved by use of a square subdomain. Similiarly, it has already been shown that the SBFEM benefits from the regularity of its domain (§3.10.1). It is reasonable to assume that these and other such individual method optimisation strategies apply when coupled.

By changing the shape of the subdomain to a square, Figure 108(a) to Figure 108(b), SBFEM domain regularity is maintained and some minor improvements were observed. However, these improvements ought not to be attributed so much to the square itself; the redefinition of the eight elements used in the discretisation of Γ_I from arcs to straight elements offers little improvement. The benefits are in that a satisfactory initial (BEM) mesh of a square subdomain can be achieved with fewer initial elements than a circular

domain. The consequence of which is that for a comparable minimal base level of accuracy, improvement in convergence rates can be gained.

However, by changing the shape in this way, the distance r separating BEM source point and field point pairs is likely to be reduced, as illustrated in Figure 108(d), which has the consequence of reducing the accuracy of the non-singular BEM integration and rate of convergence of adaptive integration scheme in §2.9. The effect of this, in turn, may be reduced by the resizing of Ω_S. However, that it ought to be accompanied by a change in element size gradation on Γ_B may be of more consequence the change in domain size itself.

This effect will be problem-dependent according to the proximity of Γ_B. The number of elements was reduced further by changing the shape of the interface Γ_I to a triangle. However, neither this nor the change in orientation of the domain as in Figure 108(c) offered (consistent) improvements in accuracy.

The rotation of the initial subdomain ought to be arbitrary, but with a subdomain corresponding orthogonally to the Cartesian axes, the unit normals to the interface remain well-defined (e.g. $\mathbf{n}(s) = \{1 \quad 0\}^T$). Low angular perturbations of the domain, however, effects these unit normals (e.g. $\mathbf{n}(s) = \{0.99999 \quad 0.0045\}^T$) and may lead to poor system matrix conditioning.

The effect parametric optimisation strategies is also subject to interpretation. For example, both methods benefit from some degree of mesh optimisation, such as through adaptive refinement schemes, and the same is expected with the DBE-SBFEM. However, mesh optimisation is then subject to its own parametric optimisation, such as the quality of the initial mesh and the

definition of its error indicators and estimators, which leads to multiple interpretations over the performance of mesh refinement. Such interpretations of the effect of individual parameter variations hampers quantifying the effect of combined parameter variations. So while each of the parameters discussed here are expected to benefit the coupled DBE-SBFEM on a problem-specific basis, determining their effect on general problems remains both outside the scope of this project and a recommendation for further research.

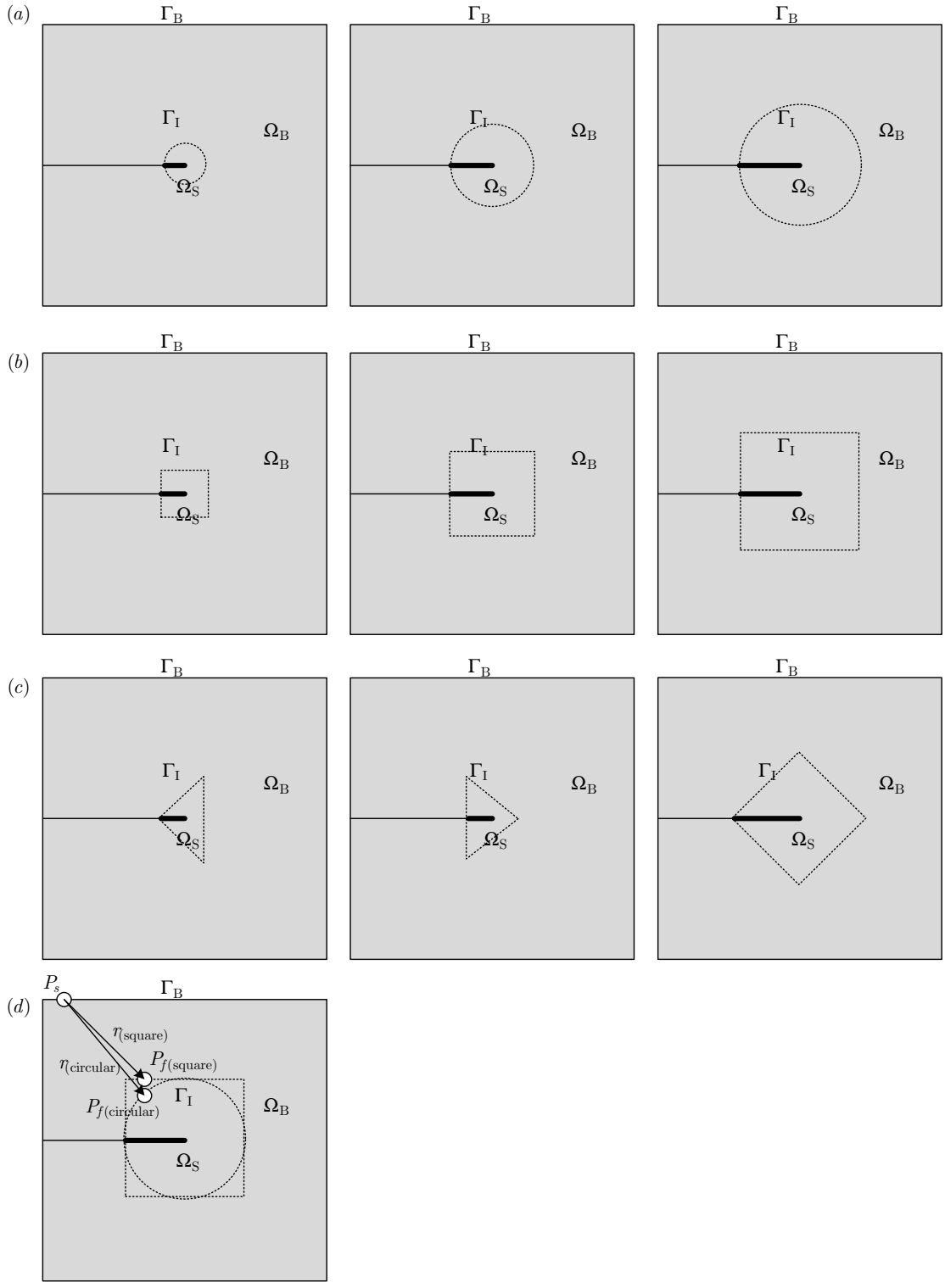

Figure 108. Parameters to be investigated further for general improvements of the DBE-SBFEM include (*a*) size, (*b*) shape and (*c*) orientation of Ω_S and (*d*) its proximity to Γ_s

5.7.2 Applications of the DBE-SBFEM

Due to the symmetric nature of the problems in §5.6.2 and §5.6.2 which the propagation angle θ is known *a priori* to be $\theta = 0$, the effect of $\mathbf{T}_\theta$ on $\mathbf{K}_\mathrm{S}$ is expected to be low and is confirmed as $\varepsilon_K \approx 10^{-13}$. The accuracy of each reanalysis iteration is described using $\varepsilon_{L^2 k}$ is illustrated in Figure 98(b). In both examples, such is the accuracy of the reanalysed solution, there is no visible distinction between the accuracy of the reanalysis and full analysis. Further results, not published here, confirm similar trends for the finer initial mesh densities in which the initial mesh is subject to uniform mesh subdivision before reanalysis is employed. With this example, where the propagation angle θ is known *a priori* to be $\theta = 0$, it is confirmed that the reanalysis accuracy associated low angular perturbation of Ω_S described in §5.5.1, extends to the global error estimator $\varepsilon_{L^2 k}$.

The mixed mode example illustrates that reanalysis can be successfully employed with the rotational perturbation of the SBFEM subdomain by transforming the stiffness matrix. Errors are based on the differences between the reanalysis result and the equivalent full analysis. These errors were greater than those for the example that required no rotation of the stiffness matrix. This could be because the condition number of the matrix of modal displacement vectors $\kappa(\Phi) \approx 10^8$ and its effect on introducing significant imaginary components to $\mathbf{c}$, as discussed in §3.10. However, as shown, for even a crude initial mesh, in which 90^o arcs are meshed with just one quadratic element, the computed errors are low.

In each case, Figure 98(a) and Figure 101(a) indicate substantial savings in computation times can be made if reanalysis is employed. For the less trivial

example in §5.6.3, the normalised computation time stabilises quicker than in the previous examples owing to the greater proportion of reusable data between analyses, demonstrating the suitability of the reanalysis of crack propagation in non-trivial domains. The rate of convergence of this difference is not illustrated as the objective of this example is to demonstrate the flexibility, not describe convergence characteristics of arbitrary models unavailable for comparison elsewhere in the literature.

It can be seen that for domains of small rotational perturbation the reanalysed matrices offer good approximations to the fully analysed equivalent. However, Figure 91 illustrates that further to the usual problem of high mesh densities contributing to errors owing to the near-paralisation of the eigenvectors, it is not recommended that reanalysis be used for domains subject to high rotational perturbation. The stability of results can be linked to the condition number of $\mathbf{K}_{\tilde{\mathrm{S}}}$, shown in Figure 91(b), which itself may be linked to $\kappa(\mathbf{\Phi})$. This may serve as an indicator that the rotational perturbation is too great for its accurate approximation to $\mathbf{K}_{\mathrm{S}}$. In this example rotational perturbation should be limited to $0.1\,\mathrm{rad}$.

5.8 Conclusion

With the new analytical integration of hyper singular BEM kernels (Simpson and Bird, 2009) and the semi-discontinuous scaled boundary finite element (Bird *et al.*, 2009a), a coupled dual boundary element-scaled boundary finite element method has been presented. Its application to fracture mechanics has yielded satisfactory results. Investigations into refining its constituent methods' parameters have provided some improvements, but caution should be taken in order to avoid a loss in general applicability. Further

investigations are recommended.

The introduction of the rotational transformation matrix facilitates the use of reanalysis for a crack propagation scheme. An example of this has been presented to demonstrate this, although a more robust propagation scheme could be considered in future work for more accurate reanalysis-based propagation. The use of reanalysis has shown to reduce the computational times for the coupled method by reusing data common to multiple analyses. These savings are exemplified when reanalysis is applied to non-trivial domains.

6 A displacement boundary integral equation-based dual boundary element method

6.1 Introduction

In this chapter, a new dual boundary element method (DBEM) formulation is introduced. As part of the present work, its motivation is presented alongside a detailed numerical formulation to demonstrate the method's suitability for applications to fracture mechanics. Formed using the *displacement boundary integral equation* (DBIE), rather than the *traction boundary integral equation* (TBIE), the new and existing formulations are compared and assessed through examples.

Unless otherwise stated, the data in numerical examples in this chapter are obtained by the development of the author's own code. For purposes of disambiguity, unless otherwise stated, the development of the new *dual (displacement BIE) BEM* (DdBEM) formulation is as a direct result of the present work.

The chapter is closed with concluding remarks.

6.2 New formulation

As described in §2.8, the use of the BEM to model both the upper and lower faces of a crack causes duplicate rows in the system described by equation (2.103). By replacing the rows in the system matrix found through DBEM collocation, with those found using DdBEM, row-uniqueness is assured and the system is solvable. The DBEM is not without its complications, however, and requires the computation of hyper-singular integrals, offers limited applicability and may increase the condition number of the system with typical engineering materials from around between 10^0 and 10^2 to around between 10^{11} and 10^{13}.

By reformulating the DBEM using the DBIE, many of these disadvantages are overcome. Moreover, the alterations to standard BEM code necessary to accommodate the DdBEM may be less demanding than the DBEM.

6.3 Numerical formulation

The need for the DBEM arises as the nodes defining the elements on the upper and lower crack surfaces are coincident. The underlying characteristic of the DBEM due to this assumption is the ill-conditioning described in §2.8.

The new formulation staggers the nodes on coincident elements such that their respective nodes are no longer coincident, as illustrated in Figure 109 also showing their respective shape functions. In the examples in the figure, the elements are shown with a finite vertical separation for illustrative purposes only and are defined coincidentally. As such, a distinction is made when collocating at each of the nodes defining the upper and lower elements.

Consider the upper element, for example. As with the DBEM, the presence of degrees of freedom on the lower element within the bounded range $-1 < \eta < 1$ causes singular behaviour at these nodes. Unlike in the DBEM, these singularities no longer coincide with existing nodes on the upper element, as indicated by the 'x' marks in Figure 109(b).

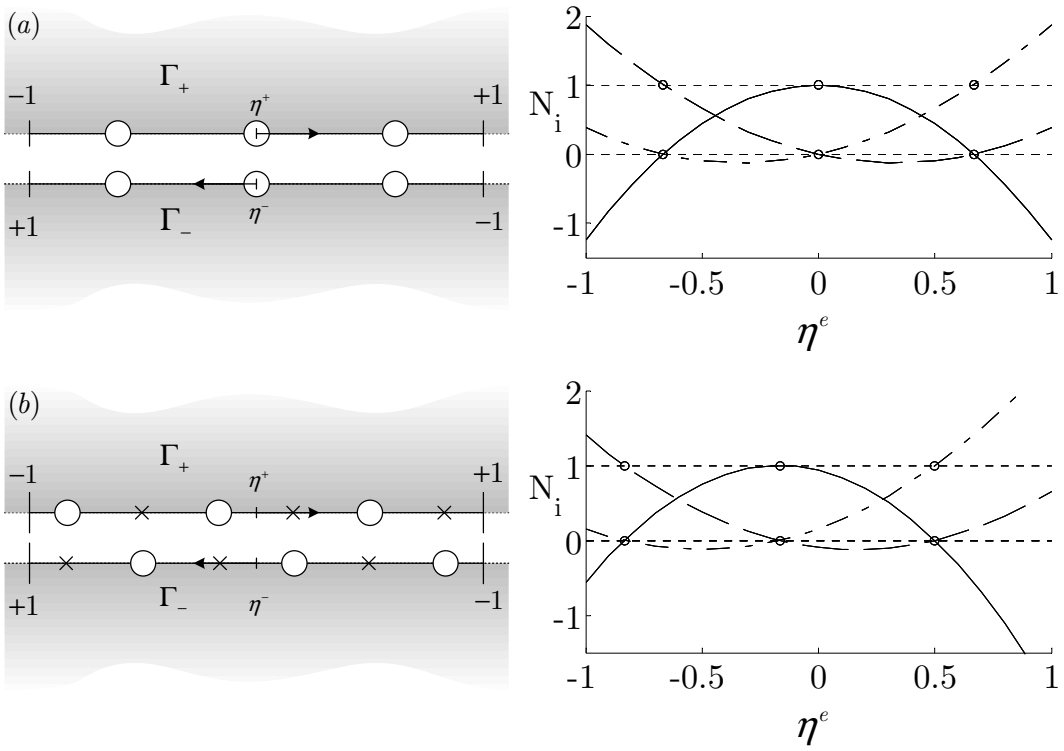

Figure 109. Coincident elements, and their respective shape functions, modelling the crack faces defined by (*a*) coincident nodes and (*b*) non-coincident nodes. The crosses indicate the local coordinates of singularities in the kernels owing to the degrees of freedom on the opposing elements

However, as the DBIE is used to integrate over the upper element, unlike with the TBIE, these singularities are merely weakly- and strongly-singular, rather than strongly- and hyper-singular. The analytical form of the integrals used in the BEM can be used in the DdBEM, hence the development as part of the

present work of equation (2.80) for general discontinuous quadratic elements. Similarly, when considering the lower element, weak and strong singularities exist due to nodes on the upper element.

6.4 Applications to fracture mechanics

6.4.1 Through crack in an infinite plate

In this example, the same approach is taken as in §2.10.3 except that, with reference to Figure 110, the DdBEM is used in on both the upper and lower crack surfaces in place of both the BEM and DBEM respectively. The displacement of the domain is illustrated in Figure 111. Again, and particularly at the crack tip (where $s=1$), the inaccuracies of this discontinuous element-based method are highlighted, as illustrated in Figure 112. The convergence characteristics due to the uniform subdivision of the mesh are illustrated in Figure 113.

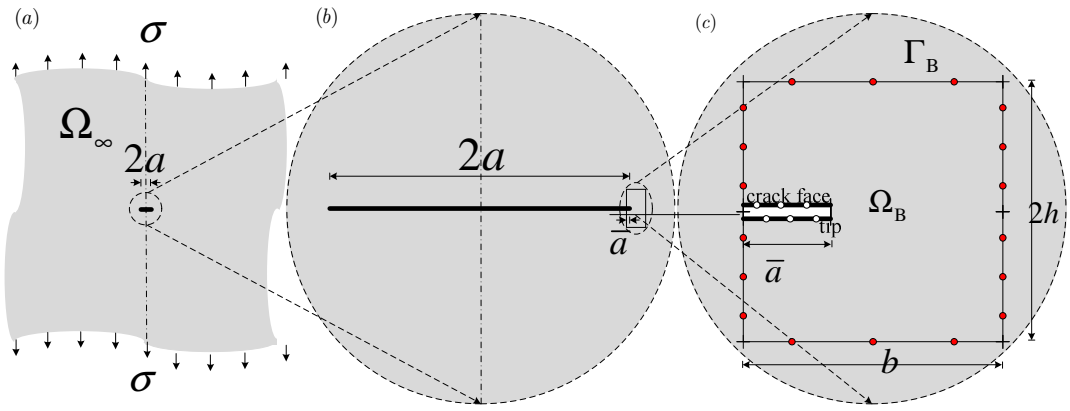

Figure 110. DdBEM analysis of (a) through crack in an infinite plate, (b) the section of the domain modelled, and (c) the mesh where red and white nodes indicate $\Gamma_{\tilde{u}}$ and Γ_u

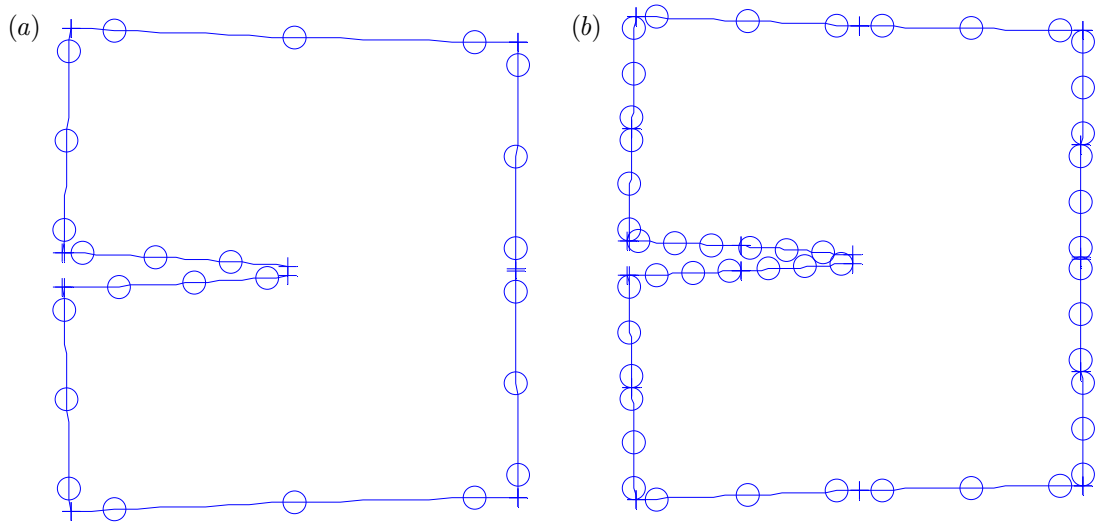

Figure 111. To-scale deformation of (a) initial mesh and (b) uniformly-refined mesh

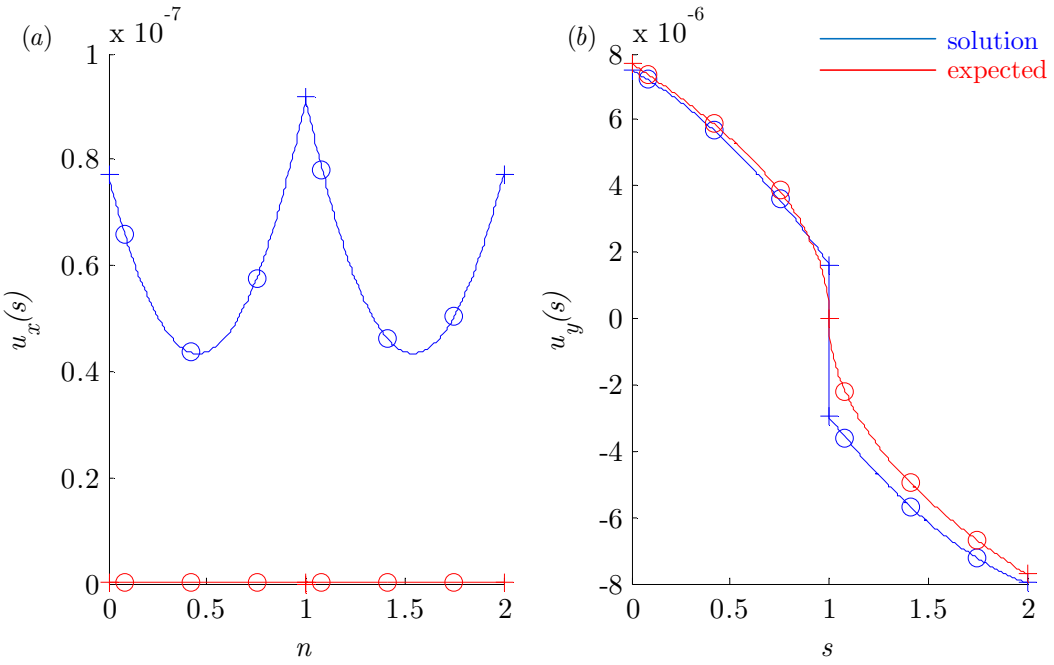

Figure 112. (a) x- and (b) y-direction displacement results on Γ_u

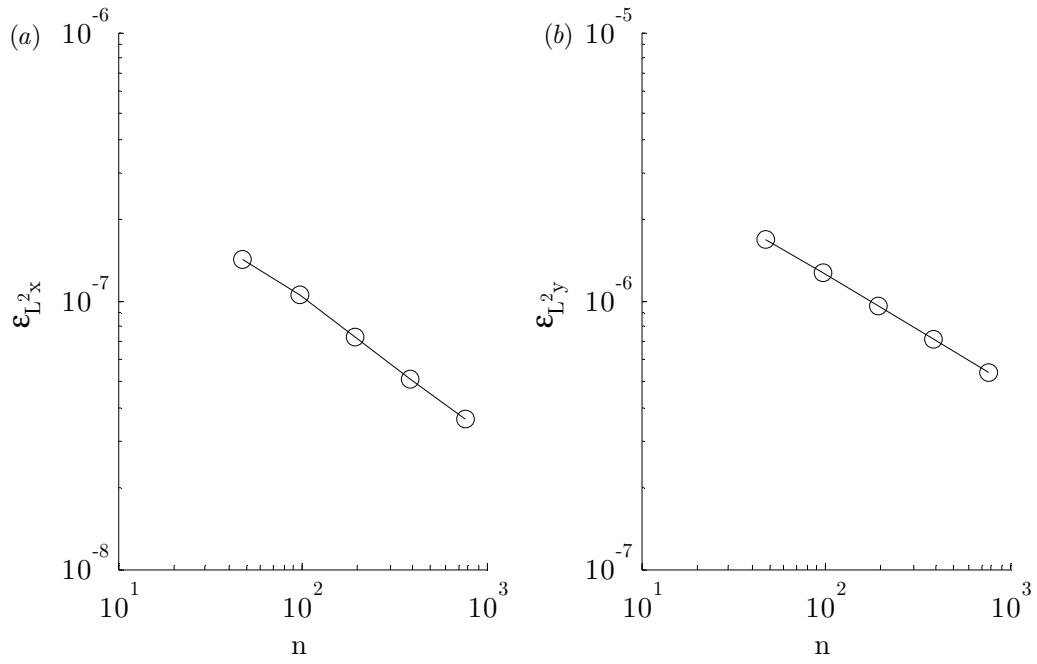

Figure 113. Convergence characteristics of global error estimators (a) ε_{L^2x} and (b) ε_{L^2y}

6.5 Discussion

Many of the disadvantages of the traditional DBEM occur in the new DdBEM. The need for discontinuous elements at coincident sections of boundary is maintained, and this lack of continuity results in noticeable jumps in the displacement solution between elements and any derived values, just as with the DBEM.

However, because the DdBEM poses no further integration problems than the BEM, boundary conditions applicable to the BEM are applicable to the DdBEM too. As such, no *a priori* knowledge or assumption of traction-free boundary conditions on coincident sections of boundary is required in order to side-step the awkward strongly-singular integration of the DBEM kernels, significantly increasing the applicability of the BEM.

The application of assumed boundary conditions has traditionally facilitated the avoidance of some singular integration in the DBEM, as discussed in §2.5.

Throughout this work, it has not been the intention to select purposely examples that offer particular advantages owing to their respective choice of configurable parameters. Thus, that the absolute accuracy of the DdBEM is lower than the DBEM in the example chosen is of less importance than its general convergence characteristics which have been demonstrated to mimic that of the DBEM. Indeed, in a manner similar to that illustrated in §2.11, it can be demonstrated the DdBEM may outperform the DBEM under certain configurations. However, it is beyond the scope of this work to optimise the DdBEM such that it may consistently outperform the DBEM in terms of accuracy, merely to demonstrate a new and simpler method of using the DBEM.

6.6 Conclusion

The existing traction boundary integral equation-based (TBIE) formulation of dual boundary element method (DBEM) has been replaced by a new formulation based on the displacement boundary integral equation (DBIE) forming the DdBEM. The new formulation represents a new means to model domains involving discontinuities, which until now, required the use of domain subdivision or the use of the existing formulation. The benefits of the new formulation include its inclusion into existing boundary element method (BEM) code with more readiness than the older formulation. Moreover, the new formulation has been demonstrated to reduce the condition number of the BEM system matrix by an order of approximately 10^9.

By no means does the author conclude this proof of principle demonstrates that the DdBEM has been exhaustively evaluated. It is recommended that further work explores the stability and usefulness of this method. But by replacing the traction boundary integral equation-based dual boundary element method with the new formulation, the coupled dual boundary element-scaled boundary finite element method can incorporate these advantages over its predecessor.

7 Discussion

7.1 Introduction

The aim of the present work is to develop and assess a new algorithm for the accurate solution of general fracture mechanics problems that retains the geometric flexibility expected by engineers. With respect to this goal, this chapter summarises the discussions on the numerical methods and their implementation. First, the usual approach to numerical method verification is discussed, prompting motivation for the alternative, and preferred, testing protocol used in this work. A comparison of the numerical methods presented in this thesis is summarised and recommendations for further research are made.

7.2 Assessment of method implementation

As part of the present work, the code of Chidgzey (Chidgzey, 2007) was made available to the author for evaluating T-stresses computed by the coupled BE-SBFEM (Chidgzey *et al.*, 2008). Several limitations were identified. The top-down approach to coding and testing prevented the clear identification of whether these limitations were characteristic of the method or its

implementation. By rewriting the code using a bottom-up approach, a better such distinction is drawn.

By considering functions as simple black-box operations for which a range of inputs provide a range of expected outputs (Appendix F), its limitations can be estimated through unit testing. Each level of functionality is then bound by the identified limitations its respective lower level functions. This offers means by which the quality of implementation can be judged. If the cause for specific test failures cannot be identified, the code is asserted for its characteristics, preventing speculation over hereditary functional failure common under the top-down approach. This is useful when high level functions, such as the implementation of the numerical methods presented here, are under scrutiny. This preference for unit tests over acceptance tests has the further benefit that the impact of addressing errors and functional limitations is more easily assessed. Together, this reduces the scope for error in the acceptance tests, providing additional confidence they are representative of the method more than its implementation.

7.3 Comparison of results

The examples of applications to fracture mechanics of each of the methods here were chosen in order to facilitate their. Each method has demonstrated some level of convergence, indicating their suitabilitly towards such problems. Convergence characteristics are defined as the rate of reduction R in error per degree of freedom n and are summarised in Table 114. Typical values of R are given as convergence has been shown to be heavily problem-specific and varies according to the type of error indicator. Caution should be taken when comparing methods as the definition and computation of each degree of

freedom varies widely between methods impacting on its efficiency. However, it can be seen that each method offers convergence for the fracture mechanics problems analysed.

Method	$O(R)$
BEM	10^{-10}
DBEM	10^{-10}
DdBEM	10^{-10}
SBFEM	10^{-4}
BE-SBFEM	10^{-10}
DBE-SBFEM	10^{-5}

Table 114. Comparison of method performance by approximate order of convergence

7.4 Assessment of methods

The BEM benefits from its versatility and ease of implementation and performs well in terms of modelling general engineering domains, but is hampered significantly by the non-polynomial nature of the crack face displacement functions in the vicinity of the crack tip that yield poor boundary and interior results. Although exacerbating such errors, the use of discontinuous elements further eases implementation; by providing additional interior points to the boundary solution, a multizone approach may offer improved accuracy but at the expense of implementation ease and efficiency. Accuracy can be improved further by the *in*-process adaptive integration scheme presented here, which, albeit computationally expensive, is less expensive than a *post*-process-based mesh refinement scheme.

The DBEM increases the flexibility of the BEM at the expense of the introduction of hyper-singular integration and, depending on material properties, a raise in condition number by a factor of around 10^8. Scaling factors may offer a reduction, but require *a priori* knowledge of the expected

ratio of traction to displacement orders of magnitude. Without the assumption of traction-free crack faces, the DBEM significantly increases in complexity as the coefficients of traction in the influence matrix can no longer be ignored. The DdBEM facilitates loaded crack faces and, as it is based on the DBIE, is no more complex to implement than the BEM. Moreover, condition numbers remain comparable to the BEM.

Although a relatively new method, the SBFEM has recently received positive reaction in the literature due to its ability to capture the stress singularities with greater accuracy than the polynomial-based BEM. However, its strengths and weaknesses have not yet been so rigorously assessed. In addition to its known line-of-sight restrictions and numerical instability under high mesh densities, the present work has identified further geometric limitations. Complex domain and boundary condition combinations lead to ill-conditioned system matrices that may precipitate numerical instability, rendering the SBFEM susceptible to inaccuracies when applied to general engineering problems and meshed with fewer than 3 elements per discretised face.

The coupled BE-SBFEM has demonstrated a balanced compromise between the efficiency and accuracy of the SBFEM and flexibility of the BEM, and the presented reformulation increases the range of boundary conditions that can be applied. However, its working assumption of symmetry hampers its attractiveness as a solution to general engineering problems.

The coupled DBE-SBFEM addresses the issue of symmetry, but at the expense of further implementation difficulties. Additional consideration is required where the subdomain interface meets the crack face. However, for this purpose, new semi-discontinuous scaled boundary finite elements have

been developed as part of the present work and have shown comparable accuracy. Through a crack propagation scheme, the method has demonstrated its suitability to the use of reanalysis in fracture mechanics problems. Significant computational savings have been observed in the rudimentary propagation algorithm presented here. Considerably higher savings are expected for a predictor/corrector-based scheme in which larger portions of the existing matrices can be reused between iterations.

7.5 Recommendations for further work

The coupled DdBE-SBFEM has not yet been implemented and remains a recommendation for further research. Its advantages over the DBE-SBFEM are expected to mimic those that the DdBEM has over the DBEM. Like the DBE-SBFEM, there is scope for improvement of the parameters relating to the interface between the BEM and SBFEM subdomains. Further research is recommended, but should regard the intention of developing a general algorithm for real fracture mechanics problems rather than a solution geared towards the optimisation of a specific, academic problem.

In addition to the interface parameters, more research is recommended on the constituent methods. The DdBEM has been shown to perform comparably to the DBEM for the selected example, it is recommended that the application of boundary conditions other than traction-free crack faces be explored. However, this new method requires substantial further research to assess its stability and suitability to general fracture mechanics problems. As with the BEM, a strategy for optimising the local nodal distribution offers scope for investigation.

Like the original form of the SBFEM, side face traction boundary conditions

must be applied in terms of modal coefficients at the side face node. Although this is not demonstrated in the present work, a similar approach is expected for the semi-discontinuous SBFEM. Without a node on the side face, however, boundary conditions cannot be applied directly. Instead, boundary conditions must be computed that once applied to the neighbouring semi-discontinuous element can be extrapolated to $\eta = \pm 1$ such that the required conditions are prescribed on the side face.

As a relatively new and unexplored method, the SBFEM remains largely in its original form (Wolf and Song, 1995). The use of side faces to model the singular functions on a geometrically linear crack face has been demonstrated both historically and in this thesis, such as in Figure 115(a). However, the use of a non-linearly varying scaling function may facilitate the modelling of a geometrically non-linear crack face. Not be confused with Figure 115(b), in which the geometric boundary is subject only to translation scaled by ξ, if the geometric boundary is subject to additional rotation, as illustrated in Figure 115(c), curved side faces can be formed. This requires an alternative mapping between the Cartesian coordinates and the scaled boundary coordinate system, but once mapped, the existing method of element-wise boundary integration leading to a modal superposition-based solution form is retained.

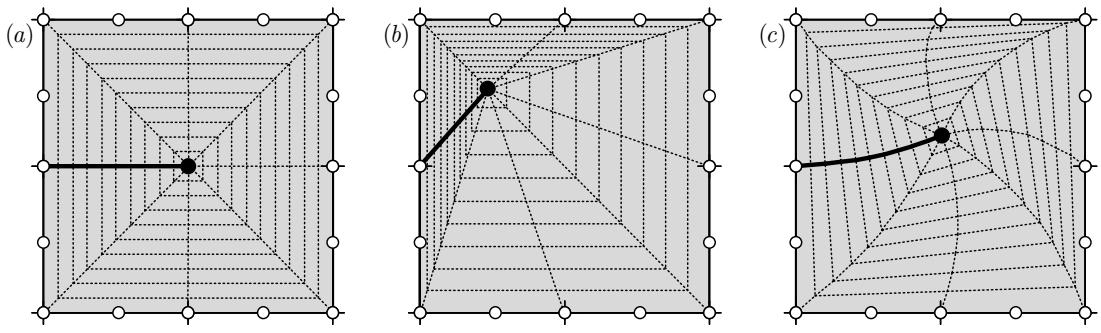

Figure 115. Geometrically linear boundary scaling about a SBFEM scaling centre

The coupled method has been demonstrated to employ reanalysis to good effect in the area of linear elastic fracture mechanics. A number of improvements to the crack propagation algorithm is possible. While the scope of the present work was to couple the methods for use in such algorithms, it does not extend to its optimised use within them. As such, it is recommended that the DBE-SFBEM and DdBEM-SBFEM with reanalysis are used in conjunction with other propagation schemes in the literature. The benefit of reanalysis is expected to be highlighted by multi-analysis iterations of crack growth such as by (Aliabadi, 1997) in which the predictor/corrector approach offers such scope for efficiency.

8 Conclusion

The aim of the work presented here was the development and assessment of a new algorithm for the accurate solution to general fracture mechanics problems that retains the geometric flexibility expected by engineers. The coupled DBE-SBFEM has demonstrated a balanced compromise between the efficiency and accuracy of the SBFEM and flexibility of the BEM. The inclusion of the DBEM negates the need for an assumption of symmetry, lending itself towards its application to general engineering problems. Further, reanalysis is used to great effect, demonstrated as part of a rudimentary crack propagation algorithm. The new DdBEM has shown promise as an alternative to the DBEM and its inclusion is expected both to reduce the method's complexity and increase its range of application to fracture mechanics in general engineering problems.

The coupled method has been implemented under a modern computer science framework using a bottom-up approach to testing that both narrows the scope for coding errors and increases their detection. Extensions have been made to each of the coupled method's constituents and by code and method generalisation, has facilitated investigations into their respective numerical

stability. Further extensions have been recommended for further research. In addition to presenting the methods through clear approaches not found elsewhere, the present work offers insight into the consequences of selected numerical parameters that were otherwise considered arbitrary.

The coupled method has been tested extensively and performed strongly against academic problems with known analytical solutions. With its general approach to parametric optimisation, it can be concluded that the coupled DBE-SBFEM with reanalysis provides a new flexible, accurate and efficient tool for general fracture mechanics problems found in engineering.

9 References

Air Accidents Investigation Branch, 2011. Report on the accident to Aerospatiale (Eurocopter) AS332 L2 Super Puma, registration G-REDL 11 nm NE of Peterhead, Scotland on 1 April 2009. UK: Department for Transport *Air Accidents Investigation Branch*, Aircraft accident report.

Aliabadi, M.H., 1997. A new generation of boundary element methods in fracture mechanics. *International Journal of Fracture*, 86, p91-125.

Aliabadi, M.H., 2002. *The boundary element method volume 2: applications in solids and structures*. John Wiley & Sons.

Ali, A. and Rajakumar, C., 2004. *The Boundary Element Method Applications in Sound and Vibration*. London: A. A. Balkema Publishers.

Astels, D., 2003. *Test-Driven Development: A Practical Guide*. Prentice Hall.

Ayatollahi, M.R., Zakeri, M. and Hassani, M.M., 2005. On the presence of T-stress in mode II crack problems. In *Proceedings of the 11th International Conference on Fracture- ICF11*. Turin, Italy,.

Becker, A.A., 1992. *The boundary element method in engineering: a complete course*. Mcgraw-Hill.

Beer, G., 2001. *Programming the boundary element method*. John Wiley & Sons.

Bird, G.E., Trevelyan, J. and Augarde, C.E., 2008a. Efficient calculation of stress intensity factors using a coupled BEM-SBFEM algorithm. In *Programme of the joint 8th World Congress on Computational Mechanics & 5th European Congress on Computational Methods in Applied Sciences and Engineering*. Venice,.

Bird, G.E., Trevelyan, J. and Augarde, C.E., 2008b. Coupling of the BEM and SBFEM for fracture mechanics. In *Proceedings of the 16th UK national conference on computational mechanics in engineering*. Newcastle, University of Newcastle.

Bird, G.E., Trevelyan, J. and Augarde, C.E., 2009a. A coupled boundary integral method for accurate computation of stress intensity factors. In *Proceedings of the 17th UK national conference on computational mechanics in engineering*. Nottingham, University of Nottingham.

Bird, G.E., Trevelyan, J. and Augarde, C.E., 2009b. A semi-discontinuous scaled boundary finite element for the coupled BEM-SBFEM. In *Proceedings of the 7th UK conference on Boundary Integral Methods*. Nottingham, University of Nottingham.

Bird, G.E., Trevelyan, J. and Augarde, C.E., 2010. A coupled BEM/Scaled boundary FEM formulation for accurate computations in linear elastic stress analysis. *Engineering Analysis with Boundary Elements (in press)*.

Bird, G.E., Trevelyan, J., Augarde, C.E., Deeks, A.J. and Chidgzey, S.R., 2007. Coupling of the BEM with the SBFEM for fracture mechanics problems. In *Proceedings of the 6th UK conference on Boundary Integral Methods*. Durham, Durham University.

Blandford, G.E., Ingraffea, A.R. and Liggett, J.A., 1981. Two-dimensional stress intensity factor computations using the boundary element method. *International journal for numerical methods in engineering*, 17, p387-404.

Charafi, A., Neves, A.C. and Wrobel, L.C., 1995. h-Hierarchical adaptive boundary element method using local reanalysis. *International Journal for Numerical Methods in Engineering*, 38(13), p.2185–2207.

Cheng, A.H.-D. and Cheng, D.T., 2005. Heritage and early history of the boundary element method. *Engineering Analysis with Boundary Elements*, 29, p268-302.

Chen, J.T. and Hong, H.-K., 1999. Review of dual boundary element methods with emphasis on hypersingular integrals and divergent series. *Applied Mechanics Reviews*, 52(1), p17-33.

Chidgzey, S.R., 2007. *Advances in the development of the scaled boundary method for applications in fracture*. Perth, Australia: Doctoral Thesis.

Chidgzey, S.R., 2007. Modal displacement calculation for SBFEM. *Internal report (unpublished)*,

Chidgzey, S.R. and Deeks, A.J., 2005. Determination of coefficients of crack tip asymptotic fields using the scaled boundary finite element method. *Engineering Fracture Mechanics*, p2019-36.

Chidgzey, S.R., Trevelyan, J. and Deeks, A.J., 2008. Coupling of the boundary element method and the scaled boundary finite element method for computations in fracture mechanics. *Computers and Structures* , 86(11-12), p1198-203.

Chuin-Shan, C., Krause, R., Petite, G.R., Banks-Sills, L. and Ingraffea, A.R., 2000. Numerical assessment of T-stress computation uinsg a p-adaptive finite element method. *International Journal of Fracture*, 107, p177-99.

Cotterell, B. and Rice, J.R., 1980. Slightly Curved or Kinked Cracks. *International Journal of Fracture, Vol. 16, No. 2, April 1980*, 16(2), p155-69.

Cruse, T.A., 1973. Application of the boundary-integral equation method to three dimensional stress analysis. *Computers and Structures*, 3, p509-27.

Cruse, T.A. and Osias, J.R., 1991. Issues in merging the finite element and boundary integral equation methods. *Mathematical Computational Modelling*, 15(3-5), p103-18.

Deeks, A.J., 2004. Prescribed side-face displacements in the scaled boundary finite-element method. *Computers and Structure*, 82(15-16), p1153-1165.

Deeks, A.J., 2009. *Personal communication with G. E. Bird and J. Trevelyan.* Durham University, Durham.

Deeks, A., J. and Wolf, J.P., 2003. Semi-analytical solution of Laplace's equation in non-equilibrating unbounded problems. *Computers and Structures*, 81, p1525-37.

Deeks, A.J. and Augarde, C.E., 2005. A meshless local Petrov-Galerkin scaled boundary method. *Computational Mechanics*, 36, p150-70.

Deeks, A.J. and Augarde, C.E., 2007. A hybrid meshless local Petrov-Galerkin method for unbounded domains. *Computer Methods in Applied Mechanics in Engineering*, 196, p843-52.

Deeks, A.J. and Wolf, J.P., 2002a. A virtual work derivation of the scaled boundary finite-element method for elastostatics. *Computational Mechanics*, 28, p489-504.

Deeks, A.J. and Wolf, J.P., 2002. An h-hierarchical adaptive procedure for the scaled boundary finite-element method. *International Journal for*

Numerical Methods in Engineering, 54, p585-605.

Deeks, A.J. and Wolf, J.P., 2002b. Stress recovery and error estimation for the scaled boundary finite-element method. *International Journal for Numerical Methods in Engineering*, 54, p557-83.

Deeks, A.J. and Wolf, J.P., 2005. Adaptive coupling of the finite-element and scaled boundary finite-element methods for non-linear analysis of unbounded media. *Computers and Geotechnics*, 32(6), p436-44.

Doherty, J.P. and Deeks, A.J., 2005. Adaptive coupling of the finite-element and scaled boundary finite-element methods for non-linear analysis of unbounded media. *Computers and Geotechnics*, 32(6), p436-44.

Dong, C.Y., 2001. An iterative FE-BE coupling method for elastostatics. *Computers and Structures*, 79, p293-99.

Elleithy, W.M., Al-Gahtani, H.J. and El-Gebeily, M., 2001. Iterative coupling of BE and FE methods in elastostatics. *Engineering Analysis with Boundary Elements*, 25, p685-95.

Ezawa, Y. and Okamoto, N., 1995. Development of contact stress analysis programs using the hybrid method of FEM and BEM. *Computers and Structures*, 57(4), p691-98.

Fedelinski, P., Aliabadi, M.H. and Rooke, D.P., 1995. A single-region time domain BEM for dynamic crack problems. *International Journal of Solids and Structures*, 32(24), p3555-71.

Fett, T., 1998. T-stresses in rectangular and circular disks. *Engineering Fracture Mechanics*, 60(5-6), p631-52.

Fett, T., 2001. Stress intensity factors and T-stress for internally cracked circular disks under various boundary conditions. *Engineering Fracture Mechanics*, 68, p1119-36.

Fleck, N.A., J., K.K. and F., A.M., 1994. The cyclical properties of engineering materials. *Acta Metallurgica et Materialia*, 42(2), p365-81.

Fowler, M., Beck, K.B.J., Opdyke, W. and Roberts, D., 1999. *Refactoring: Improving the Design of Existing Code*. Addison-Wesley Professional.

Freeman, E. and Freeman, E., 2004. *Head First Design Patters: A brain-friendly guide*. O'Reilly Media.

Garcia-Sanchez, F. and Zhang, C., 2007. A comparative study of three BEM for transient dynamic crack analysis of 2-D anisotropic solids. *Computational Mechanics*, 40, p753-69.

Griffith, A.A., 1920. The Phenomena of Rupture and Flow in Solids. *Philosophical Transactions of the Royal Society of London*, 221, p163-98.

Guiggiani, M. and Casalini, P., 1987. Direct computation of Cauchy principal value integrals in advanced boundary elements. *International Journal for Numerical Methods in Engineering*, 24, p1711-20.

Guru Prasad, K., Kane, J.H., Keyes, D.E. and Balakrishna, C., 1994. Preconditioned Krylov solvers for BEA. *International Journal for Numerical Methods in Engineering*, 37, p1651-72.

Hong, H. and Chen, J., 1988. Derivations of integral equations of elasticity. *Journal of Engineering Mechanics*, 114, p1028-44.

Irwin, G., 1957. Analysis of stresses and strains near the end of a crack traversing a plate. *Journal of Applied Mechanics*, 24, p361-64.

Karihaloo, B.L. and Xiao, Q.Z., 2001. Accurate determination of the coefficients of elastic crack tip asymtotic field by a hybrid crack element with p-adaptivity. *Engineering Fracture Mechanics*, 68, p1609-30.

Karlis, G.F., Tsinopoulos, S.V., Polyzos, D. and Beskos, D.E., 2007. Boundary element analysis of mode I and mixed mode (I and II) crack problems of 2-D gradient elasticity. *Computer Methods in Applied Mechanics and Engineering*, 196, p5092-103.

Kita, E., Higuchi, K. and Kamiya, N., 2000. Application of r- and hr- adaptive BEM to two-dimensional elastic problem. *Engineering Analysis with Boundary Elements*, 24, p31-324.

Leung, K.L., Zavareh, P.B. and Beskos, D.E., 1995. 2-D elastostatic analysis by a symmetric BEM/FEM scheme. *Engineering Analysis with Boundary Elements*, 15, p67-78.

Liao, Y.-S., Chyuan, S.-W. and Chen, J.-T., 2004. An alternatively efficient method (DBEM) for simulating the electrostatic field and levitating force of a MEMS combdrive. *Journal of micromechanics and microengineering*, 14, p.1258–1269.

Liew, K.M., Sun, Y. and Kitipornchai, S., 2007. Boundary element-free method for fracture analysis of 2-D anisotropic piezoelectric solids. *International Journal for Numerical Methods in Engineering*, 69, p729-49.

Marburg, S. and Schneider, S., 2003. Influence of element types on numeric error for acoustic boundary elements. *Journal of Compuational*

Acoustics, 11(3), p363-86.

Moes, N. and Belytschko, T., 2002. Extended finite element method for cohesive crack growth. *Engineering Fracture Mechanics*, 69, p813-33.

Oysu, C. and Fenner, R., 2006. Coupled FEM-BEM for elastoplastic contact problems using Lagrange multipliers. *Applied Mathematical Modelling*, 30, p231-47.

Padhi, G.S., Shenoi, R.A., Moy, S.S.J. and McCarthy, M.A., 2001. Analytical integration of kernal shape function product integrals in the boundary element method. *Computers and Structures*, 79, p1325-33.

Portela, A., Aliabadi, M.H. and Rooke, D.P., 1992. Dual boundary element analysis of cracked plates: singularity subtraction technique. *International Journal of Fracture*, 55, p17-28.

Portela, A., Aliabadi, H.M. and Rooke, P.D., 1992. The dual boundary element method: effective implementation for crack problems. *International journal for numerical methods in engineering*, 33, p1269-87.

Portela, A., Aliabadi, M.H. and Rooke, D.P., 1993. Dual boundary element incremental analysis of crack propagation. *Computers and Structures*, 46(2), p237-47.

Rajan, V.S.P. and Raju, K.C.J., 2002. A Novel Scaled Boundary Finite Element Method in Computational Electromagnetics. Hyderabad: http://arxiv.org/ *University of Hyderabad*,

Roylance, D., 1996. *Mechanics of Materials*. Boston: Wiley.

Saad, Y. and Schultz, M.H., 1986. GMRES: A generalized minimal residual algorithm for solving nonsymmetric linear systems. *Society for Industrial and Applied Mathematics*, 7(3), p856-69.

Saad, Y. and Schultz, M.H., 1986. GMRES: A generalized minimal residual algorithm for solving nonsymmetric linear systems. *SIAM J. Sci. Stat. Comput*, 7, p856-69.

Sfantos, G.K. and Aliabadi, M.H., 2007. Multi-scale boundary element modelling of material degradation and fracture. *Computational Methods in Applied Mechanics and Engineering*, 196(7), p1310-29.

Simpson, R., 2010. *Enrichment of the Boundary Element Method through the Partition of Unity Method for Fracture Analysis using Local and Global Formulations*. Doctoral Thesis.

Simpson, R. and Bird, G.E., 2009. The analytical computation of

hypersingular integrals in the Dual Boundary Element Method for flat quadratic elements with a general nodal distrubtion. *School of Engineering, Durham University*, Internal report (unpublished).

Simpson, R. and Trevelyan, J., 2008. Enrichment of the BEM with Partition of Unity Method for fracture and fatigue analysis. In *16th UK Conference on Computational Mechanics, (2008).* Newcastle-upon-Tyne,.

Sladek, V. and Sladek, J., 1986. The calculation of singular integrals in the boundary integral formulation of two-dimensional elastostatics. *Engineering Analysis*, 3(1), p25-35.

Sladek, V. and Sladek, J., 1991. Why use double nodes in BEM? *Engineering Analysis with Boundary Elements*, 8(2), p109-12.

Sladek, V. and Sladek, J., 1995. Regularization of hypersingular integrals in BEM formulations using various kinds of continuous elements. *Engineering Analysis with Boundary Elements*, 17, p5-18.

Song, C., 2004. A matrix function solution for the scaled boundary finite-element equation in statics. *Computer Methods in Applied Mechanics and Engineering*, 193, p2325-56.

Song, C. and Wolf, J.P., 1997. The scaled boundary finite-element method - alias consistent infinitesimal finite-element cell method - for elastodynamics. *Computational Methods in Applied Mechanics and Engineering*, 147, p329-55.

Song, C. and Wolf, J.P., 1998. Song, Ch. and Wolf, J.P. (1998), "The scaled boundary finite-element method: analytical solution in frequency domain", Computer Methods in Applied Mechanics and Engineering, Vol. 164, 249-264.. *Computer Methods in Applied Mechanics and Engineering*, 164, p249-64.

Song, C. and Wolf, J.P., 1999. Body loads in scaled boundary finite-element method. *Computer Methods in Applied Mechanics and Engineering*, 180, p117-35.

Song, C. and Wolf, J.P., 2000. The scaled boundary finite-element method - a primer: solution procedures. *Computers and Structures*, 78, p211-25.

Telles, J.C.F., 1987. A self-adaptive co-ordinate transformation for efficient numerical evaluation of general boundary element integrals. *International Journal for Numerical Methods in Engineering*, 24(5), p959-73.

Trevelyan, J. and Chidgzey, S.R., 2007. Coupled BE-SBFEM limitations.

Internal report (unpublished),

Tvergaard, V. and Hutchinson, J.W., 1994. The effect of T-stress on a mode I crack growth in a ductile solid. *International Journal of Solids and Structures*, 31(6), p823-33.

Valente, F.P. and Pina, H.L.G., 1998. Iterative solvers for BEM algebraic systems of equations. *Engineering Analysis with Boundary Elements*, 22, p117-24.

Vu, T.H. and Deeks, A.J., 2006. Use of higher order shape functions in the scaled boundary finite element method. *International Journal for Numerical Methods in Engineering*, 65(10), p1714-33.

Vu, T.H. and Deeks, A.J., 2008. A p-adaptive scaled boundary finite element method based on maximization of the error decrease rate. *Computational Mechanics*, 41, p441-55.

Westergaard, H.M., 1939. Bearing pressures and cracks. *Journal of Applied Mechanics*, 6, p.A49–A53.

Wilde, A.J. and Aliabadi, M.J., 1999. A 3-D Dual BEM formulation for the analysis of crack growth. *Computational Mechanics*, 23, p250-57.

Williams, M.L., 1957. On the stress distribution at the base of a stationary crack. *Journal of applied mechanics*, p109-14.

Wolf, J.P. and Song, C., 1995. Consistent infinitesimal finite-element cell method: in-plane motion. *Computer Methods in Applied Mechanics and Engineering*, 123(3-4), p355-70.

Wolf, J.P. and Song, C., 1995. Unit-impulse response matrix of unbounded medium by infinitesimal finite-element cell method. *Computer Methods in Applied Mechanics and Engineering*, 122(3-4), p251-72.

Wolf, J.P. and Song, C., 2000. The scaled boundary finite-element method - a primer: derivations. *Computers and Structures*, p191-210.

Xiao, Q.Z. and Karihaloo, B.L., 2007. Implementation of hybrid crack element on a general finite element mesh and in combination with XFEM. *Computer Methods in Applied Mechanics and Engineering*, 196, p1864-73.

Yang, Z.J., 2006. Application of scaled boundary finite element method in static and dynamic fracture problems. *Acta Mech Sinica*, 22, p243-56.

Yang, Z., 2006. Fully automated modelling of mixed-mode crack propagation using scaled boundary finite element method. *Engineering Fracture Mechanics*, 73, p1711-31.

Yang, Z.J. and Deeks, A.J., 2006. A frequency-domain approach for modelling transient elastodynamics using scaled boundary finite element method. *Computational Mechanics*, 40(4), p725-38.

Yang, Z.J. and Deeks, A.J., 2007. Fully-automatic modelling of cohesive crack growth using a finite element–scaled boundary finite element coupled method. *Engineering Fracture Mechanics*, 74, p.2547–2573.

Yang, Z.J., Deeks, A.J. and Hao, H., 2006. A Frobenius solution to the scaled boundary finite element equations in frequency domain for bounded media. *International Journal for Numerical Methods in Engineeing*, 70(12), p1387-408.

Yang, Z., Deeks, A.J. and Hao, H., 2007. Transient dynamic fracture analysis using scaled boundary finite element method: a frequency-domain approach. *Engineering Fracture Mechanics*, 74, p669-87.

Yang, Z.J., Zhang, Z.H., Liu, G.H. and Ooi, E.T., 2011. An h-hierarchical adaptive scaled boundary finite element method for elastodynamics. *Computers and structures*, 89, p1417-29.

Zienkiewicz, O.C. and Zhu, J.Z., 1987. A simple error estimator and adaptive procedure for practical engineering analysis. *International Journal for Numerical Methods in Engineering*, 24, p337-57.

Zienkiewicz, O.C. and Zhu, J.Z., 1992a. The superconvergent patch recovery and a posteri error estimates. Part 1: the recovery technique. *International Journal for Numerical Methods in Engineering*, 33, p1331-64.

Zienkiewicz, O.C. and Zhu, J.Z., 1992b. The superconvergent patch recovery and a posteri error estimates. Part 2: error estimates and adaptivity. *International Journal for Numerical Methods in Engineering*, 33, p1365-82.

Appendix A. Notation for BEM submatrices

This appendix describes the BEM matrix subdivision in greater detail than the main text, with focus on the practical implementation of the method in code. The BEM global system matrix $\mathbf{H}$ comprises $n/2$ sets of equations, one set per collocation point as collocated at $n/2$ nodes on the boundary from $s = 0$ to $s = S$, and thus can be subdivided into

$$\hat{\mathbf{H}} = \begin{bmatrix} \hat{\mathbf{H}}(s = s_1) \\ \vdots \\ \hat{\mathbf{H}}(s = s_{n/2}) \end{bmatrix} \tag{A.1}$$

Each instance of collocation at source point P_s provides sets of two equations that can be subdivided into L submatrices, one for each of the L elements on s

$$\hat{\mathbf{H}}(P_s) = \begin{bmatrix} \hat{\mathbf{H}}^1(P_s) & \dots & \hat{\mathbf{H}}^L(P_s) \end{bmatrix} \tag{A.2}$$

Each term comprises sets of two equations that can be subdivided into k submatrices, one for each of the number of nodes defining element e

$$\hat{\mathbf{H}}^e(P_s) = \begin{bmatrix} \hat{\mathbf{H}}^{e1}(P_s) & \dots & \hat{\mathbf{H}}^{ek}(P_s) \end{bmatrix} \tag{A.3}$$

Each term can be subdivided into four terms, corresponding to the two coefficients (columns) of each of the two degrees of freedom u_{kx}^e and u_{ky}^e associated with node k of element e

$$\hat{\mathbf{H}}^{ek}(P_s) = \begin{bmatrix} \hat{h}_{xx}^{ek}(P_s) & \hat{h}_{xy}^{ek}(P_s) \\ \hat{h}_{yx}^{ek}(P_s) & \hat{h}_{yy}^{ek}(P_s) \end{bmatrix} \tag{A.4}$$

Each such term can be expanded explicitly in terms of the portion of their respective fundamental solutions

$$\hat{\mathbf{H}}^{ek}(P_s) = \begin{bmatrix} \int_{\Gamma_e} T_{xx}^{e*}(P_s)\mathrm{d}\Gamma_e & \int_{\Gamma_e} T_{xy}^{e*}(P_s)\mathrm{d}\Gamma_e \\ \int_{\Gamma_e} T_{yx}^{e*}(P_s)\mathrm{d}\Gamma_e & \int_{\Gamma_e} T_{yy}^{e*}(P_s)\mathrm{d}\Gamma_e \end{bmatrix} \tag{A.5}$$

where, for $i, j = x, y$,

$$\int_{\Gamma_\mathrm{B}} T_{ij}^{*}(P_s, P_f)\mathrm{d}\Gamma_\mathrm{B} = \sum_{e=1}^{L} \int_{\Gamma_e} T_{ij}^{e*}(P_s)\mathrm{d}\Gamma_e \tag{A.6}$$

Defined in terms of the local coordinate η^e, these submatrices are written

$$\hat{\mathbf{H}}^{ek}(P_s) = \begin{bmatrix} \int_{-1}^{+1} T_{xx}^{e*}(P_s)N_k(\eta^e)J^e\mathrm{d}\eta^e & \int_{-1}^{+1} T_{xy}^{e*}(P_s)N_k(\eta^e)J^e\mathrm{d}\eta^e \\ \int_{-1}^{+1} T_{yx}^{e*}(P_s)N_k(\eta^e)J^e\mathrm{d}\eta^e & \int_{-1}^{+1} T_{yy}^{e*}(P_s)N_k(\eta^e)J^e\mathrm{d}\eta^e \end{bmatrix} \tag{A.7}$$

or

$$\hat{\mathbf{H}}^{ek}(P_s) = \int_{-1}^{+1} \begin{bmatrix} T_{xx}^{e*}(P_s) & T_{xy}^{e*}(P_s) \\ T_{yx}^{e*}(P_s) & T_{yy}^{e*}(P_s) \end{bmatrix} \begin{bmatrix} N_k(\eta^e) & 0 \\ 0 & N_k(\eta^e) \end{bmatrix} J^e\mathrm{d}\eta^e \tag{A.8}$$

where N_k is the k^{th} polynomial shape function and J^e is the Jacobian of element e. Similarly

$$\mathbf{G}^{ek}(P_s) = \int_{-1}^{+1} \begin{bmatrix} U_{xx}^{e*}(P_s) & U_{xy}^{e*}(P_s) \\ U_{yx}^{e*}(P_s) & U_{yy}^{e*}(P_s) \end{bmatrix} \begin{bmatrix} N_k(\boldsymbol{\eta}^e) & 0 \\ 0 & N_k(\boldsymbol{\eta}^e) \end{bmatrix} J^e \mathrm{d}\boldsymbol{\eta}^e \tag{A.9}$$

$$\mathbf{H}'^{ek}(P_s) = \int_{-1}^{+1} \begin{bmatrix} S_{xx}^{e*}(P_s) & S_{xy}^{e*}(P_s) \\ S_{yx}^{e*}(P_s) & S_{yy}^{e*}(P_s) \end{bmatrix} \begin{bmatrix} N_k(\boldsymbol{\eta}^e) & 0 \\ 0 & N_k(\boldsymbol{\eta}^e) \end{bmatrix} J^e \mathrm{d}\boldsymbol{\eta}^e \tag{A.10}$$

$$\hat{\mathbf{G}}'^{ek}(P_s) = \int_{-1}^{+1} \begin{bmatrix} D_{xx}^{e*}(P_s) & D_{xy}^{e*}(P_s) \\ D_{yx}^{e*}(P_s) & D_{yy}^{e*}(P_s) \end{bmatrix} \begin{bmatrix} N_k(\boldsymbol{\eta}^e) & 0 \\ 0 & N_k(\boldsymbol{\eta}^e) \end{bmatrix} J^e \mathrm{d}\boldsymbol{\eta}^e \tag{A.11}$$

where

$$\begin{bmatrix} S_{xx}^{e*}(P_s) & S_{xx}^{e*}(P_s) \\ S_{xx}^{e*}(P_s) & S_{xx}^{e*}(P_s) \end{bmatrix} = \begin{bmatrix} n_x(P_s) & 0 & n_y(P_s) & 0 \\ 0 & n_x(P_s) & 0 & n_y(P_s) \end{bmatrix} \begin{bmatrix} S_{xxx}^* & S_{xxy}^* \\ S_{xyx}^* & S_{xyy}^* \\ S_{yxx}^* & S_{xyy}^* \\ S_{yyx}^* & S_{yyy}^* \end{bmatrix} \tag{A.12}$$

$$\begin{bmatrix} D_{xx}^{e*} & D_{xy}^{e*} \\ D_{yx}^{e*} & D_{yy}^{e*} \end{bmatrix} = \begin{bmatrix} n_x(P_s) & 0 & n_y(P_s) & 0 \\ 0 & n_x(P_s) & 0 & n_y(P_s) \end{bmatrix} \begin{bmatrix} D_{xxx}^* & D_{xxy}^* \\ D_{xyx}^* & D_{xyy}^* \\ D_{yxx}^* & D_{xyy}^* \\ D_{yyx}^* & D_{yyy}^* \end{bmatrix} \tag{A.13}$$

Further, the displacements $\mathbf{u}^{ek}$ and tractions $\mathbf{t}^{ek}$ corresponding to node k of element e are denoted

$$\mathbf{u}^{ek} = \begin{Bmatrix} u_x^{ek} \\ u_y^{ek} \end{Bmatrix} \tag{A.14}$$

$$\mathbf{t}^{ek} = \begin{Bmatrix} t_x^{ek} \\ t_y^{ek} \end{Bmatrix} \tag{A.15}$$

Appendix B. Displacement modes of a square domain

This appendix illustrates 64 sample displacement modes (red) associated with the deformation of a domain (black). This appendix is included for reference only and it should be noted that the order of the modes is arbitrary. Some of the more identifiable modes are summarised in the table below.

Number (m)	Mode	Description
1		y-translation
2		x-translation
3		expansion
4		pinch
5		y-stretch
6		rotation

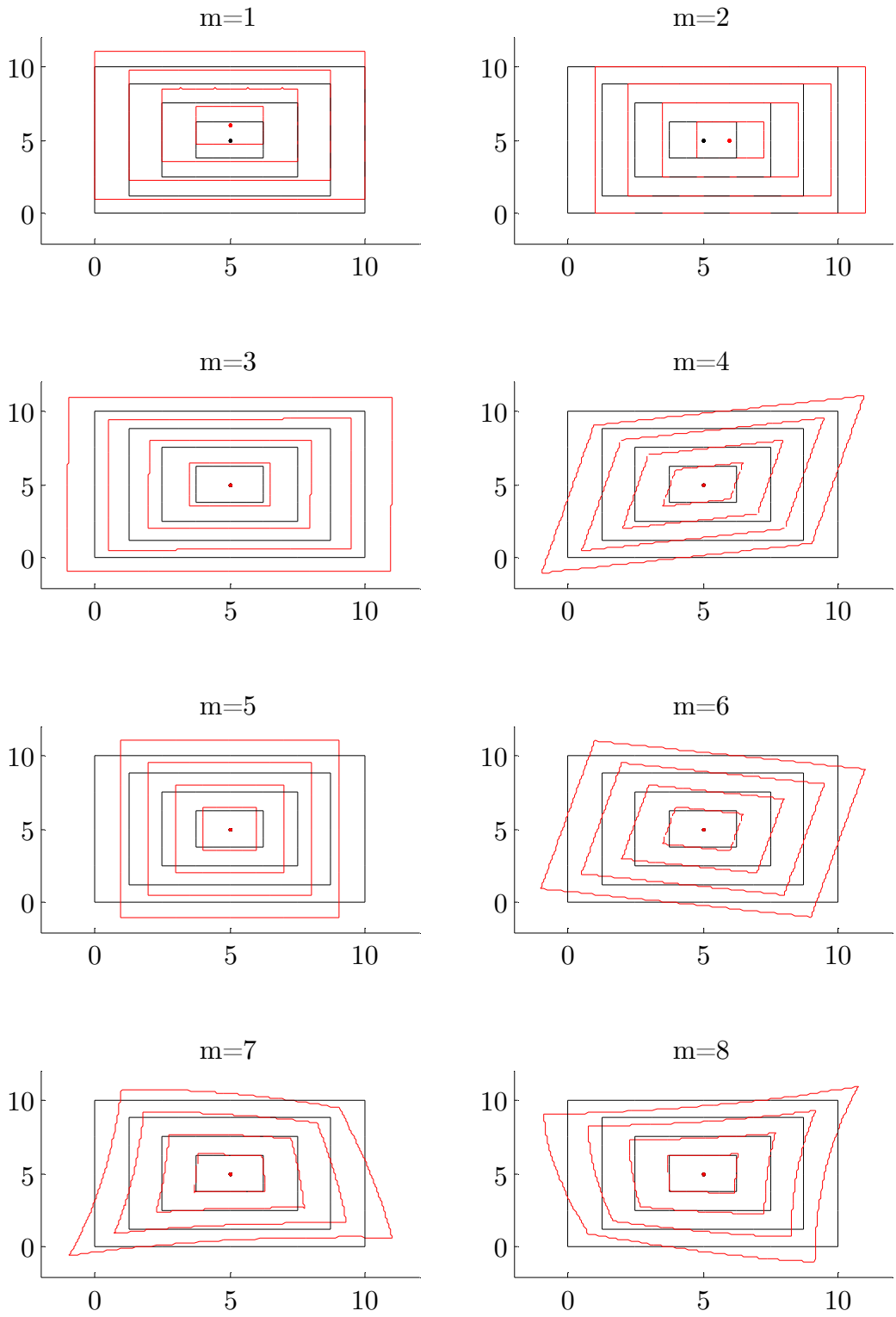
m=1
m=2
m=3
m=4
m=5
m=6
m=7
m=8
10
5
0
0
5
10

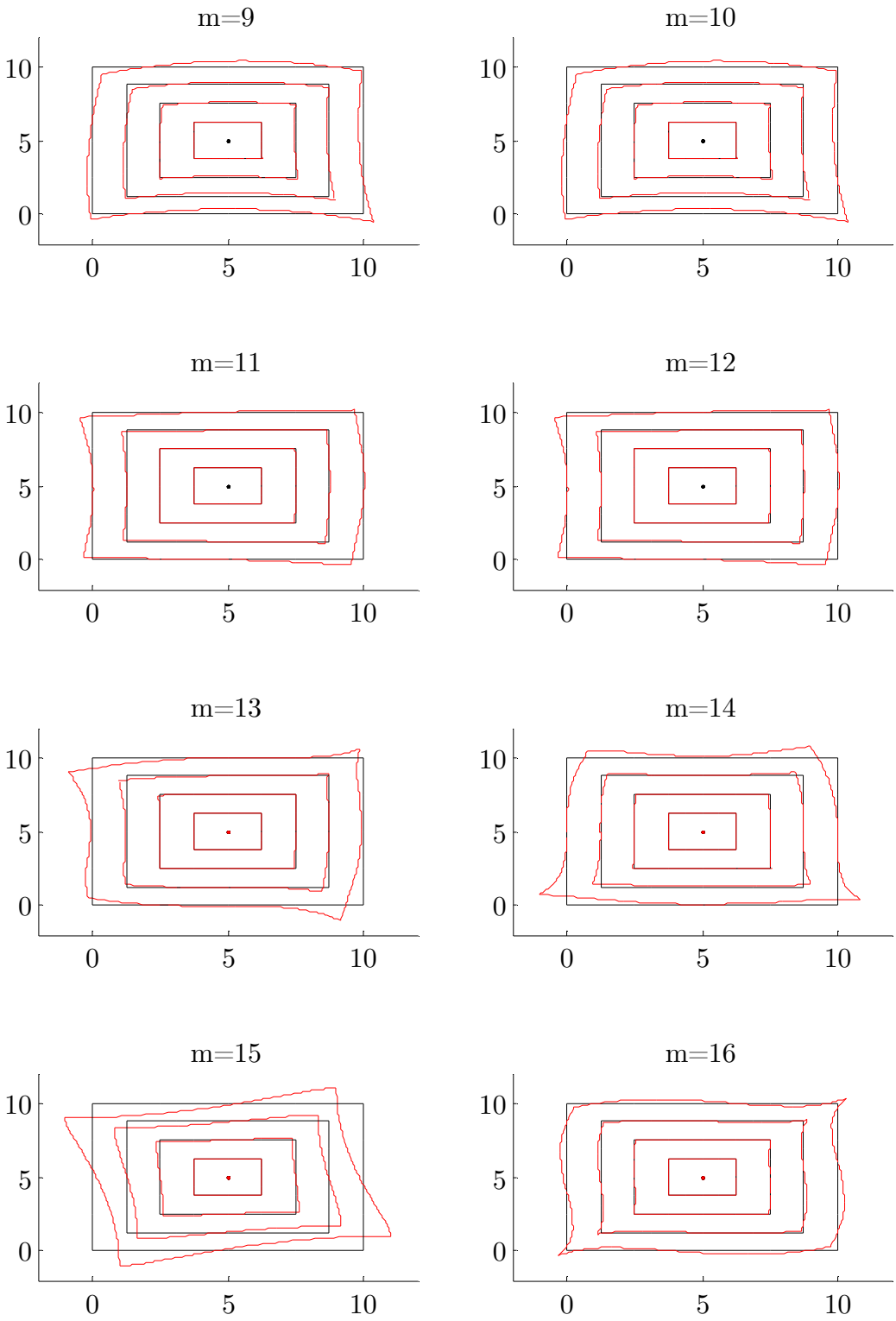
m=9
m=10
m=11
m=12
m=13
m=14
m=15
m=16
0
5
10

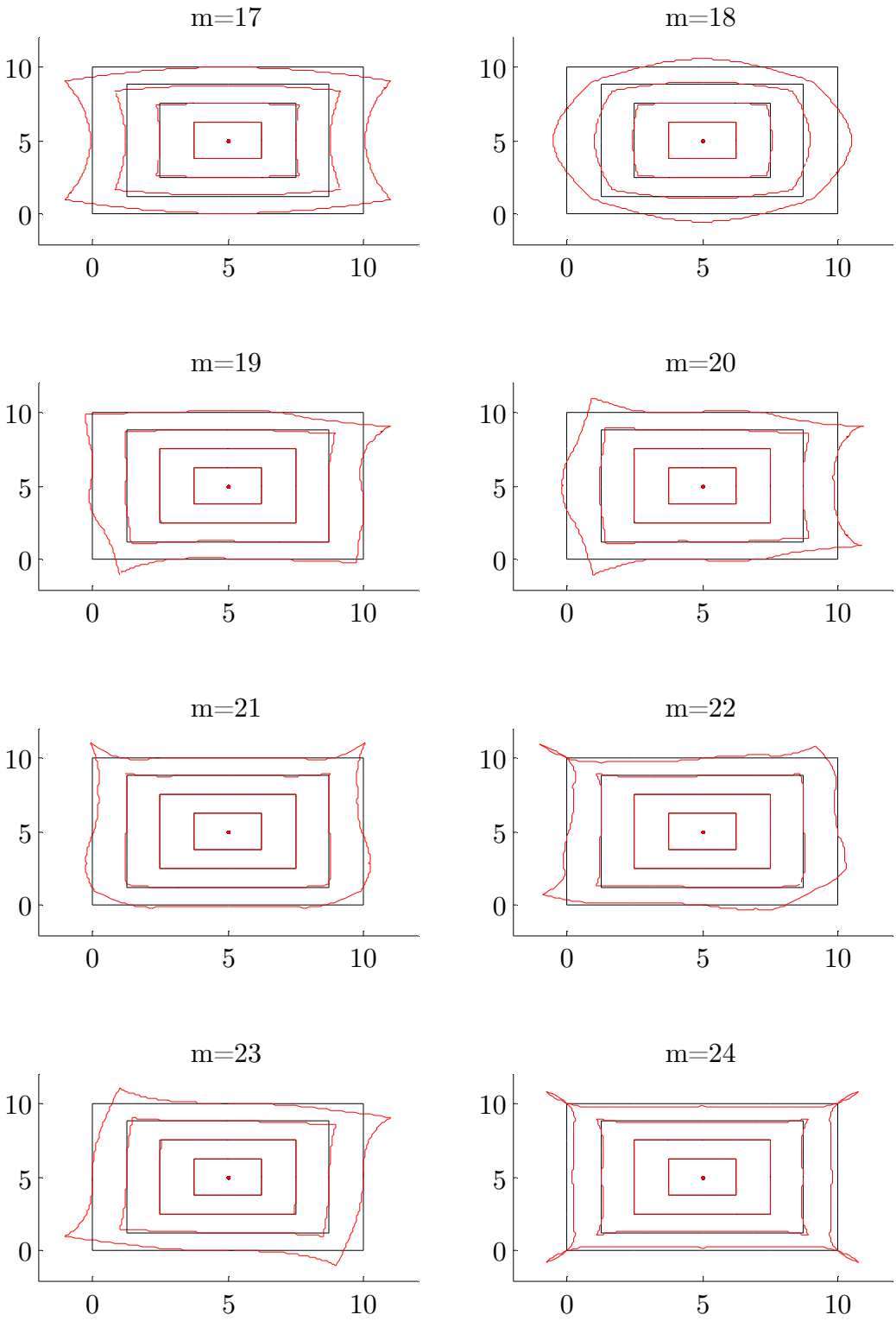
m=17
m=18
m=19
m=20
m=21
m=22
m=23
m=24
0
5
10

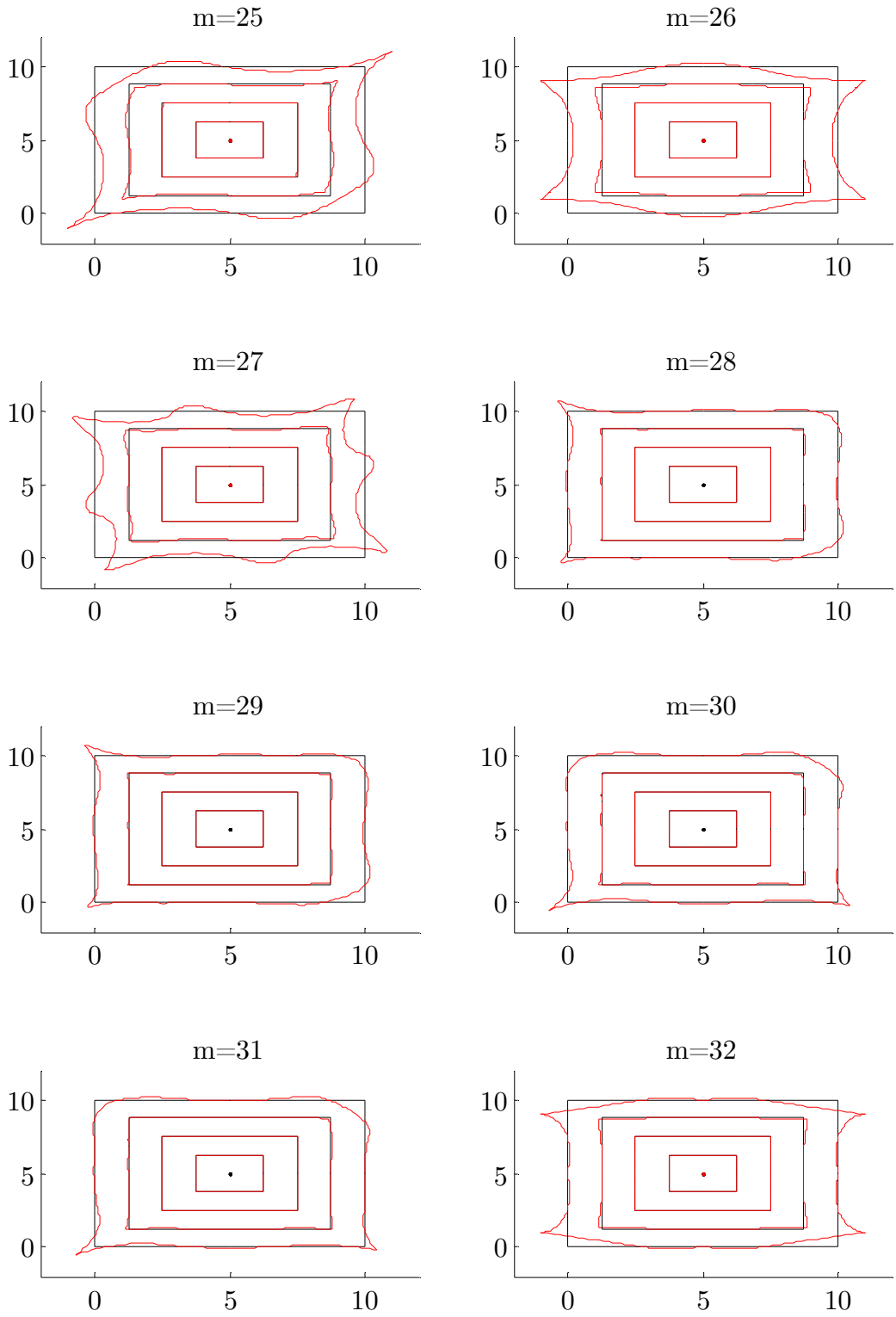
m=25
m=26
m=27
m=28
m=29
m=30
m=31
m=32
0
5
10

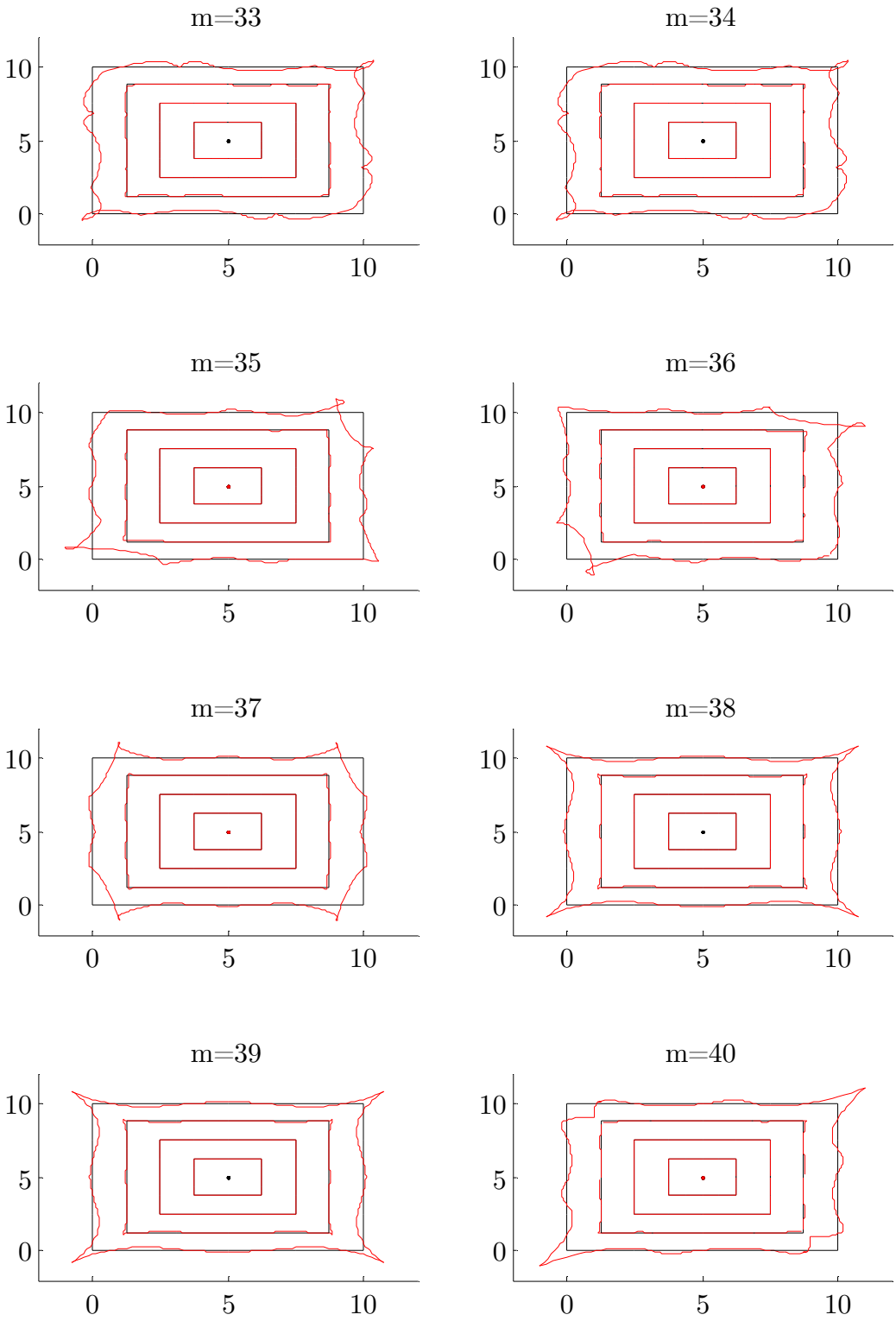
m=33
m=34
m=35
m=36
m=37
m=38
m=39
m=40
0
5
10

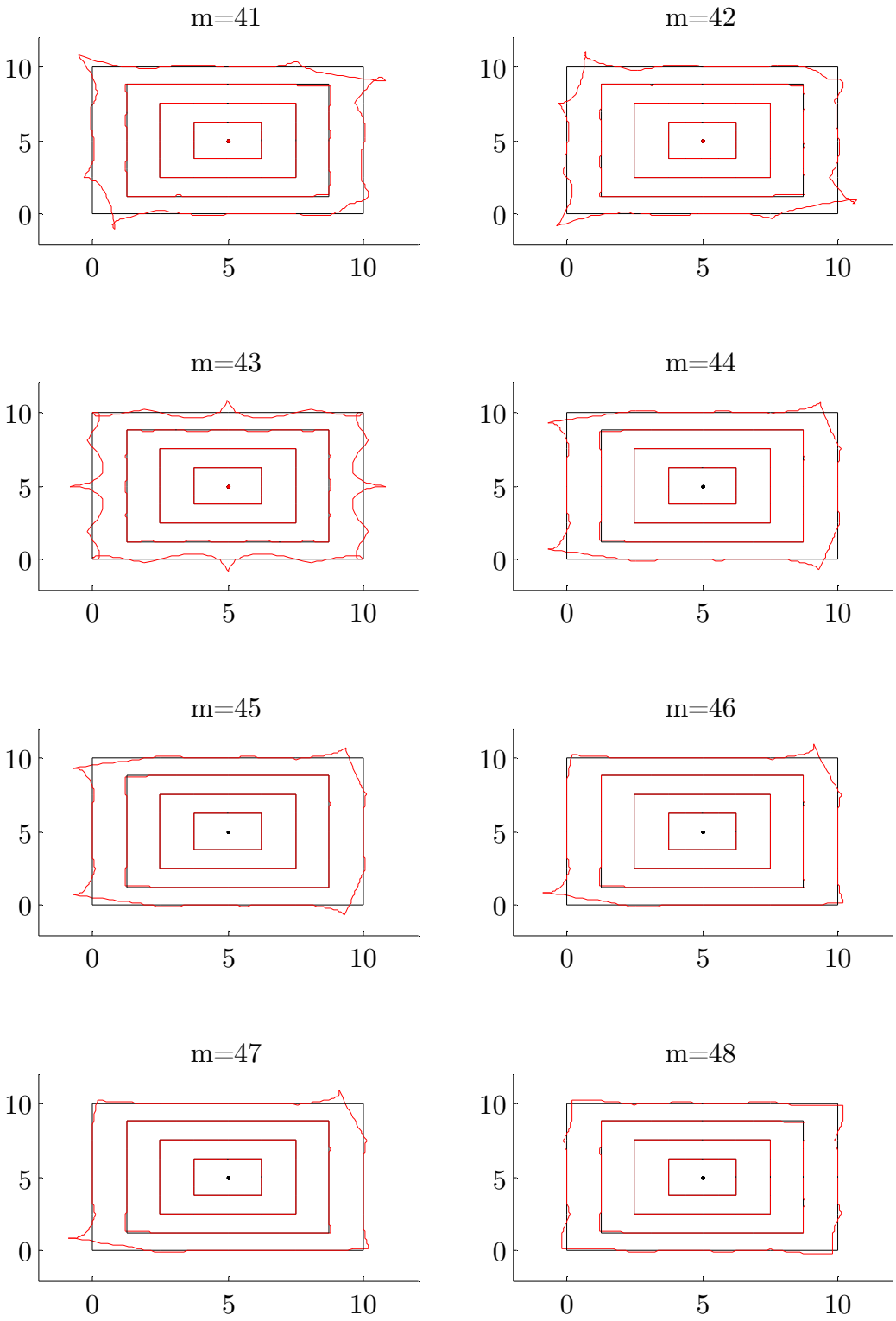
m=41
m=42
m=43
m=44
m=45
m=46
m=47
m=48
0
5
10

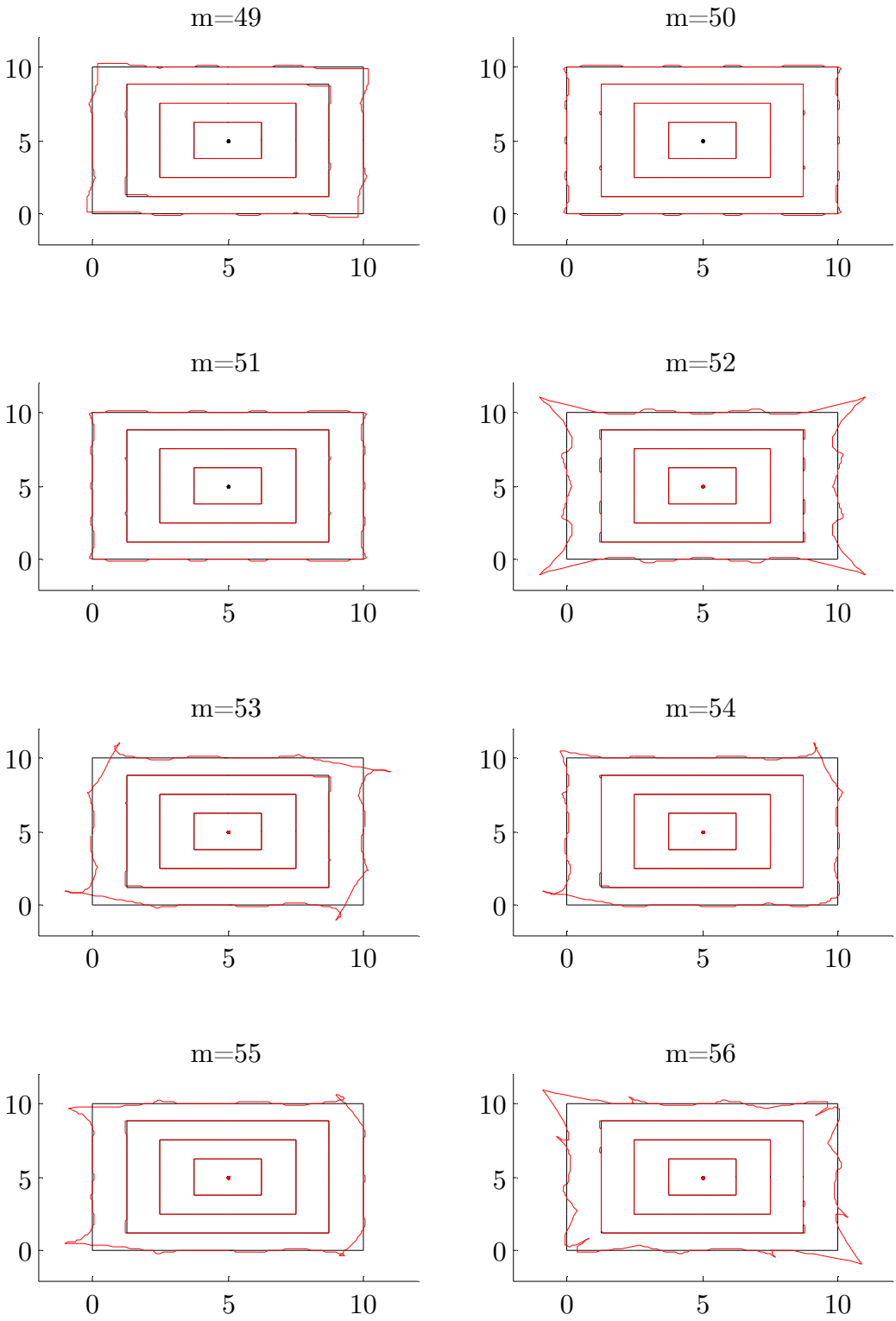
m=49
m=50
m=51
m=52
m=53
m=54
m=55
m=56
10
5
0
0
5
10

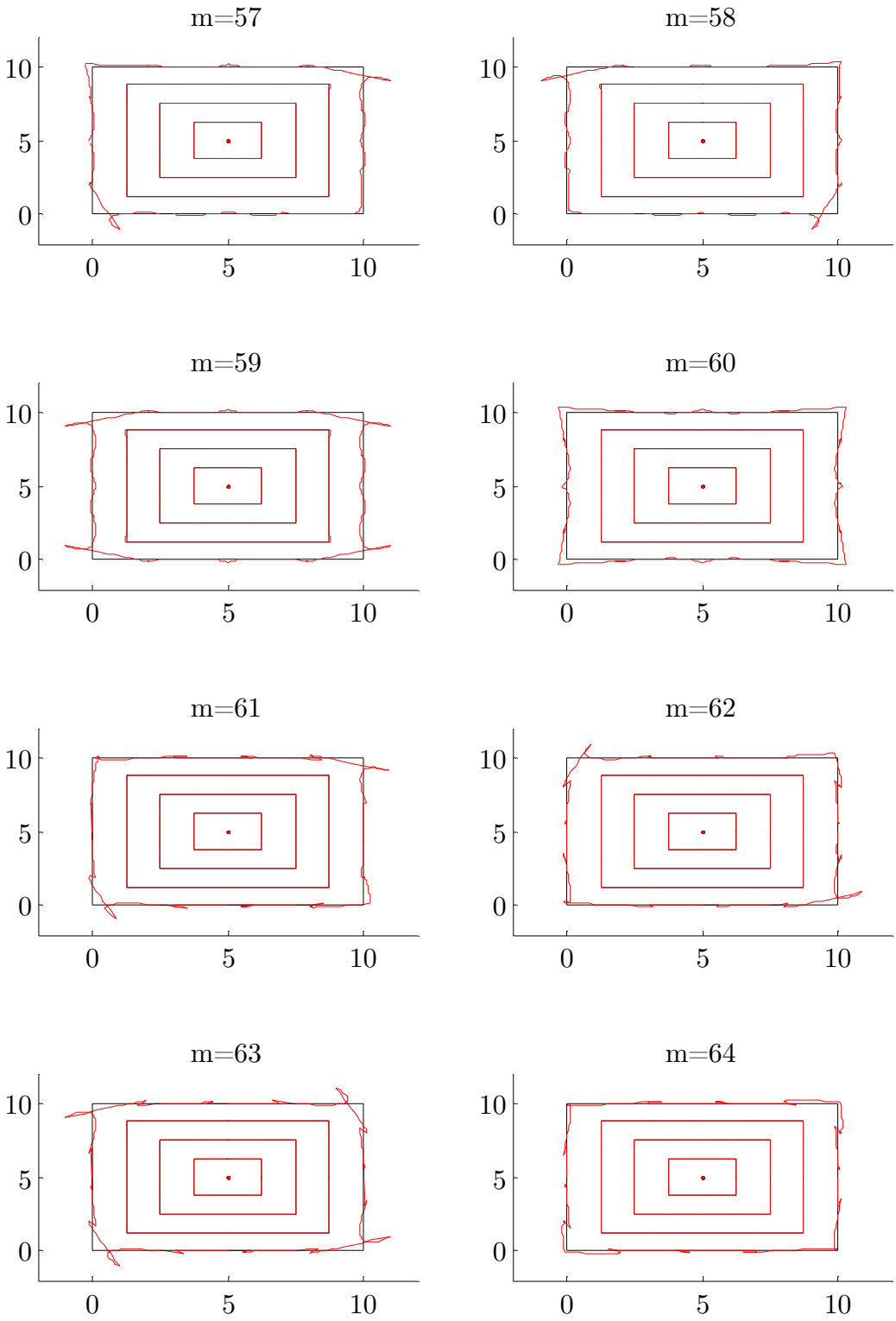
m=57
m=58
m=59
m=60
m=61
m=62
m=63
m=64
10
5
0
0
5
10

Appendix C. Displacement modes of a triangular domain

Included purely for reasons of comparison with Appendix B, this appendix illustrates some of the modes associated with a triangular domain. It can be noted some of the modes are similar to those in Appendix B, but that the order may differ. In both cases, the mode orders are in principle, arbitrary, but their formulation using the scaled boundary finite element method ensures that some modes are formed in the same order.

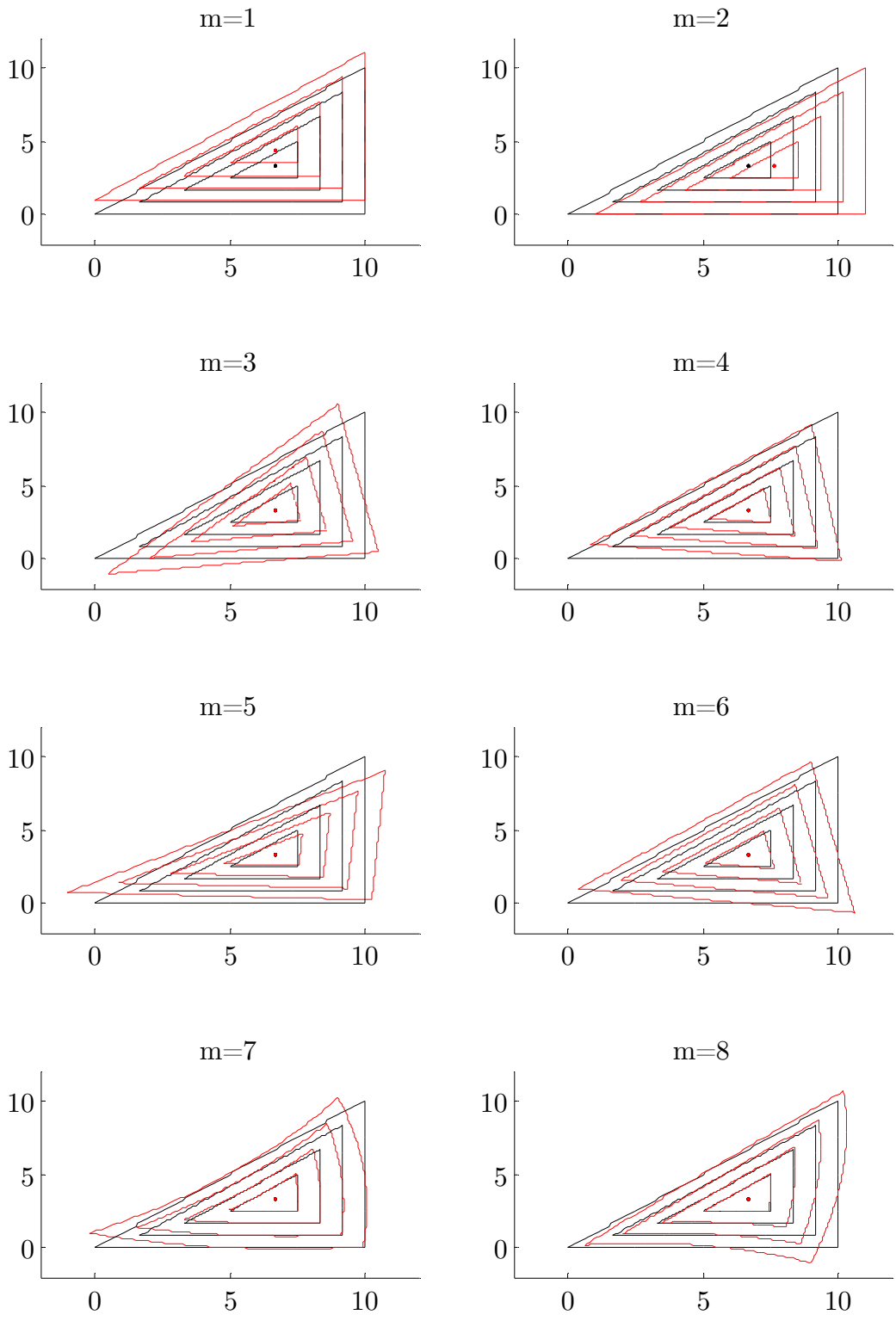
m=1
m=2
m=3
m=4
m=5
m=6
m=7
m=8
10
5
0
0
5
10

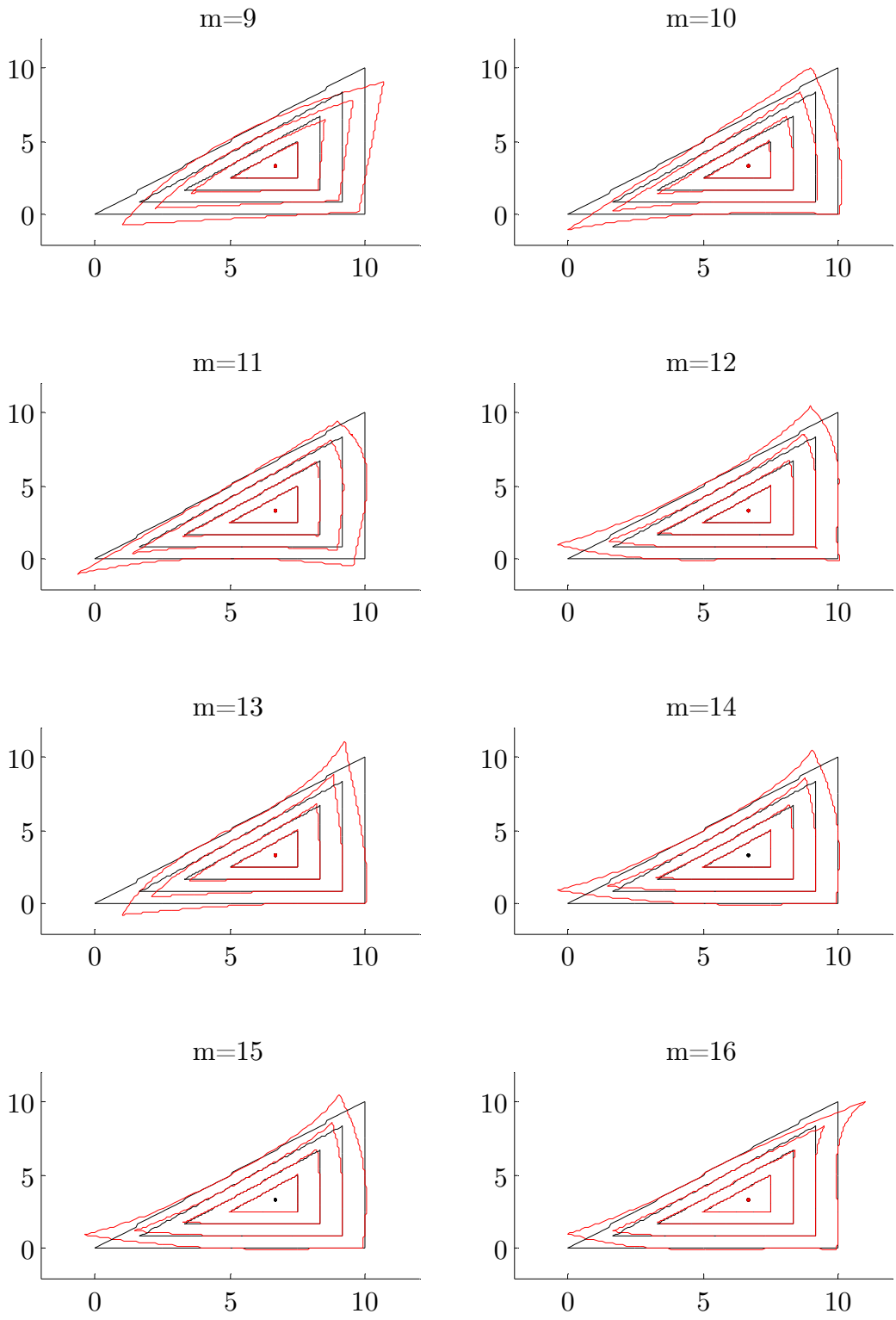
m=9
m=10
m=11
m=12
m=13
m=14
m=15
m=16
0
5
10

Appendix D. Stress and strain transformation for the SBFEM

This appendix details the transformation of the terms necessary in equation (3.8) for the derivation of the scaled boundary finite element method (SBFEM). This appendix extends the transformation as described by Deeks and Wolf (Deeks and Wolf, 2002a).

For any point $p(x, y)$ relative to some fixed Cartesian origin (x_0, y_0) within a domain Ω, with body forces neglected, internal equilibrium requires

$$\mathbf{L}^{\mathrm{T}}\boldsymbol{\sigma}(x, y) = 0 \tag{D.1}$$

where the stresses at $p(x, y)$ are given by

$$\boldsymbol{\sigma}(x, y) = \begin{Bmatrix} \sigma_{xx} & \sigma_{yy} & \sigma_{xy} \end{Bmatrix}^{\mathrm{T}} \tag{D.2}$$

and $\mathbf{L}$ is the linear operator that relates the displacements $\mathbf{u}(x, y)$ and the strains $\boldsymbol{\varepsilon}(x, y)$ such that

$$\boldsymbol{\varepsilon}(x, y) = \mathbf{L}\mathbf{u}(x, y) \tag{D.3}$$

where

$$\mathbf{L} = \begin{bmatrix} \dfrac{\partial}{\partial x} & 0 \\ 0 & \dfrac{\partial}{\partial y} \\ \dfrac{\partial}{\partial y} & \dfrac{\partial}{\partial x} \end{bmatrix} \tag{D.4}$$

$$\boldsymbol{\varepsilon}(x,y) = \begin{Bmatrix} \sigma_{xx} & \sigma_{yy} & \sigma_{xy} \end{Bmatrix}^{\mathrm{T}} \tag{D.5}$$

$$\mathbf{u}(x,y) = \begin{Bmatrix} u_x & u_y \end{Bmatrix}^{\mathrm{T}} \tag{D.6}$$

These stresses and strains are related by the elasticity matrix $\mathbf{D}$ such that

$$\boldsymbol{\sigma}(x,y) = \mathbf{D}\boldsymbol{\varepsilon}(x,y) \tag{D.7}$$

where

$$\mathbf{D} = \frac{E}{(1+\nu)(1-2\nu)} \begin{bmatrix} 1-\nu & \nu & 0 \\ \upsilon & 1-\nu & 0 \\ 0 & 0 & \frac{1-2\nu}{2} \end{bmatrix} \tag{D.8}$$

for plane strain models and

$$\mathbf{D}_\sigma = \frac{E}{1-\nu^2} \begin{bmatrix} 1 & \nu & 0 \\ \nu & 1 & 0 \\ 0 & 0 & \frac{1-\nu}{2} \end{bmatrix} \tag{D.9}$$

for plane stress models. Decomposing $\mathbf{L}$ gives

$$\mathbf{L} = \mathbf{L}_1 \frac{\partial}{\partial x} + \mathbf{L}_2 \frac{\partial}{\partial y} \tag{D.10}$$

where

$$\mathbf{L}_1 = \begin{bmatrix} 1 & 0 \\ 0 & 0 \\ 0 & 1 \end{bmatrix} \tag{D.11}$$

$$\mathbf{L}_2 = \begin{bmatrix} 0 & 0 \\ 0 & 1 \\ 1 & 0 \end{bmatrix} \tag{D.12}$$

These partial derivatives in the Cartesian system are related to the partial derivatives in the scaled boundary co-ordinate system by

$$\frac{\partial}{\partial \xi} = \frac{\partial}{\partial x}\frac{\partial x}{\partial \xi} + \frac{\partial y}{\partial \xi}\frac{\partial}{\partial y} \tag{D.13}$$

$$\frac{\partial}{\partial s} = \frac{\partial}{\partial x}\frac{\partial x}{\partial s} + \frac{\partial}{\partial y}\frac{\partial y}{\partial s} \tag{D.14}$$

or in the Jacobian matrix form

$$\begin{Bmatrix} \frac{\partial}{\partial \xi} \\ \frac{\partial}{\partial s} \end{Bmatrix} = \begin{bmatrix} \frac{\partial x}{\partial \xi} & \frac{\partial y}{\partial \xi} \\ \frac{\partial x}{\partial s} & \frac{\partial y}{\partial s} \end{bmatrix} \begin{Bmatrix} \frac{\partial}{\partial x} \\ \frac{\partial}{\partial y} \end{Bmatrix} \tag{D.15}$$

Taking partial derivatives of equations with respect to ξ

$$\frac{\partial x}{\partial \xi} = x(s) \tag{D.16}$$

$$\frac{\partial y}{\partial \xi} = y(s) \tag{D.17}$$

and with respect to s

$$\frac{\partial x}{\partial s} = \xi x(s)_{,s} \tag{D.18}$$

$$\frac{\partial y}{\partial s} = \xi y(s)_{,s} \tag{D.19}$$

which, when substituted into equation (D.15) gives

$$\begin{Bmatrix} \frac{\partial}{\partial \xi} \\ \frac{\partial}{\partial s} \end{Bmatrix} = \begin{bmatrix} x(s) & y(s) \\ \xi x(s)_{,s} & \xi y(s)_{,s} \end{bmatrix} \begin{Bmatrix} \frac{\partial}{\partial x} \\ \frac{\partial}{\partial y} \end{Bmatrix} \tag{D.20}$$

or

$$\begin{Bmatrix} \dfrac{\partial}{\partial \xi} \\ \dfrac{1}{\xi}\dfrac{\partial}{\partial s} \end{Bmatrix} = \begin{bmatrix} x(s) & y(s) \\ x(s)_{,s} & y(s)_{,s} \end{bmatrix} \begin{Bmatrix} \dfrac{\partial}{\partial x} \\ \dfrac{\partial}{\partial y} \end{Bmatrix} \tag{D.21}$$

which by introducing Jacobian matrix $\mathbf{J}(s)$

$$\begin{Bmatrix} \dfrac{\partial}{\partial \xi} \\ \dfrac{1}{\xi}\dfrac{\partial}{\partial s} \end{Bmatrix} = \mathbf{J}(s) \begin{Bmatrix} \dfrac{\partial}{\partial x} \\ \dfrac{\partial}{\partial y} \end{Bmatrix} \tag{D.22}$$

gives

$$\begin{Bmatrix} \dfrac{\partial}{\partial x} \\ \dfrac{\partial}{\partial y} \end{Bmatrix} = \frac{1}{|\mathbf{J}(s)|} \begin{bmatrix} y(s)_{,s} & -y(s) \\ -x(s)_{,s} & x(s) \end{bmatrix} \begin{Bmatrix} \dfrac{\partial}{\partial \xi} \\ \dfrac{1}{\xi}\dfrac{\partial}{\partial s} \end{Bmatrix} \tag{D.23}$$

where the shorthand comma notation "," denotes a derivative and

$$|\mathbf{J}(s)| = x(s)y(s)_{,s} - y(s)x(s)_{,s} \tag{D.24}$$

Thus, $\mathbf{L}$ is rewritten

$$\mathbf{L} = \mathbf{L}_1 \frac{1}{|\mathbf{J}(s)|}\left(y(s)_{,s} \frac{\partial}{\partial \xi} - y(s)\frac{1}{\xi}\frac{\partial}{\partial s} \right) + \mathbf{L}_2 \frac{1}{|\mathbf{J}(s)|}\left(-x(s)_{,s} \frac{\partial}{\partial \xi} + x(s)\frac{1}{\xi}\frac{\partial}{\partial s} \right) \tag{D.25}$$

or for convenience

$$\mathbf{L} = \mathbf{b}_1(s)\frac{\partial}{\partial \xi} + \mathbf{b}_2(s)\frac{1}{\xi}\frac{\partial}{\partial s} \tag{D.26}$$

where

$$\mathbf{b}_1(s) = \frac{1}{|\mathbf{J}(s)|}\left(\mathbf{L}_1 y(s)_{,s} - \mathbf{L}_2 x(s)_{,s}\right) \tag{D.27}$$

$$\mathbf{b}_2(s) = \frac{1}{|\mathbf{J}(s)|}\left(-\mathbf{L}_1 y(s) - \mathbf{L}_2 x(s)\right) \tag{D.28}$$

By transforming the strains from Cartesian to the scaled boundary coordinate system

$$\boldsymbol{\varepsilon}(\xi, s) = \mathbf{L}\,\mathbf{u}(\xi, s) \tag{D.29}$$

and discretising in the s-direction, it follows

$$\delta\boldsymbol{\varepsilon}_h(\xi, s) = \mathbf{L}\mathbf{N}(s)\delta\mathbf{u}(\xi) \tag{D.30}$$

or

$$\delta\boldsymbol{\varepsilon}_h(\xi, s) = \mathbf{b}_1(s)\mathbf{N}(s)\frac{\partial}{\partial\xi}\delta\mathbf{u}(\xi) + \frac{1}{\xi}\mathbf{b}_2(s)\mathbf{N}(s)\frac{\partial}{\partial s}\delta\mathbf{u}(\xi) \tag{D.31}$$

which, for convenience, is rewritten

$$\delta\boldsymbol{\varepsilon}_h(\xi, s) = \mathbf{B}_1(s)\delta\mathbf{u}(\xi)_{,\xi} + \frac{1}{\xi}\mathbf{B}_2(s)\delta\mathbf{u}(\xi) \tag{D.32}$$

and the $h$subscript indicates an approximation to its respective parameter and is indicative of the level of discretisation[vii], and

$$\mathbf{B}_1(s) = \mathbf{b}_1(s)\mathbf{N}(s) \tag{D.33}$$

$$\mathbf{B}_2(s) = \mathbf{b}_2(s)\mathbf{N}(s)_{,s} \tag{D.34}$$

[vii] Conventionally, the use of this subscript indicates that which the approximation is expected to offer improvement with h-adaptivity; with the SBFEM, h-adaptivity alone may not be sufficient to improve this approximation.

Similarly, by transforming the stresses from Cartesian to the scaled boundary coordinate system

$$\boldsymbol{\sigma}(\xi, s) = \mathbf{D}\boldsymbol{\varepsilon}(\xi, s) \tag{D.35}$$

and discretising in the s-direction, it follows

$$\boldsymbol{\sigma}_h(\xi, s) = \mathbf{D}\left(\mathbf{B}_1(s)\boldsymbol{\delta}\mathbf{u}(\xi)_{,\xi} + \frac{1}{\xi}\mathbf{B}_2(s)\boldsymbol{\delta}\mathbf{u}(\xi) \right) \tag{D.36}$$

The change in volume $\mathrm{d}\boldsymbol{\Omega}$ of the domain is given by

$$\mathrm{d}\Omega = |\mathbf{J}(\xi, s)|\xi \mathrm{d}\xi \mathrm{d}s \tag{D.37}$$

where $|\mathbf{J}(\xi, s)|$ is the determinant of the Jacobian at the boundary. Because at the boundary $\xi = 1$, this can be rewritten with in terms of s only

$$\mathrm{d}\Omega = |\mathbf{J}(s)|\xi \mathrm{d}\xi \mathrm{d}s \tag{D.38}$$

Thus, the transformed principle of virtual work statement, transformed from the Cartesian coordinate system

$$\int_{\Gamma_S} \delta u(x,y)^{\mathrm{T}} t(x,y) \mathrm{d}\Gamma_S - \int_{\Omega_S} \delta\varepsilon(x,y)^{\mathrm{T}} \sigma(x,y) \mathrm{d}\Omega_S = 0 \tag{D.39}$$

into the scaled boundary coordinate system

$$\int_{\Gamma_S} \delta u(s)^{\mathrm{T}} t(s) \mathrm{d}\Gamma_S - \int_{\Omega_S} \delta\varepsilon(\xi,s)^{\mathrm{T}} \sigma(\xi,s) \mathrm{d}\Omega_S = 0 \tag{D.40}$$

is given by

$$\int_{\Omega} \delta\boldsymbol{\varepsilon}_h(\xi,s)^{\mathrm{T}}\boldsymbol{\sigma}_h(\xi,s)\mathrm{d}\Omega$$
$$-\int_S\int_0^1 \left[\mathbf{B}_1(s)\delta\mathbf{u}(\xi)_{,\xi} + \frac{1}{\xi}\mathbf{B}_2(s)\delta\mathbf{u}(\xi)\right]^{\mathrm{T}}\left[\mathbf{D}\mathbf{B}_1(s)\delta\mathbf{u}(\xi)_{,\xi} + \mathbf{D}\mathbf{B}_2(s)\frac{1}{\xi}\delta\mathbf{u}(\xi)\right]|\mathbf{J}(s)|\xi\mathrm{d}\xi\mathrm{d}s$$
$$= \mathbf{0} \tag{D.41}$$

or

$$\delta\mathbf{u}(\xi_\Gamma)^{\mathrm{T}}\left(\mathbf{E}_0\mathbf{u}(\xi_\Gamma)_{,\xi} + \mathbf{E}_1{}^{\mathrm{T}}\mathbf{u}(\xi_\Gamma) - \mathbf{p}(\xi_\Gamma)\right)$$
$$-\int_0^1 \delta\mathbf{u}(\xi)^{\mathrm{T}}\left(\mathbf{E}_0\xi\mathbf{u}(\xi)_{,\xi\xi} + \left(\mathbf{E}_0 + \mathbf{E}_1{}^{\mathrm{T}} - \mathbf{E}_1\right)\mathbf{u}(\xi)_{,\xi} - \frac{1}{\xi}\mathbf{E}_2\mathbf{u}(\xi)\right)\mathrm{d}\xi$$
$$= 0 \tag{D.42}$$

where ξ_Γ indicates ξ at the boundary, i.e. where $\xi = 1$.

Appendix E. Traction-force transformation

This appendix details the transformation of nodal forces into equivalent tractions, as necessary in the coupling of the boundary element method (BEM) and the scaled boundary finite element method (SBFEM) as described in this thesis.

Consider a domain Ω bounded by Γ, subdivided into a BEM subdomain Ω_B bounded by Γ_B, and a SBFEM subdomain Ω_S bounded by Γ_S, separated by a common interface Γ_I, as illustrated in Figure 116(a) and (b). For compatibility across Γ_I, the nodal displacements of an interface element from the perspective of the BEM region must match those of the SBFEM. Similarly, for equilibrium across the interface, the tractions on the BEM side of the element must match those of the SBFEM. However, because the SBFEM formulates a displacement-force relationship, these forces must be transformed into tractions (or *vice versa*) in order to satisfy these conditions. For the element shown in Figure 116, the relationship between the nodal forces f_i^{ek} and equivalent nodal tractions t_i^{ek}, for $i = x, y$ and $k = 1, 2, 3$, is given by

$$\begin{Bmatrix} f_i^{e1} \\ f_i^{e2} \\ f_i^{e3} \end{Bmatrix} = \begin{bmatrix} \int_{-1}^{+1} N_1 N_1 J(\eta^e)\mathrm{d}\eta^e & \int_{-1}^{+1} N_1 N_2 J(\eta^e)\mathrm{d}\eta^e & \int_{-1}^{+1} N_1 N_3 J(\eta^e)\mathrm{d}\eta^e \\ \int_{-1}^{+1} N_2 N_1 J(\eta^e)\mathrm{d}\eta^e & \int_{-1}^{+1} N_2 N_2 J(\eta^e)\mathrm{d}\eta^e & \int_{-1}^{+1} N_2 N_3 J(\eta^e)\mathrm{d}\eta^e \\ \int_{-1}^{+1} N_3 N_1 J(\eta^e)\mathrm{d}\eta^e & \int_{-1}^{+1} N_3 N_2 J(\eta^e)\mathrm{d}\eta^e & \int_{-1}^{+1} N_3 N_3 J(\eta^e)\mathrm{d}\eta^e \end{bmatrix}^e \begin{Bmatrix} t_i^{e1} \\ t_i^{e2} \\ t_i^{e3} \end{Bmatrix} \tag{E.1}$$

or

$$\mathbf{f}^e = \mathbf{M}^e \mathbf{t}^e \tag{E.2}$$

where $N_k(\eta^e)$ is denoted as N_k for brevity (Becker, 1992). Thus, a system can be made by enforcing equilibrium across all the interface elements

$$\mathbf{f} = (-)\mathbf{M}\mathbf{t} \tag{E.3}$$

where the minus sign is introduced for convention as the unit normal at the nodes of the interface element differs from the perspective of the BEM and SBFEM by a factor of -1, as illustrated in Figure 116(c) and (d).

The assumption here is that the Cartesian coordinate systems local to both subdomains are in the same direction. In the case that the Cartesian coordinate systems of Ω_S (x_S, y_S) differs from that of Ω_B (x_B, y_B) by an angle of θ, then the following transformation should be included in relating the BEM tractions to the SBFEM forces

$$\mathbf{f} = -\mathbf{t}_\theta \mathbf{M}\mathbf{t} \tag{E.4}$$

where $\mathbf{t}_\theta$ is the transformation matrix

$$\mathbf{t}_\theta = \begin{bmatrix} \cos\theta & -\sin\theta \\ \sin\theta & \cos\theta \end{bmatrix} \tag{E.5}$$

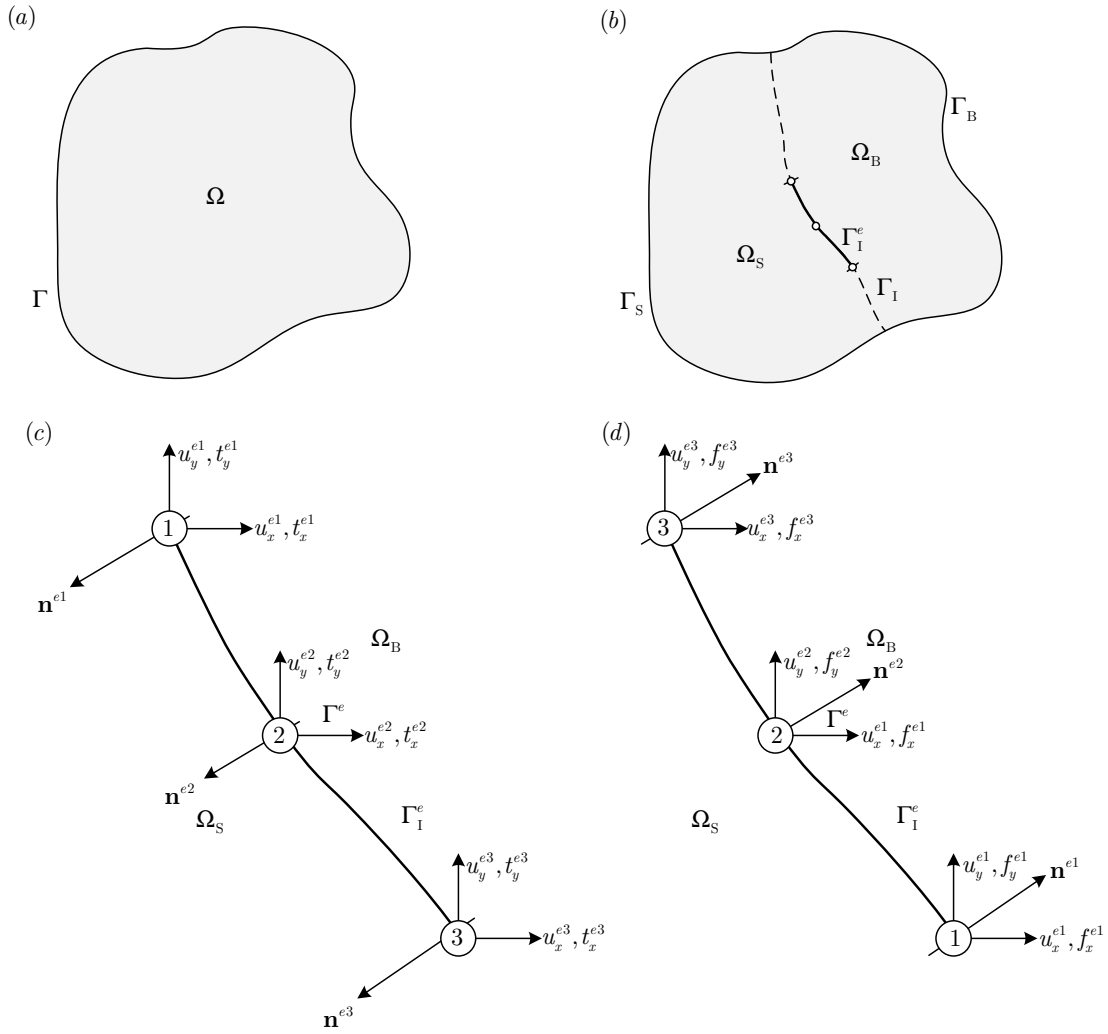

Figure 116. Subdivision of domain (a) Ω and Γ into (b) Ω_{B}, Ω_{S}, Γ_{B}, Γ_{S} and Γ_{I} and the interface elements from the perspective of (c) the BEM and (d) the SBFEM

Appendix F. Functional testing

Consider the following function

$$f(x, y) = xy \tag{F.1}$$

and the results of its implementation by these MATLAB codes.

Implementation 1

```
function result = f(x, y)
      result = x + y;
end
```

x	y	expected f(x,y)	actual f(x,y)	Result
0	0	0	0	pass
1	1	1	2	fail
2	2	4	4	pass
-3	-3	9	-6	fail
-4	4	-16	0	fail
1. 0000000000000001	1	1. 0000000000000001	2	fail

Implementation 2

```
function result = f(x, y)
      result = abs(x * y);
end
```

x	y	expected f(x,y)	actual f(x,y)	Result
0	0	0	0	pass
1	1	1	1	pass
2	2	4	4	pass
-3	-3	9	9	pass
-4	4	-16	16	fail
1. 0000000000000001	1	1. 0000000000000001	1	fail

Implementation 3

```
function result = f(x, y)
      result = x * y;
end
```

x	y	expected f(x,y)	actual f(x,y)	Result
0	0	0	0	pass
1	1	1	1	pass
2	2	4	4	pass
-3	-3	-9	-9	pass
-4	4	-16	-16	pass
1. 0000000000000001	1	1. 0000000000000001	1	fail

It can be seen that each implementation offers a working solution. By increasing the range of cases chosen to tests the implementations, their respective limitations become clearer. It may be possible to prove the range of limitations of a particular function. But in general terms, this is not practical and instead an estimation of its limitations is made. This estimation may be improved by increasing the range of tests applied to the function.

This approach can be taken for all such 'black-box' functional testing, regardless of its complexity. However, the simpler the function, the easier it is to determine an exact expected result and so the more reliable the test. Well-written code can be tested in this way without concern for the reliability of any lower-level functionality; the assertion that the use of a lower-level function conforms to the limitations of that function should suffice. Such lower-level functionality should be tested separately.

Appendix G. Code integrity

This appendix summaries the efforts made by the author to restrict the coding errors and to take confidence in the validity of the results.

At the start of the project, individual SBFEM and BEM codes were available to the author to assist in the development of the coupled BE-SBFEM algorithm. However, the SBFEM code written by Chidgzey *et al.* was deemed insufficiently flexible to demonstrate its robustness and to offer reliable results with confidence and the BEM code written by Trevelyan *et al.* was geared towards commercial and teaching goals, rather than the evolutionary support of additional academic functionality. Thus, the was decision made to rewrite in full all code associated with this project under a modern computer science framework using established design patterns (Freeman and Freeman, 2004) complemented by a protocol of automated testing.

Vigorous unit-testing (Astels, 2003) helped prevent additional errors creeping into the code as the result of rectifying other errors. The wide range of acceptance tests outlined below illustrates the robustness of the code and allows the user to analyse the results with confidence that the end product

conforms to a required quality. Further, a normalised evolution of the code achieved by refactoring (Fowler *et al.*, 1999) offered more structure and maintainability to the software than that of a more *ad hoc* approach often found in academic engineering code.

Some of the acceptance testing included the parametric testing of benchmark problems with known, analytical solutions. With each problem type, a range of models were analysed and the results compared to the analytical solution, with mesh-refinement convergence assessed and monitored. Parametric variations included model geometry, mesh density, material properties, boundary conditions etc and mixtures of domain and subdomain types.

Despite the 'black box' nature of the algorithms described in this thesis and the testing methods geared towards such operations time and resource constraints have prevented this approach being used to the extent to which its developer would have preferred. Pragmatic decisions have been made to reduce some testing in order to further develop the code, leading to certain assumptions about its quality. In some areas, computational efficiency has been sacrificed for improved maintainability and as such, some of the computational times offered in the results in this thesis should be observed with a degree of caution.